Microphysically based modelling of fault friction and earthquake rupture

M. P. A. van den Ende

Utrecht Studies in Earth Sciences
Nº. 153

Members of the dissertation committee:

prof. dr. Stephen Cox
Earth Dynamics Group, Australian National University
Acton, Australia

prof. dr. Arwen Deuss
Seismology Group, Utrecht University
Utrecht, the Netherlands

prof. dr. Julia Morgan
Department of Earth Sciences, Rice University
Houston, Texas, United States of America

prof. dr. Stefan Nielsen
Department of Earth Sciences, Durham University
Durham, United Kingdom

dr. Hiroyuki Noda
Disaster Prevention Research Institute, Kyoto University
Kyoto, Japan

This study was conducted at the High Pressure and Temperature Laboratory (Experimental Rock Deformation Group), Department of Earth Sciences, Faculty of Geosciences, Utrecht University, Utrecht, the Netherlands

This study was funded by the European Research Council

Printed by: Gildeprint, Enschede

ISBN/EAN: 978-90-6266-504-4

Cover image: Discrete Element Model of a direct shear experiment (see Chapter 4)

Microphysically based modelling of fault friction and earthquake rupture

Microfysisch modelleren van wrijving op breuken en scheuring van aardbevingen

(met een samenvatting in het Nederlands)

Proefschrift

ter verkrijging van de graad van doctor aan de Universiteit Utrecht op gezag van de rector magnificus prof. dr. H.R.B.M. Kummeling, ingevolge het besluit van het college voor promoties in het openbaar te verdedigen op vrijdag 15 juni 2018 des middags te 2.30 uur

door

Martijn Peter Anton van den Ende

geboren op 24 september 1990 te 's-Gravenhage

Promotor: Prof. dr. C. J. Spiers

Copromotor: Dr. A. R. Niemeijer

"There's always one more bug"

Lubarsky's Law of Cybernetic Entomology

Contents

Summary **XIII**

Samenvatting **XIX**

1 General introduction **1**
1.1 Motivation and scope of this study 2
1.2 The seismic character and structure of faults 3
1.3 Characterisation of fault rocks in a laboratory setting 7
1.4 Models for fault friction 12
1.4.1 Slip weakening 12
1.4.2 Rate-and-state friction 13
1.4.3 Microphysically based models 16
1.5 Aims of this thesis 20

2 Investigating compaction by intergranular pressure solution using the Discrete Element Method **23**
2.1 Introduction 25
2.2 Previous work on compaction via pressure solution 29
2.2.1 Constitutive relations for pressure solution 29
2.2.2 Effect of a distributed grain size 32
2.3 Numerical methods and procedure 33
2.3.1 Basic DEM approach 33
2.3.2 Numerical stability and scaling 37
2.3.3 Validation tests 40

2.3.4 Testing effects of friction and distributed grain size 43
2.4 Results of benchmark simulations 46
2.4.1 Comparison with laboratory experiments 46
2.4.2 Stress dependence 48
2.4.3 Grain size dependence 49
2.5 Potential mechanisms for strain rate reduction 50
2.5.1 Effect of interparticle friction 50
2.5.2 Effects of a distributed grain size 52
2.6 Conclusions 57
Appendix 2.A Experimental procedure 61
Appendix 2.B Effect of stiffness 65
Appendix 2.C Data availability 66

3 Influence of grain boundary structural evolution on pressure solution creep rates 67
3.1 Introduction 69
3.2 Previous work on pressure solution and grain boundary healing 70
3.2.1 Pressure solution in theory and experiment 70
3.2.2 Pressure solution retardation mechanisms 72
3.2.3 Observations of grain boundary structure 74
3.2.4 Thermodynamics of grain boundary healing and sealing 76
3.3 Microphysical model for grain boundary evolution 78
3.3.1 Grain boundary evolution model 78
3.3.2 Grain boundary connectivity 85
3.3.3 Scale-dependence of grain boundary topography 88
3.3.4 Analytical model for pressure solution with grain boundary evolution 89
3.4 Analytical model predictions versus experiments on halite 91
3.5 DEM model for pressure solution with grain boundary evolution 93
3.5.1 Basic DEM approach 94
3.5.2 Numerical stability and scaling relations 98
3.5.3 DEM model procedure 98
3.6 Simulation results and comparison with data of *Schutjens* (1991b) . . . 100
3.7 Discussion 102

3.7.1 Structure and dynamics of a wetted grain contact under stress . 104
3.7.2 Relation between grain boundary evolution and intergranular pressure solution 105
3.7.3 Implications of the present findings for pressure solution in nature 106
3.8 Conclusions 108
Appendix 3.A Laboratory procedure of *Schutjens* (1991b) 111

4 An investigation into the role of time-dependent cohesion in interseismic frictional restrengthening 113
4.1 Introduction 115
4.1.1 Previous work on interseismic restrengthening 117
4.2 Laboratory methods 121
4.2.1 Description of apparatus 121
4.2.2 Sample material and preparation 123
4.2.3 Laboratory procedure 124
4.2.4 Data analysis 125
4.2.4.1 Time-dependence of friction and cohesion 125
4.2.4.2 Localisation of shear strain 126
4.3 Numerical methods 127
4.3.1 General description of the Discrete Element Method 127
4.3.2 DEM implementation of pressure solution 131
4.3.3 DEM implementation of grain boundary evolution and cohesion . 132
4.3.4 Numerical stability and scaling 136
4.3.5 Simulation set-up and procedure 137
4.4 Laboratory results 140
4.5 Numerical results 145
4.5.1 Initial sliding and hold behaviour 145
4.5.2 Resliding behaviour 147
4.5.3 Frictional restrengthening 149
4.5.4 Localisation of shear strain 152
4.6 Discussion 155
4.6.1 Comparison with previous work 155
4.6.2 Localisation in laboratory and numerical experiments 156
4.6.3 Mechanisms for time-dependent restrengthening 158

4.6.4 Operation of grain boundary evolution in nature 160
4.6.5 Implications for the seismic cycle 162
4.7 Summary and conclusions 164

5 A comparison between rate-and-state friction and microphysical models, based on simulations of fault slip 167
5.1 Introduction 169
5.2 Microphysical framework 173
5.3 Numerical methods 181
5.3.1 Implementation of the microphysical model 181
5.3.2 Simulation procedure 183
5.3.2.1 Model set-up 183
5.3.2.2 Comparison of the CNS implementation with rate-and-state friction 187
5.4 Results 189
5.4.1 Steady-state behaviour 189
5.4.2 Transient fault slip behaviour 194
5.5 Discussion 197
5.5.1 Velocity-dependence of friction 198
5.5.2 Comparison of the RSF simulation with previous work 201
5.5.3 Event magnitude and frictional stability 202
5.5.4 Rupture nucleation 204
5.5.5 Rupture arrest 209
5.5.6 Modes of fault slip 211
5.5.7 The role of dynamic weakening processes and frictional heating . 214
5.5.8 Implications and outlook 216
5.6 Conclusions 217
Appendix 5.A Description of the boundary element method 219
Appendix 5.B Slip weakening and characteristic length scale 221

6 Microphysical mechanisms behind giant earthquakes and seismic supercycles 225
6.1 Introduction 227
6.2 Key observations 230

6.2.1 (Palaeo)seismological and geodetic observations of earthquake recurrence . . . 230
6.2.2 Structure and composition of heterogeneous fault zones . . . 233
6.2.3 Results from rate-and-state based modelling studies . . . 237
6.3 Approach and objectives of the present study . . . 239
6.3.1 General model framework . . . 240
6.3.2 Aims of this study . . . 242
6.4 Numerical methods . . . 243
6.4.1 Description of the microphysical model . . . 243
6.4.2 Description of the boundary element method . . . 247
6.4.3 Simulation procedures . . . 248
6.4.3.1 Single- and double-asperity faults . . . 248
6.4.3.2 Heterogeneous faults . . . 251
6.5 Results . . . 253
6.5.1 Single- and double-asperity faults . . . 253
6.5.2 Heterogeneous faults . . . 257
6.5.2.1 Seismic character . . . 257
6.5.2.2 Fault stress and slip deficit . . . 266
6.5.2.3 Nucleation and initiation of T-instabilities . . . 267
6.6 Discussion . . . 271
6.6.1 Mechanisms behind T-instabilities and generality of results . . . 271
6.6.2 Analysis of a single asperity . . . 275
6.6.3 Comparison with rate-and-state friction . . . 280
6.6.4 Interpreting T-instabilities as giant earthquakes . . . 283
6.6.5 Implications of the adopted model rheology . . . 285
6.6.6 Forecasting and precursors of giant earthquakes: implications and outlook . . . 286
6.7 Conclusions . . . 289
Appendix 6.A Rendering the heterogeneous fault structure . . . 291
Appendix 6.B Generating the event catalogue . . . 293

7 Conclusions and outlook **295**
7.1 Main findings of this thesis and their implications . . . 296
7.1.1 Long-term fault gouge densification . . . 296

7.1.2 The importance of time-dependent cohesion 297
7.1.3 Extrapolation of laboratory results through microphysical models 298
7.1.4 Micro-mechanics of earthquakes 299
7.2 General implications for numerical modelling of fault friction 301
7.3 Unresolved issues and future research perspectives 302
7.3.1 The kinetics of fluid-rock interactions 302
7.3.2 The relevance of grain boundary evolution in nature 303
7.3.3 Granular flow parameters H, ϕ_c 304
7.3.4 Localisation and nanograin formation 305
7.3.5 Dynamic weakening 305

Acknowledgements **337**

Curriculum Vitae **345**

List of Figures

1.1 Characteristic structure and rheology of faults 6
1.2 Schematic diagram of the microphysical models 17

2.1 Overview of particle interactions in Discrete Elements 35
2.2 Comparison between laboratory and numerical compaction tests 48
2.3 Sensitivity of model strain rates to applied stress 50
2.4 Sensitivity of model strain rates to particle size 51
2.5 Effects of interparticle friction on compaction behaviour 52
2.6 Pressure solution compaction rates for various particle size distributions 54
2.7 Interparticle stress measurements for various particle size distributions 55
2.A.1 Experimental set-up for uniaxial compaction tests 62
2.A.2 Uniaxial compaction data for granular $NaNO_3$ aggregates 64
2.B.1 Effect of particle stiffness on numerical compaction behaviour 65

3.1 Synopsis of the grain geometries adopted in this work 79
3.2 Results of the isostatic compaction experiments by *Schutjens* (1991b) . 92
3.3 Comparison between analytical models and laboratory results 95
3.4 Geometry of the virtual DEM sample 96
3.5 Comparison between DEM simulations and laboratory results 103

4.1 Schematic illustrations of fluid-rock interactions 120
4.2 Sample assembly and rotary shear apparatus 122
4.3 Overview of the DEM particle interactions and sample geometry 128
4.4 Mechanical results from experiment u473 141

4.5 Overview of the mechanical response of the laboratory samples 143
4.6 Analysis of the time-dependence of friction and cohesion 144
4.7 Mechanical data from the DEM slide-hold simulations 146
4.8 Overview of DEM resliding behaviour 148
4.9 Detailed view of DEM resliding behaviour 150
4.10 Comparison between laboratory and numerical experiments 152
4.11 Localisation behaviour during resliding simulations 154

5.1 Velocity dependence of friction, as predicted by the CNS model 179
5.2 Geometry and boundary conditions of the seismic cycle simulations . . 184
5.3 Representative examples of velocity-step simulations 188
5.4 Depth profiles of μ_{ss}, ϕ_{ss}, and $(a-b)$ for $H = 0.5$ 190
5.5 Depth profiles of μ_{ss}, ϕ_{ss}, and $(a-b)$ for $H = 0.2$ 191
5.6 Spatio-temporal evolution of fault slip for the CNS simulation with $H = 0.5$ 194
5.7 Spatio-temporal evolution of fault slip for the CNS simulation with $H = 0.2$ 195
5.8 Spatio-temporal evolution of fault slip for the RSF simulation 196
5.9 Time series of the depth-averaged friction coefficient and maximum slip velocity 198
5.10 Steady-state depth profiles of $(a-b)$ for various imposed velocities . . 200
5.11 Snapshots of seismic event nucleation and arrest 205
5.12 Depth-profiles and time-series of crack tip propagation and fault slip velocities 208
5.13 Depth-profiles of the interseismic coupling ratio 213
5.B.1 Fracture energy predicted for the CNS model 221

6.1 Visual representation of the fault structure and rheology 234
6.2 Time series of single-asperity simulations ($Z_{ps} = 3 \times 10^{-15}$ Pa^{-1} s^{-1}) . 253
6.3 Time series of single-asperity simulations ($Z_{ps} = 4 \times 10^{-15}$ Pa^{-1} s^{-1}) . 254
6.4 Time series of double-asperity simulations 256
6.5 Filled contour maps of fault slip velocity for a double-asperity simulation 257
6.6 Filled contour maps of fault slip velocity for Set 1 (various D) 258
6.7 Filled contour maps of fault slip velocity for Set 2 (various D) 259

6.8 Filled contour maps of fault slip velocity for Set 1 (various f) 260
6.9 Filled contour maps of fault slip velocity for Set 2 (various f) 261
6.10 Frequency-magnitude distributions of the heterogeneous fault simulations 265
6.11 Average coefficient of friction under which the model fault operates . . 266
6.12 Nucleation behaviour of Set 1 268
6.13 Nucleation behaviour of Set 2 269
6.14 Synoptic illustration of the nucleation of a frictional instability 273
6.15 Style of the instabilities generated by a single-asperity system 279

List of Tables

2.1 Discrete Element Method parameters for validation tests 38
2.2 Discrete Element Method parameters for specific compaction simulations 45

3.1 Parameters used in the analytical model simulations 94
3.2 Parameters used in the DEM simulations 101
3.A.1 Summary of experimental parameters reported by *Schutjens* (1991b) . 112

4.1 List of laboratory experiments 127
4.2 Parameters used in the DEM simulations 140

5.1 List of symbols and parameters for the seismic cycle simulations 182

6.1 List of frequently used symbols and parameters (1) 249
6.2 List of frequently used symbols and parameters (2) 250

Summary

Despite their destructive potential and the disruptive impact that earthquakes have on society, little is known about the exact mechanisms through which earthquakes nucleate and dynamic ruptures propagate. This hampers earthquake hazard assessments and forecasting attempts, which are at present largely based on statistical inferences rather than on physical principles. Laboratory studies of fault friction may contribute to the reliability of earthquake hazard assessments by detailed investigation of the mechanisms involved in fault rock deformation. However, the spatial- and temporal scales of a typical laboratory experiment are dwarfed by those of natural faults and earthquakes, and so upscaling of the laboratory results is required. The extrapolation is often performed through a mathematical framework called *rate-and-state friction* (RSF for short). While the RSF framework is commonly adopted in modelling studies for its mathematical convenience, it is empirical in nature, and so predictions made through the RSF framework must be interpreted with great care.

In this thesis, alternative means of upscaling are explored that are based on physical principles and that have a micro-mechanical origin, as opposed to being empirical. This is done by conducting laboratory experiments, and interpreting the results in terms of micro-scale processes that constitute deformation, such as frictional grain sliding (granular flow) and pressure solution creep. Constitutive relations describing these micro-scale processes are subsequently implemented into numerical models, and the model predictions are tested against laboratory results. Finally, the microphysically based numerical models are used to extrapolate the laboratory observations to natural scales and conditions, and to make predictions pertaining to the natural seismic cycle.

In **Chapter 1**, I give an overview of the present state of knowledge of fault rock deformation, both from experimental and modelling perspectives, and create a scope for this study by highlighting currently unresolved issues. In particular, I focus on the dependence of fault strength on environmental conditions (e.g. temperature), and on loading velocity, which have previously been identified to control the occurrence of earthquakes in the Earth's crust, but are not fully accounted for by commonly used models for fault friction. This chapter is concluded by the formulation of research aims for the thesis chapters that follow.

Fault gouge compaction during interseismic times, facilitated by pressure solution, has been recognised in many studies to operate under seismogenic conditions at significant rates. Constitutive relations describing aggregate compaction by pressure solution therefore play an important role in physically based rheological descriptions of fault rock deformation. While analytical models for pressure solution generally predict the compaction of high-porosity aggregates well, they tend to severely overestimate compaction rates at low porosities, as seen in laboratory compaction tests. Since fault gouges at seismogenic depths likely exhibit low porosities, this discrepancy needs to be clarified. In **Chapter 2**, the theory of intergranular pressure solution creep is revisited, and constitutive relations for pressure solution creep at the grain contact scale are implemented into a Discrete Element Method (DEM) framework. These extended DEM formulations are subsequently employed to numerically simulate uniaxial creep tests, and the model results are compared with those of the simulated laboratory tests, and with analytical solutions. The validated DEM model is then used to systematically investigate various factors that could impact the overall rate of compaction. The results of this study show that inter-grain friction and polydispersed grain size distributions cannot explain the observed retardation of creep rates, as seen in laboratory experiments, and so other mechanisms need to be considered.

As an alternative to the factors mentioned above, it has been hypothesised that a non-stationary, evolving grain boundary structure could inhibit the rate of pressure solution creep, resulting in a reduction of compaction rates and a discrepancy between laboratory data and analytical models that do not account for this effect. Following-up on the preceding chapter, **Chapter 3** explores this hypothesis by presenting a new model for the structural evolution of grain contacts undergoing pressure solution. This

model is derived on the basis of the interplay between elastic strain energy stored in contact asperities and the surface energy of wetted interfaces, and explicitly considers the grain boundary structure in relation to the transport properties of the grain contact zone. Analysis of previous laboratory results shows a favourable agreement with analytical and DEM models for pressure solution that incorporate an evolving grain boundary structure, demonstrating the feasibility of this mechanism for controlling long-term (interseismic) gouge densification rates. This model furthermore predicts that polymineralic gouges are less prone to retardation of compaction rates, a hypothesis that is supported by laboratory observations.

In addition to controlling the overall rate of compaction, grain boundary structural evolution may generate grain-scale cohesion, contributing to the rate of time-dependent strengthening of faults. In the majority of fault friction studies, the contribution of cohesion to the overall fault strength is neglected, and little is know about the mechanisms of generating cohesion in faults. In **Chapter 4**, a suite of laboratory friction experiments designed to assess the time-dependence of the coefficient of friction, and that of cohesion independently, is presented. These experiments clearly show that the internal coefficient of friction and sample cohesion exhibit a time-dependence that is markedly different from one another, suggesting different underlying mechanisms. Numerical DEM simulations that incorporate pressure solution and grain boundary evolution are subsequently performed, mimicking the procedure and conditions of the laboratory experiments. In these simulations, the observed rates of increase of the internal coefficient of friction and of sample cohesion closely match the laboratory values. By comparing numerical simulations with and without grain contact cohesion generated by the structural evolution of the grain contact, the role of cohesion in fault strength and slip stability is illustrated, showing higher weakening rates and faster slip velocities in the presence of cohesion. In addition to the grain boundary structural evolution, other mechanisms that generate grain cohesion likely operate within natural fault zones, and so time-dependent fault cohesion should generally be considered in numerical simulations of fault slip.

The above-summarised chapters consider fault gouge deformation at spatial- and temporal scales relevant for a laboratory setting. However, one of the main applications of microphysically based models is the extrapolation to natural scales and conditions.

In **Chapter 5**, the upscaling based on microphysical model formulations is rigorously performed by implementing one particular class of microphysical models, the *Chen-Niemeijer-Spiers* ("CNS") model, into a numerical seismic cycle simulator, QDYN. The CNS model is governed by the interplay between granular flow and pressure solution creep, two deformation mechanisms that are highly relevant for gouge deformation in nature and in experiments, and that have been investigated intensively in previous chapters of this thesis. The microphysically based seismic cycle simulator is then employed to simulate the long-term seismic cycle slip behaviour of a crustal strike-slip fault, following classical RSF-based numerical studies. The outcomes of the microphysically based simulations are subsequently compared with the results of simulations that are governed by RSF. This comparison shows that the CNS model is capable of reproducing a wide range of fault slip behaviours under natural scales and conditions, previously ascribed only to RSF, although marked differences exist between CNS- and RSF-based simulations in terms of seismic event magnitude and nucleation behaviour. These differences are explained from a microphysical perspective, which facilitates the (qualitative) extrapolation of laboratory results to nature. This chapter then continues to explore a number of features of the CNS numerical simulations, including rupture nucleation and arrest, and rupture propagation speeds.

The avenues newly opened by the microphysically based seismic cycle simulator are explored further in **Chapter 6**, which considers earthquake nucleation and rupture on a more realistic fault structure, following numerous field geologic reports. Field studies indicate that the compositional heterogeneity in large seismogenic fault zones leads to relative contributions of pressure solution creep to the total deformation that are spatially variable. This observation is readily interpretable by the CNS model, and accordingly incorporated in numerical simulations of fault slip. The numerical simulations reveal two different modes of earthquake rupture: frequently occurring, small earthquakes that only rupture a portion of the total fault length, and that are controlled by the local distribution of seismogenic asperities. Occasionally, a seismic event nucleates which spans the full extent of the model fault, largely independent of the local distribution of seismogenic asperities, and which ruptures through regions consisting predominantly of nominally stable, plastically deforming fault segments. It is found that this mode of earthquake rupture is governed by a rheological transition occurring within the nominally stable fault segments, facilitated by an elevated stress

state due to spatially heterogeneous fault slip. The occurrence of fault-spanning earthquakes in the simulations is interpreted to be analogous to the occurrence of great ($M_w > 8$) and giant ($M_w > 9$) earthquakes on subduction megathrusts, which has considerable implications for long-term seismic hazard assessments: while the regular, small earthquakes generated in the simulations occur quasi-randomly in time and space, the large, fault-spanning earthquakes only occur when the fault as a whole has achieved a certain state of stress (i.e. when the fault is 'ready'). This makes the latter class of earthquakes time-predictable on the basis of seismic moment accumulation rates, and non-stochastic as opposed to what is typically assumed in hazard assessments.

This thesis is concluded by **Chapter 7**, which summarises the main findings and implications of this work. In addition, unresolved issues are identified, and directives for future work are provided. The overall conclusion of this thesis is that many crucial aspects of time-dependent fault strengthening and earthquake nucleation are neglected when micro-scale processes are not considered. Microphysical models provide a solid basis for the interpretation of laboratory data, and are suitable means for the extrapolation of laboratory results through their implementation into numerical models. Doing so offers many new opportunities for the investigation of fault rock friction, earthquake nucleation, and rupture propagation. In turn, this will lead to an improved basis for the extrapolation of laboratory results to nature, and ultimately to more reliable earthquake hazard assessments.

Samenvatting

Aardbevingen hebben een grote, vaak ontwrichtende, impact op de maatschappij. Desondanks is er nog maar weinig bekend over de precieze mechanismen waardoor aardbevingen ontstaan. Mede hierdoor worden risicoanalyses voor aardbevingsgebieden voornamelijk bepaald door statistische methodes, in plaats van methodes die gebaseerd zijn op fysische principes. Frictie experimenten in het laboratorium kunnen bijdragen aan het verbeteren van risicoanalyses door de mechanismen die een belangrijke rol spelen bij deformatie van breukgesteenten in detail te bestuderen. Echter, de schaal waarop dit gebeurt in een laboratorium is vele malen kleiner dan in de natuur, zowel ruimtelijk als in tijd. Het is dus nodig om de laboratorium resultaten op te schalen, iets dat vaak wordt gedaan middels een wiskundig raamwerk genaamd *rate-and-state friction* (afgekort tot RSF). De formuleringen in het RSF raamwerk zijn wiskundig eenvoudig in het gebruik, en mede hierom wordt RSF veelvuldig gebruikt in numerieke modellen. De formuleringen hebben echter een empirische oorsprong, waardoor de voorspellingen die voortkomen uit het RSF raamwerk met grote voorzichtigheid geïnterpreteerd moeten worden.

In dit proefschrift bekijk ik alternatieve methodes voor het opschalen van laboratorium resultaten, op basis van fysische principes met een micro-mechanische oorsprong. Dit doe ik door middel van laboratorium experimenten, en door de interpretatie van de resultaten in termen van de microprocessen die leiden tot deformatie, zoals het schuiven van korrels en kruip door drukoplossing. De constitutievergelijkingen die deze processen beschrijven worden vervolgens geïmplementeerd in numerieke modellen, en

de voorspellingen van deze modellen vergelijk ik met laboratorium resultaten. Uiteindelijk gebruik ik de microfysisch onderbouwde numerieke modellen om laboratorium observaties op te schalen naar de dimensies en condities van natuurlijke breuken, en om voorspellingen te doen omtrent natuurlijke cycli van aardbevingen.

In **Hoofdstuk 1** geef ik een overzicht van de huidige kennis over deformatie van breukgesteenten, vanuit zowel een experimenteel- als een modelperspectief, en baken ik het onderwerp van dit proefschrift af door de huidige vraagstukken de benoemen. De focus ligt met name op de afhankelijkheid van de sterkte van breuken van omgevingsvariabelen (zoals temperatuur) en deformatiesnelheid. Deze zijn door eerdere studies aangemerkt als controlerende factoren voor het ontstaan van bevingen in de aardkorst. Dit hoofdstuk wordt afgesloten met een nauwkeurige formulering van de onderzoeksdoelen voor de hoofstukken die volgen.

De compactie van breukmeel (het poedervormige product van wrijving langs de breuk) tijdens de interseismische periode, gefaciliteerd door drukoplossing, vindt doorgaans plaats in een aanzienlijk tempo op dieptes waar aardbevingen ontstaan, iets wat door vele studies is onderstreept. Constitutievergelijkingen die de compactie van aggregaten door drukoplossing beschrijven spelen daarom een belangrijke rol in fysische omschrijvingen van het mechanisch gedrag van breuken. Hoewel analytische modellen voor drukoplossing over het algemeen goed in staat zijn om de compactie van aggregaten met hoge porositeit te voorspellen, hebben ze de neiging om de snelheden van compactie bij lage porositeit sterk te overschatten. Dit is geobserveerd in compactie experimenten in het laboratorium. Het is van belang deze discrepantie te verklaren, aangezien breukmeel op seismogene dieptes waarschijnlijk een lage porositeit heeft. In **Hoofdstuk 2** wordt de theorie achter drukoplossing in detail bekeken, en worden constitutievergelijkingen voor kruip op korrelcontacten door drukoplossing geïmplementeerd in een raamwerk van de zogenaamde Discrete Elementen Methode (DEM). Deze uitgebreide DEM formuleringen worden vervolgens gebruikt om laboratorium experimenten numeriek te simuleren. Het gevalideerde DEM model wordt daarna ingezet om op systematische wijze verschillende factoren te testen die invloed kunnen hebben op de compactiesnelheid. De resultaten van deze studie laten zien dat wrijving tussen de korrels noch polydisperse korrelgrootteverdelingen voldoende in staat zijn om het compactiegedrag geobserveerd in laboratorium experimenten te verklaren. Andere

mechanismen moeten dus overwogen worden.

Als een alternatief voor de hierboven genoemde factoren, is de hypothese gesteld dat veranderingen in de structuur van een korrelcontact het tempo van drukoplossing kan verlagen, met een vermindering van de snelheid van compactie als gevolg. Dit zou het verschil kunnen verklaren tussen laboratorium resultaten en de voorspellingen van analytische modellen die met dit effect geen rekening houden. Voortbouwend op het vorige hoofdstuk wordt in **Hoofdstuk 3** deze hypothese verkend door middel van een nieuw model voor de verandering van de structuur op korrelcontacten tijdens drukoplossing. Dit model is afgeleid op basis van de interactie tussen elastische deformatie van contactpunten en de oppervlakte-energie van bevochtigde oppervlakken. De relatie tussen de structuur van het korrelcontact en de transporteigenschappen wordt hierin expliciet meegenomen. De analyse van eerdere laboratorium resultaten laat een goede overeenkomst zien met analytische en DEM modellen voor drukoplossing met een veranderende contactstructuur. Dit toont aan dat dit mechanisme in staat is om de snelheden van verdichting van breukmeel te controleren over langere tijdsperiodes. Daarnaast voorspelt het model dat breukmeel van heterogene samenstelling minder vatbaar is voor het vertragen van het tempo van drukoplossing, wat wordt ondersteund door laboratorium observaties.

Naast dat een veranderende contactstructuur het tempo van compactie kan controleren, kan het mogelijk ook leiden tot cohesie op de schaal van een korrelcontact. Dit draagt vervolgens bij aan de tijdsafhankelijke sterkte van breuken. In het merendeel van eerdere studies naar breukwrijving wordt de bijdrage van cohesie genegeerd, en er is momenteel weinig bekend over de mechanismen die leiden tot cohesie. In **Hoofdstuk 4** wordt een reeks aan laboratorium experimenten gepresenteerd, welke zijn ontworpen om de tijdsafhankelijkheid van zowel de wrijvingscoëfficiënt als de cohesie onafhankelijk van elkaar te bepalen. Deze experimenten laten duidelijk zien dat de wrijvingscoëfficiënt en cohesie een tijdsafhankelijkheid hebben die sterk van elkaar verschilt, wat suggereert dat de onderliggende mechanismen verschillend zijn. Numerieke DEM simulaties worden uitgevoerd die de experimentele procedure en condities nabootsen, en waarin drukoplossing en een veranderende structuur van korrelcontacten zijn opgenomen. De snelheid van toename van de wrijvingscoëfficiënt en de cohesie zoals geobserveerd in de simulaties komt overeen met de waardes gemeten in het laboratorium. Door

numerieke simulaties met en zonder cohesie op de korrelcontacten, gegenereerd door de veranderende contactstructuur, te vergelijken, wordt de rol die cohesie speelt in de sterkte en stabiliteit van breuken geïllustreerd. In de aanwezigheid van cohesie wordt een snellere verzwakking en snellere beweging van de breuk waargenomen. Naast een veranderende contactstructuur kunnen ook andere mechanismen leiden tot cohesie in natuurlijke breukzones. Tijdsafhankelijke cohesie in breuken zou daarom in ogenschouw genomen moeten worden in numerieke simulaties van breukbeweging.

De hierboven genoemde hoofdstukken beschouwen de deformatie van breukgesteentes op een schaal in ruimte en tijd relevant voor de laboratoriumomgeving. Echter, een belangrijke toepassing van microfysische modellen is de extrapolatie naar natuurlijke schalen en condities. In **Hoofdstuk 5** wordt het opschalen gebaseerd op formuleringen van microfysische modellen op grondige wijze uitgevoerd. Hiervoor wordt het zogenaamde *Chen-Niemeijer-Spiers* ("CNS") model geïmplementeerd in een numerieke aardbevingssimulator, QDYN. Aan de basis van het CNS model ligt de interactie tussen het schuiven van korrels en kruip door drukoplossing, twee deformatie mechanismen die zeer relevant zijn voor de deformatie van breukmeel in natuur zowel als experimenten, en die in detail zijn bekeken in de voorgaande hoofdstukken van dit proefschrift. De microfysisch gebaseerde aardbevingssimulator wordt vervolgens ingezet om het lange-termijn gedrag van een zijschuivingsbreuk te simuleren, in navolging van klassieke RSF-gebaseerde modelstudies. De resultaten van de microfysisch gebaseerde simulaties worden vervolgens vergeleken met de resultaten van simulaties gebaseerd op RSF. Deze vergelijking laat zien dat het CNS model in staat is om een wijd bereik aan breukbewegingen te reproduceren onder natuurlijke omstandigheden, welke voorheen enkel werden toegekend aan RSF. Er zijn echter wel grote verschillen tussen CNS- en RSF-gebaseerde simulaties in termen van de magnitude en het nucleatiegedrag van de aardbevingen. Deze verschillen worden verklaard vanuit een microfysisch perspectief, wat een (kwalitatieve) extrapolatie van laboratorium resultaten faciliteert. In dit hoofdstuk wordt vervolgens een aantal kenmerken verkend van de CNS numerieke simulaties, met onder andere het ontstaan en stoppen van scheuring van aardbevingen, en de voortplantingssnelheid van dergelijke scheuring.

De nieuwe perspectieven geboden door de microfysisch gebaseerde aardbevingssimulator worden verder verkend in **Hoofdstuk 6**, waarin het ontstaan en scheuren van

aardbevingen in een meer realistische breukstructuur wordt bekeken. Veldgeologische studies geven aan dat de compositionele heterogeniteit in grote seismogene breukzones resulteert in ruimtelijk variërende bijdrages van kruip door drukoplossing aan de totale deformatie. Deze observatie is direct te interpreteren middels het CNS model, en kan overeenkomstig worden opgenomen in numerieke simulaties van breukbeweging. De simulaties onthullen twee verschillende wijzen van scheuring van aardbevingen: aan de ene kant zijn er veelvuldig voorkomende, kleine aardbevingen die enkel een gedeelte van de totale breuk scheuren. Aan de andere kant zijn er zo nu en dan aardbevingen die de volledige lengte van de breuk overbruggen, grotendeels onafhankelijk van de lokale verdeling van seismogene contactpunten, en die scheuren door gebieden voornamelijk bestaande uit nominaal stabiele, plastisch deformerende breuksegmenten. Deze wijze van scheuring van aardbevingen wordt gecontroleerd door een reologische transitie. Deze vindt plaats binnenin de nominaal stabiele breuksegmenten, mogelijk gemaakt door een verhoogde staat van spanning als een resultaat van ruimtelijk heterogene breukbeweging. Het ontstaan van breuk-omvattende aardbevingen in de simulaties wordt geïnterpreteerd als een analoog voor het ontstaan van grote ($M_w > 8$) en gigantische ($M_w > 9$) aardbevingen op subductie overschuivingen, wat aanzienlijke implicaties heeft voor lange-termijn analyses van aardbevingsrisico: in tegenstelling tot de normale, kleine aardbevingen die quasi-willekeurig voorkomen in tijd en ruimte, vinden de grote, breuk-omvattende aardbevingen alleen plaats wanneer de breuk in zijn geheel een bepaalde spanningsstaat heeft bereikt (dat is, wanneer de breuk 'gereed' is). Dit maakt het tweede type aardbevingen voorspelbaar op basis van het tempo van toenemen van seismisch moment. Daarnaast is het tweede type aardbevingen niet willekeurig, iets dat over het algemeen wordt aangenomen in risicoanalyses.

Dit proefschrift wordt afgesloten met **Hoofdstuk 7**, waarin een samenvatting wordt gegeven van de voornaamste bevindingen en implicaties van dit werk. Daarnaast worden onopgeloste vraagstukken aangeduid, en worden aanbevelingen gegeven voor toekomstig werk. De algehele conclusie van dit proefschrift is dat het voor vele cruciale aspecten van het tijdsafhankelijk aansterken van breuken en het ontstaan van aardbevingen essentieel is om microprocessen in ogenschouw te nemen. De implementatie van microfysische principes in numerieke modellen legt een fundament voor het betrouwbaar interpreteren van laboratorium resultaten. Deze benadering biedt nieuwe perspectieven voor het onderzoek naar wrijving op breuken, het ontstaan en de voortplanting van scheuring van

aardbevingen. Dit zal vervolgens leiden tot een verbeterde basis voor het extrapoleren van laboratorium resultaten naar de natuur, en uiteindelijk tot meer betrouwbare risicoanalyses van aardbevingen.

Chapter 1

General introduction

1.1 Motivation and scope of this study

Earthquakes are among the most destructive of natural hazards known, and lead to considerable loss of life and property world-wide every year (*Guha-Sapir et al.*, 2016). To reduce the risk associated with seismic events, earthquake hazard assessments are made to estimate the probability of an earthquake of a given magnitude occurring within a chosen time interval, typically in the range of 30 to 100 years (i.e. the long-term earthquake potential; *Petersen et al.*, 2015; *Satake*, 2015; *Sykes et al.*, 1999; *WGCEP*, 1988). Based on these assessments, national disaster programmes and engineering policies are established (*Kanamori*, 2003). However, the reliability of statistically based earthquake hazard assessments, particularly for large events, is severely hampered by the complexity displayed by earthquakes. A classical example is given by the Parkfield earthquake sequence: between 1857 and 1966, the Parkfield section of the San Andreas fault was found to quasi-periodically produce a M_w 6.0 event every 22 years on average, with the next event being anticipated before 1993 (*Bakun and Lindh*, 1985; *Bakun and McEvilly*, 1984). The event did not occur until 2004, raising the question as to why the 2004 event fell out of its historical sequence.

One major contributor to the uncertainty in earthquake hazard assessments, is the relatively short history of modern instrumental recordings in comparison to the recurrence time of large earthquakes. Instrumental records date back no further than 100 years in most places (*McCaffrey*, 2008), whereas large earthquakes with coseismic fault displacements of several metres are expected to recur only once every few centuries (*Satake and Atwater*, 2007). Attempting to perform rigorous statistical analyses on an earthquake catalogue of limited size inherently raises concerns regarding the statistical significance of the outcomes (*Kagan*, 1997; *McCaffrey*, 2008). In order to improve seismic hazard assessments, physical constraints are sought to complement and support statistical analyses of earthquake recurrence times and magnitudes.

As a direct approach to probing the behaviour of faults, laboratory rock deformation experiments have greatly contributed to our understanding of rock friction and seismogenesis. Since the pioneering work of *Brace and Byerlee* (1966) and *Dieterich* (1972), numerous laboratory studies have identified dependencies of steady-state fault friction on e.g. temperature (*Blanpied et al.*, 1998; *Chester and Higgs*, 1992; *Den Hartog et al.*,

2012; *He et al.*, 2007; *Sawai et al.*, 2016), composition (*Bos et al.*, 2000a; *Carpenter et al.*, 2016b; *Kaproth et al.*, 2016), normal stress (*Carpenter et al.*, 2016a; *Chester*, 1994; *Sawai et al.*, 2016), and perhaps most importantly, slip velocity (*Carpenter et al.*, 2016a; *Den Hartog et al.*, 2012; *Reinen et al.*, 1992; *Tesei et al.*, 2014). Laboratory measurements serve as direct input for numerical models, that most commonly employ empirical constitutive relations (e.g. *Lapusta and Rice*, 2003; *Tse and Rice*, 1986). Because of the large variability in the frictional response of rocks, and its highly complex relation with some of the aforementioned quantities, it is questionable to directly apply laboratory-derived values for describing rock friction at natural scales and *in-situ* conditions, which challenges the use of numerical simulations that hinge on empirical formulations.

To overcome this problem, it is paramount to develop a fundamental understanding of fault rock friction that is based on physical principles. Physically based theoretical models can then be used to generalise laboratory results and describe the behaviour of natural faults on temporal and spatial scales beyond those of the laboratory. In this thesis, I combine laboratory observations with microphysical models and numerical techniques to simulate fault rock deformation, both in the laboratory and in nature. The laboratory experiments provide new insights into the micro-mechanics of friction, and serve as a benchmark for analytical and numerical models. In turn, the theoretical models developed in this thesis are used to address previously formulated questions and hypotheses, and offer means to extrapolate laboratory results to nature. Through this integrated approach, I aim to complement existing theories of fault friction and earthquake rupture with models based on microphysical concepts, widening the scope for future seismic hazard assessments.

1.2 The seismic character and structure of faults

Well before the emergence of general plate tectonic theories, it was recognised by *Reid* (1910), presenting his elastic rebound theory, that the 1906 San Francisco earthquake was a catastrophic result of elastic strain release. Since then, facilitated by advances in seismological and geodetical instrumentation, various other phenomena have been identified that can episodically release strain, including (very) low frequency earthquakes

(*Ito and Obara*, 2006; *Obara and Ito*, 2005), slow slip (*Gomberg*, 2010; *Miller et al.*, 2002; *Ohta et al.*, 2006), and non-volcanic tremor (*Obara*, 2002; *Rogers and Dragert*, 2003). The existence of a variety of slip transients suggest a spectrum rather than discrete modes of fault slip (*Gomberg et al.*, 2016; *Peng and Gomberg*, 2010), an interpretation which receives further support from laboratory studies (*Leeman et al.*, 2016; *Scuderi et al.*, 2016). The existence of a spectrum of slip further elicits the possibility that all of these transient phenomena share a common underlying mechanism, but also raises the question what ultimately controls the mode of fault slip.

An important question from a seismic hazard perspective, is that of an upper limit of event magnitude or cut-off magnitude (*Kagan*, 1997). For subduction zone settings it has been debated whether or not each subduction region is intrinsically capable of hosting a $M_w > 9$ event (*Kagan*, 1997; *McCaffrey*, 2008). Based on statistical correlations, e.g. between subducting plate age and maximum recorded event magnitude (*Ruff and Kanamori*, 1980), it was argued that the Andaman and Japan Trench regions were incapable of nucleating M_w 9 events. However, mounting evidence opposed such models (*Goldfinger et al.*, 2013; *McCaffrey*, 1997; *Pacheco et al.*, 1993; *Stein and Okal*, 2007), with the 2004 Sumatra-Andaman and 2011 Tohoku-Oki M_w 9.1 events serving as prime violations. The paucity in instrumental records of giant earthquakes may therefore simply be a statistical deficiency, emanating from an incomplete earthquake catalogue for a given region (*Kagan and Jackson*, 2013; *McCaffrey*, 2008).

Since our instrumental record of regional seismicity falls short with respect to the recurrence time of large earthquakes, attempts are made to extend a given region's earthquake catalogue by examining geological recordings of seismic events. Palaeoseismological studies have reported numerous large earthquakes that are largely absent in present-day instrumental or historical records, documented by e.g. deep-sea turbidites (*Goldfinger et al.*, 2012; *Ratzov et al.*, 2015), tsunami and estuarine deposits (*Cisternas et al.*, 2005), and coral microatolls (*Philibosian et al.*, 2017; *Sieh et al.*, 2008). These studies have revealed 'supercycles' of clustered earthquake occurrences (*Philibosian et al.*, 2017; *Ratzov et al.*, 2015; *Schlagenhauf et al.*, 2011), or cycles of anomalously large events superimposed onto regular earthquake cycles (*Goldfinger et al.*, 2013, 2012). These observations provoke the question of whether these cycles can be predicted, and what underlying physical mechanisms potentially drive long-term

periodicity. Answering such questions can greatly advance seismic hazard assessments.

A critical step towards uncovering earthquake source mechanisms, is relating seismological observations to the physical and chemical properties of the fault zone. In the case of the commonly observed Gutenberg-Richter frequency-magnitude distribution of seismic events (*Gutenberg and Richter*, 1944, 1956), the asperity model (*Lay and Kanamori*, 1981; *Seno*, 2003) establishes a widely-accepted relation between the earthquake magnitude and fault zone structure. In this model, the fault zone is envisioned to exhibit mechanically strong, seismogenic patches ('asperities') of various extent, embedded within an aseismic matrix. Large earthquakes are then thought to nucleate within large asperities, possibly interacting with (clusters of) neighbouring asperities. It could thus be argued that a fractal distribution in asperity size results in a similarly fractal (or power-law) distribution in earthquake magnitudes (*Seno*, 2003). It is, however, not directly evident which geological features should serve as a seismological asperity. As an example, seamounts have been suggested to form mechanical barriers or asperities that host nucleation and dynamic rupture of large earthquakes (*Cloos*, 1992), though compelling evidence has been presented that challenges this view (*Mochizuki et al.*, 2008; *Wang and Bilek*, 2011). In field studies, it has been recognised that large fault zones and tectonic mélanges exhumed from seismogenic depths most commonly feature a block-in-matrix structure of competent lenses embedded within a phyllosilicate-rich, ductile matrix (*Collettini et al.*, 2011; *Fagereng and Sibson*, 2010; *Faulkner et al.*, 2003; *Kimura et al.*, 2012; *Niemeijer and Vissers*, 2014). The competent lenses, which tend to follow a power-law distribution in size (*Fagereng*, 2011), are candidates for seismological asperities, in particular since these lenses are associated with localised, cataclastic deformation (*Collettini et al.*, 2011; *Faulkner et al.*, 2003; *Niemeijer and Vissers*, 2014).

Detailed inspection of the various compositional units comprising a fault zone provides further insights into the rheology of the fault and the mechanisms behind seismogenesis. The vast majority of surface outcrops of faults exhumed from the seismogenic zone, as well as fault zone material retrieved in drilling campaigns, shows evidence for fluid-rock interactions, most notably pressure solution in the form of grain indentations or dissolution seams and vein infill (*Bullock et al.*, 2014; *Fagereng*, 2011; *Hadizadeh et al.*, 2012; *Holdsworth et al.*, 2011; *Jefferies et al.*, 2006; *Kimura et al.*, 2012; *Smeraglia et al.*, 2017). Additionally, pressure solution is often found to be

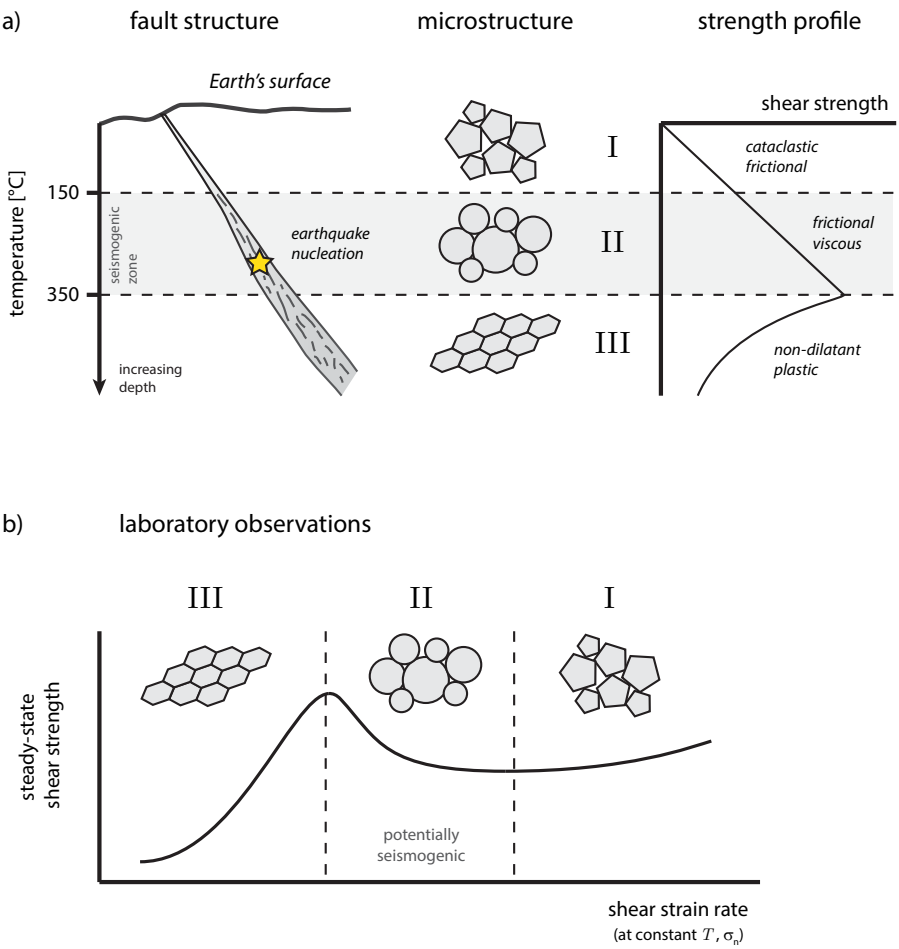

Fig. 1.1: a) A schematic depiction of a fault zone, with its seismogenic zone approximately bounded by the 150 °C and 350 °C isotherms (e.g. *Bonner*, 2003; *Sibson*, 1982). Associated with the distribution of seismicity are three main deformation regimes of (I) cataclastic frictional sliding at low temperatures and shallow depths, (II) frictional-viscous sliding at intermediate depths, and (III) plastic or viscous flow at greater depths (*Holdsworth et al.*, 2001; *Imber et al.*, 2001; *Sibson*, 1977); b) Schematic diagram of steady-state shear strength as a function of shear strain rate, as observed in experiments (*Shimamoto*, 1986; *Takahashi et al.*, 2017; *Verberne et al.*, 2017) and as predicted by the CNS model. The same deformation regimes as inferred by field studies (regimes I, II, and III) are observed in laboratory experiments as a function of strain rate (for a given temperature T and normal stress σ_n).

contemporaneous with granular flow (grain sliding and neighbour swapping), indicating that, on the timescale of a seismic cycle, there exists an interplay between non-dilatant pressure solution creep and dilatant granular flow (*Hadizadeh et al.*, 2012; *Holdsworth et al.*, 2011). As fluid-rock interactions are well known to be sensitive to temperature, the operation of pressure solution gives rise to a depth-dependence of fault rheology.

A conceptual fault model that is widely advocated essentially follows the classical Sibson-Scholz classification of crustal faults (*Holdsworth et al.*, 2001; *Scholz*, 1988; *Sibson*, 1977, see Fig. 1.1a): at shallow depths (upper 1-4 km; interval I in Fig. 1.1a) shear deformation is accommodated by cataclastic processes (granular flow and grain comminution), largely in the absence of fluid-rock interactions, producing unconsolidated fault gouges and cataclasites (*Marone*, 1998; *Sibson*, 1977). At intermediate depth ranges (typically 5-15 km; interval II), where fluid-rock interactions operate at appreciable rates, fault gouges are thought to consolidate and lithify, through which the fault strengthens and may nucleate unstable slip (*Angevine et al.*, 1982; *Collettini and Holdsworth*, 2004; *Marone*, 1998). Lastly, at lower-crustal conditions (interval III), temperatures are sufficient to activate plastic flow mechanisms, so that fault zones deform aseismically (*Holdsworth et al.*, 2001; *Schmid and Handy*, 1991; *Sibson*, 1977, 1982). The transitions between subsequent deformation regimes are then representative for the upper- and lower boundaries of the seismogenic zone (*Brace and Byerlee*, 1970; *Marone*, 1998; *Sibson*, 1982). This fault model, however, is mostly qualitative, receiving little quantitative support as few modelling studies consider the interplay between the relevant deformation mechanisms. Furthermore, additional quantitative methods are required to relate this general description of a mature fault structure to the observed spectrum of transient fault slip, and the seismic character of large faults.

1.3 Characterisation of fault rocks in a laboratory setting

Laboratory experiments occupy a central position in gaining quantitative understanding of the behaviour of faults. Early work on friction was performed mostly from a perspective of engineering and metallurgy (e.g. *Bowden and Hughes*, 1939; *Bowden*

et al., 1943; *Bridgman*, 1936). Insights resulting from these experimental studies have lead to the development of the *adhesion theory* of friction (see *Scholz*, 2002), formulated by *Bowden and Tabor* (1964), in which friction emerges from the interactions of load supporting surface irregularities, generally referred to as asperities (with no implied relation to the seismological asperities mentioned in the previous section). Adhesion theory was later extended and superseded by formulations more relevant for contact-scale deformation of rock interfaces (e.g. *Greenwood and Williamson*, 1966; *Scholz and Engelder*, 1976), although the interaction between asperities remains fundamental to these formulations.

Even though stick-slip frictional instabilities were already recognised by *Bridgman* (1936), the analogy between laboratory stick-slip events and natural earthquakes was fully appreciated by *Brace and Byerlee* (1966), making the link between 'jerky' sliding of rock interfaces in their experiments and the elastic rebound theory presented by *Reid* (1910). *Brace and Byerlee* (1966) also noted that the occurrence and magnitude of the stick-slip events was strongly affected by temperature and loading velocity, referring to the high-temperature laboratory work of *Griggs et al.* (1960). This was later elaborated on by *Brace and Byerlee* (1970), who revealed a transition from stick-slip to stable sliding with increasing temperature, and proposed that this transition was the cause for the termination of seismicity with depth in California. The observed effect of temperature on rock friction led *Dieterich* (1972) to draw parallels between rock friction and deformation of metals, motivating a suite of slide-hold-slide experiments to investigate the increase in 'static' friction with hold duration, as previously demonstrated for metals (*Rabinowicz*, 1965). In these experiments, *Dieterich* observed a logarithmic increase in static friction with time, i.e. $\mu_s \propto \log_{10} t$, and noted that this time-dependent increase in friction would facilitate stick-slip motion. The time-dependence of friction was subsequently discussed in the framework of adhesion theory and plastic deformation of contact asperities, though *Dieterich* also noted that the observed time-dependence appeared to be related to the presence of gouge, the granular product of frictional wear. By noting that earlier powder metallurgy studies had reported a dependence of powder frictional strength on the degree of compaction, the exact mechanism for the time-dependence of friction could not be unequivocally identified (*Dieterich*, 1972).

By interpreting rock friction to result from asperity interactions, time-dependent

deformation and strengthening of contact asperities consequently results in a velocity-dependence of friction in shear deformation (*Dieterich*, 1978). As two surfaces are sheared over one another, the characteristic lifetime of a given pair of asperities is inversely proportional to the relative velocity at which the two interfaces are moving, and so higher velocities would result in lower overall frictional resistance if asperity contacts strengthen over time. This inverse relationship between laboratory fault strength and slip velocity has been demonstrated experimentally (*Dieterich*, 1978; *Scholz and Engelder*, 1976), although the converse, i.e. increasing fault strength with increasing slip velocity, has also been observed at higher velocities (*Heslot et al.*, 1994). Without implying a specific underlying mechanism, the reduction in fault strength with increasing slip rate is generally referred to as velocity-weakening, with the converse being referred to as velocity-strengthening (*Ruina*, 1980). Velocity-weakening behaviour is commonly considered to be a requirement for recurrent frictional instabilities (such as stick-slips and earthquakes; *Gu et al.*, 1984; *Ruina*, 1983).

To further elucidate the mechanism behind the time-dependent strength of faults, *Dieterich and Kilgore* (1994) performed optical analyses on bare PMMA/glass interfaces. In these analyses, it was demonstrated that the contact asperities between two compressed interfaces increased in size with time in a logarithmic fashion, in a similar way to that of static friction increasing with time. Under various imposed normal stresses and interface roughness amplitudes, the contact area of the asperities was found to obey a power-law size distribution (*Dieterich and Kilgore*, 1996), consistent with the fractal surface topography of rock interfaces measured by *Brown and Scholz* (1985). Furthermore, the observed cumulative contact area was found to be controlled by the yield strength of the asperities. Hence, these observations suggest a compelling relation between surface topography, contact asperity deformation, and time-dependent fault strength. On the other hand, since natural faults accommodate deformation within one or multiple layers of gouge and (ultra)cataclasite (*Chester and Chester*, 1998; *Faulkner et al.*, 2003), the relevance of the interaction between discrete surfaces can be challenged, as granular media exhibit a rich array of deformation modes, such as grain sliding, neighbour swapping, rotation of individual or clusters of grains, and grain breakage. In numerical studies employing the Discrete Element Method, *Guo and Morgan* (2004, 2008) showed that grain rotation contributes significantly to the measured frictional response of an aggregate. Furthermore, thermal imaging experiments performed by

Mair et al. (2006) showed marked differences in the signature of frictional heating of either rough, bare surfaces, or gouge layers: while rough surfaces displayed distinct heat spots, revealing interaction between contact asperities as envisioned by e.g. *Dieterich and Kilgore* (1994), a layer of gouge displayed only diffuse heat patterns, suggesting that deformation within a gouge layer was not controlled by a small set of discrete asperities, but rather by the collective behaviour of the aggregate. Hence, the interpretation of the time-dependence of fault strength is not as clear for gouges as it is for bare interfaces, and mechanisms such as gouge compaction needs reconsidering (as was also noted by *Dieterich*, 1972).

In addition to experiments conducted on bare surfaces, many friction experiments have been conducted on gouge materials. These include gouges derived from natural faults (*Boulton et al.*, 2012, 2014; *Carpenter et al.*, 2009; *Collettini et al.*, 2011; *Niemeijer et al.*, 2016; *Sawai et al.*, 2016; *Tesei et al.*, 2014), simulated gouges (*Blanpied et al.*, 1991, 1995, 1998; *Carpenter et al.*, 2009; *Chester*, 1994; *Chester and Higgs*, 1992; *Den Hartog et al.*, 2012, 2013; *He et al.*, 2013, 2007; *Ito and Ikari*, 2015; *Saffer and Marone*, 2003; *Verberne et al.*, 2015), and analogue materials (*Buijze et al.*, 2017; *Leeman et al.*, 2015; *Niemeijer et al.*, 2008; *Takahashi et al.*, 2017), all of which have been tested at ambient laboratory conditions (e.g. *Carpenter et al.*, 2009; *Leeman et al.*, 2015; *Saffer and Marone*, 2003) or elevated (in-situ) pressure-temperature conditions (e.g. *Blanpied et al.*, 1998; *Chester*, 1994; *Niemeijer et al.*, 2016; *Verberne et al.*, 2015). Although the micro-mechanics of gouge deformation are different from those of bare surface deformation, similar macroscopic features have been observed. Friction tests conducted on gouges generally show a dependence of friction on temperature (*Blanpied et al.*, 1991, 1995, 1998; *Chester and Higgs*, 1992; *Den Hartog et al.*, 2012; *He et al.*, 2007), sliding velocity (*Carpenter et al.*, 2016a; *Collettini et al.*, 2011; *Den Hartog et al.*, 2012; *Reinen et al.*, 1992), normal stress (*Carpenter et al.*, 2016a; *Chester*, 1994; *Sawai et al.*, 2016), gouge composition (*Bos et al.*, 2000a; *Den Hartog et al.*, 2012; *Kaproth et al.*, 2016), gouge layer thickness (*Anthony and Marone*, 2005; *Marone and Kilgore*, 1993), fluid composition and chemistry (*Bos and Spiers*, 2002a; *Feucht and Logan*, 1990; *Frye*, 2002), and grain shape (*Anthony and Marone*, 2005; *Mair et al.*, 2002). This vast number of controlling quantities merely underlines the complex interactions and degrees of freedom that a granular aggregate may exhibit, and so developing a unifying theory for gouges may seem a daunting task. However, in spite of the sensitivity of gouge

friction to a large number of quantities, certain general aspects can be discerned (see Fig. 1.1b):

1. At low velocities, and high temperature or normal stress, many simulated and natural fault materials exhibit velocity-strengthening ductile creep (regime III in Fig. 1.1b). Strain is accommodated by plastic deformation (*Kawamoto and Shimamoto*, 1998; *Reinen et al.*, 1992), pressure solution (*Bos et al.*, 2000a; *Niemeijer and Spiers*, 2006), or a combination of these, in conjunction with frictional slip on phyllosilicates where present (*Bos et al.*, 2000a; *Den Hartog et al.*, 2012). The gouge structure is typically dense and mylonitic (*Bos et al.*, 2000a; *Takahashi et al.*, 2017).

2. At intermediate velocities, temperature, or normal stress, gouge strength decreases with increasing velocity or decreasing temperature, accompanied by an increase in porosity and cataclasic features (regime II; *Niemeijer and Spiers*, 2006; *Takahashi et al.*, 2017). In the presence of a reactive pore fluid, pressure solution is recognised to operate concurrently with granular flow (*Bos et al.*, 2000b; *Niemeijer and Spiers*, 2006), which exerts strong controls on the steady-state gouge porosity (*Niemeijer and Spiers*, 2007).

3. At high velocities, low temperature, and low normal stress, fault friction increases with increasing velocity or decreasing temperature, with little evidence for the operation of fluid-rock interactions (*Niemeijer and Spiers*, 2006), hence producing a highly porous and unconsolidated cataclastic microstructure (regime I).

The spectrum of microstructures that can be observed as a function of strain rate is similarly observed in nature as a function of temperature. This suggests that the effects of strain rate and temperature are either analogous to or interchangeable with one another, a concept that has previously been employed by *Tenthorey and Cox* (2006). Continuing this analogy, and following the interpretations of *Brace and Byerlee* (1970), *Sibson* (1977), and *Marone* (1998), the three aforementioned deformation regimes that are observed as a function of strain rate then correspond with deep, intermediate, and shallow portions of a fault, providing experimental support for seismological hypocentral estimates and geological interpretations of crustal strength profiles. The correspondence between microstructures observed in laboratory experiments and in

nature (*Fagereng and Den Hartog*, 2016; *Imber et al.*, 2008; *Rowe et al.*, 2011) confirm that the deformation mechanisms operating in the experiments are relevant for natural in-situ conditions, and so facilitate the extrapolation of laboratory results to nature. In the same way, experiments conducted on analogue materials, such as halite, can be confidently interpreted in terms of the operative micro-scale processes (*Bos et al.*, 2000b; *Shimamoto*, 1986).

1.4 Models for fault friction

As mentioned in Section 1.1, laboratory experiments represent a scale much smaller than appropriate for natural faults. Hence, in order to upscale laboratory results to nature, models of fault rock deformation are essential. In this section, I will discuss the development, application, and limitations of three commonly used models describing the behaviour of faults, which are, in order, slip weakening, rate-and-state friction, and microphysical models.

1.4.1 Slip weakening

As a mechanism for the stick-slip behaviour observed by *Brace and Byerlee* (1966), *Byerlee* (1970) proposed that frictional instabilities arise from sudden weakening of an interface due to fault slip, characterising rock friction through a spring-block analogy. Several weakening mechanisms were considered, with brittle failure of contact asperities being regarded most appropriate for brittle rocks: abrupt failure of one or more asperities causes sudden weakening of the fault, producing a frictional instability for a sufficiently low shear stiffness of the fault's surrounding medium (experimental apparatus or host rock). In this view, contact asperities generated from fault surface roughness would coincide with seismological asperities, i.e. the nucleation site of a seismic event. One corollary remarked by *Dieterich* (1979), is that a 'healing' mechanism is required to restore the shear strength of the fault for long-term, repeated slip events. Nevertheless, slip-dependent constitutive laws are commonly adopted in analytical and numerical modelling studies of fault slip (*Campillo and Ionescu*, 1997; *Day*, 1982; *Fukuyama et al.*,

2003; *Ide and Takeo*, 1997; *Yamashita and Ohnaka*, 1992), notably for its convenient functional form (e.g. *Andrews*, 1976a,b; *Ida*, 1972):

$$\tau(d) = \begin{cases} \tau_p - (\tau_p - \tau_r)\,\frac{d}{d_c}, & \text{if } d < d_c \\ \tau_r, & \text{if } d \geq d_c \end{cases} \tag{1.1}$$

in which $\tau(d)$ is the shear strength of the fault as a function of slip displacement d, τ_p is an initial (peak) value of the static shear strength, τ_r is the residual (dynamic or kinetic) shear strength, and d_c is a characteristic distance over which the fault weakens. The value of d_c can be measured in laboratory experiments (e.g. *Ohnaka*, 2003), or estimated from seismological inversion (*Ide and Takeo*, 1997), though there exist large discrepancies between the two estimates, varying from tens of µm in a typical laboratory experiment, to up to several metres in seismological inferences (*Marone and Kilgore*, 1993; *Mikumo et al.*, 2003; *Scholz*, 1998). Moreover, dynamic weakening (dramatic fault weakening at high slip velocities; see *Tullis*, 2007) likely operates in natural seismogenic faults and typically exhibits large characteristic slip distances (*Di Toro et al.*, 2004; *Violay et al.*, 2013). Experimental measurements of d_c at low velocities likely bear no relation with seismological estimates, which furthermore represent spatial averages over the rupture area and total fault slip rather than point measurements. Additionally, d_c is found to depend on numerous quantities, such as normal stress, temperature, and pore fluid chemistry (*Ohnaka*, 2013), which makes the extrapolation of laboratory measured values to nature more challenging.

1.4.2 Rate-and-state friction

On a timescale of several seismic cycles, a fault needs to preserve a finite frictional strength in order to store elastic strain energy. This necessitates a mechanism that restores fault strength between two subsequent slip events (*Dieterich*, 1979). Motivated by the laboratory observations that frictional strength increases logarithmically with time, an empirical formulation, the *rate-and-state friction* (RSF) formulation, was proposed that describes the value of the instantaneous coefficient of friction μ as a function of slip velocity V and 'state' θ, of which the most common form reads

(*Dieterich*, 1979; *Ruina*, 1983):

$$\mu(V,\theta) = \mu^* + a\ln\left(\frac{V}{V^*}\right) + b\ln\left(\frac{V^*\theta}{D_c}\right) \tag{1.2}$$

where μ^* is a reference value of μ defined at reference velocity V^*. The parameters a and b respectively denote the magnitudes of the instantaneous 'direct effect', and time- or slip-dependent 'evolution effect', which evolves over a characteristic slip distance D_c. The state parameter θ evolves with time or slip following a generic ordinary differential equation $\dot{\theta} = f(\theta, V, ...)$, and is commonly chosen to follow either the 'ageing' law (*Dieterich*, 1979) or the 'slip' law (*Ruina*, 1983), defined respectively as:

$$\frac{\mathrm{d}\theta}{\mathrm{d}t} = 1 - \frac{V\theta}{D_c} \tag{1.3a}$$

$$\frac{\mathrm{d}\theta}{\mathrm{d}t} = -\frac{V\theta}{D_c}\ln\left(\frac{V\theta}{D_c}\right) \tag{1.3b}$$

At steady-state, $\dot{\theta} = 0$, so that both state evolution laws reduce θ to D_c/V. In the view of rate-and-state friction as resulting from asperity creep, the state parameter θ at steady-state is interpreted as an average lifetime of contact asperities, corresponding to D_c/V (*Dieterich*, 1979). Away from steady-state, this interpretation is less straightforward. Regardless, substitution of $\theta = D_c/V$ simplifies Eqn. (1.2) to:

$$\mu(V,\theta) = \mu^* + (a-b)\ln\left(\frac{V}{V^*}\right) \tag{1.4}$$

It is clear from the above relation that the steady-state coefficient of friction given by the RSF formulation is logarithmically velocity-dependent, with $(a-b) > 0$ indicating velocity-strengthening, and $(a-b) < 0$ indicating velocity-weakening behaviour. It was demonstrated by *Ruina* (1983) that, within the framework of rate-and-state friction, a velocity-weakening material is potentially unstable (*Gu et al.*, 1984; *Rice and Ruina*, 1983), and so may generate a frictional instability in the form of repeated stick-slips or recurring earthquakes. This notion prompted numerous laboratory studies to investigate the seismogenic potential of fault rocks by interpreting velocity-step test results in terms of $(a-b)$ (e.g. *Blanpied et al.*, 1991; *Chester*, 1994; *Marone et al.*, 1990).

One major advantage of RSF over a more simple slip weakening constitutive formulation, is that it describes a wide range of laboratory experiments, including velocity-step tests (*Blanpied et al.*, 1998; *Chester*, 1994; *He et al.*, 2013), slide-hold-slide tests (*Beeler et al.*, 2001; *Marone and Saffer*, 2015), and the unstable sliding behaviour of spring-blocks (*Favreau et al.*, 1999; *He et al.*, 1998; *Rice et al.*, 2001). Furthermore, RSF is widely used in numerical simulations of seismic cycles (*Noda et al.*, 2017; *Rice*, 1993; *Tse and Rice*, 1986), earthquake statistics (*Hillers et al.*, 2007; *Luo et al.*, 2017b), and investigations into the nucleation of both slow slip events and regular earthquakes (*Ariyoshi et al.*, 2012; *Hawthorne and Rubin*, 2013; *Shibazaki and Iio*, 2003). The standardised RSF formulation allows for comparison of laboratory results by experimental determination of a, b, and D_c (*Blanpied et al.*, 1998; *He et al.*, 2016; *Marone et al.*, 1990, and many others). This is typically done by empirically fitting the RSF constitutive relations with constant coefficients to the laboratory data (*Blanpied et al.*, 1998; *Reinen and Weeks*, 1993), though this procedure disregards underlying physical processes. The constitutive parameters obtained from laboratory experiments are subsequently used in numerical modelling studies to investigate the behaviour of natural faults (e.g. *Lapusta and Rice*, 2003; *Tse and Rice*, 1986). In this way, experimental results are extrapolated beyond the temporal and spatial scales of the laboratory in a consistent manner. However, as summarised in Section 1.3, laboratory studies have overwhelmingly demonstrated that the frictional strength of a given material depends on a multitude of physical and chemical quantities, and so a, b, and D_c are not simply material constants. Given the vast differences between a laboratory setting and nature, direct extrapolation of laboratory measurements of rate-and-state parameters is of questionable validity.

The dependence of the RSF parameters of Westerly Granite on temperature (or crustal depth) has been investigated intensively by *Blanpied et al.* (1991, 1995, 1998). In this work, it is convincingly shown that granite gouge exhibits $(a-b) > 0$ at temperatures < 100 °C and > 350 °C, and $(a-b) < 0$ at intermediate temperatures corresponding with hypocentral depth estimates of the San Andreas Fault (see also Fig. 1.1b). However, since the physical interpretation of a, b, and D_c is not immediately clear, it is difficult to rigorously assess the legitimacy of this correspondence. In addition to the temperature dependence of $(a-b)$, *Blanpied et al.* (1995) also observed a velocity dependence of $(a-b)$ at constant temperature. The velocity dependence of

frictional parameters is generally not considered in theoretical studies employing the RSF framework, but could be of crucial importance to natural faults, which experience orders of magnitude variations in slip velocity over the course of a seismic cycle.

To alleviate the problem of velocity-dependent constitutive parameters, other forms of Eqn. (1.2) have been proposed that feature a cut-off parameter to enforce a transition from velocity-weakening to velocity-strengthening with increasing slip velocity (*Okubo*, 1989; *Rubin*, 2011). Similarly, different formulations connect low-velocity frictional behaviour to dynamic weakening (*Beeler et al.*, 2008; *Rice*, 2006; *Spagnuolo et al.*, 2016). Like the original RSF formulation, these extended formulations are not supported by physical principles, but are instead proposed on an *ad hoc* basis. Generally speaking, the constitutive parameters of the rate-and-state friction framework hold no obvious general physical interpretation beyond the classical asperity lifetime concepts, which greatly impedes the extrapolation of experimentally determined values of a and b to nature, as the effect of laboratory constraints (e.g. size, velocity, time) cannot be readily evaluated.

1.4.3 Microphysically based models

In an attempt to provide a physical interpretation to the rate-and-state friction framework, several workers have considered the micro-scale physical interactions between asperities, similar to the classical work of e.g. *Bowden and Tabor* (1964). One of the earlier of such attempts was made by *Brechet and Estrin* (1994), who assumed an Arrhenius-type exponential creep mechanism for a fixed number of contact asperities (see Fig. 1.2a), ultimately arriving at a macroscopic expression for the steady-state shear strength as a function of sliding velocity. This final relation featured a logarithmic velocity-dependence, exhibiting a functional form that bears resemblance with the classical and extended rate-and-state frameworks, and predicting marked transitions from velocity-strengthening to velocity-weakening and back to velocity-strengthening with increasing velocity. A similar formalism was later adopted by e.g. *Baumberger et al.* (1999), *Rice* (2006), *Putelat et al.* (2011), and *Aharonov and Scholz* (2017). These theoretical treatments have in common that, ultimately, the coefficient of friction is controlled by the stress supported by the contact asperities, relative to the material

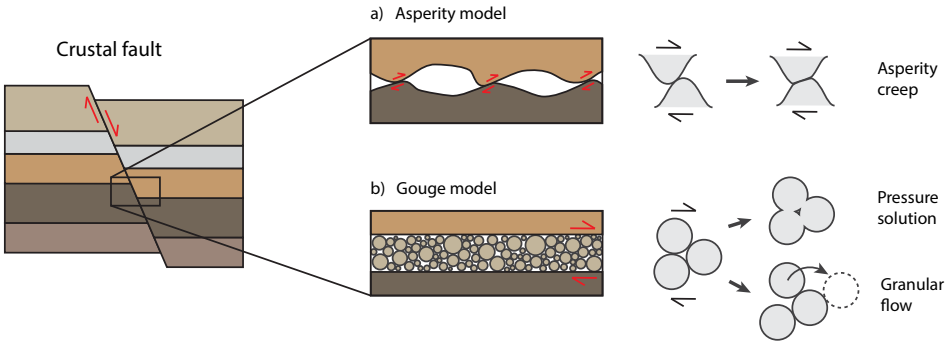

Fig. 1.2: Schematic diagram of two common interpretations of fault rock friction. a) Classically, shear deformation is thought to be accommodated by creep of (small) contact asperities on a fault (e.g. *Brechet and Estrin*, 1994); b) In models of gouge deformation, strain is accommodated by granular flow and pressure solution (e.g. *Den Hartog and Spiers*, 2014; *Niemeijer and Spiers*, 2007).

plastic yield strength or indentation hardness. While this physical interpretation may hold for purely plastically deforming interfaces, such as PMMA (*Baumberger et al.*, 1999) or metals (*Brechet and Estrin*, 1994), its applicability to granular rock materials is not evident. Since most faults are gouge filled (*Chester and Chester*, 1998; *Demurtas et al.*, 2016; *Rowe et al.*, 2011), interpretations of fault friction purely based on the concept of asperity lifetime are inadequate.

As discussed in Section 1.3, the added degrees of freedom that granular aggregates exhibit with respect to bare rock interfaces (e.g. grain rearrangement; Fig 1.2b) allow for a wider range of deformation modes. One particular aspect of interest for gouge deformation is bulk compaction and corresponding porosity reduction. As was already noted by *Dieterich* (1972), aggregate compaction leads to strengthening of a gouge. Moreover, with increasing compaction (and hence decreasing porosity), the average stress supported by each grain-grain contact reduces. This has important consequences for the interpretation that time-dependent strengthening originates from asperity creep: an aggregate that is initially deforming at steady-state (i.e. constant microstructure and porosity) exhibits a time-statistically constant asperity stress. Upon a downward perturbation in sliding velocity, such as a velocity down-step or initiation

of a hold, the porosity decreases by mechanical settling in response to a diminishing shear stress (*Karner and Marone*, 2001), as well as by time-dependent compaction by e.g. pressure solution creep (*Niemeijer et al.*, 2008; *Niemeijer and Spiers*, 2006). As a result, the average stress supported by each grain-grain contact reduces, so that the stress supported by the contact asperities may drop well below its yield strength. By definition of the yield stress, no significant asperity creep takes place thereafter, and so no further fault strengthening is expected through a mechanism of asperity creep. By contrast, laboratory slide-hold-slide tests show continued gouge strengthening even for large amounts of compaction (*Niemeijer et al.*, 2008), which is suggestive for other mechanisms that may operate concurrent with or substitute asperity creep. Finally, the presence and composition of a pore fluid have been shown to exert strong controls on the rate of restrengthening (*Bos and Spiers*, 2002a; *Nakatani and Scholz*, 2004; *Pluymakers and Niemeijer*, 2015), which is not expected for the envisioned asperity deformation mechanisms (crystal plasticity).

Since classical consideration from tribology and metallurgy may not directly apply to gouge deformation, other approaches need to be adopted to explain the vast array of laboratory observations, and to provide a basis for the extrapolation of laboratory results to nature. Important information regarding the operative deformation mechanisms can be obtained from microstructural analysis, which has served as a basis for the interpretation of many laboratory and field studies (*Chester et al.*, 1993; *Den Hartog et al.*, 2012; *Rowe et al.*, 2011; *Smith et al.*, 2011; *Spagnuolo et al.*, 2015; *Verberne et al.*, 2014a). There exist only few microphysical models that attempt to describe fault gouge deformation while simultaneously making predictions pertaining to the gouge microstructure, and evolution thereof (*Bos and Spiers*, 2002b; *Chen and Spiers*, 2016; *Den Hartog and Spiers*, 2014; *Niemeijer and Spiers*, 2007). As pointed out in Section 1.3, microstructural information is of key importance in relating the outcomes of laboratory experiments to natural faults. By providing microstructural predictions, the accuracy and relevance of the mechanical predictions of these microphysical models, as well as their limitations, can be assessed. Furthermore, the microphysical models hold great advantage over empirical constitutive relations, in that the model parameters have a transparent physical meaning, and so independent experiments or analytical techniques can be designed to constrain their values.

One class of microphysical models that will be investigated in this thesis, is the model formulations proposed by *Niemeijer and Spiers* (2007) and *Chen and Spiers* (2016) (referred to as the "CNS" model), which consider the deformation of gouges consisting predominantly of clast-forming minerals, such as calcite, quartz, and halite. In the CNS model framework, the mechanical response of a representative volume element of gouge results from the parallel operation of dilatant granular flow, and a non-dilatant, time-dependent creep mechanism such as pressure solution, which facilitate strain accommodation within the gouge body (see Fig. 1.2b). In the most basic form, the mechanics of the model are described by a set of two ordinary differential equations (*Chen and Spiers*, 2016):

$$\frac{\mathrm{d}\tau}{\mathrm{d}t} = k\left(V_{imp} - h\left[\dot{\gamma}_{gr} + \dot{\gamma}_{ps}\right]\right) \tag{1.5a}$$

$$\frac{\mathrm{d}\phi}{\mathrm{d}t} = -\left(1-\phi\right)\left(\dot{\varepsilon}_{gr} + \dot{\varepsilon}_{ps}\right) \tag{1.5b}$$

The first equation results from a simple elastic equilibrium equation, in which τ is the shear stress supported by the gouge, k is the shear stiffness of the surrounding medium, V_{imp} is the externally imposed loading velocity. The instantaneous slip velocity V of the model fault is given as $V = h\left[\dot{\gamma}_{gr} + \dot{\gamma}_{ps}\right]$, with h being the thickness of the gouge layer, and $\dot{\gamma}_x$ being the shear strain rate accommodated by granular flow (gr) and pressure solution (ps). The second equation relates the average gouge porosity to the normal strain rates $\dot{\varepsilon}_x$ of granular flow and pressure solution, and embodies the competition between dilatant and non-dilatant deformation mechanisms. By adopting constitutive relations for granular flow (*Chen and Spiers*, 2016; *Niemeijer and Spiers*, 2007) and pressure solution (e.g. *Lehner*, 1995; *Pluymakers and Spiers*, 2014), which both are dependent on the state of stress and gouge porosity, a complete description of the mechanics of a zero-dimensional spring-block fault is obtained.

Following *Niemeijer and Spiers* (2007) and *Chen and Spiers* (2016) (see also *Den Hartog and Spiers*, 2014), three steady-state deformation regimes emerge from the dynamics of the CNS model (see Fig. 1.1b): at low imposed velocities, or equivalently high temperatures and normal stress, shear strain is entirely accommodated by ductile pressure solution creep of a dense gouge, which is inherently velocity-strengthening (regime III). At intermediate velocities, dilatant granular flow operates concurrently

with non-dilatant pressure solution creep, resulting in a dynamic steady-state gouge porosity which increases towards higher velocities. Since a dense gouge is mechanically stronger than a porous one, the increase in steady-state porosity with velocity in turn produces velocity-weakening behaviour (regime II). Lastly, when the imposed velocity is high compared to the kinetics of pressure solution, strain is accommodated exclusively by granular flow and porosity asymptotically approaches a maximum attainable value. In the absence of gouge dilatation, the overall velocity-dependence of friction turns positive again (i.e. velocity-strengthening; regime I), as frictional sliding of individual grain contacts is thought to be velocity-strengthening (*Chen and Spiers*, 2016; *Den Hartog and Spiers*, 2014).

The steady-state frictional behaviour and microstructural state of the gouge predicted by the CNS model are in good agreement with the laboratory and field studies cited in Section 1.2 and 1.3, and thus the CNS model serves as a suitable candidate for the extrapolation of laboratory results. Moreover, although the CNS model is based on principles that are fundamentally different from the original approach taken by *Bowden and Tabor* (1964) and *Brechet and Estrin* (1994), the transient mechanical response of the simulated gouge dictated by Eqn. (1.5) closely resembles transient behaviour previously ascribed to rate-and-state friction – see *Chen and Niemeijer* (2017) and *Chen et al.* (2017b) for an in-depth comparison between CNS and RSF. This resemblance warrants further exploration of the CNS model behaviour in the framework of large-scale fault deformation and natural seismicity.

1.5 Aims of this thesis

Although microphysical models hold potential to explain laboratory and field observations in a quantitative way, they are currently limited to application in the framework of a spring-block fault geometry. In order to study the mechanics of natural faults, microphysical model formulations need to be further developed to account for experimental observations, and need to be cast within a numerical framework to allow upscaling. In this thesis, I will employ a Discrete Element Method package (LAMMPS; *Plimpton*, 1995) to numerically investigate aggregate deformation at the scale of laboratory samples, and a Boundary Element Method seismic cycle simulator (QDYN;

Luo et al., 2017a) to simulate earthquake cycles at the scale of the Earth's upper crust. The Discrete Element Method will be based on similar principles as the CNS model, but with fewer constraints on the model gouge microstructure, as the dynamics of the aggregate are not prescribed by macroscopic constitutive relations. By contrast, the Boundary Element Method will rely on the constitutive relations provided by the CNS model framework, but will address spatial- and timescales that are inaccessible by laboratory tests and Discrete Element Method simulations.

Utilising the numerical instruments offered by both of these two techniques opens up new opportunities to interpret laboratory results, and to explore fault and earthquake mechanics based on microphysical principles. In this way, laboratory, field, and seismological observations may be combined in a unifying description of fault friction. This perspective motivates the following aims for this thesis:

1. To investigate the compaction behaviour of granular fault gouges
   Compaction by intergranular pressure solution is of great importance to fault rock deformation in nature and in laboratory experiments, as well as for the mechanics of the CNS model. However, previous laboratory work has shown that long-term aggregate compaction rates are greatly overestimated by analytical models for pressure solution (*Niemeijer et al.*, 2002; *Schutjens*, 1991b; *Van Noort et al.*, 2008a). I will investigate this discrepancy by comparing the predictions of existing analytical models with the outcomes of compaction experiments and numerical models. To this end, contact-scale formulations for pressure solution and grain boundary structural evolution will be implemented in a Discrete Element Method framework.

2. To examine fault restrengthening behaviour during interseismic periods
   One major challenge for the extrapolation of laboratory results to nature, is the wide gap between typical laboratory test durations and the natural seismic cycle. After validation of the Discrete Element Method approach by comparison with laboratory compaction data, the interplay between fluid-rock interactions and granular flow is investigated further, both experimentally and numerically, with focus on time-dependent compaction and lithification during the seismic cycle.

3. To explore the upscaled behaviour of the CNS model, applied to natural faults
   In order to facilitate the upscaling of laboratory friction results, constitutive relations for pressure solution and granular flow are implemented into the seismic cycle simulator QDYN. The mechanics of a simulated crustal strike-slip fault (c.f. *Tse and Rice*, 1986) are subsequently investigated, and the outcomes compared with classical rate-and-state friction. This comparison will reveal similarities and fundamental differences between microphysical and rate-and-state formulations, and to what extent rate-and-state friction can be unified with microphysically based models.

4. To study the mechanics of a geologically realistic, heterogeneous fault
   Natural faults are generally heterogeneous in their composition and structure, to a degree that cannot be simulated in a laboratory setting. Many observations of earthquake nucleation and rupture are attributed to spatial heterogeneity, and this complexity hinders earthquake hazard assessments and forecasting attempts by obscuring underlying trends. I will use the numerical implementation of the CNS microphysical model to investigate earthquake rupture within a heterogeneous fault, and compare the simulation outcomes with (palaeo)seismological and geodetic observations. By doing so, some of the complex features of natural earthquakes may be generalised, which then provide directives for earthquake hazard assessments.

Chapter 2

Investigating compaction by intergranular pressure solution using the Discrete Element Method

Martijn P. A. van den Ende, George Marketos,
André R. Niemeijer, and Christopher J. Spiers

Published in: *Journal of Geophysical Research: Solid Earth* 123, 2018

doi:10.1002/2017JB014440

Abstract

Intergranular pressure solution creep is an important deformation mechanism in the Earth's crust. The phenomenon has been frequently studied and several analytical models have been proposed that describe its constitutive behaviour. These models require assumptions regarding the geometry of the aggregate and the grain size distribution in order to solve for the contact stresses, and often neglect shear tractions. Furthermore, analytical models tend to overestimate experimental compaction rates at low porosities, an observation for which the underlying mechanisms remain to be elucidated. Here we present a conceptually simple, 3D Discrete Element Method (DEM) approach for simulating intergranular pressure solution creep that explicitly models individual grains, relaxing many of the assumptions that are required by analytical models. The DEM model is validated against experiments by direct comparison of macroscopic sample compaction rates. Furthermore, the sensitivity of the overall DEM compaction rate to the grain size and applied stress is tested. The effects of the interparticle friction and of a distributed grain size on macroscopic strain rates are subsequently investigated. Overall, we find that the DEM model is capable of reproducing realistic compaction behaviour, and that the strain rates produced by the model are in good agreement with uniaxial compaction experiments. Characteristic features, such as the dependence of the strain rate on grain size and applied stress, as predicted by analytical models, are also observed in the simulations. DEM results show that interparticle friction and a distributed grain size affect the compaction rates by less than half an order of magnitude.

2.1 Introduction

Intergranular pressure solution (IPS, sometimes referred to as (dis)solution-precipitation creep or even "chemical compaction") is known to be an important time-dependent deformation mechanism in the wet regions of the Earth's crust, under conditions of relatively low stress and temperature, down to depths of 20 km (*Elliott*, 1973; *Lehner*, 1990; *Rutter*, 1976, 1983; *Spiers et al.*, 2004). Pressure solution is highly relevant for compaction of sedimentary rocks during diagenesis (*Croizé et al.*, 2010; *Tada and Siever*, 1989; *Yang*, 2000), but also for shear deformation of dense rocks under greenschist metamorphic conditions (*Elliott*, 1973; *Stöckhert et al.*, 1999), and in controlling the frictional behaviour of faults (*Bos et al.*, 2000b; *Hickman and Evans*, 1992; *Sleep and Blanpied*, 1992).

Numerous analytical models exist that describe the microphysical processes operating during pressure solution and the kinetics of creep, especially for the case of compaction by IPS (e.g. *Lehner*, 1990; *Shimizu*, 1995; *Spiers and Schutjens*, 1990). These have been tested against a large number of experiments (e.g. *Dewers and Hajash*, 1995; *Raj*, 1982; *Spiers and Schutjens*, 1990). However, these models are limited in their ability to capture realistic packing geometries by the necessity to assume single-sized grains arranged in a regular packing (cubic or hexagonal). This simplification is required to analytically express grain contact area, grain contact stress distribution and pore wall area as functions of strain or porosity. In addition, many models assume that no shear tractions exist on a grain contact, i.e. that the friction between grains is negligible. However, friction may be significant in compaction experiments on granular aggregates. Finally, these models tend to overestimate the compaction rates of low-porosity aggregates by up to several orders of magnitude (e.g. *Niemeijer et al.*, 2002; *Schutjens*, 1991b). This exposes a gap in our understanding of the micro-scale processes operating at these conditions, which limits the confidence with which experimental results can be extrapolated to natural conditions, particularly for those cases that involve relatively low porosities (< 15 %). Within a geological context, making predictions of the long-term compaction behaviour of natural faults systems, sedimentary basins, and hydrocarbon reservoirs based on laboratory data may therefore not be warranted.

Classically, much of the (numerical) modelling work done on IPS is related to the

compaction of aggregates and the upscaling of laboratory results to nature. Several numerical procedures have been proposed that address the stability of dissolving interfaces (*Ghoussoub and Leroy*, 2001; *Koehn et al.*, 2006), the initiation of stylolitisation (*Dewers and Hajash*, 1995), self-organisation of compacting systems (*Ortoleva*, 1994), and compaction of sedimentary basins (*Dewers and Hajash*, 1995; *Renard et al.*, 1999; *Yang*, 2000). In particular, basin compaction provides scientific challenges with great relevance for industrial applications, for it is well known that the (terminal) porosities observed in sedimentary formations cannot be readily explained by analytical compaction models for pressure solution. Instead, it is often found that geological reservoirs exhibit porosities that are directly related to their maximum burial depth, rather than geological age and burial history (*Giles et al.*, 1998). This (apparent) equilibrium state is in strong contrast with the nature of pressure solution, which is inherently a non-equilibrium process (e.g. *Lehner and Bataille*, 1985). Attempts have been made to explain this equilibrium state by consideration of plastic (*Palciauskas and Domenico*, 1989) and viscoplastic (*Revil*, 2001) creep that would render the instantaneous porosity a function of effective stress, or by consideration of supra-hydrostatic fluid pressures resulting from densification (*Yang*, 2000). Alternatively, the existence of a 'yield' stress for pressure solution has been proposed on the basis of a vanishing driving force to explain the observed depth-dependency of porosity (*Revil*, 2001; *Van Noort et al.*, 2008b). Furthermore, the presence of cations such as Al^{3+}, e.g. resulting from mica dissolution, can dramatically reduce the rates of quartz dissolution (and likely also precipitation; *Iler*, 1973; *Spiers et al.*, 2004).

In addition to driving the compaction of sedimentary basis, IPS is well known to operate in gouge-filled faults under upper- and mid-crustal conditions (*Chester and Chester*, 1998; *Evans and Chester*, 1995). Densification and creep of faults by IPS has been put forward as a mechanism for long-term evolution of fault strength during interseismic periods (e.g. *Angevine et al.*, 1982; *Sleep and Blanpied*, 1992), and has been employed to investigate the frictional stability and rheology of faults (*Chen and Spiers*, 2016; *Den Hartog and Spiers*, 2014; *Niemeijer and Spiers*, 2007). In spite of the similarities between sedimentary basin compaction and fault densification, the operation of IPS in fault gouges differs in that pervasive cataclastic processes need to be considered, particularly at shear deformation rates that are relevant for earthquake nucleation (*Niemeijer and Spiers*, 2006). For instance, the existence of an equilibrium

state, as seen in geological reservoirs, can be questioned when grain-grain contacts are continuously rejuvenated by granular flow.

Simulating creep of a granular aggregate by IPS using the Discrete Element Method (DEM) has several advantages over conventional analytical models: first of all, DEM does not require the assumptions of a single-valued grain size and regular packing, as the stresses are calculated per particle. The positions, velocities, and forces acting on an individual particle can be evaluated at any given time during the simulation. This grants insights into the distribution of deformation occurring within a sample, which is very difficult to access in real-world experiments. Secondly, the governing physics is implemented at the particle scale and various deformation mechanisms can operate simultaneously (for example pressure solution and grain boundary sliding). By combining or excluding different mechanisms, the relative importance of a single mechanism can be tested. Lastly, and perhaps most importantly, individual parameters such as the interparticle friction coefficient, kinetic constants, and particle stiffness can be readily modified to investigate the role that these parameters may play in the overall deformation behaviour. These features make DEM a suitable method for studying the dynamics of granular aggregates, particularly in the context of deformation of fault gouges where granular flow, cataclasis, and fluid-rock interactions are prevalent.

So far only a few studies have attempted to simulate compaction by IPS with DEM (*Bernabé and Evans*, 2014; *Zheng and Elsworth*, 2012, 2013). *Zheng and Elsworth* (2012) related the convergence rate of particles in a stressed aggregate to the undersaturation of the solute in the pore fluid through a sophisticated two-dimensional DEM scheme, but comparison with compaction data on quartz sand reported by *Niemeijer et al.* (2002) showed that the compaction rates were underestimated by the model. It was argued by the authors that this reflected a difference in grain size distribution between the model and experiment, but this hypothesis was not tested further. Comparison with the open-system compaction experiments of *Yasuhara* (2003) showed better agreement. *Bernabé and Evans* (2014) used a three-dimensional DEM model to investigate long-term compaction behaviour of quartz with explicit coupling of the interface reaction and diffusion kinetics through the pore fluid saturation state, but the resulting compaction rates were not compared to experimental data. In order to simulate compaction over long timescales (up to 10 000 years), *Bernabé and Evans* (2014) assumed that the

DEM aggregate was always in mechanical equilibrium, so that an iterative relaxation technique could be employed for efficient time integration of the aggregate. While the assumption of quasi-static compaction is believed to be valid in these simulations, it is overly restrictive for the simulation of aggregate deformation in the dynamic regime, which is relevant for e.g. fault and earthquake mechanics. Furthermore, to simplify the implementation process, *Bernabé and Evans* (2014) chose to omit interparticle friction from the model, which leaves open questions to the role that it might play in the compaction behaviour. For direct comparison with experimental results (where grain-grain and grain-wall friction may play a significant role), interparticle friction in the DEM model has been included in the current study.

The aim of this work is to present a conceptually and numerically simple way of modelling IPS in DEM, so that it can be readily incorporated in future DEM studies of the mechanics of fault gouges. The relevant grain contact input parameters are the ones used in analytical IPS models (e.g. by *Spiers et al.*, 1990), and elasticity at the contacts is accounted for using a standard DEM approach. To validate the resulting (three-dimensional) DEM model, we conduct short-term compaction experiments on granular halite and directly compare the experimental compaction rates with those of the simulations. In this way, we test if the DEM model is capable of reproducing experimental compaction data without prescribing the evolution of the particle contact area with bulk strain, as required by analytical models. We explore if the proposed DEM approach preserves the grain size and stress exponents, as theoretically predicted for frictionless particles arranged in a regular close-packing, for a non-zero interparticle friction. We then proceed to investigate the effects of interparticle friction and of a polydisperse grain size distribution on the overall compaction behaviour to assess if these effects could explain the discrepancy between compaction rates predicted by analytical models and those observed in experiments. Since granular flow is not yet fully understood, we only consider compaction in the absence of pervasive granular flow in this work, which we leave for future study. In summary, the aims of this work are to:

1. present a method for modelling pressure solution creep using DEM
2. assess the validity of the model by comparison with dedicated compaction experiments, and with theoretical predictions

3. investigate the effect of grain contact friction on the macroscopic compaction rates

4. investigate the effects of a non-uniform grain size distribution on the long-term compaction behaviour

Since analytical models fail to explain the reduction in strain rates at low porosities (*Niemeijer et al.*, 2002; *Schutjens*, 1991b), there is potential for the Discrete Element Method to shed new light onto this problem by systematically investigating parameters such as grain contact friction and grain size distribution. These again will also be highly relevant for the mechanics of fault gouges.

2.2 Previous work on compaction via pressure solution

2.2.1 Constitutive relations for pressure solution

It is widely accepted that the thermodynamic driving force for pressure solution in chemically closed systems is provided by gradients in chemical potential, induced by gradients in stress around grain surfaces. Much work has been done on deriving theoretical models (e.g. *Lehner*, 1995; *Pluymakers and Spiers*, 2014; *Rutter*, 1976; *Shimizu*, 1995) that relate the rate of deformation to the applied stress, temperature and nominal grain diameter. These models assume that an interconnected network of fluid is present within the grain boundaries, either as a dynamically stable, island-channel network (*Raj*, 1982; *Spiers and Schutjens*, 1990), or as an adsorbed thin film (*Robin*, 1978; *Rutter*, 1983). By dissolving mass at the highly stressed grain contacts and reprecipitating it at lower stress interfaces or at stress-free pore walls, mass is transferred through the grain boundary fluid and creep is achieved perpendicular to the direction of the locally-acting normal stress, producing deformation parallel to the local normal stress direction (i.e. parallel to the contact normal). This assumes that the resistance to grain boundary sliding is negligible, or alternatively that the dissolution/precipitation is only possible normal to grain surfaces (*Lehner*, 1990; *Shimizu*, 1995). In the situation

where it is assumed that there is no mass transport out of the system, the process of pressure solution is a series of three consecutive serial processes: (1) dissolution of material at the highly stressed grain contacts, (2) diffusion of the dissolved solid out of these contacts into the pore space, and (3) precipitation on interfaces supporting lower stress, including the pore walls. Assuming (near) steady-state transfer, the kinetic process that proceeds at the lowest rate will then control the overall rate of deformation (*Lehner*, 1990; *Raj*, 1982). Numerous authors have derived constitutive equations for pressure solution at single circular grain contacts (e.g. *Pluymakers and Spiers*, 2014; *Rutter*, 1976; *Shimizu*, 1995; *Spiers and Schutjens*, 1990). For compaction of a porous aggregate idealised as an array of spherical grains arranged in a regular packing, essentially equivalent equations were obtained, which take the following form for both isostatic and uniaxial compaction (*Spiers et al.*, 2004):

$$\dot{\varepsilon}_s = A_s \frac{I_s \Omega}{RT} \frac{\sigma_e}{d} f_s(\phi) \tag{2.1a}$$

$$\dot{\varepsilon}_d = A_d \frac{(DCS)\Omega}{RT} \frac{\sigma_e}{d^3} f_d(\phi) \tag{2.1b}$$

$$\dot{\varepsilon}_p = A_p \frac{I_p \Omega}{RT} \frac{\sigma_e}{d} f_p(\phi) \tag{2.1c}$$

Here, the subscripts s, d and p denote dissolution-, diffusion- and precipitation-controlled kinetics respectively, $\dot{\varepsilon}$ is the rate of deformation, A a geometric constant, d the mean grain size, σ_e the effective stress (applied stress minus pore fluid pressure), Ω the molar volume of the solid, R the universal gas constant, T the absolute temperature, D the effective diffusion coefficient of the ionic species in the grain boundary, C the equilibrium solubility of the solid, S the (mean) thickness of the fluid phase in the grain boundary zone, and $f(\phi)$ a dimensionless function of porosity (ϕ) which accounts for the evolution of contact area and pore wall area during compaction. The rate constants for grain boundary dissolution (I_s), precipitation (I_p) and for grain boundary diffusion (DCS) vary with temperature and are expected to exhibit an Arrhenius dependence on temperature, i.e. to take the form:

$$I = I_0 \exp\left(-\frac{\Delta H_s}{RT}\right) \tag{2.2}$$

for I_s and I_p (*Van Noort and Spiers*, 2009), and

$$(DCS) = (DCS)_0 \exp\left(-\frac{\Delta H_d}{RT}\right) \tag{2.3}$$

for (DCS) (e.g. *Spiers et al.*, 1990). Here, ΔH is the apparent activation energy associated with each process. For highly soluble materials at room temperature, such as alkali metal salts, dissolution and precipitation are relatively fast, and diffusion along the grain boundary controls the creep rate, even for small grain sizes. By contrast, low solubility solids, such as quartz, often show interface-reaction controlled kinetics (*Spiers et al.*, 2004). The linear form of Eqn. (2.1) holds well for small departures from equilibrium, i.e. for small contact stresses. However, when the driving force for IPS is large, a non-linear relation between strain rate and effective stress is more appropriate (see e.g. *Niemeijer et al.*, 2002; *Pluymakers and Spiers*, 2014).

Spiers et al. (1990) systematically investigated the effect of temperature, mean grain size, and applied normal stress on the deformation (creep) rate of granular halite (NaCl), in the range of 20-90 °C, 100-275 µm, and 0.5-2.2 MPa respectively. Grain sizes were controlled to lie in narrow ranges by sieving (near monodispersed). From the grain size dependence of the creep rate, *Spiers et al.* (1990) inferred that (at room temperature) diffusion of mass along the grain boundaries was the rate controlling process, and derived the values for the constitutive parameters $(DCS)_0 = (2.76 \pm 1.40) \times 10^{-15}\,\mathrm{m^3\,s^{-1}}$ and $\Delta H_d = 24.53\,\mathrm{kJ\,mol^{-1}}$ as appearing in Eqn. (2.3). These parameters were derived by fitting Eqn. (2.1b) to the laboratory dataset, and assuming that the aggregate can be represented by a regular packing of single-sized spheres, and that the values of $(DCS)_0$ and ΔH_d are independent of temperature, stress, and grain size. Since the values of these kinetic or constitutive parameters are relatively well constrained for halite (*De Meer et al.*, 2002; *Hickman and Evans*, 1995; *Schutjens and Spiers*, 1999; *Spiers and Schutjens*, 1990; *Urai et al.*, 1986), creep experiments conducted on granular halite will be used here for comparison with the DEM simulation outcomes, and for validation of the DEM model.

2.2.2 Effect of a distributed grain size

It is well known that various sedimentary and transport processes can produce a wide range of grain size distributions in sedimentary rocks (*McLaren and Bowles*, 1985; *Visher*, 1969). Similarly, cataclastic fault rocks are commonly characterised by a power-law grain size distribution (*Storti et al.*, 2003). However, for mathematical convenience, analytical models typically assume a uniform grain size. In order to compare the analytical models with experiments, the mean grain size of the experiment is commonly chosen as the reference grain size. To address the potential effects of a distributed grain size on IPS, *Niemeijer et al.* (2009) conducted compaction experiments on granular halite aggregates with various mean grain sizes and distributions. They observed a strong correlation between the coefficient of variation (standard deviation normalised with respect to the mean) of the grain size distribution and the measured volumetric strain rate. Specifically, the strain rate was found to increase markedly with increasing coefficient of variation (i.e. with a widening distribution). *Niemeijer et al.* (2009) attributed this behaviour to the presence of the smaller grains within the wider distribution, which allowed for enhanced creep rates. Since the theory of diffusion-controlled IPS predicts an inverse cubic dependence of strain rates on grain size (Eqn. (2.1b)), it is expected that the mass transfer rate will be higher for smaller grains if the contact stresses are the same. However, in a porous aggregate where the majority of the load is carried by a network of larger grains, effectively shielding smaller grains, the stresses acting on the smaller grains might be much lower than those acting on the larger grains, thus leading to lower macroscopic sample strain rates. Which of these competing effects dominates the overall compaction behaviour of a porous aggregate is not clear.

To investigate the effect of a distributed grain size on creep of polycrystalline materials, *Ter Heege et al.* (2004) proposed a composite flow law for grain size sensitive and grain size insensitive creep, taking into account the possibility of a log-normally distributed grain size. This flow law was derived for two end-member assumptions: that of sample-homogeneous stress, or of sample-homogeneous strain rate. When either end-member assumption is applied to IPS, it is found that the predicted creep rate decreases with increasing coefficient of variation. It should be noted that the model was derived for a bulk crystalline material, rather than a porous granular aggregate: the

assumption that either the stress or the strain rate is homogeneously distributed over the sample is not valid for high-porosity aggregates. However, as a granular sample densifies, i.e. porosity decreases, it is expected that the assumptions of the model by *Ter Heege et al.* (2004) are more closely met, and that the dependence on the width of the grain size distribution changes. This hypothesis is difficult to test experimentally, but can be tested numerically using the Discrete Element Method.

2.3 Numerical methods and procedure

2.3.1 Basic DEM approach

The Discrete Element Method is a widely used numerical method for modelling the mechanics of discontinuous (granular) media and aggregates. While the method as originally proposed by *Cundall and Strack* (1979) has remained essentially unchanged, ongoing advances in computational performance are allowing for larger, more complex simulations that resemble the geometry and scale of the object of study increasingly well. The DEM method involves identifying which particles interact with one another, calculating the forces associated with each particle-particle contact and hence acting on each particle, and integrating the accelerations (as calculated from forces through Newton's second law of motion) to obtain individual particle velocities and positions. By prescribing the way each particle interacts with its neighbours at the microscale (e.g. Hookean- or Hertzian, elastic-frictional), DEM aims to realistically capture the macroscopic material response to dynamic or kinematic boundary conditions imposed on the system. In the present study, we employ the open-source software package granular LAMMPS (*Landry et al.*, 2003; *Plimpton*, 1995), as modified by *Marketos* (2013) and further modified for pressure solution.

For simplicity, the particles considered here are perfectly spherical, indestructible, and unbonded, in the sense that no tensile forces are allowed and no moments of force are transmitted between them. The particles can be of different size, so that a realistic grain size distribution can be simulated. A size-independent (constant) coefficient of friction is used to describe the sliding resistance at grain contacts. All the stresses

(and forces) present in the system are assumed to be effective stresses (total stress minus the pore fluid pressure), and local excess pore pressures are assumed to dissipate instantaneously, as porosities are high. When two particles are in contact, the elastic restoring force acting in a direction perpendicular to the contact plane is typically calculated through a force-displacement law, e.g. through Eqn. (2.4) below for a linear contact spring:

$$F_n = k_n \Delta x_{el} \tag{2.4}$$

where F_n is the normal contact force, k_n is the normal stiffness and Δx_{el} is the elastic centre-to-centre displacement or conceptual overlap between the particles (see Fig. 2.1). A similar equation applies for the shear forces. The elastic shear displacement Δy is incremented each time step by the relative particle displacements, and the maximum shear force is constrained by a frictional slider. Since most natural materials feature irregular, indented or even sutured grain surfaces, it is unlikely that stressed contacts in such a material exhibit perfect Hertzian elasticity. Instead, many materials seem to display stress-strain relationships that are approximately linear (e.g. *Nakata et al.*, 1999), or fall between idealised Hookean and Hertzian behaviour (e.g. *Cole and Hopkins*, 2016). Furthermore, the operation of pressure solution rapidly grows and flattens the grain contacts, so that the elastic response will quickly become sub-Hertzian. In the absence of a unifying elastic theory that is practical for implementation in DEM, we simply adopt a linear force-displacement law, and take $k_n = k_s = k$.

In a system where IPS is possible, besides the elastic and frictional interactions usually considered in DEM, as soon as a stress acts on a particle contact, pressure solution will be activated at a rate V_{ps} that is proportional to the effective stress on the contact. In order to mimic the approach of grain centres and overall densification of the system in DEM, we propose here that the centre-to-centre displacement or total overlap Δx_t should be reduced by the total non-elastic overlap (i.e. the dissolved particle contact layer thickness) δ, so that the resulting, elastically maintained contact force after dissolution becomes:

$$F_n = k \Delta x_{el} = k \left(\Delta x_t - \delta \right) \tag{2.5}$$

In each time step, δ is then incremented by $2V_{ps} \times \Delta t$ (factor 2 accounting for each dissolving particle). When the forces applied at the boundaries of the system are held

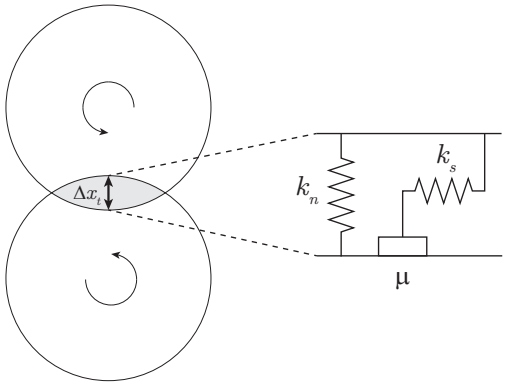

Fig. 2.1: The elastic-frictional interaction between two particles sharing a single contact is represented by a linear spring in the normal direction, and a spring and frictional slider in the shear direction. The force perpendicular to the plane of contact is calculated as $F_n = k_n \Delta x_{el} = k_n (\Delta x_t - \delta)$, where k_n is the normal contact stiffness and Δx_{el} is the elastic overlap in the normal direction, Δx_t is the total overlap, and δ is the non-elastic overlap (i.e. dissolved contact layer thickness). The elastic restoring force tangential to the plane of contact is calculated incrementally as $F_s = k_s \sum \Delta y$, as it typically done in DEM, where k_s is the shear stiffness and Δy is the lateral relative displacement caused by relative motion tangential to the plane of contact, or by relative rotation. The shear force is limited by the frictional slider to $F_{s,max} = \mu F_n$, with μ being a (constant) coefficient of friction.

constant (i.e. simulating a creep test), the average force on the contacts, and hence Δx_{el}, remains constant. Continuous dissolution at the contact (i.e. increasing δ) will then result in an increasing total overlap Δx_t, producing compaction of the system over time. Alternatively, if the positions of the boundaries are kept fixed after some initial force is applied (i.e. simulating a stress relaxation test), the average total overlap Δx_t remains constant, but δ increases with ongoing dissolution. This causes F_n to decrease and the sample stresses to relax.

The rate of pressure solution V_{ps} (i.e. the rate of change of δ) follows directly from the theory of pressure solution for a single contact (*Lehner*, 1995; *Pluymakers and*

Spiers, 2014; *Rutter*, 1976) and can be written in the form:

$$V_{ps,i} = Z_i \frac{F_n}{A_c} \tag{2.6a}$$

$$V_{ps,d} = Z_d \frac{\pi F_n}{A_c^2} \tag{2.6b}$$

Here the subscripts i and d represent interface-reaction controlled (dissolution or precipitation) and diffusion controlled respectively, V_{ps} is the rate at which the overlapping zone 'dissolves' (i.e. at which δ increases), Z is a kinetic constant representing the temperature-dependent kinetics of dissolution, precipitation (units: m Pa^{-1} s^{-1}) or diffusion (units: m^3 Pa^{-1} s^{-1}), and A_c is the area of the circular intersection between the two spherical bodies, which is assumed to be fluid filled. The pore fluid itself is not modelled directly, and is assumed to be homogeneous in composition (solute concentration) and present throughout the system. Because pressure solution on the contacts effectively acts as a linear viscous dashpot, no additional viscous damping is used in the simulations, except for when a new sample is created (as will be discussed later).

It is well known that the rate of interfacial ion detachment/attachment in highly soluble salts, such as NaCl, is sufficiently rapid that mass transfer rates are controlled by diffusion, even over short length scales. By comparison of end-member constitutive relations for diffusion- and interface reaction controlled IPS, and by assuming values for (DCS) and the reaction rate constant of 10^{-19} m^3 s^{-1} (*Spiers et al.*, 1990) and 10^{-4} m s^{-1} (*Alkattan et al.*, 1997; *Scrutton and Grootscholten*, 1981), respectively, it can be shown that IPS is rate-limited by diffusion for length scales larger than about 60 nm. In practice, this means that the kinetics of IPS of halite will always be controlled by diffusion (*Spiers et al.*, 2004), even for small grain contact areas that are characteristic for the early stages of a compaction experiment. Hence, in this study we only consider diffusion-controlled kinetics, governed by Eqn. (2.6b) in the simulations. Note that Eqn. (2.6a) could have easily been implemented as well.

While pressure solution operates (i.e. $V_{ps} > 0$), the total overlap Δx_t of the two spherical particles continuously increases. The total area of contact A_c is calculated each time step as the area of intersection of two spheres, which increases non-linearly

with Δx_t. Hence, it follows from Eqn. (2.6) that pressure solution is a self-limiting process: with ongoing pressure solution, A_c increases and V_{ps} decreases. This makes our DEM formulation self-consistent, without further need for a porosity function (see Eqn. (2.1)) that accounts for the evolution of the contact area with increasing compaction. Furthermore, at constant F_n, the contribution of elastic deformation to the total overlap remains constant at $\Delta x_{el} = F_n/k$, whereas the contribution from dissolution by pressure solution (δ) continuously increases. For bulk strains larger than the average elastic strain, pressure solution quickly dominates in determining the size of the particle contact (i.e. $\delta \gg \Delta x_{el}$). Following this line of reasoning, it is expected that even for modest compaction strains, the choice for the elastic parameters plays a second-order role on the rates of deformation (as will be discussed in Section 2.3.3).

For the entire duration of the simulations, the diameter of the particles remains constant, and the particle shape does not deviate from spherical. In our current DEM approach, reprecipitation of the dissolved mass onto the pore walls is not modelled explicitly, in the sense that mass redistribution by pressure solution does not result in local reduction of the pore volume. Hence, the area of the dissolving contacts is not affected by reprecipitation. For relatively small strains (i.e. high porosities), the total contact area is small compared to the total pore wall area and this assumption holds. For large strains however, reprecipitation should be taken into account, and a method accounting for the mass redistribution during the DEM simulation (like that employed by *Zheng and Elsworth* (2012)) should be considered. Preliminary calculations show that for a porosity of 10 % the relative error in contact area is less than 10 %. Note that for the porosity calculations we only consider the total solid mass present in the system, which, for a chemically closed system (with respect to the solid mass), is constant in time, so that our estimates of bulk porosity are not affected. Additionally, since the fluid phase is not modelled explicitly (i.e. no advective transport is considered), mass conservation is implicit in our DEM approach.

2.3.2 Numerical stability and scaling

Table 2.1: The relevant parameters as used in the simulations aimed to be compared to and validated by experimental data (as reported in Fig. 2.2). Only those symbols are given that were reported in the text. The parameter values that were not known in, or not applicable to the experiments are not provided. The values of $(DCS)_0$ and ΔH_d, which are used to calculate Z_d (at 40 °C), are taken from *Spiers et al.* (1990).

Parameter	**Symbol**	**Value (range)**		**Units**
		Experiment	Simulation	
Grain radius	r	33.5 (31.5-35.5) $\times 10^{-6}$	1.06 (1.00-1.12)	m
Mass density	ρ	2.1×10^{3}	2.1×10^{3}	kg m^{-3}
Compaction vessel radius	-	1.075×10^{-3}	34.127	m
Axial stress	σ_n	1.08×10^{6}	1.08×10^{6}	Pa
Particle stiffness	k	-	2.65×10^{9}	N m^{-1}
Particle friction coefficient	μ_p	-	0.6	-
Wall friction coefficient	-	-	0.1	-
Kinetic constant	$(DCS)_0$	2.79 (1.39-4.19) $\times 10^{-15}$	-	m^3 s^{-1}
Activation energy	ΔH_d	2.45 (2.36-2.55) $\times 10^{4}$	-	J mol^{-1}
Molar volume	Ω	2.69×10^{-5}	-	m^3 mol^{-1}
Pressure solution constant	Z_d	9.58 (4.77-14.4) $\times 10^{-27}$	10^{-13}	m^3 Pa^{-1} s^{-1}
Number of particles	-	-	20 000	-
Time step	Δt	-	1.82×10^{-4}	s

To ensure numerical stability, the time step employed during the simulation is constrained to $\Delta t = t_c/10$. The critical time step t_c is defined as $t_c = \sqrt{m/k}$, where m is the mass of a particle, and chosen such that a mechanical perturbation of a given particle cannot travel farther than its direct neighbours, and is proportional to the highest eigenperiod of the system (*Cundall and Strack*, 1979). For realistic particle sizes, of the order of 10-100 µm, the limiting time step reduces to values that are computationally not feasible for simulating the timescales of real-life experiments (hours to days). Therefore, in order to simulate experimental procedures, either the kinetics of pressure solution have to be non-dimensionalised (i.e. scaling time), or the limiting time step has to be artificially increased by increasing the mass density ρ of the particles (i.e. density scaling), a technique commonly used in DEM (e.g. *Cui and O'Sullivan*, 2006; *Ng*, 2006; *O'Sullivan et al.*, 2003). Here, we increased the time step by using particle sizes near unity while keeping the mass density at 2100 kg m^{-3}. Then, we chose to non-dimensionalise time and strain rate as:

$$t' = tZ_d\sigma_n r^{-3} \tag{2.7a}$$

$$\dot{\varepsilon}' = \dot{\varepsilon} r^3 Z_d^{-1} \sigma_n^{-1} \tag{2.7b}$$

where Z_d is the diffusion controlled kinetic constant, σ_n the externally applied axial stress. Following numerous studies (e.g. *Pluymakers and Spiers*, 2014; *Rutter*, 1976), the diffusion controlled kinetic constant can be expressed as:

$$Z_d = \frac{4(DCS)\Omega}{RT} \tag{2.8}$$

where the product (DCS) is related to temperature according to Eqn. (2.3). Note that the above equation only consists of thermodynamic quantities and material properties, and is therefore independent of the assumed packing geometry, grain size, and stress distribution within the sample. Hence Z_d is a constant and can be used in scaling. The (minimum) particle radius r scales all spatial dimensions (i.e. $x' = xr^{-1}$), which makes all dimensions of the simulation domain proportional to the particle size. Since mass is not rescaled, this approach is essentially equivalent to density scaling, while being more convenient for obtaining the optimal degree of scaling. When scaling in this way, particle accelerations and inertial effects need to be closely considered, so as to remain

within the quasi-static regime of deformation. A suitable degree of scaling was found in small-scale sensitivity tests to achieve reasonable computation times, while minimising the effects of inertia on the macroscopic compaction behaviour as a result of the chosen degree of scaling.

2.3.3 Validation tests

The validation of the model was done by comparing experimental compaction rates (see Section 2.4.1) with those from DEM simulations. These simulations will from here on be referred to as simulation set A. The following procedure was adopted in the validation DEM model run: the DEM sample was rendered by generating 20 000 particles at random locations within a cylindrical simulation domain of similar (scaled) diameter as the real-life counterpart, after which they were allowed to settle by gravity. This mimics the way lab-samples were prepared, where the powdered sample material was poured into a cylindrical, 1D compaction vessel. During the settling of the particles, particle body forces were artificially reduced ('damped') to lower the time for the aggregate to come to rest. After settling, gravity and artificial damping were turned off, and the DEM sample was precompacted 'dry' by applying an axial compressive load cycled between 1 and 10 times the load used during 'wet' compaction. Load cycling was repeated until the porosity did not change by more than 0.1 % (absolute value) between consecutive cycles. All simulations were conducted in a zero lateral strain (i.e. uniaxial strain) geometry, and the load was imposed by downward migration of the planar wall bounding the top of the simulation domain, the area of which was constant throughout the simulation. A proportional controller algorithm was used to maintain the stress (force divided by the wall area) exerted by the top wall at a prescribed value (within 0.01 % of the target value), as described by *Marketos* (2013). This essentially sets the boundary velocity to be proportional to the difference between a target stress and the instantaneous stress supported by the wall. By adopting this procedure of load cycling, a realistic initial porosity of 40.43 % was obtained for this particular sample. After precompaction, a constant axial load was applied to simulate creep testing conditions. Pressure solution was then activated numerically, after the sample had reached equilibrium, simulating the addition of a saturated solution phase at atmospheric pressure, and the sample was allowed to compact. The parameters used

in this simulation, as well as their real-world counterparts (if applicable), are reported in Table 2.1.

The validation of the DEM model was done by comparing the macroscopic compaction rates produced by the model with those measured in the benchmark experiments, in the absence of grain boundary healing. The implementation of the pressure solution contact law was considered to be valid if the strain rates produced by the model at a given porosity would be in the same range as the strain rates measured in the experiments at identical values of porosity. To take into account the uncertainty of the kinetic parameters as reported by *Spiers et al.* (1990), the simulations were scaled to a minimum, a maximum, and a mean estimate of the parameter Z_d from Eqn. (2.7b) (see Table 2.1 for the parameter values, and Figure 2.2 for the results). The (scaled) kinetic parameter was adopted as reported by *Spiers et al.* (1990), and the model was not further 'calibrated' by varying Z_d in the DEM simulations. Note that, although the value of Z_d was derived from laboratory experiments conducted in a similar way as reported here, there is no circularity in our approach: the analytical models that were compared with experiments to constrain Z_d were derived for a single contact, and thus require upscaling to the size of the aggregate to simulate the evolution of particle contact area and stress with sample strain or porosity. In the DEM approach, this evolution is virtually unconstrained, as only the shape of the particle-particle contact is determined by the DEM assumption of spherical particles. Hence, the characteristic evolution of strain rate with sample porosity emerges spontaneously from the DEM simulations, which is then directly compared with laboratory data.

The possible role that the particle stiffness may play is systematically investigated by repeating the above procedure for different DEM samples, with each simulation exhibiting a particle stiffness that is either identical to, 10 times lower, or 10 times higher than the value used in the reference simulation described above (simulation set A; see Appendix 2.B). For each chosen particle stiffness, three unique samples ('sister samples') were generated and deformed to get a measure of the numerical sample variability. At 32 % porosity, the variability in strain rate between the sister samples lies within 1 % of the average value (Fig. 2.B.1). By comparison of the simulations exhibiting different stiffnesses, it is seen that even such a large variation in stiffness (two orders of magnitude) has only a minor effect on the compaction rates after strains

of a few per cent, particularly when considering the uncertainty in (DCS) value and variability of the laboratory experiments. These results also show that the simulation outcomes are not very sensitive to the initial packing configuration, such as local porosity variations, and that the compaction behaviour is mostly controlled by the IPS kinetic parameter Z_d.

After validation of the contact model by direct comparison with experiments, additional verification simulations were run to investigate the model dependency on stress and grain size. The aim of these numerical experiments was to compare the DEM model trends with theoretical predictions. For convenience, new samples were created for each simulation set following a somewhat different numerical procedure than was adopted for simulation set A. First, a total of 4500 particles were generated at random locations in a rectangular simulation domain. The dimensions of the rectangular simulation box were scaled to the particle size, so that the lateral sides of the box had a length of 15 particle diameters. To eliminate possible boundary effects, periodic lateral boundaries were employed, i.e. particles at a vertical side of the simulation box interacted with those at the opposite side. In the axial direction, regular (non-periodic) boundaries were employed. To investigate the possible role of friction, two interparticle coefficients of friction were tested ($\mu_p = 0.01$ and $\mu_p = 0.6$). The DEM sample was precompacted by cyclically varying the load between 1 and 10 times the load that was used during the rest of the simulations. A total of 5 cycles were performed. In the simulations that were conducted to test the stress dependence of the model (from here on referred to as simulation set B), the axial stress was varied between simulations in the range of 0.1-1.0 MPa, while the particle diameter was set to unity for all particles. In the tests that were conducted to investigate the grain size dependence (simulation set C), the applied axial stress was 1.0 MPa and the particle radius was varied from simulation to simulation in the range of 0.1-1.0 units of length. Pressure solution was then activated and the sample was compacted until a final porosity of 30 % was reached. The value of the kinetic constant Z_d was set to 10^{-13} in simulation set B, and to 10^{-14} in simulation set C. These values were chosen so as to maintain a reasonable computation time for the chosen particle sizes. Note that these particle sizes were arbitrarily chosen, and that therefore the spatial dimensions were not physically meaningful. However, for the compaction experiments, the inertia of the particles did not affect the observed compaction rates, and so the results are representative.

2.3.4 Testing effects of friction and distributed grain size

Since shear stresses have been typically excluded from analytical expressions for IPS, it is worthwhile to systematically investigate the effect of friction on the macroscopic rate of compaction. To this end, a new set of simulations (simulation set D) was run following a similar procedure as was adopted for simulation set B. In these simulations, a sample consisting of 4500 particles was generated with an interparticle friction coefficient of 0.01. After precompaction and load cycling, the aggregate was subjected to an axial stress of 1 MPa. Using this precompacted sample as a starting point, 8 new simulations were initiated, each with a different interparticle friction coefficient of 0.01, 0.05, 0.10, 0.20, 0.30, 0.50, 0.70, and 1.00. Then, pressure solution was turned on and each simulation was run for 1000 model seconds, and the resulting macroscopic compaction rates were compared. This procedure ensured identical starting microstructure (porosity, coordination number, etc.) for each simulation, regardless of the friction values chosen for 'wet' compaction phase.

A final set of simulations was run to investigate the effect of a distributed particle size with DEM (simulation set E). Five samples were generated by rendering 10 000 particles in a box with periodic lateral boundaries. The radius of each particle was randomly sampled from a Gaussian distribution with unit mean radius and a prescribed coefficient of variation ν, defined as the standard deviation normalised by the mean value. The five samples were assigned a coefficient of variation of $\nu = \{0.0, 0.1, 0.2, 0.3, 0.4\}$. To prevent excessively small or large particles to be created, the Gaussian distribution was clipped at a distance $\pm 2\nu$ from the mean. A value of $\nu = 0.0$ implies a single particle size, which was used as a reference. After the particles had settled by gravity, the sample was subjected to a load of 5.0 MPa and pressure solution was activated. The sample was then compacted until a final porosity of 20 % was reached. The stress acting on each particle-particle contact was outputted at 0.5 % intervals of porosity, so that the relative contribution of each particle to the overall compaction rate could be analysed. Note that the initial porosities varied between samples, owing to differences in particle size distribution. For an unbiased comparison between the various simulations, all macroscopic compaction data are reported as a function of porosity, rather than strain (as is common in many studies).

The details of the parameters and characteristics of all of the simulations are summarised in Table 2.2.

Table 2.2: The parameters and characteristics as used in the various sets of simulations. See text for a description of the different simulation sets.

Parameter	**A**	**B**	**C**	**D**	**E**	**Units**
Contact stiffness[a]	2.65×10^9	2.65×10^9	2.65×10^9	2.65×10^9	2.65×10^9	N m^{-1}
Friction coefficient	0.6	0.01 or 0.6[b]	0.01 or 0.6[b]	0.01-1.0	0.6	-
Mass density	2100	2100	2100	2100	2100	kg m^{-3}
Radius (min/max)	(1/1.12)	0.5	0.1-1.0	1.0	variable[c]	m
Size distribution	uniform	monodisperse	monodisperse	monodisperse	Gaussian	-
Lateral boundary conditions[d]	rigid cylinder	periodic	periodic	periodic	periodic	-
Applied stress	1.08	0.1 - 1	1	1	5	MPa
Wall stiffness	2.65×10^9	2.65×10^9	2.65×10^9	2.65×10^9	2.65×10^9	N m^{-1}
Wall friction coefficient	0.1	0	0	0	0	-

[a] Identical values were used for both the normal- and shear stiffness

[b] Two identical simulation sets were run with different friction values

[c] Particle radii were sampled from a Gaussian distribution with a mean of 1 m and ν of 0, 0.1, 0.2, 0.3, and 0.4

[d] In the axial direction, a constant stress boundary condition was applied by a rigid planar wall

2.4 Results of benchmark simulations

2.4.1 Comparison with laboratory experiments

To validate the DEM model, we compared the outcome of DEM compaction tests to the results of compaction experiments conducted on porous halite aggregates. Most experimental work on halite has focused on intermediate- to long-term compaction behaviour (see e.g. *Gratier et al.*, 2013, for an extensive summary), hence little data are available for the compaction of aggregates of high porosity, which require a high temporal resolution in the first hour or so of a typical experiment. To serve as a benchmark for validation of the DEM model, a total of six one-hour compaction experiments were conducted on halite aggregates to obtain data with the required temporal resolution. The choice for short-duration compaction tests was dually motivated: first of all, to simulate a short-duration test in DEM, slower (scaled) kinetics can be employed to reduce the inertial effects that may affect the initially rapid stages of compaction (see Section 2.3.2). Secondly, the relatively high porosities would ensure a minimal effect of grain boundary healing on the overall compaction behaviour (*Van Noort et al.*, 2008b; *Zubtsov et al.*, 2004). An extensive description of the experimental methods is given in Appendix 2.A.

The strain rate evolution with porosity obtained in the compaction experiments is plotted in Fig. 2.2. The final porosities obtained after approximately one hour of compaction were similar, reaching values of 30.73 ± 2.02 %. Samples with a higher initial porosity generally also showed a higher final porosity. The strain rates produced at a given porosity varied within a band of roughly half an order in magnitude, which we took as a range of the experimental uncertainty. This variability may have been caused by initial (local) variations in porosity, grain size, or packing geometry, which may have manifested more explicitly in the relatively small samples used in this study.

Since the experimental results reported by *Spiers et al.* (1990) provide a range of values for Z_d, one simulation was run in simulation set A and the resulting strain rates scaled back according to three different values: one for a low estimate of $Z_d = 0.503 \times 10^{-26}$, one for a high value of 1.51×10^{-26}, and one with an average value of

1.01×10^{-26} m^3 Pa^{-1} s^{-1}. These estimates are based on the statistical uncertainties in the determination of $(DCS)_0$ and ΔH_d reported by *Spiers et al.* (1990), and they reflect the variability of their experimental results. The strain rate versus porosity results of this simulation are directly compared to the experimental data in Fig. 2.2. This shows that end-member estimates of Z_d envelope the range of experimental strain rates for porosities in the range of 30-37 %. At porosities higher than 37 % the DEM model seems to severely overestimate the experimental rates of compaction. This can likely be explained by the fact that in the DEM simulations the initial area of contact between two particles, before initiation of pressure solution, is purely due to elastic compression, and is very small owing to the spherical geometry of the particles. In the benchmark experiments, the shape of the grains, being non-spherical, leads to larger initial areas of contact. This results in unrealistically small particle contact areas and high contact stresses in the DEM model, and hence larger strain rates produced in the simulations during initial stages of compaction. Analytical models suffer the same discrepancy when the porosity function tends to infinity. At larger strains, this initial discrepancy vanishes and a much better agreement is found between the DEM simulations and the laboratory experiments. Order of magnitude estimates of the sample permeability reveal that expulsion of the pore fluid (i.e. viscous advection) is very unlikely to impede the rate of compaction at this range of porosities.

When we compare the DEM simulation results to an analytical model (model D3 in *Pluymakers and Spiers*, 2014) with the same kinetic parameters as used in the mean estimate, we find good agreement between the two. While the analytical model tends to predict slightly higher compaction rates, the evolution of the strain rate with porosity is similar. This suggests that the contact-scale physics is implemented sufficiently well to capture the macroscopic response that is predicted by the analytical models, which are based on the same physical principles. Hence we can conclude that the proposed DEM contact law is capable of reproducing the compaction behaviour realistically, and can be used to investigate more complex granular aggregates for which analytical expressions do not exist.

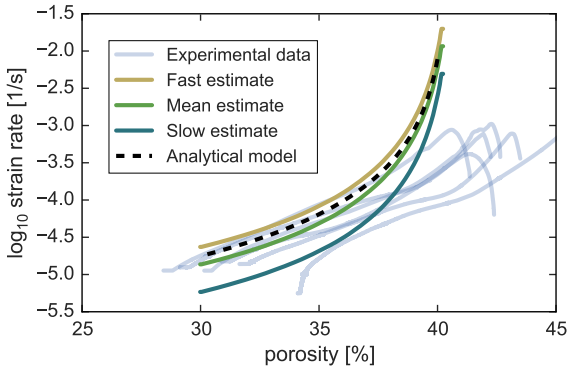

Fig. 2.2: Experimental compaction results for wet halite (applied stress $\sigma_n = 1.08$ MPa; starting grain size $63 < d < 71$ µm; average starting porosity 43 %) as compared with results from simulations conducted at similar conditions, and with the results of the analytical model by *Pluymakers and Spiers* (2014) (model "D3"). The starting porosity for the simulations was 41 %.

2.4.2 Stress dependence

Let us now consider the dependence of the sample strain rate on the applied axial (effective) stress. From theory it is expected that (for low effective stress) the pressure solution creep rate is linearly proportional to the applied effective stress (see Equation (2.1); *Lehner*, 1995; *Rutter*, 1976). This is also observed in compaction experiments (e.g. *Spiers et al.*, 1990), although sometimes a higher stress exponent is observed (see *Gratier et al.*, 2013). It can be shown that Eqn. (2.6) produces a stress exponent of +1 for a cubic close-packed system, in agreement with theoretical values. However, in randomly-packed aggregates, each particle contact may exhibit a different orientation and magnitude of the locally acting normal stress, which continuously evolves due to growth of the contact area. The resulting macroscopic compaction rate then represents a bulk averaged outcome of all local contributions of contact stress to the strain rate. Because of the internal heterogeneity of stress, a proportional relationship between the stress imposed at the boundaries of the simulation domain and the overall strain rate is

not guaranteed for the DEM simulations. A new set of simulations (simulation set B) was therefore run so as to test the stress dependence of the DEM model.

First, a series of simulations was run with varying axial stress (0.10, 0.18, 0.32, 0.56 and 1.0 MPa) and with a near-zero coefficient of interparticle friction ($\mu_p = 0.01$). The DEM samples were compacted down to a porosity of 30 %. At 30.5 % porosity, the instantaneous strain rate was measured and plotted against the applied axial stress in Fig. 2.3 (blue dots). The best-fit line through the data has a slope of 1.004 ± 0.001, which indicates that $\dot{\varepsilon} \propto \sigma_n$, as was expected from theory.

Next, a set of simulations were run with the same axial stresses, but with a different interparticle friction coefficient of 0.6 (see Fig. 2.3; red triangles). Although the enhanced friction coefficient reduced the rates of compaction by about half an order of magnitude, it did not alter the stress dependence in the model. For easy comparison, the strain rates reported in Fig. 2.3 were all normalised to the corresponding strain rate of the simulation where $\sigma_n = 1.0$ MPa and $\mu_p = 0.6$. This result suggests that any deviations of stress exponent from the theoretical value of 1, as observed in experiments, are unlikely to be related to interparticle friction.

2.4.3 Grain size dependence

Similar to the stress exponent, it is expected from theory and experiments that diffusion controlled IPS creep rates are inversely proportional to the cube of the grain size, i.e. $\dot{\varepsilon} \propto d^{-3}$ (see Eqn. (2.1b)). With the same reasoning as was put forward for the stress exponent (see Section 2.4.2), Eqn. (2.6b) does not guarantee a grain size exponent of -3 for disordered aggregates. The procedure for testing the grain size dependence of the DEM model (simulation set C) was similar to that of the stress dependence simulations. A constant axial stress of 1 MPa was applied to each of the five samples with different tested uniform particle sizes (0.10, 0.18, 0.32, 0.56, and 1.0 units of length). The interparticle coefficient of friction was 0.01 in the first set of simulations, and was 0.6 in the second set. The log of the strain rate, measured at 30.5 % porosity, was normalised to the corresponding strain rate of the simulation where $r = 1$ and $\mu_p = 0.6$, and was then plotted against the log of the particle radius in Fig. 2.4. The slope of the best fit line was very close to -3 for both sets of simulations, which indicates that

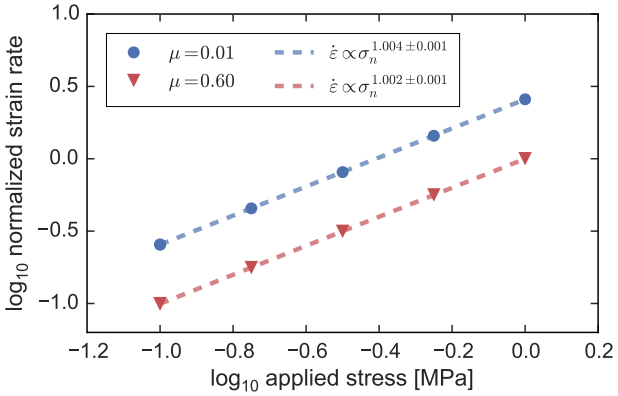

Fig. 2.3: DEM results showing the sensitivity of the overall strain rate to the applied stress, as measured at 30.5 % porosity, for a low interparticle coefficient of friction of $\mu = 0.01$ and for a high coefficient of friction of $\mu = 0.60$. Although the simulation with the higher coefficient of friction compacts more slowly (lower strain rates), the stress dependence does not change measurably. The reference value of strain rate is taken at $\sigma_n = 1.0$ MPa for $\mu = 0.60$.

$\dot{\varepsilon} \propto d^{-3}$, as was expected from theory, and that the grain size exponent is independent of interparticle friction.

2.5 Potential mechanisms for strain rate reduction

2.5.1 Effect of interparticle friction

From the simulation results reported in Figures 2.3 and 2.4, it is apparent that an increase in interparticle friction effectively reduces the overall compaction rates, although it does not affect the stress and grain size dependence. The evolution of the porosity with time, as observed from simulation set D, as well as the strain rates measured at fixed porosities in the range of 28-34 % for the different values of μ_p, are plotted in Fig. 2.5. These results demonstrate that the compaction rates are systematically

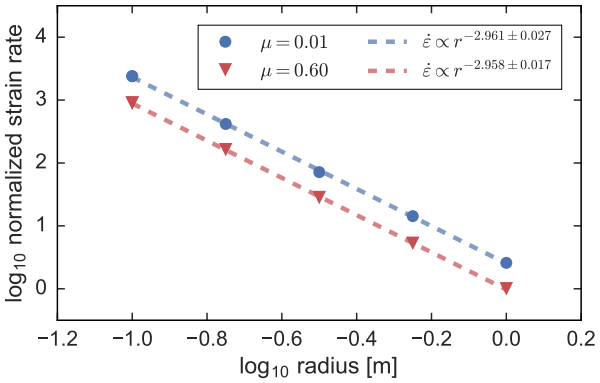

Fig. 2.4: DEM results showing the sensitivity of the overall strain rate to the grain size, as measured at 30.5 % porosity. Similar to the stress dependence simulations, two interparticle friction coefficients were tested, ($\mu = 0.01$ and $\mu = 0.60$). The interparticle friction does not affect the grain size dependence, but it does decrease the strain rate by a factor of 3, going from a friction coefficient of 0.01 to 0.6. The reference value of strain rate is taken at $r = 1.0$ for $\mu = 0.60$.

reduced with increasing coefficient of friction, by up to a factor of 3 (half an order of magnitude). The reduction of strain rates with increasing coefficient of friction is also observed in the data plotted in Figures 2.3 and 2.4. Furthermore, the effect of friction seems to diminish only slightly with decreasing porosity in the range of investigated porosities. The order of magnitude difference in strain rate ($\log \dot{\varepsilon}_{0.01} - \log \dot{\varepsilon}_{1.0}$) of $\mu_p = 0.01$ and that of $\mu_p = 1.0$ at 34 % porosity is 0.510, and at 28 % it is 0.472. This implies that the effect of interparticle friction is only weakly dependent on porosity in the range of porosities investigated.

It should be noted that the kinetic parameter $(DCS)_0$ for diffusion controlled IPS as determined by *Spiers et al.* (1990) was obtained by fitting an expression of a similar functional form as Eqn. (2.1b). Since (2.1b) does not explicitly take into account any effects of interparticle friction, the value of $(DCS)_0$ is convolved with any contributions of friction to the overall compaction rates. If the contribution of friction is assumed

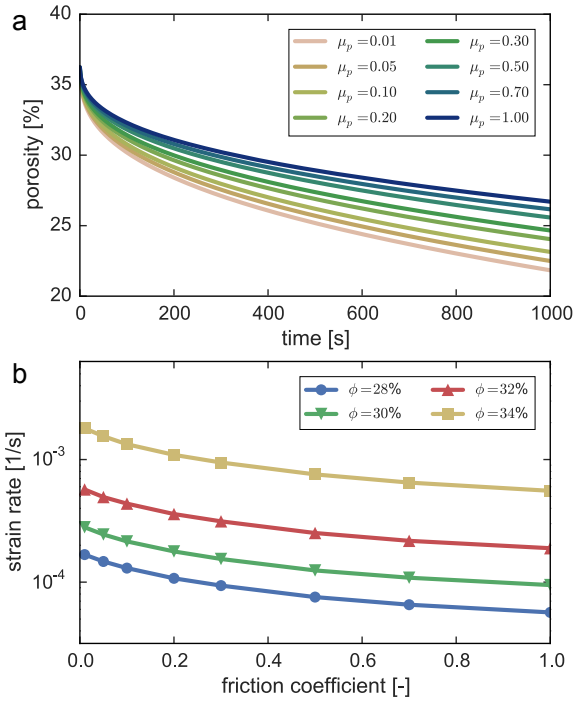

Fig. 2.5: The effect of interparticle friction on the compaction behaviour of the DEM simulations. a) Overview of porosity evolution for interparticle friction coefficients ranging from 0.01 to 1.00. b) Overall strain rate as a function of the interparticle friction coefficient, as measured at various porosities in the range of 28-34 %.

to be independent of porosity, then friction cannot directly explain the tendency of analytical models to overestimate experimental compaction rates, particularly at lower porosities.

2.5.2 Effects of a distributed grain size

As discussed in Section 2.2.2, *Niemeijer et al.* (2009) report enhanced compaction rates in granular aggregates with a wider grain size distribution. To gain some insights into

the effects of a distributed grain size, a number of compaction simulations were run with various grain size distributions (simulation set E), characterised by the coefficient of variation ν. In Fig. 2.6a the overall compaction rate is plotted against bulk sample porosity for each simulation. For porosities > 32 % the strain rates are clearly enhanced by the distributed grain size: for a given value of porosity, the strain rates increase with increasing width of the distribution. This is consistent with the results of *Niemeijer et al.* (2009), although the enhancement of the strain rate obtained in the simulations is less than what was observed in the experiments. At around 32 % a crossover at which the overall strain rates decrease with increasing ν occurs in our simulations. The decrease in strain rate with increasing ν is a feature that is not observed in experiments, but is predicted by the model of *Ter Heege et al.* (2004).

It would be instructive to first consider the microscopic state of stress, i.e. the stress supported by individual particle contacts. To this end, we define the average particle stress as the total vertical stress of all contacts associated with a given particle, divided by its coordination number, i.e.:

$$\tilde{\sigma}^j = \frac{1}{N_c} \sum_{i=1}^{N_c} \sigma_{z,i}^j \tag{2.9}$$

where N_c is the coordination number of particle j, and $\sigma_{z,i}^j$ is the is the vertical component of the normal stress (normal force F_n divided by contact area A_c) exerted by particle i on j. Then, a probability density function $P(x)$ can be defined that describes the distribution of $\tilde{\sigma}$ over all the particles such that:

$$\int_{-\infty}^{+\infty} P(x)\mathrm{d}x = 1 \tag{2.10}$$

Note that the probability density, unlike the absolute probability, is allowed to locally exceed 1. For convenience, we define $x = \tilde{\sigma}/\tilde{\sigma}_{35\%}$, with $\tilde{\sigma}_{35\%}$ being the average particle stress measured at a bulk sample porosity of 35 %. Then, $P(x)$ is calculated at intervals of 5 % of absolute porosity as to obtain the evolution of the distribution of stress with increasing strain. The results of this analysis are displayed in Fig. 2.7, which clearly show that with decreasing porosity (increasing strain) 1) the average stress supported by the particles decreases (curves shifting left over the x-axis), and 2) the stress becomes

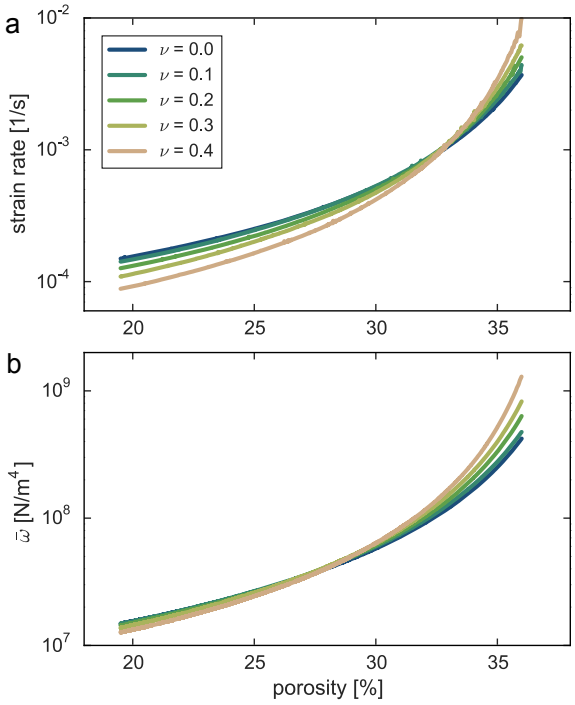

Fig. 2.6: DEM results for creep tests performed on samples with a fixed mean particle size but varying values of the width of the grain size distribution, expressed in terms of the coefficient of variation, ν. a) The evolution of macroscopic strain rate with porosity. During the initial stages of compaction, where the porosities are high (> 32 %), the strain rates are enhanced for higher values of ν, whereas during the final stages of compaction the compaction rates are diminished with increasing ν. b) Evolution of contact parameter $\bar{\omega}$ with porosity. A similar crossover is found in $\bar{\omega}$ as in $\dot{\varepsilon}$, but at a lower value of porosity.

more homogeneously distributed, as indicated by a significant local increase in $P(x)$. The first observation can be directly related to the notion that the average contact area A_c grows with ongoing pressure solution, as discussed in Section 2.3.1. In continuum descriptions of IPS (e.g. Eqn. (2.1)), this evolution of the contact area is represented by an arbitrarily defined porosity function, which likely does not capture the detailed evolution of stress as seen in Fig. 2.7.

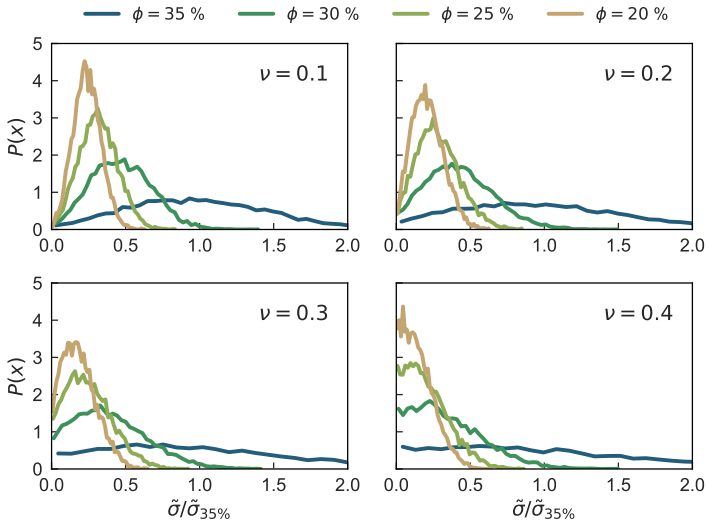

Fig. 2.7: Probability density functions of interparticle stress measured at four different bulk porosities (see legend), and for four different particle size distributions (individual panels). With decreasing porosity, both the magnitude and heterogeneity of the particle stress decrease.

The second observation that the stress distribution becomes more homogeneous with increasing strain is readily explained by the negative feedback loop that is induced by Eqn. (2.6): when the stress on a given contact is higher than average, it will experience enhanced rates of pressure solution (high V_{ps}), and so the stress on the contact will decrease more rapidly as A_c grows, in turn resulting in lower V_{ps}. This also implies that force chains initially present in the system will broaden and dilute as compaction progresses, and that it is unlikely that such a system supports localisation of strain.

With this additional knowledge of the internal distribution of stress, we can now attempt to relate this observed crossover in strain rates to the internal stress distribution. It is expected that the distribution of contact stresses within the sample is related to the distribution of the particle sizes (e.g. *Marketos and Bolton*, 2007; *Torok et al.*, 2005). However, it is not directly evident from experiments how the average contact stress changes with the width of the particle size distribution, and how it relates to

the overall compaction behaviour. To evaluate this, we calculate the axial (vertical) component of the normal force ($F_{z,i}$) acting on each particle-particle contact, as well as the area of contact ($A_{c,i}$), and record these quantities at regular intervals of 0.5 % porosity during the simulations. The bulk-averaged, axial contact stress $\bar{\sigma}_c$ is then obtained as:

$$\bar{\sigma}_c = \frac{\sum_{i=1}^{N} F_{z,i}}{\sum_{i=1}^{N} A_{c,i}} \tag{2.11}$$

Most analytical expressions for IPS only consider a uniform (mean) grain size, and therefore the contribution of the diffusion distance to the strain rate can be directly related to the grain size and total strain (or porosity). The predicted strain rates for a given grain size and porosity are then linearly proportional to the (applied) normal stress (see Eqn. (2.1b)). However, it is non-trivial to achieve such relations for a non-uniform grain size, and therefore we choose to explicitly include the evolution of the diffusion distance in our analysis by defining a new quantity, $\bar{\omega}$, following Eqn. (2.6b):

$$\bar{\omega} = \frac{\bar{\sigma}_c}{\bar{A}_c} = \frac{N \sum_{i=1}^{N} F_{z,i}}{\left(\sum_{i=1}^{N} A_{c,i} \right)^2} \tag{2.12}$$

The parameter $\bar{\omega}$ describes the average properties of the particle contacts that drive pressure solution, and is proportional to the macroscopic strain rate, i.e. $\dot{\varepsilon} \propto \bar{\omega}$. The evolution of $\bar{\omega}$ with porosity is plotted in Fig. 2.6b, and shows a similar crossover as the overall strain rate. This suggests that the change in compaction behaviour in our DEM model is related to changes in the internal distribution of stress and contact area. However, the porosity at which this crossover of $\bar{\omega}$ occurs is about 5 % lower (in absolute value) than that of $\dot{\varepsilon}$. This implies that for a given $\bar{\omega}$, $\dot{\varepsilon}$ decreases with increasing width of the particle size distribution. We were not able to elucidate this behaviour with our current analysis, and it is possibly a consequence of the geometrical arrangement of particles within the sample. Yet, it can be concluded that the evolution of the internal state of stress and contact area in a polydisperse aggregate may in part explain the change in strain rate dependence on ν, helping to reconcile the experimental observations of *Niemeijer et al.* (2009) to the analytical model of *Ter Heege et al.*

(2004).

While there is a clear effect of grain size distribution on the overall rate of compaction, this effect is generally less than half an order of magnitude for the largest value of ν investigated. Hence, polydispersity on its own cannot directly explain the large discrepancies between analytical predictions and experimentally observed compaction rates. However, it should be noted that in this study only a Gaussian distribution was considered, and that other types of grain size distributions (e.g. power-law or bimodal) may produce a different distribution of contact stresses and strain rates, for instance when large particles are fully immersed in a matrix of small particles. Additionally, the shape of the grains and that of the grain-grain contacts could strongly affect the magnitude and distribution of the contact stresses. We reserve further investigations of the various effect of grain size distributions and grain shapes for future studies.

2.6 Conclusions

In this study, we have proposed a new DEM contact law and constructed a DEM model accounting for friction and pressure solution at the grain contacts, using a pressure solution contact law extracted from previous macro-scale expressions for IPS. The novelty of the implementation lies in that the DEM particle overlap is used to model dissolved material, of which the dissolution rate is directly linked to micro-scale physical models. By comparison of the DEM results with uniaxial compaction experiments conducted on granular halite with a narrow grain size distribution, we found that the DEM model is capable of realistically describing the macroscopic compaction behaviour as seen in the experiments. The verified numerical model was then used to investigate the effects of inter-grain friction and of non-uniform grain sizes on the creep rates of granular halite.

It was found that interparticle friction can reduce the compaction rates by up to half an order of magnitude. The amount of reduction of compaction rates was independent of porosity and absolute strain rate. Furthermore, interparticle friction did not seem to affect the dependency of strain rate on the grain size and stress, which were identical for simulations with an interparticle friction coefficient of 0.01 and 0.6. However, it

is likely that the estimates of $(DCS)_0$ (a DEM input parameter), as obtained from experiments, are already affected by any effects of friction, and hence friction itself cannot explain the discrepancy between analytical model estimates and experimental compaction rates, which can exceed several orders of magnitude difference.

When considering the effect of a distributed grain size, it was found that with increasing degree of polydispersity (i.e. wider grain size distribution) the bulk-average value of ω (i.e. contact stress over contact area) increased, promoting overall compaction rates. This was in agreement with the results of earlier experiments on halite with a distributed grain size by *Niemeijer et al.* (2009), who observed enhanced strain rates in more polydispersed samples. However, as the porosity decreased below 32 %, $\bar{\omega}$ decreased faster with increasing ν and the effect reversed, i.e. with increasing degree of polydispersity the average contact stress and strain rate decreased. This is consistent with the analysis of *Ter Heege et al.* (2004), who derived a composite flow law accounting for a log-normally distributed grain size, and predicted a reduction in strain rates with increasing polydispersity for bulk (low porosity) materials. However, this effect of the grain size distribution was small (less that half an order of magnitude) and is likely to play only a minor role in the overall compaction behaviour in experiments, when a log-normal distribution is considered. In these simulations it was also observed that with increasing compaction, the contact stresses become more narrowly (i.e. more homogeneously) distributed over the aggregate by preferentially dissolving material at the more highly stressed particle contacts. This can have important implications for other phenomena that have been linked to IPS, such as shear deformation of granular fault gouges under conditions where fluid-rock interactions are prevalent.

Another conclusion is that interparticle friction and a log-normally distributed grain size cannot explain the observed discrepancies between experimental compaction rates and predictions by analytical models. Hence, other mechanisms that may impede compaction by pressure solution need to be considered, particularly for understanding the long-term evolution of large-scale geodynamical systems, such as compacting sedimentary basins and hydrocarbon reservoirs. A possible candidate mechanism is the process of sealing of the grain contact by grain boundary healing due to growth of contact asperities (see *Van Noort et al.*, 2008b). It is left for future studies to investigate the role of this mechanism on the overall deformation rates. Nonetheless,

we have demonstrated that the Discrete Element Method can successfully be used to simulate pressure solution in granular aggregates, and that the model can be used to relate micro-scale processes to macroscopic compaction behaviour.

Appendices

2.A Experimental procedure

To validate the DEM model, we compared the outcome of DEM compaction tests to the results of compaction experiments conducted on porous halite aggregates. For these experiments, a dead-weight uniaxial set-up was employed similar to the one used by *De Meer and Spiers* (1997) and *Zhang et al.* (2002) – see Fig. 2.A.1. The sample material was contained within a glass capillary tube (2.15 mm inner diameter), which was supported in a brass base plate. A dead-weight provided a constant load throughout the experiment, transmitted to the sample through steel pistons that were located in the glass tube above and below the sample. A filter paper disk was placed between the top piston and the sample to prevent grains of sample material lodging between the piston and the glass tube and thus increasing the friction between the piston and the tube wall. In addition, the walls of the glass tube were coated with a thin layer of graphite to reduce the effects of the wall friction. The dead-weight, glass tube and brass base plate were housed in a rigid plastic support tube to ensure proper alignment. The entire apparatus was then placed inside a polystyrene foam box that was temperature-controlled at 40.0 ± 0.1 °C. Movement of the dead-weight, i.e. compaction of the sample, was measured using a capacitive 'gap sensor' transducer (Baumer Electric, type IWA 18U 9001; 3.0 mm over 10 V full-scale, 16-bit A/D resolution). The gap sensor output was logged at a rate varying from 100 to 0.01 Hz, depending on the creep rate (i.e. higher creep rates were logged at higher logging rates).

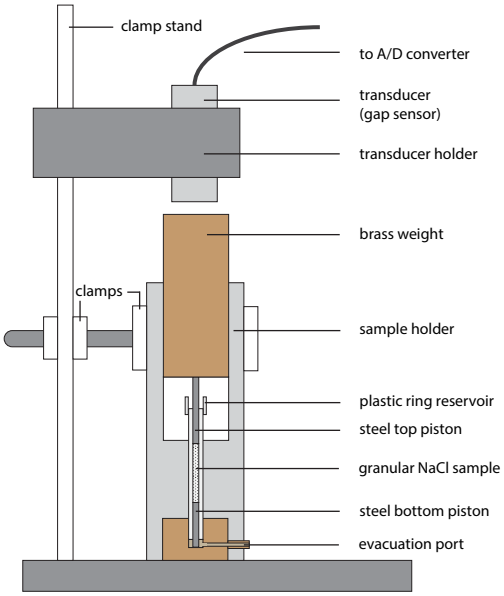

Fig. 2.A.1: Schematic diagram of the experimental setup as used for the uniaxial compaction experiments. After *Visser et al.* (2012).

The sample material used here consisted of analytical grade halite (VWR Chemicals BV), sieved to a grain size fraction in the range 63-71 µm. While the coarser fractions commonly display an idiomorphic (cubic) habit, the grains in the fraction used here were less idiomorphic in shape with non-smooth surfaces and jagged edges. After sieving, the sample material was stored in a dry-room (humidity < 25 %RH) to prevent moisture adsorption, and was then dried in an oven at 50 °C for at least 2 hours together with the glass tubes and pistons used, before assembling the individual components.

In conducting the experiments, each sample was first precompacted dry at 3.85 MPa axial stress for 30 minutes to ensure a reproducible 'locked' starting microstructure with an average starting porosity of 43.1 ± 1.7 %. The apparatus was then removed from the box and the sample length was measured using a travelling microscope with an instrumental precision of 0.01 mm. The sample porosity was calculated based on this estimate of the sample length and the sample mass present in the capillary tube

as weighed after the sample was prepared. From error propagation analysis, it was found the porosity could be determined with a precision of 0.5 % absolute value. In these calculations, no corrections had to be made for transport of solid mass out of the system, as the pore fluid was presaturated with the sample material at the experimental conditions, so that no bulk dissolution could have occurred. Since presaturation was carried out using unstressed sample material, the added solution would have been minutely undersaturated with respect to the loaded sample, due to the increase in mean Helmholtz energy of the grains in the sample associated with the grain scale elastic deformation, which is of the order of $\sigma_n^2 \Omega / \left(2 \left[1 - \phi\right] E\right)$, E being the Young's modulus of the material (37 GPa). This simple order of magnitude calculation shows that at 38 % porosity the maximum increase in solubility is 4.3×10^{-5} % of the unstressed reference value. This compares negligibly to the enhanced solubility at the stressed grain contacts (up to 25 % of the unstressed reference value), and so the effect of elastic loading of the solid framework can be ignored. Additionally, since diffusion is the rate limiting step for IPS in halite, the solute concentration in the open pores is buffered by the pore wall solubility, inhibiting long-range advective or diffusive transport.

After measuring the sample height, the apparatus was again placed in the polystyrene foam box and an axial stress of 1.08 MPa was applied. The sample was then allowed to equilibrate with the temperature of the box, and any thermal perturbations caused by opening and closing of the box were recovered during this period. After thermal equilibrium was attained, a saturated brine solution was introduced to the system, with the load still applied, by filling the plastic ring fluid reservoir at the top of the container and applying a partial vacuum via the base plate using a syringe. The fluid penetrated and saturated the sample within a second in most cases. The fluid reservoir was subsequently topped with a droplet of silicone oil to prevent evaporation, and the evacuation tube connected to the base plate was closed off using a clamp. During the procedure of adding the pore fluid, the polystyrene box was opened for about 20 seconds to provide access to the apparatus, which caused the temperature to drop by a few degrees. The brine solution was stored in a container situated inside the box to ensure equilibrium of the pore fluid at the experimental conditions. As soon as the pore fluid was introduced, the sample started to compact, which marked the beginning of the wet compaction phase. After wet compaction for one hour, the experiment was terminated, the apparatus removed from the box, and the sample length re-measured

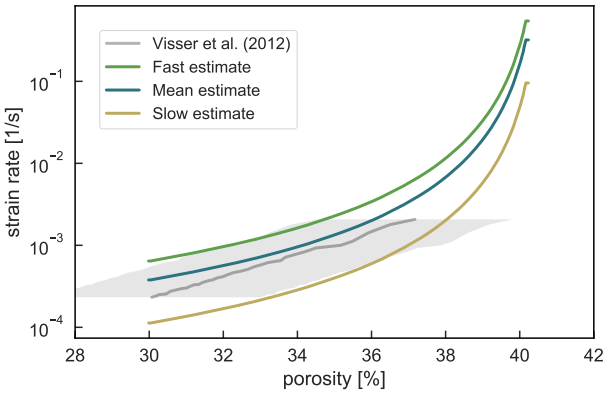

Fig. 2.A.2: Uniaxial compaction data for granular $NaNO_3$ from *Visser et al.* (2012), for the conditions and porosities for which the behavior is expected to be dominated by pressure solution. The experimental variability in starting porosity is reflected by the gray shaded area. The laboratory data is compared with DEM simulation data, with a mean, a slow, and a fast estimate of the kinetic parameter $DCS = (5.7 \pm 4) \times 10^{-19}\,\mathrm{m}^3\,\mathrm{s}^{-1}$.

using the travelling microscope.

During data processing, the strain rates are obtained from temporal differentiation of the dead-weight position data by means of ordinary least-squares inversion with a variable window size centred around each individual data point. The window size is decided based on a user-provided tolerance for the variation of the dependent variable (which was set to a strain of 0.1 %). This means that the differentiated data is implicitly filtered, in a similar way as the Savitzky-Golay method provides a smoothed (optionally differentiated) signal. When differentiation is performed within a window of constant size (e.g. through a central differences scheme), the low-strain rate data tends to show significant noise, whereas the high-strain rate data tends to become clipped or inaccurate, so that only a limited data range is well-resolved.

In addition to the experiments conducted on halite, a comparison is made with the uniaxial compaction experiments conducted by *Visser et al.* (2012), who employed a similar method as described above. The comparison between DEM simulations and

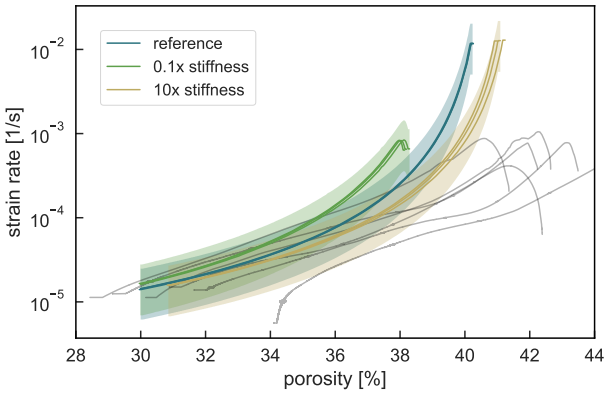

Fig. 2.B.1: Investigation of the effect of stiffness, by repeating simulation set A for three different stiffnesses (see legend). For each chosen value of stiffness, three random samples are generated to test the reproducibility. The uncertainty in the kinetic parameters is given by the shaded area around each simulation curve. The DEM simulations are compared with the experimental compaction data (gray lines).

laboratory data is shown in Fig. 2.A.2. The applied normal stress was reported by *Visser et al.* (2012) to be 1.25 MPa, the mean grain size 39 µm, and initial porosity 40.5 ± 2.5 %.

2.B Effect of stiffness

As mentioned in Section 2.3.1, there exists large uncertainty in the elastic behaviour of single grain contacts, which tend not to follow perfect Hookean or Hertzian elasticity. However, since with increasing compaction the contribution of elastic strain becomes small relative to the contribution of pressure solution, it can be expected that the role played by elasticity diminishes over time. To test this hypothesis, we repeated simulation set A with three different choices for the particle stiffness: a reference value of 2.65×10^9 N m^{-1}, a value 10 times lower than the reference, and a value 10 times

higher than the reference. Furthermore, for each chosen stiffness value, the simulation was repeated with three different random packings, as to investigate the reproducibility of the method. The results these simulations, as compared with the experimental compaction data, are presented in Fig. 2.B.1. In this figure, the uncertainty in the kinetic parameters is indicated by the shaded areas.

The results show that an increasing stiffness systematically increases the initial porosity, i.e. the porosity that was attained after the dry precompaction phase. However, when pressure solution is turned on and the sample compacts, this effect vanishes over about 2 % reduction in absolute value of porosity, after which all simulations follow a similar trajectory. Based on these simulation results, no inference can be made regarding the accuracy of the chosen stiffness model and parameters, as pressure solution dominates the overall compaction behaviour. In spite of the large range of particle stiffness that is covered (two orders of magnitude), the variation in strain rates due to stiffness falls well within the uncertainty in the kinetic parameters and experimental reproducibility. For each chosen particle stiffness, the DEM simulations show excellent reproducibility, as attested by the overlapping curves.

2.C Data availability

Laboratory and model data are available as *Van den Ende* (2017): Experimental and model data of aggregate compaction by pressure solution. GFZ Data Services. http://doi.org/10.5880/fidgeo.2017.018

Chapter 3

Influence of grain boundary structural evolution on pressure solution creep rates

Martijn P. A. van den Ende, George Marketos,
André R. Niemeijer, and Christopher J. Spiers

Abstract

Intergranular pressure solution is a well-known rock deformation mechanism in wet regions of the upper crust, and has been widely studied, especially in the framework of compaction of granular materials, such as reservoir sandstones and fault rocks. Several analytical models exist that describe compaction creep by stress-induced mass transport, and the parameters involved are relatively well constrained by laboratory experiments. While these models are capable of predicting compaction behaviour observed at relatively high porosities, they often overestimate compaction rates at porosities below 20 % by up to several orders of magnitude. This suggests that the microphysical processes operating at low porosities are different and are not captured well by existing models. The implication is that available models cannot be extrapolated to describe compaction of sediments and fault rocks to the low porosities often reached under natural conditions. To address this problem, we propose a new, thermodynamic model that describes the decline of pressure solution rates within individual grain contacts as a result of time-averaged growth of asperities or islands and associated constriction of the grain boundary diffusion path (here termed grain boundary evolution). The resulting constitutive equations for single grain-grain contacts are then combined and solved semi-analytically. These are also implemented into a Discrete Element Method (DEM) numerical framework. The compaction rates predicted by the semi-analytical and DEM models are compared with those measured in high-strain compaction experiments on wet granular halite. Both approaches predict a significant reduction in compaction rate, when grain boundary evolution is considered, which compares favourably with the experimental compaction data. However, to closely reproduce the entire experimental data set, we need to assume that the average thickness of the grain boundary zone depends on the length scale of grain contacts. It follows that, to improve pressure solution models further, the evolution of the topography of dissolving grain contacts needs to be better characterised.

3.1 Introduction

Intergranular pressure solution, or dissolution-precipitation creep, is an important mechanism of time-dependent deformation of rocks under wet, upper-crustal conditions (*Lehner*, 1990; *Rutter*, 1976; *Spiers et al.*, 2004, 1990). Its relevance is recognised, in particular, in relation to the compaction of granular rock materials (*Croizé et al.*, 2010; *Gratier*, 1987; *Karner et al.*, 2003; *Spiers and Schutjens*, 1990; *Tada and Siever*, 1989), in shear deformation of dense rocks under greenschist and blueschist metamorphic conditions (*Elliott*, 1973; *Stöckhert et al.*, 1999), and in controlling the frictional behaviour and strengthening of faults (*Blanpied et al.*, 1992; *Bos et al.*, 2000b; *Jefferies et al.*, 2006; *Karner et al.*, 1997; *Niemeijer and Spiers*, 2006). Crucial for the operation of pressure solution is the presence of a grain boundary solution phase in the form of an adsorbed thin film (*Robin*, 1978; *Rutter*, 1983), or of a dynamically-stable island-channel structure (*Lehner*, 1990; *Raj*, 1982; *Spiers and Schutjens*, 1990). Numerous models have been developed to describe the micro-scale processes that operate during pressure solution (e.g. *Lehner*, 1990; *Shimizu*, 1995; *Spiers et al.*, 1990), and the constitutive parameters involved have been constrained in a range of different laboratory experiments (e.g. *Dewers and Hajash*, 1995; *Gratier et al.*, 2009; *Raj*, 1982; *Rutter*, 1976; *Spiers et al.*, 1990; *Van Noort et al.*, 2008a). However, many experimental studies investigating densification by pressure solution consider timescales that are insufficient to reach low porosities (< 15 %), being limited by the relatively slow kinetics of the process. Studies in which low porosities are achieved report compaction rates that fall orders of magnitude below values that are predicted by analytical models for pressure solution creep (*Niemeijer et al.*, 2002; *Schutjens*, 1991b).

This discrepancy exposes an important shortcoming in our understanding of the micro-scale processes at play, and limits our ability to reliably extrapolate laboratory results to nature. For example, time-dependent fault zone restrengthening and fluid pressure build-up in faults have been proposed to result from densification by pressure solution creep (*Angevine et al.*, 1982; *Sleep and Blanpied*, 1992). Estimates of long-term (centennial) fault zone restrengthening accordingly require accurate descriptions of pressure solution creep over the full range of attainable fault rock porosities. As a candidate mechanism for the retardation of pressure solution at low porosities,

sealing/healing of grain boundaries due to surface-energy driven mass transfer has been suggested (*Hickman and Evans*, 1991; *Van Noort et al.*, 2008b; *Visser*, 1999). Crack- and grain boundary healing or sealing, driven by surface energy reduction, has similarly been suggested as a mechanism for fault rock restrengthening (*Beeler and Hickman*, 2015; *Brantley*, 1992; *Hickman and Evans*, 1992).

Here, we develop an analytical expression that describes the evolution of grain boundary structure during deformation by pressure solution, and its effect on the rate of pressure solution. The constitutive relations that result are incorporated into a Discrete Element Method (DEM) framework for modelling pressure solution, as described in Chapter 2 (and extended here; see also *Van den Ende et al.*, 2018b), and the interplay between pressure solution and grain boundary healing is investigated numerically. To validate the model, we compare the compaction rates predicted by the DEM model with the laboratory data on densification of granular halite provided by *Schutjens* (1991b). We find that grain boundary evolution involving increasing solid-solid contact area with time can readily explain the observed reduction in strain rate. Agreement between model and experiment is improved further if the thickness of the grain boundary zone is set to increase with increasing grain contact length scale, following a fractal scaling relationship.

3.2 Previous work on pressure solution and grain boundary healing

3.2.1 Pressure solution in theory and experiment

In general, pressure solution in a porous rock system where there is no long-range mass transport can be seen as a series of three consecutive processes: (1) dissolution of material at stressed grain-grain contacts, (2) diffusion of the dissolved mass out of the grain contact zone, and (3) precipitation on the pore walls. Which of these serial processes controls the overall rate of pressure solution is determined by kinetics of dissolution, diffusion, and precipitation, respectively. When it is assumed that only one process controls the kinetics of pressure solution, then for the case of either 1D

or isotropic compaction, the macroscopic strain rate can be described by one of the following analytical expressions (*Pluymakers and Spiers*, 2014; *Rutter*, 1976; *Shimizu*, 1995; *Spiers and Schutjens*, 1990):

$$\dot{\varepsilon}_s = A_s \frac{I_s \Omega}{RT} \frac{\sigma_e}{d} f_s(\phi) \tag{3.1a}$$

$$\dot{\varepsilon}_d = A_d \frac{(DCS)\Omega}{RT} \frac{\sigma_e}{d^3} f_d(\phi) \tag{3.1b}$$

$$\dot{\varepsilon}_p = A_p \frac{I_p \Omega}{RT} \frac{\sigma_e}{d} f_p(\phi) \tag{3.1c}$$

Here, the subscripts s, d and p denote dissolution-, diffusion- and precipitation-controlled kinetics respectively, $\dot{\varepsilon}_x$ is the corresponding volumetric strain rate, A_x a geometric constant, d the mean grain size, σ_e the effective stress (applied axial stress or confining pressure minus pore fluid pressure), Ω the molar volume of the solid, R the universal gas constant, T the absolute temperature, D the effective diffusion coefficient of the ionic species dissolved in the grain boundary fluid, C the solubility of a flat, unstressed solid interface, S the (mean) thickness of fluid in the grain boundary zone, and $f_x(\phi)$ a dimensionless function of porosity (ϕ) which accounts for the evolution of contact area and pore wall area during compaction. The rate coefficients for grain boundary dissolution (I_s), precipitation (I_p) and for diffusion within the grain boundary (DCS) vary with temperature and exhibit an Arrhenius dependence on temperature, i.e. to take the form:

$$I_x = I_{x,0} \exp\left(-\frac{\Delta H_x}{RT}\right) \tag{3.2}$$

for I_s and I_p (*Van Noort and Spiers*, 2009), and

$$(DCS) = (DCS)_0 \exp\left(-\frac{\Delta H_d}{RT}\right) \tag{3.3}$$

for (DCS) (e.g. *Spiers and Schutjens*, 1990; *Spiers et al.*, 1990). Here, ΔH_x is the apparent activation energy associated with each process. For highly soluble materials at room temperature, such as alkali metal salts, diffusion along the grain boundary controls the creep rate as dissolution and precipitation are relatively fast, whereas low solubility solids often show interface-reaction controlled kinetics (*Niemeijer et al.*, 2002;

Spiers et al., 2004).

As mentioned above, the kinetics of diffusion-controlled pressure solution are governed by the combined product DCS. This parameter encompasses the structure of the grain boundary through the effective cross-section (mean fluid thickness) and the effects of any surface force interactions between the solid, the fluid, and the dissolved ionic species. Effects of grain boundary diffusion path tortuosity can be accounted for by replacing D with an effective value of D. For steady-state pressure solution, many analytical models assume a dynamically-stable island-channel grain boundary structure (*Lehner*, 1990; *Raj*, 1982; *Spiers and Schutjens*, 1990), in which contact asperities and surrounding grain boundary interfaces undergo continuous dissolution and precipitation. In this way, the grain boundary does not attain equilibrium, but a rough, time-statistically steady-state structure is expected to arise (*Lehner*, 1990). However, the assumption of steady-state compaction may be violated when the stresses on the grain-grain contacts decrease and surface energy driving forces start to play a role in controlling the energy balance within, and the structure of the grain boundary (*Schutjens and Spiers*, 1999; *Van Noort et al.*, 2008b; *Visser*, 1999).

3.2.2 Pressure solution retardation mechanisms

In hydrostatic compaction experiments conducted on granular quartz (*Niemeijer et al.*, 2002) and on halite (*Schutjens*, 1991b), it has been observed that for low porosities, volumetric strain rates can fall to values several orders of magnitude lower than predicted by analytical models for pressure solution (e.g. Eqn. (3.1)), despite good agreement reported at higher porosity values. These observations on compacting aggregates suggest a gap in our understanding of pressure solution, particularly at low porosities. A number of explanations have been proposed for the retardation effect seen at low porosities:

1. Contamination: *Niemeijer et al.* (2002) suggested that interface reactions (dissolution or precipitation) were inhibited at low porosities by trace abundances of metallic cations, such as Cu^{2+}, derived from the gradually corroding capsule containing the quartz sample material. However, in experiments conducted on halite

(*Schutjens*, 1991b), a material that is well known to exhibit diffusion-controlled pressure solution rates (*Spiers et al.*, 2004), similar reductions in strain rates were observed. Furthermore, in the compaction tests of *Schutjens* (1991b) the salt sample material was contained by a latex balloon, so that contamination of the pore fluid can be eliminated as a retardation mechanism in these experiments.

2. Grain contact shape: The starting material in the experiments conducted by *Schutjens* (1991b) is characterised by idiomorphic grain shapes with a typical cubic habit of which the edges and corners are slightly rounded, so that initially the shape of the corner-face grain contacts is approximately circular. However, with increasing strain the grain contacts become more triangular, in correspondence with the cubic grain shape. *Spiers and Schutjens* (1990) argued that this change in grain contact morphology could qualitatively explain the deceleration in pressure solution creep rates with increasing strain, and corresponding change in the sensitivity of compaction rates to the total strain (porosity), illustrated by the analysis of two end-member grain contact geometries. In the porosity range of 10-15 %, a change from circular to triangular grain contact geometry would theoretically affect compaction rates by a factor 1-2, which is insufficient to explain the observed discrepancy of several orders of magnitude in this porosity range.

3. Pore wall curvature: Uniaxial compaction tests conducted by *Visser et al.* (2012) on granular $NaNO_3$ revealed that for small grain size fractions, pressure solution was measurably slower than expected from analytical models. This behaviour was attributed to the non-negligible contribution of the pore wall curvature to the thermodynamic driving force for pressure solution. For grain sizes smaller than 20 µm and applied stresses lower than 0.025 MPa, the pore wall interface energy term approached the magnitude of the stress on the contact, and so surface tension started to compete with stress as the driving force for pressure solution, resulting in diminished compaction rates. However, for typical values of d and P_e or σ_e as employed by *Schutjens* (1991b) and *Niemeijer et al.* (2002), the competing force resulting from the surface curvature of the pore wall is negligibly small (of the order of several kPa) and therefore does not compete with contact stress as a thermodynamic driving force.

4. Fluid overpressure: At porosities near the percolation threshold for a pore network (around 3 %; *Van der Marck*, 1996), disconnection of the pore space can result in local build-up of fluid pressure, lowering σ_e and therefore diminishing compaction rates. Additionally, pressure solution may become limited by the availability of pore wall area, i.e. become precipitation-controlled (*De Meer and Spiers*, 1999). However, these mechanisms cannot explain the divergence between experimental and model strain rates at porosities in the range of 10-20 %, where porosity is fully connected and grain size dependence shows that pressure solution in halite is still diffusion-controlled (*Schutjens*, 1991b).

5. Grain boundary structure: Numerous laboratory experiments (*De Meer et al.*, 2005, 2002; *Renard et al.*, 2012; *Schutjens and Spiers*, 1999), and theoretical considerations (*Gal et al.*, 1998; *Ghoussoub and Leroy*, 2001), point to the existence of a dynamically-stable island-channel grain boundary structure during pressure solution. The kinetics of diffusion-controlled pressure solution are strongly dependent on the topography and topology of this island-channel structure, through the combined product DCS (where D represents an effective diffusion coefficient). During steady-state pressure solution creep, the grain boundary structure is expected to remain time-statistically invariant, so that DCS is constant. However, several experiments (e.g. *Schutjens and Spiers*, 1999) have shown that the grain boundary structure is rough and open at high effective contact stress, and much more constricted at low effective stress. It is therefore expected that the product DCS is lower in low porosity aggregates (i.e. low contact stress) than at high porosity.

Of the mechanisms discussed above, only the last holds potential to explain the large discrepancy between analytical model predictions and observed compaction rates. We will accordingly consider the evolution of the internal grain boundary structure during pressure solution in more detail.

3.2.3 Observations of grain boundary structure

First, let us summarise a number of key observations regarding the structure of grain boundaries. *Desbois et al.* (2012) analysed the fluid distribution in dense natural

salt samples from the Qom Kuh salt fountain (central Iran) using cryogenic scanning electron microscopy, and observed numerous examples of narrow and straight contacts, and arrays of isolated grain boundary fluid inclusions. From these observations, the authors concluded that grain boundary healing must have operated under the low stress conditions (up to 1 MPa of contact stress) experienced by the sample. Similar features were observed by *Urai et al.* (1986) in natural rock salt samples from the Asse Mine (Germany). After experimental deformation under non-dilatant conditions, the samples predominantly showed sub-continuous fluid films, indicating (dynamic) wetting of the grain boundaries. However, one year after the test was terminated, the morphology of the grain boundaries had changed substantially: the sub-continuous fluid films had broken down to form discontinuous arrays of fluid inclusions, very similar to the (healed) starting material.

In a series of see-through experiments, *Renard et al.* (2012) used optical imaging techniques to monitor the evolution of asperity contacts between flat glass and halite interfaces, onto which a constant normal stress of 0.26 MPa was applied. In a nominally dry environment, the total surface area occupied by asperities remained well below 1 % (= 1 µm^2) of the imaged region. However, when a saturated brine was added, the asperities started to grow laterally, becoming easily visible (up to about 300 µm). During growth, insufficient convergence was measured to explain the expansion of the asperities by plastic creep. Rather, the process was explained by diffusive mass transfer driven by excess surface tension acting at the asperities margins.

The experiments conducted by *Schutjens and Spiers* (1999) were similar in that the edge of a prismatic halite crystal was pressed against a flat halite or glass plate. The contact stresses employed fell in the range of 2-5 MPa for most of the test duration. As opposed to *Renard et al.* (2012) and *Hickman and Evans* (1991, 1992, 1995), significant convergence rates were found in all of their experiments, and widening of the contact could be explained entirely by the convergence of the two bodies, rather than by neck growth as suggested by *Hickman and Evans* (1991, 1992, 1995). Concurrently, initial roughness within the contact was gradually smoothed out below optical detection (< 1 µm). When the applied load was instantaneously increased, the grain contact topography became rejuvenated within minutes before slowly vanishing again. Hence, in the framework of a the island-channel model, competition between contact stress

and surface energy driving forces is expected to control the topography of a stressed grain contact.

These laboratory observations reveal an interplay between the stress supported by a loaded contact, causing dynamic roughening and dissolution, and local variations in surface energy driving growth of contact asperities. The lateral growth of contact asperities/islands strongly controls the structure of the grain boundary zone by decreasing the mean thickness and overall connectivity of the grain boundary fluid, ultimately resulting in isolated fluid pockets, as typically observed in long-term deformation tests and natural salt samples (e.g. *Desbois et al.*, 2012; *Urai et al.*, 1986). By reducing the connectivity and diffusive properties of a grain boundary, it is expected that grain boundary healing can significantly reduce rates of diffusion-controlled pressure solution creep, or enforce a switch in rate controlling mechanism from interface-reaction controlled to diffusion-controlled pressure solution, hence explaining the significant reduction in compaction rates reported in a number compaction experiments of granular aggregates (*Niemeijer et al.*, 2002; *Schutjens*, 1991b). We will proceed to use these notions to formulate a grain-scale description for the structural evolution of stressed grain contacts during pressure solution.

3.2.4 Thermodynamics of grain boundary healing and sealing

In order to further comprehend the evolution of grain contacts under stress, we will first review basic thermodynamic concepts that are prerequisites for developing a model for grain boundary structural change during pressure solution.

The chemical equilibrium at a triple junction between two grains of an isotropic solid plus a fluid phase can be described by the Young-Dupré relation (e.g. *Holness*, 1992):

$$\gamma_{ss} = 2\gamma_{sl} \cos\left(\frac{\theta_{eq}}{2}\right) \tag{3.4}$$

Here, γ_{sl} and γ_{ss} denote the solid-liquid and solid-solid interfacial energy, respectively, and θ_{eq} denotes the dihedral angle at equilibrium. It was shown by *Visser* and coworkers (*Van Noort et al.*, 2008b; *Visser*, 1999) that when the dihedral angle θ at the contact

margin deviates from the equilibrium value θ_{eq}, a thermodynamic force F (in N m^{-1}) is exerted on the contact margin, given by:

$$F = 2\gamma_{sl}\left(\cos\frac{\theta}{2} - \cos\frac{\theta_{eq}}{2}\right) = 2\gamma_{sl}\Delta\cos\frac{\theta}{2} \tag{3.5}$$

This force may drive lateral spreading (neck growth) or retreat (marginal dissolution or undercutting) of the solid-solid contact. A dynamically wetted island-channel structure represents a non-equilibrium, hence elevated energy state, which is thought to be maintained by local stress-induced perturbations that may overcome any surface energy reduction effects (*Lehner*, 1990; *Spiers and Schutjens*, 1990; *Visser*, 1999). However, if the stress on the grain contact is removed, or is reduced below a threshold value at which the local stress perturbations are insufficient to maintain a dynamically wetted state, the solid-liquid interfaces within a grain boundary will re-configure towards a configuration of disconnected pockets of fluids that (locally) minimises the interfacial and total energy content of the grain boundary. In the case of static growth of the asperities, this process is referred to as *grain boundary healing* (*Van Noort et al.*, 2008b; *Visser*, 1999).

Following *Visser* (1999) and *Van Noort et al.* (2008b), one can express the potential for lateral growth of stressed asperities within a grain-grain contact in terms of a competition between the effects of the applied stress on the elastic strain energy f_{el} and surface energy. In this treatment, the asperities are viewed as small, dynamically migrating islands with constant height and a dynamic dihedral angle of $\theta = 0$. Then, the chemical potential for lateral growth (at low fluid pressure) is expressed as (*Van Noort et al.*, 2008b):

$$\Delta\mu_i = \frac{F}{S} - \Delta f_{el} = \frac{2\gamma_{sl}}{S}\Delta\cos\frac{\theta}{2} - \frac{(\sigma_c/\alpha)^2}{2E} \tag{3.6}$$

Here, Δf_{el} is the difference between the average value of f_{el} from the stressed island to the grain contact margin, σ_c denotes the mean effective normal stress on the grain contact scale (i.e. $\sigma_n - P_f$ at the contact), α the relative asperity area fraction, and E the Young's modulus. If $\Delta\mu_i > 0$, lateral growth of the asperities occurs, driven by the surface energy force F (first term in the right-hand side of the equality), dominating over Δf_{el} (second term in the right-hand side). If $\Delta\mu_i < 0$, net dissolution occurs due

to dominance of the stored elastic energy Δf_{el}. The criterion for static island growth, hence grain boundary healing, is then defined by the condition $\Delta\mu_i > 0$, so that the critical effective stress σ_{crit} below which healing occurs can be written in terms of the equilibrium condition:

$$\sigma_{crit} = 2\alpha\sqrt{E\frac{\gamma_{sl}}{S}\Delta\cos\frac{\theta}{2}} \tag{3.7}$$

For effective contact stresses lower than σ_{crit}, the surface energy term in Eqn. (3.6) dominates, and nett growth of the asperities results in healing of the grain boundary. This criterion subdivides the dynamic wetting versus grain boundary healing fields, but does not provide information regarding the rate of asperity growth in a transient state, in either stressed (pressure dissolving) or unstressed grain contacts. To gain more insight into the interplay between structural evolution of grain boundaries and compaction by pressure solution, we propose a new model below.

3.3 Microphysical model for the effects of grain boundary structural change on pressure solution

3.3.1 Grain boundary evolution model

Following *Lehner* (1990), the grain boundary zone during pressure solution is envisioned to consist of a dynamically rough topography of contact asperities (islands) that are separated by a continuous, interconnected network of interstitial fluid (channels) – see Fig. 3.1. In previous studies deriving expressions for steady-state pressure solution creep, it is generally assumed that the island-channel network is a steady-state structure of which the properties, averaged over the entire grain boundary, remain constant over time (*Lehner*, 1990; *Raj*, 1982; *Spiers and Schutjens*, 1990). Similarly, we assume the average height of the grain boundary topography (S) to be time-invariant. The total area of the grain contact A_c that is occupied by islands (i.e. solid-solid contacts) is denoted by A_{ss}. The contact area A_c increases as grain to grain convergence proceeds by pressure solution. It is convenient to define the relative island occupation ratio as

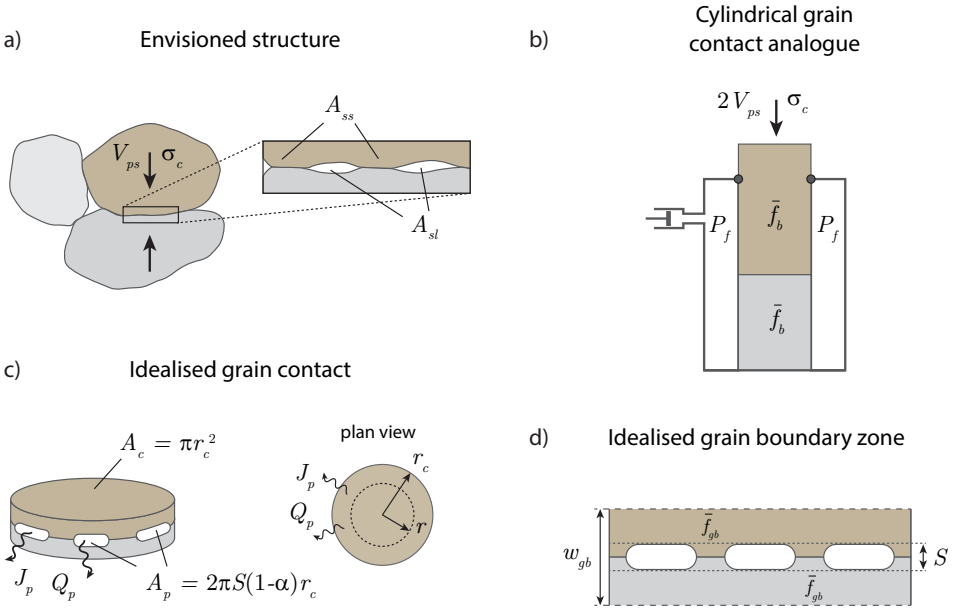

Fig. 3.1: Synopsis of the grain geometries adopted in this work. a) During pressure solution, the envisioned grain contacts exhibit a dynamically stable island-channel structure (c.f. *Lehner*, 1990), in which the total cross-sectional area of solid-solid contact points (the islands) is A_{ss}, and the total cross-sectional area that is open to the interstitial fluid (the channels) is A_{sl}; b) In deriving the analytical constitutive relations, a cylindrical grain geometry is assumed. The solid framework is submersed in a fluid of constant pressure P_f and loaded axially with a total stress σ_c, which raises the mean free energy density of each grain to $\bar{f}_b$ and causes convergence at a rate $2V_{ps}$; c) The grain contact is envisioned as a disc-shaped region of thickness w_{gb}, cross-sectional area A_c and radius r_c. Mass is transported out of the grain contact region through the open periphery A_p; d) Within the grain boundary region, the solid has a mean free energy density $\bar{f}_{gb}$. The average height of the islands and channels is denoted by S.

$\alpha \equiv A_{ss}/A_c$. From this definition it follows that the area occupied by channels A_{sl} is $(1-\alpha)\,A_c$. During active pressure solution creep, mass is transported through the grain boundary peripheral area A_p by a diffusive flux J_p, which is defined positive when directed outward from the grain boundary into the pore space. Similarly, when the grain boundary area occupied by islands increases (i.e. when α increases), fluid is

expelled out of the grain boundary, defining a positive advective flux Q_p, carrying a mean solute concentration $\bar{C}$.

Let us now consider a single disc-shaped contact between two cylindrical grains with depictions and assumptions given in Fig. 3.1 (specifically Fig. 3.1b-d). During active pressure solution with island growth, and assuming constant solid density, the mass/volume balance for the solid in the cylindrical, two-grain contact is given by:

$$\begin{aligned} 2A_c V_{ps} &= A_p J_p + \bar{C} Q_p + \frac{\mathrm{d}\left(A_{ss} S\right)}{\mathrm{d}t} + \frac{\mathrm{d}\left(\bar{C} A_{sl} S\right)}{\mathrm{d}t} \\ &= A_p J_p + A_c S \bar{C} \frac{\mathrm{d}\alpha}{\mathrm{d}t} + A_c S \frac{\mathrm{d}\alpha}{\mathrm{d}t} + A_c \left(1-\alpha\right) S \frac{\mathrm{d}\bar{C}}{\mathrm{d}t} - A_c S \bar{C} \frac{\mathrm{d}\alpha}{\mathrm{d}t} \\ &\approx A_p J_p + A_c S \frac{\mathrm{d}\alpha}{\mathrm{d}t} \end{aligned} \tag{3.8}$$

In the first line of this equation, the different terms represent, in order: mass dissolved from the grain contact by pressure solution, the diffusive and advective mass fluxes through the grain contact periphery, respectively, the solid mass stored in the islands, and the mass stored as dissolved species in the channels (all in units $\mathrm{m}^3\ \mathrm{s}^{-1}$). We neglect minor changes occurring in the mean solid concentration $\bar{C}$ in the grain boundary fluid. By noting that all solid volume expelled from the contact ($A_p J_p$) will be precipitated on the free grain or pore walls when diffusion is rate-controlling, and that the fluid volume expelled from the grain contact must equal the increase in grain boundary island volume ($A_c S \dot{\alpha}$), the fluid volume ν^f displaced against the fluid pressure P_f must be:

$$\frac{\mathrm{d}\nu^f}{\mathrm{d}t} = A_p J_p + A_c S \frac{\mathrm{d}\alpha}{\mathrm{d}t} = 2A_c V_{ps} \tag{3.9}$$

Following *Lehner* (1990, 1995), the energy/entropy balance for the two-grain system represented in Fig. 3.1b, neglecting contributions related to minor changes in solute concentration in the fluid phase, can be written as:

$$\dot{W} = \dot{F} + \dot{E}_s + \dot{\Delta} \tag{3.10}$$

where $\dot{W}$ is the mechanical work input rate, $\dot{F}$ is the rate of increase of Helmholtz energy of the solid phase, $\dot{E}_s$ accounts for the changes in surface stored energy caused

by island growth/contraction, and $\dot{\Delta} \geq 0$ is the rate of dissipation due to irreversible processes (all in units of J s^{-1}).

For the nett work input rate, we can write (using Eqns. (3.8) and (3.9)):

$$\dot{W} = 2\sigma_c A_c V_{ps} - P_f \frac{\mathrm{d}\nu^f}{\mathrm{d}t} = 2\left[\sigma_c - P_f\right] A_c V_{ps} \tag{3.11}$$

Then, for $\dot{F}$ we can write $\dot{F} = \dot{F}_b + \dot{F}_{gb}$, i.e. as the sum of the energy changes occurring in the grain bodies ($\dot{F}_b$) and the solid portion of the grain boundary zone ($\dot{F}_{gb}$). Here, $\dot{F}_b$ is the energy change due to mass removal from the grain bodies ($-2\bar{f}_b A_c V_{ps}$), plus the energy stored in mass precipitation on the pore walls ($+2\bar{f}_b A_p J_p$), so that, using Eqn. (3.8), gives:

$$\frac{\mathrm{d}F_b}{\mathrm{d}t} = \bar{f}_b \left(A_p J_p - 2A_c V_{ps}\right) = -\bar{f}_b A_c S \frac{\mathrm{d}\alpha}{\mathrm{d}t} \tag{3.12}$$

where $\bar{f}_b$ is the mean free energy density of solid stored in the grain body (units: J m^{-3}). In turn:

$$\frac{\mathrm{d}F_{gb}}{\mathrm{d}t} = \frac{\mathrm{d}\left(\bar{f}_{gb}\nu^s_{gb}\right)}{\mathrm{d}t} = \bar{f}_{gb}\frac{\mathrm{d}\nu^s_{gb}}{\mathrm{d}t} + \nu^s_{gb}\frac{\mathrm{d}\bar{f}_{gb}}{\mathrm{d}t} \tag{3.13}$$

where $\bar{f}_{gb}$ is the mean free energy density of the solid in the perturbed grain boundary zone, and ν^s_{gb} is the volume of solid in the grain boundary zone. Clearly, from Fig. 3.1d, $\dot{\nu}^s_{gb} = A_c S \dot{\alpha}$. Using this relation, we combine Eqns. (3.12) and (3.13) to give:

$$\frac{\mathrm{d}F}{\mathrm{d}t} = \frac{\mathrm{d}F_b}{\mathrm{d}t} + \frac{\mathrm{d}F_{gb}}{\mathrm{d}t} = \left(\bar{f}_{gb} - \bar{f}_b\right) A_c S \frac{\mathrm{d}\alpha}{\mathrm{d}t} + \nu^s_{gb}\frac{\mathrm{d}\bar{f}_{gb}}{\mathrm{d}t} \tag{3.14}$$

In the above relation, the first term on the right hand-side represents the excess solid energy stored in the grain boundary zone as the islands grow in volume, and the second corresponds to the change in grain boundary solid energy due to changing stress/strain concentrations in the evolving grain boundary structure.

The interfacial energy stored in the grain boundary zone is simply the sum $E_s = \gamma_{ss} A_c \alpha + 2\gamma_{sl} A_c \left(1 - \alpha\right)$ of solid-solid (ss) and solid-liquid (sl) interfacial energy (γ) terms (factor 2 accounting for the solid-liquid interfaces on both sides of the contact).

This means that:

$$\dot{E}_s = \gamma_{ss} A_c \frac{\mathrm{d}\alpha}{\mathrm{d}t} - 2\gamma_{sl} A_c \frac{\mathrm{d}\alpha}{\mathrm{d}t} = (\gamma_{ss} - 2\gamma_{sl})\, A_c \frac{\mathrm{d}\alpha}{\mathrm{d}t} \tag{3.15}$$

The solid-solid and solid-liquid surface energy terms are then related through the Young-Dupré relation (*Holness*, 1992) as given in Eqn. (3.4):

$$\gamma_{ss} = 2\gamma_{sl} \cos\frac{\theta_{eq}}{2} \tag{3.4 revisited}$$

Substitution of this relation into Eqn. (3.15) gives:

$$\dot{E}_s = -2\gamma_{sl}\left(1 - \cos\frac{\theta_{eq}}{2}\right) A_c \frac{\mathrm{d}\alpha}{\mathrm{d}t} = -2\gamma_{sl}\Delta\cos\frac{\theta}{2} A_c \frac{\mathrm{d}\alpha}{\mathrm{d}t} \tag{3.16}$$

Note that the above definition of $\Delta\cos(\theta/2)$ is equivalent to that of *Visser* (1999) as given in Eqn. (3.5) when $\theta = 0$, which is in full agreement with the idealised grain boundary geometry displayed in Fig. 3.1d.

From Eqn. (3.10), we hence obtain for the total dissipation:

$$\begin{aligned} \dot{\Delta} &= \dot{W} - \dot{F} - \dot{E}_s \\ &= 2\left[\sigma_c - P_f\right] A_c V_{ps} + \left[\frac{2\gamma_{sl}}{S}\Delta\cos\frac{\theta}{2} - \left(\bar{f}_{gb} - \bar{f}_b\right)\right] A_c S \frac{\mathrm{d}\alpha}{\mathrm{d}t} - \nu^s_{gb}\frac{\mathrm{d}\bar{f}_{gb}}{\mathrm{d}t} \end{aligned} \tag{3.17}$$

During active pressure solution with negligible inelastic deformation of the solid framework, this dissipation will be caused by the internal grain contact mass transfer process. Assuming that the rate of mass transfer is controlled by diffusion, then the dominant dissipative process will be radial grain boundary diffusion, with any internal short range diffusional dissipation being negligible. Hence, we can express the rate of dissipation for a radial increment $\mathrm{d}r$ due to radial diffusion as (*Lehner*, 1990; *Pluymakers and Spiers*, 2014):

$$\mathrm{d}\dot{\Delta} = -J_r a_p \frac{\partial\mu}{\partial r}\mathrm{d}r \tag{3.18}$$

where $a_p = 2(1-\alpha) S\pi r$ is the peripheral area at radius r that is open to the radial diffusive flux J_r. The diffusive flux is driven by a gradient in chemical potential μ, as

given by Fick's first law:

$$J_r = -\frac{DC\Omega}{RT}\frac{\partial \mu}{\partial r} \tag{3.19}$$

Rewriting the solid mass balance Eqn. (3.8) for a grain boundary element explicitly for the diffusive flux, and substituting Eqn. (3.19) gives:

$$\begin{aligned} J_r = \frac{a_c}{a_p}\left(2V_{ps} - S\frac{\mathrm{d}\alpha}{\mathrm{d}t}\right) &= -\frac{DC\Omega}{RT}\frac{\partial \mu}{\partial r} \\ \Rightarrow \frac{\partial \mu}{\partial r} &= -\frac{RT}{DC\Omega}\frac{a_c}{a_p}\left(2V_{ps} - S\frac{\mathrm{d}\alpha}{\mathrm{d}t}\right) \end{aligned} \tag{3.20}$$

with $a_c = \pi r^2$ at radius r. Substituting Eqn. (3.20) into (3.18), and integrating over the grain contact area gives the final expression for $\dot{\Delta}$:

$$\begin{aligned} \dot{\Delta} &= \frac{DC\Omega}{RT}\int_0^{r_c} a_p \left(\frac{\partial \mu}{\partial r}\right)^2 \mathrm{d}r \\ &= \frac{\pi}{2}\frac{RT}{DCS\left(1-\alpha\right)\Omega}\left(2V_{ps} - S\frac{\mathrm{d}\alpha}{\mathrm{d}t}\right)^2 \int_0^{r_c} r^3 \mathrm{d}r \\ &= A_c\frac{r_c^2}{8}\frac{RT}{DCS\left(1-\alpha\right)\Omega}\left(2V_{ps} - S\frac{\mathrm{d}\alpha}{\mathrm{d}t}\right)^2 \end{aligned} \tag{3.21}$$

Combining Eqn. (3.17) and (3.21), and noting that $\nu_{gb}^s = \left[w_{gb} - \left(1-\alpha\right)S\right]A_c$ (see Fig. 3.1d), now leads to the result:

$$\begin{aligned} 2\left[\sigma_c - P_f\right]V_{ps} + \left[\frac{2\gamma_{sl}}{S}\Delta\cos\frac{\theta}{2} - \left(\bar{f}_{gb} - \bar{f}_b\right)\right]S\frac{\mathrm{d}\alpha}{\mathrm{d}t} - \left[w_{gb} - \left(1-\alpha\right)S\right]\frac{\mathrm{d}\bar{f}_{gb}}{\mathrm{d}t} \\ = \frac{r_c^2}{8}\frac{RT}{DCS\left(1-\alpha\right)\Omega}\left(2V_{ps} - S\frac{\mathrm{d}\alpha}{\mathrm{d}t}\right)^2 \end{aligned} \tag{3.22}$$

Assuming that the grain boundary zone is thin, so that $w_{gb} \to S$, it is reasonable to suppose that the main contribution to the excess free energy density in the grain boundary solid over the grain bodies, i.e. to $\left(\bar{f}_{gb} - \bar{f}_b\right)$, will be provided by the strain energy f_i stored in the highly loaded grain boundary islands. Taking this to be

dominated by the elastic strain energy, we can write (c.f. *Van Noort et al.*, 2008b):

$$\left(\bar{f}_{gb} - \bar{f}_b\right) \approx f_i = \frac{1}{2E}\left(\frac{\sigma_c}{\alpha}\right)^2 \tag{3.23}$$

where E is the Young's modulus of the solid. Writing $\bar{f}_{gb} \approx f_i + \bar{f}_b$ and noting that $\bar{f}_b$, the free energy density in the grain bodies, is constant at constant σ_c, it follows for $\mathrm{d}\bar{f}_{gb}/\mathrm{d}t$ in Eqn. (3.22) that:

$$\frac{\mathrm{d}\bar{f}_{gb}}{\mathrm{d}t} = \frac{\mathrm{d}f_i}{\mathrm{d}t} = \frac{\sigma_c^2}{2E}\frac{\mathrm{d}\left(\alpha^{-2}\right)}{\mathrm{d}t} = -\frac{\sigma_c^2}{E}\frac{1}{\alpha^3}\frac{\mathrm{d}\alpha}{\mathrm{d}t} \tag{3.24}$$

Putting these relations for $\left(\bar{f}_{gb} - \bar{f}_b\right)$ and $\mathrm{d}\bar{f}_{gb}/\mathrm{d}t$ into (3.22) and taking $w_{gb} \approx S$ now yields:

$$\begin{aligned} 2\left[\sigma_c - P_f\right]V_{ps} + \left[\frac{2\gamma_{sl}}{S}\Delta\cos\frac{\theta}{2} + \frac{1}{2E}\left(\frac{\sigma_c}{\alpha}\right)^2\right]S\frac{\mathrm{d}\alpha}{\mathrm{d}t} \\ = \frac{r_c^2}{8}\frac{RT}{DCS\left(1-\alpha\right)\Omega}\left(2V_{ps} - S\frac{\mathrm{d}\alpha}{\mathrm{d}t}\right)^2 \end{aligned} \tag{3.25}$$

For the steady-state case, when there is no evolution in grain boundary structure ($\dot{\alpha} = 0$), this relation reduces to the standard equation for pressure solution convergence velocity at a cylindrical grain contact (*Pluymakers and Spiers*, 2014):

$$V_{ps} = \frac{4DCS\left(1-\alpha\right)\Omega}{RTr_c^2}\left[\sigma_c - P_f\right] \tag{3.26}$$

When the pressure solution rate slows down to approach zero due to obstruction of radial diffusion with increasing α, i.e. as $V_{ps} \to 0$, Eqn. (3.25) reduces to:

$$S\frac{\mathrm{d}\alpha}{\mathrm{d}t} = \frac{8DCS\left(1-\alpha\right)\Omega}{RTr_c^2}\left[\frac{2\gamma_{sl}}{S}\Delta\cos\frac{\theta}{2} + \frac{1}{2E}\left(\frac{\sigma_c}{\alpha}\right)^2\right] \tag{3.27}$$

which expresses the rate of increase in contact area fraction occupied by islands of solid-solid contact under non-equilibrium conditions (compared with the condition for removal of an equilibrium grain boundary structure from equilibrium given by *Van Noort et al.*, 2008b). Note that Eqn. (3.27) describes the rate of island area increase

during active pressure solution. The onset of static island growth is still described by the equilibrium condition given by *Van Noort et al.* (2008b) as:

$$\Delta\mu_i = \frac{2\gamma_{sl}}{S}\Delta\cos\frac{\theta}{2} - \frac{1}{2E}\left(\frac{\sigma_c}{\alpha}\right)^2 = 0 \qquad \text{(3.6 revisited)}$$

This equilibrium criterion marks an unstable fixed point, in that any value of σ_c/α above a critical value will cause nett contraction of the islands ($\Delta\mu_i < 0$), which in turn decreases α and farther removes the grain boundary from the equilibrium point. Similarly, once σ_c/α falls below a critical value determined by Eqn. (3.6) (i.e. $\Delta\mu_i > 0$), island growth causes σ_c/α to decrease further, continuing to remove the grain boundary farther from equilibrium. Initially, α will likely be small (of the order of a few per cent; *Van Noort et al.*, 2008b), so that the onset of static island growth can only be reached by lowering σ_c by porosity reduction (compaction). It is therefore expected that there exists a critical aggregate porosity below which island growth initiates (*Van Noort et al.*, 2008b).

Equation (3.25) is an ill-conditioned equation containing two unknowns, V_{ps} and $\dot{\alpha}$, and cannot be solved analytically without further constraints linking V_{ps} and $\dot{\alpha}$, beyond the end-member cases represented by Eqns. (3.26) and (3.27). In the absence of such constraints, and noting the numerous simplifications and approximations made in deriving Eqn. (3.25) for V_{ps} and $\dot{\alpha}$, a first-order solution to acquiring V_{ps} and $\dot{\alpha}$ can be obtained by assuming that at any instant the pressure solution process and the tendency for islands to increase in area operate independently. In line with this, we take the rate of pressure solution at an evolving grain contact to be given by Eqn. (3.26) at any instant, with α evolving with time according to Eqn. (3.27).

3.3.2 Grain boundary connectivity

It was mentioned in Section 3.2.3 that the connectivity and diffusive properties of a grain boundary depend on the structure of the grain contact. The evolution of the grain boundary as described by the above model formulations must therefore be reflected by the transport properties of the grain boundary, which we will detail below.

Several microstructural studies have shown that healed grain boundaries contain arrays of fluid inclusions in the form of isolated spheres or tubes (e.g. *Desbois et al.*, 2012; *Hickman and Evans*, 1991; *Urai et al.*, 1986). In grain boundaries that show a lesser degree of healing, these tubes connect up with neighbouring inclusions to form a network that connect the interior of the grain boundary to the pore space (*Ghoussoub and Leroy*, 2001; *Spiers and Schutjens*, 1990). Also finer scale structures can be observed, possibly related to local lattice defects (*Schenk and Urai*, 2004; *Schutjens and Spiers*, 1999). If the density of inclusions, tubes, and pits is high enough, they can provide an interconnected pathway from the centre of the grain boundary into the pore space. In general, this will apply both to a statically healing grain boundary, but also to a dynamically wetted grain boundary island-channel structure undergoing progressive structural evolution during pressure solution. To estimate the probability that a given location within the grain boundary is connected to the pore space, and to quantify how the transport properties of the grain boundary change with asperity size and area fraction, we employ percolation theory, following standard percolation theory formulations (see *Stauffer and Aharony*, 1992).

In this framework, any random location in the grain boundary rim is assigned an 'open' or 'closed' state. In our current view of a grain boundary, the open state corresponds to a channel, being open to the diffusive mass flux. The closed state can be seen as an asperity (solid-solid) contact. The probability p of a site being open is related to the relative asperity contact area α as:

$$p = \frac{A_{sl}}{A_c} = \frac{A_c\,(1-\alpha)}{A_c} = 1 - \alpha \tag{3.28}$$

The probability of a site being closed is then $(1-p) = \alpha$. It can be shown that in an infinitely large system, clusters of open sites that traverse the entire length of the system exist (i.e. percolation occurs) only when $p > p_c$. The value of p_c can be calculated (analytically or numerically) for various geometries, or, in the current situation, can be estimated from microstructural estimates of α in the fully-healed state (so that $p_c = 1 - \alpha_c$), assuming that mass and fluid transport do not proceed once a contact has fully healed. Furthermore, numerous universal scaling relations have been derived that describe transport properties of the system. For instance, the effective diffusivity

of a system of infinite size can be expressed as:

$$D^{eff} \propto (p - p_c)^{\nu} \tag{3.29}$$

Here, ν assumes a value of 1.16 in 2D (*Sahimi*, 2003). To determine the proportionality constant, we assume that in the initial, unhealed state, $\alpha = \alpha_0$, $p = p_0 = 1 - \alpha_0$, and $D^{eff} = D^0$, so that (3.29) becomes:

$$D = D^{eff} = D^0 \left(\frac{p - p_c}{p_0 - p_c} \right)^{\nu} = D^0 \left(\frac{\alpha_c - \alpha}{\alpha_c - \alpha_0} \right)^{\nu} \tag{3.30}$$

Note that we assumed that the system is infinite in size, which is a valid approximation when the size of the grain-grain contact far exceeds the characteristic size of an open site (etch pit, fluid inclusion, or tube size). In the case where this assumption is not valid, the percolation threshold p_c is expected to decrease in magnitude, and percolation of the system is more likely. Additional scaling can be performed to better represent percolating clusters of finite size (see *Stauffer and Aharony*, 1992).

As the asperities increase in size, α increases towards α_c and p approaches p_c. For $p \leq p_c$ (and equivalently $\alpha \geq \alpha_c$), no percolation occurs and the grain boundary is said to to be fully healed, effectively terminating pressure solution. Mass transfer may still occur internally to restructure the island-channel network, breaking up the network in tubes and isolated fluid inclusions (*Brantley*, 1992). During this, the proportion of fluid stored in the grain boundary is thought to remain unchanged. Based on microstructural accounts of healed grain boundaries (see e.g. *Desbois et al.*, 2012; *Ghoussoub and Leroy*, 2001; *Schutjens*, 1991b; *Urai et al.*, 1986), we estimate that the grain contact surface area occupied by solid falls between 0.5 and 0.8, which bounds the range of values for α_c. The value of p_0 is estimated to exceed 0.9, corresponding to $\alpha_0 < 0.1$, as suggested by *Renard et al.* (2012) and *Van Noort et al.* (2008b), although it can be argued that near the onset of grain boundary healing, α attains higher values (*Van Noort et al.*, 2008b). Taking then values of p_0, p_c, α_0, and α_c, and using Eqn. (3.27) to describe $\dot{\alpha}$, Eqn. (3.30) now provides a description of the evolution of D^{eff}.

It is evident how a moderation of the transport properties of the grain boundary can result in a reduction of the rate of pressure solution, if it is limited by the rate of diffusion (like for halite at room temperature). In the case that the rate of pressure

solution is controlled by the interface reaction rate (like for quartz in the experiments of *Niemeijer et al.*, 2002), the influence of an evolving grain boundary structure will only manifest itself in the overall pressure solution rate when D^{eff} has been reduced sufficiently for the process to become controlled by the rate of diffusion. In other words, a switch in rate-limiting process is anticipated in materials for which pressure solution is initially interface-reaction controlled.

3.3.3 Scale-dependence of grain boundary topography

Throughout this section, it has been assumed that the average grain boundary roughness S is time- and scale-invariant. However, it cannot be excluded that this roughness is dependent on the size of the contact, or on grain boundary stress (c.f. *Schutjens and Spiers*, 1999). We will explore this possibility in more detail by considering a scale-dependence of S.

It has been suggested in numerous studies that (dynamic) interfaces are self-affine, including natural faults and joints (*Brodsky et al.*, 2016; *Brown and Scholz*, 1985; *Candela et al.*, 2012), processed or naturally corroded metal surfaces (*Majumdar and Tien*, 1990; *Shanhua et al.*, 2015; *Zahouani et al.*, 1998), and various geomaterials (*Avnir et al.*, 1984; *Dieterich and Kilgore*, 1996; *Wong et al.*, 1986). Owing to its self-affine character, a given surface will appear smoother at larger length-scales. When it is assumed that the average thickness of a grain boundary is controlled by its roughness, then self-affinity implies that $S \propto L^H$, where L is a characteristic length scale (i.e. the size of the contact), and H is the Hurst exponent (with $H \neq 1$ for self-affine surfaces; *Brodsky et al.*, 2016). A dynamically evolving grain boundary may not obey such a scaling law, as the topography may be strongly controlled by fluid-rock interactions. However, a size-dependent topography is well established for stylolites over 4-5 orders of magnitude (see *Gratier et al.*, 2013, and references therein), and has previously been reported for grain interfaces undergoing pressure solution at the µm-scale (*De Meer et al.*, 2005, 2002; *Schutjens and Spiers*, 1999). *De Meer et al.* (2005) report that the average grain boundary thickness increases with increasing contact width. This can also be inferred from the observed increase in kinetic constant DCS with

increasing contact width (*De Meer et al.*, 2002), assuming that D and C are scale-independent. Furthermore, *Schutjens and Spiers* (1999) observed contact roughness at all resolvable scales, ranging from tens of µm to a few hundred nm, suggesting a fractal topography. Finally, stressed interfaces deforming by elastic and/or plastic yield are well characterised by a fractal relationship (*Brown and Scholz*, 1985; *Dieterich and Kilgore*, 1996).

Since the chemical potential for asperity growth (or undercutting) depends strongly on S (see Eqn. (3.27)), the possibility that S scales with contact size needs to be considered. Therefore, we define S to vary with r_c following a power-law scaling relationship, in line with our preceding discussion of such effects. More specifically:

$$S = S^{ref} \left(\frac{r_c}{r_c^{ref}} \right)^H \tag{3.31}$$

Here, S^{ref} is a reference value corresponding to a radius of contact r_c^{ref}, and H is the Hurst exponent. A value of $H = 0$ results in a scale-independent (constant) value of S. Using this relation, the asperity growth rate as predicted by Eqn. (3.27) is altered through the surface energy term, which contains S in the denominator. For consistency, the value of S as appearing in the experimentally determined product DCS in Eqn. (3.1b) is also scaled using the above relation, so that both the rate of pressure solution and that of asperity growth are affected by the simulated changes in topography. When scaling DCS, we assume that the experimentally determined value of this product corresponds to DCS^{ref}, so that the product scales as $DCS^{ref} \left(r_c / r_c^{ref} \right)^H$. Note that Eqn. (3.31) is purely empirical in nature, and therefore has little predictive power. However, we will only use this relationship to investigate the possible effects of a scale-dependent contact roughness on the grain boundary healing behaviour, by comparing simulations with constant S to those where S is scaled.

3.3.4 Analytical model for pressure solution with grain boundary evolution

Classically, the constitutive relations for pressure solution creep are derived for a single contact, before being upscaled to the size of the (porous) aggregate, assuming an

average unit-cell geometry and stress distribution (see e.g. *Pluymakers and Spiers*, 2014; *Rutter*, 1976; *Spiers and Schutjens*, 1990). The resulting differential equation is then solved to yield the evolution of strain rate with porosity (or strain). We will refer to this type of solution procedure as analytical, as the up-scaling is done analytically. On the other hand, upscaling can also be done numerically by implementing the single-contact constitutive law of the grain contact scale using DEM, which eliminates the need for assuming a uniform distribution of stress or strain within the sample. For high porosity aggregates (where grain boundary evolution is assumed to be negligible) and for narrow grain size ranges, good agreement is found between the analytical and DEM model predictions for compaction creep by pressure solution (Chapter 2; see also *Van den Ende et al.*, 2018b). Hence, it is useful to compare analytical model results for pressure solution with grain boundary evolution, with numerical simulations to assess the validity of the present analytical up-scaling assumptions. Additionally, such comparison is useful for testing the numerical implementation of our model, essentially validating the DEM implementation.

For obtaining a description of pressure solution with grain boundary evolution analytically, we adopt classical treatments of the model aggregate by assuming a well-defined relationship between bulk porosity and the area (or equivalent radius) of an individual grain-grain contact. This relationship reads (*Pluymakers and Spiers*, 2014):

$$r_c = d\sqrt{\frac{F}{\pi Z} f(\phi)} \tag{3.32}$$

Here, F is a shape factor that assumes a value of π for spherical grains, and Z is the bulk-average coordination number. $f(\phi)$ is a smooth function that describes the evolution of contact area with porosity, and is chosen such that $f(\phi_0) = 0$ and $f(0) = 1$. C.f. *Spiers et al.* (2004), we define $f(\phi)$ as:

$$f(\phi) = \frac{\phi_0 - \phi}{\phi_0} \tag{3.33}$$

In this expression, ϕ_0 roughly corresponds to the porosity at the start of the experiment, where the area of contact of grains is relatively small. Using relation (3.32), the constitutive equations (3.26) and (3.27) can then be upscaled from a single grain-grain

contact to an assembly of packed grains to give:

$$\dot{\varepsilon} = 4\pi A_\varepsilon \left(\frac{Z}{F}\right)^2 \frac{DCS\,(1-\alpha)\,\Omega}{RT} \frac{\sigma_e}{d^3 f(\phi)^2} \tag{3.34a}$$

$$\frac{\mathrm{d}\phi}{\mathrm{d}t} = -\,(1-\phi)\,\dot{\varepsilon} \tag{3.34b}$$

$$\frac{\mathrm{d}\alpha}{\mathrm{d}t} = 8\pi \frac{Z}{F} \frac{DC\,(1-\alpha)\,\Omega}{RTd^2 f(\phi)} \left(\frac{2\gamma_{sl}}{S}\Delta \cos\frac{\theta}{2} + \frac{1}{2E}\left[\frac{Z}{F}\frac{\sigma_e}{\alpha f(\phi)}\right]^2\right) \tag{3.34c}$$

Here, A_ε is a geometric factor that assumes a value of 6 for isotropic compaction. D is modified by α through Eqn. (3.30) and S by r_c through Eqn. (3.31). The full set of coupled differential equations (Eqn. (3.34)), complemented with Eqn. (3.30) and (3.31), is solved iteratively using the *SciPy* ODE package (*Jones et al.*, 2001) to yield the evolution of D, α, strain rate, strain and porosity with time.

3.4 Analytical model predictions versus experiments on halite

Here, we compare the deformation rates measured by *Schutjens* (1991b) in long-term compaction experiments with the results of our extended model for pressure solution plus grain boundary evolution as expressed by Eqn. (3.34). For this comparison, we require laboratory data from high-strain ($\phi < 15$ %) compaction tests performed under conditions for which pressure solution is the dominant deformation mechanism, limiting the contribution of e.g. microcracking to the overall rate of compaction. Moreover, the kinetics of pressure solution need to be well constrained, so that uncertainties in the model constitutive parameters can be excluded to contribute to discrepancies between the laboratory data and model predictions. To our best knowledge, only the data set reported by *Schutjens* (1991b) satisfies these specific criteria, and so we will compare our model outcomes to this data set.

We start by comparing the predictions of grain boundary evolution (Eqn. (3.34)) for a constant value of S with the laboratory data of *Schutjens* (1991b) (see Fig. 3.2 –

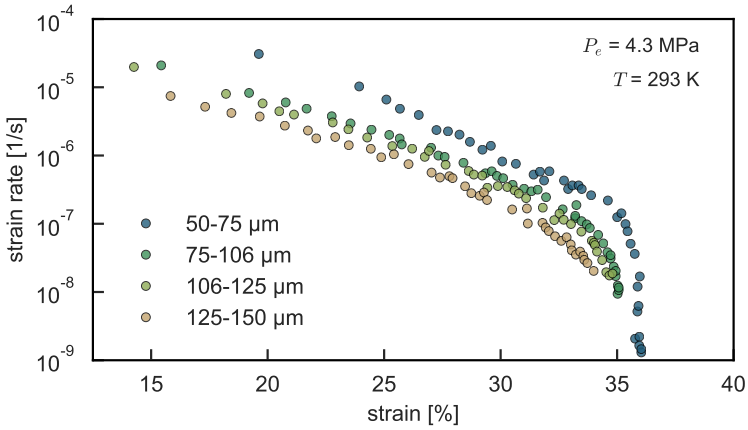

Fig. 3.2: Digitised results of the isostatic compaction experiments on NaCl reported by *Schutjens* (1991b). The experiments were performed at room temperature conditions, and the test samples were subjected to a servo-controlled effective pressure of 4.3 MPa.

constructed from his Fig. 3.14, taking ϕ_0 as reported in Appendix 3.A). This comparison is made for each experiment individually – see Fig. 3.3. The parameters used in the analytical models are given in Table 3.1. First, we examine a model that does not consider grain boundary evolution, i.e. using Eqn. (3.34) with $\dot{\alpha} = 0$, so that α and D are constant. At high porosities, there is acceptable agreement between the strain rates predicted by the model and measured in the experiments, but for porosities < 25 % the analytical model starts to overestimate the compaction rates – see Fig. 3.3. Near the terminal porosity of the experiments the mismatch between model and experimental strain rates is up to several orders of magnitude, illustrating that the existing theory of pressure solution does not describe the compaction behaviour at porosities below 20 %.

Next, we consider a model where the grain boundary structure evolves, with $\dot{\alpha}$ being described by Eqn. (3.34c), and D being modified by the instantaneous value of α in accordance with Eqn. (3.30). The comparison between the experimental data and model predictions including grain boundary evolution (Fig. 3.3) shows that when a constant value of $S = 325$ nm is taken, only the data for a grain size range of 125-150 µm can be

accurately represented by the model (Fig. 3.3d), while for all other grain size ranges, the model overestimates experimental compaction rates and underestimates the terminal porosity. Although the model with constant S broadly displays the same features as the experimental data, the fit between the analytical models and compaction data is much improved by allowing S to evolve with the size of the grain contact (Eqn. (3.31)), suggesting a scale dependence of S as discussed in Section 3.3.3. However, it should be noted that in the analytical model approach, upscaling from the grain contact scale to that of the aggregate (i.e. relating mean grain contact size to porosity) involves an empirical porosity function $f(\phi)$. While this has been shown to be accurate for a wide porosity range (*Niemeijer et al.*, 2002; *Van den Ende et al.*, 2018b; *Zhang et al.*, 2010), it cannot be excluded that the apparent scale dependence of S stems from the functional form of $f(\phi)$, which may not accurately represent the evolution of grain contact area and coordination number with porosity in the experimental samples at lower porosities. Additionally, the polydispersed (multi-valued) distribution of grain sizes in the laboratory aggregates may affect the apparent scale dependence of S. Both these concerns can be addressed by simulating the laboratory experiments using the Discrete Element Method.

3.5 DEM model for compaction by pressure solution with grain boundary evolution

To further investigate the above possibility of an erroneous effect of $f(\phi)$, we implement the grain-scale physical processes into a Discrete Element Model (DEM) formulation. In DEM, the macroscopic (upscaled) behaviour emerges spontaneously from the collection of grain-scale interactions between particles that constitute the aggregate. While DEM relies on the same grain-scale physical processes as the analytical models, it does not require a prescribed porosity function, and so DEM can be used to test the hypothesis that S is scale dependent. To this end, we have implemented our constitutive relations for the rates of pressure solution and asperity growth of single grain contacts in a Discrete Element Method framework, following Chapter 2 and *Van den Ende et al.* (2018b).

Table 3.1: Parameters used in the analytical model simulations. The sequence of grain sizes above correspond to the mean of the grain size ranges of experiments L1, L2, L3, and L4 respectively (see Table 3.A.1). References: a) *Spiers et al.* (1990); b) *Visser* (1999) using the approximation by *Israelachvili* (1986); c) *Lewis and Holness* (1996).

Parameter	**Value**	**Units**
Nominal grain diameter	62.5, 90.5, 115.5, 137.5	µm
Effective pressure (P_e)	4.3	MPa
Initial porosity (ϕ_0)	40.0	%
Geometric constant (A_ε)	6	-
Grain shape factor (F)	π	-
Grain coordination number (Z)	6	-
Kinetic constant (DCS)	1.22×10^{-19}[a]	$m^3\ s^{-1}$
Molar volume (Ω)	2.69×10^{-5}	$m^3\ mol^{-1}$
Temperature (T)	294	K
Surface energy (γ_{sl})	0.2[b]	$J\ m^{-2}$
Dihedral angle mismatch ($\Delta \cos \frac{\theta}{2}$)	0.18[c]	-
Asperity Young's modulus (E)	37	GPa
Initial asperity occupation ratio (α_0)	0.15	-
Terminal asperity occupation ratio (α_c)	0.8	-
Reference grain boundary thickness (S^{ref})	325	nm
Reference contact radius (r_c^{ref})	35	µm
Hurst exponent (H)	0.5	-

3.5.1 Basic DEM approach

In this study, we use the open-source DEM software package granular LAMMPS (*Landry et al.*, 2003; *Plimpton*, 1995) as modified by *Marketos* (2013) and in Chapter 2 to accommodate intergranular pressure solution. Further modifications are detailed below.

As is customary in DEM, it is assumed here that the particles are indestructible and perfectly spherical, and that they are unbonded, i.e. that no tensile forces or moments of force can be transmitted between the particles. Two particles are in contact when

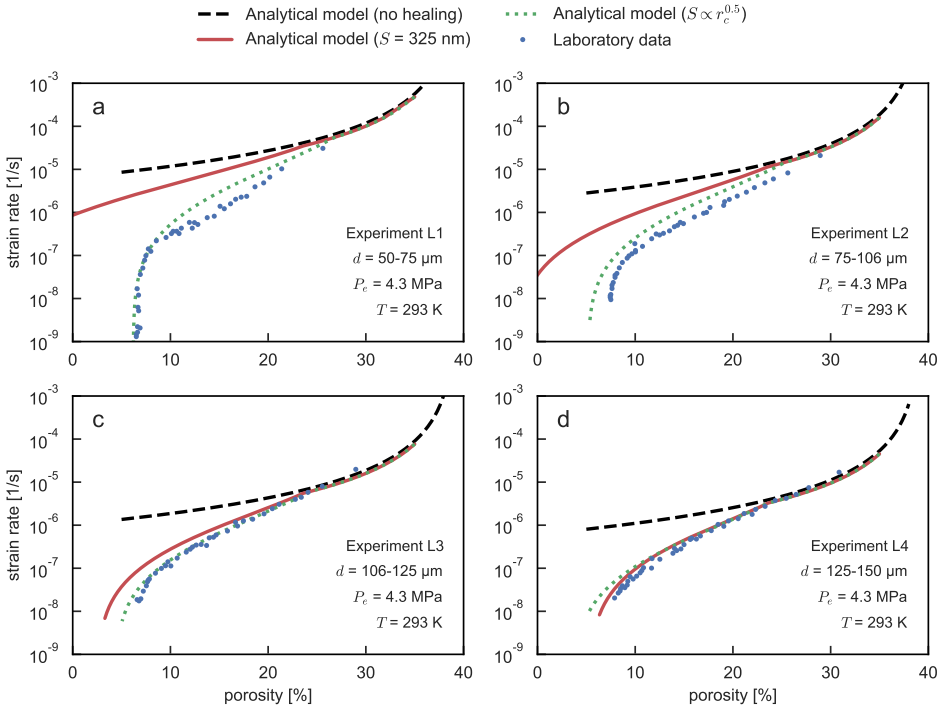

Fig. 3.3: Comparison between analytical models and the laboratory results of *Schutjens* (1991b). For each laboratory data set, three model results are shown: one where no grain boundary evolution is considered (i.e. Eqn. (3.34) with $\dot{\alpha} = 0$), one where grain boundary evolution is considered with a constant value of $S = 325$ nm, and one where grain boundary evolution is considered with $S \propto r_c^H$. Experimental parameters are as indicated in each panel.

the distance between their centroids is less than the sum of their respective radii, which results in a mutual overlap of size Δx_{el} (see Fig. 3.4). This overlap then results in an elastic restoring force acting normal to the contact plane, which is assumed here to be represented by a contact spring that follows a linear force-displacement relationship:

$$F_n = k_n \Delta x_{el} \tag{3.35}$$

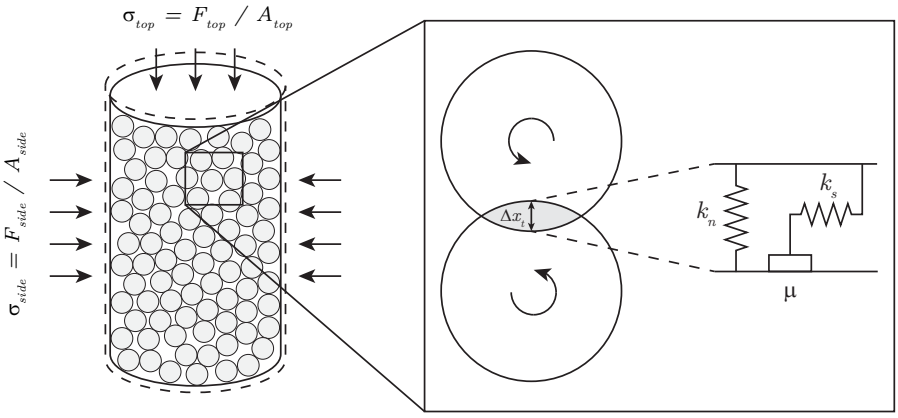

Fig. 3.4: Geometry of the virtual DEM sample. A cylindrical aggregate is subjected to a servo-controlled triaxial stress state. At the contact scale, particles interact through elastic-frictional forces, and exhibit dissolution in the contact plane normal direction.

Here, F_n is the normal contact force, and k_n the normal stiffness. A similar equation applies to the shear forces:

$$\vec{F}_s = \begin{cases} k_s \Delta \vec{s}_{el}, & \text{if } \left\| \vec{F}_s \right\| < \mu F_n \\ \mu_p F_n \frac{\Delta \vec{s}_{el}}{\|\Delta \vec{s}_{el}\|}, & \text{otherwise} \end{cases} \tag{3.36}$$

$\vec{F}_s$ denotes the vector of the shear force acting in the plane of the contact, k_s the shear stiffness, $\Delta \vec{s}_{el}$ the vector of the elastic shear displacement, and $\|\cdot\|$ denotes the Euclidean norm. The value of $\Delta \vec{s}_{el}$ is updated incrementally each time step by integration of the relative particle velocities. μ_p is a size-independent, constant coefficient of friction, which restricts the shear force to the frictional limit. In all of the simulations reported in this work, we assume the stresses to be effective stresses (i.e. $\sigma_n - P_f$), with constant and sample uniform P_f (i.e. drained conditions).

To simulate creep by intergranular pressure solution, we adopt the method developed in Chapter 2, in which the normal force activates pressure solution on the contact at a rate V_{ps}^{DEM} proportional to the effective contact normal stress. Convergence of the

particle centroids, and hence overall densification of the aggregate, is simulated by reducing the total particle overlap Δx_t by the non-elastic overlap (i.e. the dissolved contact layer thickness) δ, so that the contact normal force becomes:

$$F_n = k_n \Delta x_{el} = k_n \left(\Delta x_t - \delta \right) \tag{3.37}$$

By incrementing δ every time step by $2V_{ps}^{DEM} \times \Delta t$ (factor 2 accounting for each dissolving particle), the total particle overlap Δx_t is continuously increased over the course of a simulation. Since it is assumed that dissolution only occurs normal to the contact plane, $\Delta \vec{s}_{el}$ and hence $\vec{F}_s$ are not affected by pressure solution. The rate of pressure solution V_{ps}^{DEM} follows from Eqn. (3.26), and is given by:

$$V_{ps}^{DEM} = Z_{ps} \left(1 - \alpha \right) \frac{\pi F_n}{A_c^2} \tag{3.38}$$

Here A_c is the area of the contact plane, which is defined by the circular intersection between the two spherical particles. Z_{ps} is a (temperature-dependent) kinetic constant, given by:

$$Z_{ps} = \frac{4 \left(DCS \right) \Omega}{RT} \tag{3.39}$$

During the simulations, the values of D, and S are modified in accordance with Eqns. (3.30) and (3.31), respectively.

The history of deformation, i.e. the values of δ and α, are stored and updated for each particle-contact pair individually. When two particles are brought into contact and a new particle pair is created, δ and α are assigned initial values of 0 and α_0, respectively. δ is incremented by V_{ps}^{DEM}, and α evolves according to $\dot{\alpha}$, given by Equations (3.38) and (3.27) respectively. Note that, like for the analytical simulations, grain boundary evolution is only initiated when the criterion $\Delta \mu_i > 0$ in Eqn. (3.6) is met. This criterion is evaluated every time step for each particle contact individually.

Since the diffusive transport properties of the contact are controlled by the properties of the percolating cluster (Eqn. (3.30)), α cannot exceed $\alpha_c = 1 - p_c$, as D asymptotically approaches zero and neck growth effectively terminates. In practice, α can exceed this threshold value due to the finite numerical precision and time step size, and therefore we conditionally set D to 0 for $\alpha \geq \alpha_c$, corresponding to a fully-healed state.

3.5.2 Numerical stability and scaling relations

To guarantee numerical stability, a simulation time step must be chosen such that $\Delta t < t_c$, t_c being the critical time step defined as $t_c = \sqrt{m/k}$, where m is the mass of the smallest particle (*Cundall and Strack*, 1979). In all of the simulations reported here, we adopt a time step $\Delta t = t_c/10$. When the particles sizes are in the same range of the grain sizes typically used in laboratory experiments (of the order of 10-100 µm), t_c reduces to values that are computationally intractable for simulating the time scales of those experiments, usually ranging from hours to tens of days. Therefore the time step must be increased artificially while maintaining numerical stability, which is done by altering the mass of the particles in an approach that is essentially similar to density scaling (e.g. *Cui and O'Sullivan*, 2006; *Ng*, 2006; *O'Sullivan et al.*, 2003). The particle size was taken near unity, while maintaining a mass density of 2100 kg m^{-3}, effectively altering its equivalent density. Furthermore, time is scaled as:

$$t' = t\frac{Z_{ps}^0 P_e}{r^3} \tag{3.40}$$

Here, P_e is the externally applied (constant) effective pressure, and r is the particle radius. The parameter Z_{ps}^0 is obtained as:

$$Z_{ps}^0 = \frac{4D^0 C S^{ref} \Omega}{RT} = \text{const} \tag{3.41}$$

The value of Z_{ps}^0 is constant throughout the simulations, and is therefore suitable for scaling. All spatial dimensions are scaled to the particle size r.

3.5.3 DEM model procedure

In order to test our analytical expressions for grain boundary healing, and to assess if this mechanism could explain the observed reduction in strain rates, we simulated the hydrostatic compaction experiments by *Schutjens* (1991b) using DEM. The adopted procedure was as follows:

1. First, a cylindrical simulation domain was defined with an initial height of 40 particle diameters and cylinder diameter of 15 particle diameters (see Fig. 3.4). The domain was bounded by rigid, frictionless walls. The sample was generated by spawning 9000 particles at random locations within the cylinder. The particle sizes were sampled from a uniform distribution defined by the grain size ranges reported in Table 3.A.1. The aggregate was then allowed to settle under gravity, simulating the procedure of pouring a granular sample into a containment vessel. During settling, particle accelerations were artificially damped to reduce the time required by the aggregate to come to rest.

2. After the particles had settled, a constant isotropic confining pressure of 4.3 MPa was applied. This was done by controlling the total stress acting on the top and circumferential walls. The total force exerted by the particles on a wall was summed up and divided by the total area of that wall to obtain the average stress supported by it. As the dimensions of the sample changed by compaction, the instantaneous area of the top and circumferential walls as used in the stress calculations were updated accordingly. During the precompaction procedure, creep by pressure solution and asperity growth were disallowed, mimicking the dry precompaction phase of *Schutjens* (1991b), except for any plastic deformation.

3. As soon as the forces exerted by the walls equilibrated, gravity and damping were turned off and pressure solution and asperity growth were activated instantaneously, thus simulating the rapid infiltration of a pore fluid by vacuum flushing. The DEM sample was then allowed to compact and densify under constant confining pressure, and volumetric changes were obtained from the instantaneous positions of the walls. We calculated bulk aggregate porosities (ϕ) from the total mass of the particles present in the system, and the dimensions of the cylindrical simulation domain. The volumetric strain rate was then calculated as:

$$\dot{\varepsilon}_v = -\frac{1}{(1-\phi)}\frac{\mathrm{d}\phi}{\mathrm{d}t} \tag{3.42}$$

   The rate of porosity change was estimated by taking the time-derivative of the instantaneous sample porosity, employing an algorithm similar to the Savitzky-Golay method with variable window size, so that both high and low strain rates could be determined with similar accuracy.

4. In the first set of simulations, we chose a scale-independent value for the grain boundary thickness of $S = 325$ nm for all grain size ranges. In the second set of simulations, we allowed S to scale with the size of the particle contact following Eqn. (3.31). Since the values of S^{ref}, r_c^{ref}, and H are not well constrained experimentally, we simply calibrated these values manually by comparing the DEM model results with the laboratory data. By doing so, no information could be gained regarding the validity of the scaling relationship, or its parameter values beyond the conditions of the experiments investigated here. Values of $S^{ref} = 280$ nm, $r_c^{ref} = 16$ µm, and $H = 0.5$ produced reasonable agreement between the model results and the experiments. During all DEM simulations, D was calculated for each particle contact individually, in accordance with Eqn. (3.30) and the instantaneous value of α of the given contact.

An overview of the parameters used in the simulations is presented in Table 3.2.

3.6 Simulation results and comparison with data of *Schutjens* (1991b)

When the average grain boundary thickness is kept constant at $S = 325$ nm (red curves in Fig. 3.5), but allow for changes in α and D, good agreement is found between the DEM model predictions and the laboratory data, but only for the experiments with large nominal grain size (experiments L3 and L4 – see Fig. 3.5c and d, respectively). For the experiments with smaller grain sizes, L1 and L2 (Fig. 3.5a and b), the compaction rates produced by the model severely overestimate the experimental data. The discrepancy between the models and experiments seems to increase continuously with decreasing grain size, which suggests that the grain size dependence is not captured well by the model with constant S. When S is varied according to Eqn. (3.31) (purple curves in Fig. 3.5), much better agreement between the models and experiments is found for all grain sizes investigated. Hence, it could be argued that the scale-dependence of S introduces sufficient detail to the model to reproduce the grain size dependence of grain boundary healing.

Table 3.2: Parameters used in the DEM simulations. The sequences reported correspond to the simulations of experiments L1, L2, L3, and L4 respectively (see Table 3.A.1). References: a) *Spiers et al.* (1990); b) *Visser* (1999) using the approximation by *Israelachvili* (1986); c) *Lewis and Holness* (1996).

Parameter	**Value**	**Units**
Number of particles	9000	-
Particle contact stiffness	2.65×10^9	N m^{-1}
Particle friction coefficient	0.6	-
Particle density	2100	kg m^{-3}
Particle diameter range	50-75, 75-106, 106-125, 125-150	µm
Particle size distribution	uniform	
Wall stiffness	2.65×10^9	N m^{-1}
Wall friction coefficient	0.0	-
Applied pressure (P_e)	4.3	MPa
Initial porosity (ϕ_0)	40.1, 40.0, 40.5, 40.3	%
Simulation time step	0.026, 0.088, 0.249, 0.408	s
Total simulated time	1.81×10^6	s
Kinetic constant (Z^0_{ps})	5.38×10^{-27}[a]	m^3 Pa^{-1} s^{-1}
Surface energy (γ_{sl})	0.2[b]	J m^{-2}
Dihedral angle mismatch ($\Delta \cos \frac{\theta}{2}$)	0.18[c]	-
Asperity Young's modulus (E)	37	GPa
Initial asperity occupation ratio (α_0)	0.15	-
Terminal asperity occupation ratio	0.8	-
Ref. grain boundary thickness (S^{ref})	280	nm
Ref. contact radius (r_c^{ref})	16	µm
Hurst exponent (H)	0.5	-

When the DEM results are compared with predictions from the analytical models (with and without grain boundary evolution), we find a good agreement between the DEM model with scale-dependent S, and its analytical counterpart. When S is assumed constant, the DEM model suffers similar discrepancies between laboratory data and model outcomes as the analytical model with constant S (as seen in Fig. 3.3). This is

a strong indication that the analytical up-scaling, i.e. the use of $f(\phi)$ to describe the evolution of contact size with porosity, is a reasonable approach for the full range of attainable porosities. At the very least, it shows that DEM and the analytical models share a similar evolution of contact area with strain. However, in the DEM simulations, a different value of r_c^{ref} was chosen to correspond to S^{ref} than in the analytical models, to produce the same fit with the laboratory data. This difference in r_c^{ref} expresses itself as a constant with a value of 2.2, which might be related to the choice for A_ε or Z in Eqn. (3.34a) not accurately reflecting the initial DEM packing geometry.

3.7 Discussion

This study has addressed the compaction behaviour of wet aggregates by pressure solution, and the discrepancy between laboratory compaction data, detailed at low porosities, and the much faster predictions of analytical models for compaction by pressure solution (*Niemeijer et al.*, 2002; *Schutjens*, 1991b). As a possible mechanism for the retardation of pressure solution creep rates, we investigate the effect of an evolving grain boundary structure during pressure solution on the overall compaction rate. To this end, we derived analytical expressions for the evolution in solid-solid contact or island area within stressed grain contacts undergoing pressure solution, and implemented these expressions into a numerical Discrete Element Method framework.

The analytical and numerical models have been compared with laboratory data for isostatic compaction of NaCl aggregates, as reported by *Schutjens* (1991b). The comparison shows good agreement regarding the trends in densification rates, demonstrating that grain boundary evolution involving an increase in solid-solid contact area associated with a decrease in surface energy can explain the retardation of pressure solution creep rates. However, in order to explain the laboratory data set for the entire range of sample grain sizes, we had to allow for a scale-dependent value of the mean thickness (S) of the grain boundary interstitial fluid. When a self-affine scaling relation between S and the size of the grain contact is assumed, good agreement is found between the laboratory data, and the analytical and numerical models for all grain size ranges.

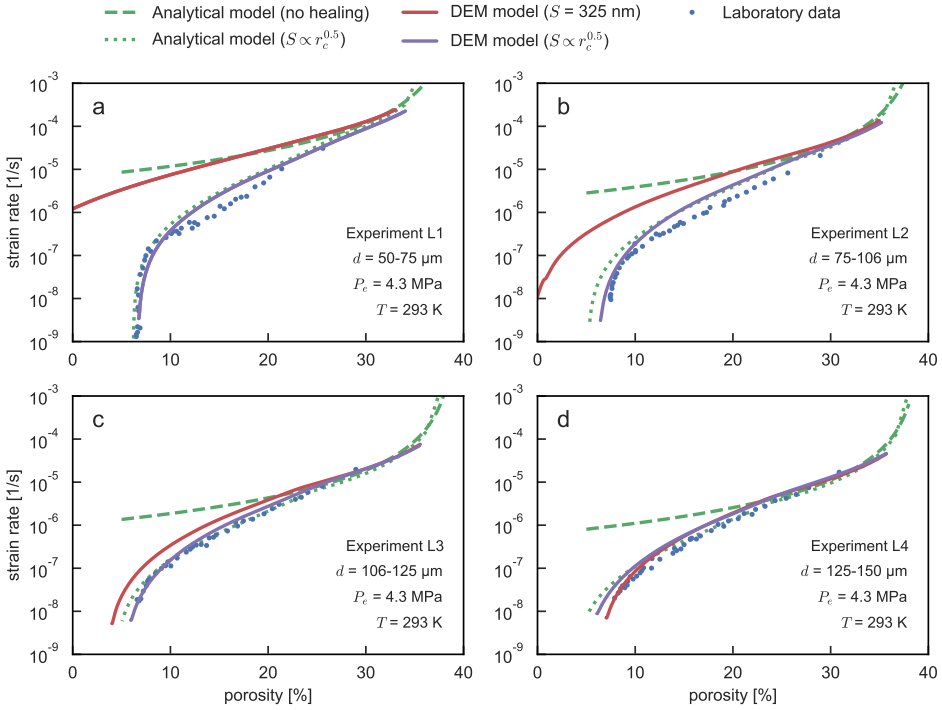

Fig. 3.5: Comparison between analytical models, DEM simulations, and the laboratory results of *Schutjens* (1991b). For each experimental data set, two DEM simulations were run: one with a constant grain boundary topography of $S = 325$ nm, and one where S was scaled according to Eqn. (3.31). The analytical models are adopted from *Pluymakers and Spiers* (2014) and modified as described in Section 3.3.4. Experimental parameters are as indicated in each panel.

In spite of the good quantitative match between the laboratory data and the models, a number of issues remain unresolved. Most notably, the structure and dynamics of a wetted grain boundary, and its relation to pressure solution, require further discussion. In addition, the relevance and implications of the present findings for pressure solution in nature requires examination. These topics will be addressed in the following sections.

3.7.1 Structure and dynamics of a wetted grain contact under stress

In classical analytical treatments of steady-state pressure solution (e.g. *Lehner*, 1995; *Pluymakers and Spiers*, 2014; *Spiers and Schutjens*, 1990), the smallest scale that is explicitly considered encompasses a segment of a grain contact over which a representative average grain boundary structure can be assumed. The local dynamics of grain contact structure is not made explicit in these models. Instead, a fixed, steady-state structure is assumed. However, for a rigorous investigation of the evolution of the structure of a wetted grain boundary under stress, this local scale needs to be considered explicitly, without assuming steady-state. In our analysis presented in Section 3.3.1, we made a number of simplifying assumptions regarding the distribution of the local free energy and the structure of the grain boundary zone. These assumptions were required in order to derive simple closed-form expressions for the structural evolution of the grain boundary, given our present knowledge on the processes that control the dynamics of dissolution, diffusion, and precipitation at the scale of a single island.

An important gap in our knowledge remains the lack of a quantitative description of the processes that cause the grain boundary to remain dynamically rough when subjected to a sufficiently high state of stress. See-through experiments demonstrate that an optically flat interface undergoing pressure solution can regenerate a rough topography when the stress supported by the interface is raised (*Schutjens and Spiers*, 1999). Such behaviour is not reflected by our present model describing grain boundary evolution (Eqn. (3.27)). Closely related to these observations, is the possibility that the grain boundary roughness, and correspondingly the mean thickness S of the interstitial fluid film, are scale-dependent. In-situ spectroscopy experiments performed by *De Meer et al.* (2005) on a single grain contact revealed that S increases over time, concurrent with widening of the stressed interface. However, it is presently not clear whether this is a transient effect, or if a steady-state value of S is attained for a constant size of the contact.

Some of the above questions may be addressed by means of (numerical) modelling with regard of the relevant processes at the scale of an individual island (e.g. *Ghoussoub and Leroy*, 2001), taking into account local values of stress, free energy in the solid, and

solute concentration in the interstitial fluid. If local physical processes are captured with sufficient detail, the structural evolution of the grain boundary (i.e. of α and of S) should emerge spontaneously.

3.7.2 Relation between grain boundary evolution and intergranular pressure solution

When considering static island growth driven by surface energy (e.g. *Van Noort et al.*, 2008b), each individual island may have an unconstrained (infinite) lifetime, in that it may grow without being completely removed by dissolution over the lifetime of the grain contact. However, in order to achieve grain convergence when pressure solution operates, it is required that the entire grain boundary zone fully dissolves and rejuvenates its islands in a finite amount of time. If this were not the case, i.e. if islands would not fully dissolve, then nett dissolution would only occur by deepening of the channels (increasing S), which does not produce grain convergence. As a corollary, the lifetime of each individual island must be finite (i.e. it must fully dissolve), and new islands must form by non-uniform dissolution and compression of the grain contact, if pressure solution were to operate. This provokes a paradoxical interpretation of the grain boundary evolution model described in Section 3.3: an increasing value of α (the area occupied by islands) seems suggestive of growth of individual islands, similar to the case of static island growth with no pressure solution. However, α reflects a spatial average of the total area occupied by islands, rather than describing the size and shape of individual islands. During active pressure solution, the nett rate of dissolution of islands may be reduced (induced by local changes in free energy) compared to the rate of formation of islands, resulting in a nett increase in α, even though islands still exhibit a finite lifetime.

Although it is explicitly assumed in the model derivation of Section 3.3.1 that pressure solution is operative during (dynamic) grain boundary evolution, it can be questioned whether this assumption is valid, or whether pressure solution is immediately arrested as soon as the nett volume occupied by islands starts to increase (static growth). A number of optical imaging experiments report negligible convergence during growth

of interface asperities (*Renard et al.*, 2012), or of the stressed contact between a plano-convex lens pressed against a flat plate (*Beeler and Hickman*, 2015; *Hickman and Evans*, 1991, 1992), under conditions favourable for pressure solution. These observations suggest that pressure solution does not operate during structural evolution of the grain contact. However, as was noted by *Schutjens and Spiers* (1999), the plano-convex geometry employed in the experiments of *Hickman and Evans* (1991, 1992) (and of *Beeler and Hickman*, 2015) promotes contact growth due to the large radius of curvature at the contact margin. In the experiments of *Renard et al.* (2012), the nominal contact stress was low (0.26 MPa), and the contact asperities large in size (up to 300 µm). These experiments may therefore not be representative for our envisioned dynamic island-channel structure at the scale of tens to a few hundred nm.

In optically monitored grain-to-grain contact experiments conducted by *Schutjens and Spiers* (1999), all experiments showed convergence concurrent with an evolving grain boundary structure. Particularly, their experiment T4 displayed a gradual smoothing of an initially rough grain contact over the course of 25 days, until an optically smooth interface topography was achieved. Upon step-wise increasing the load on the contact, the grain contact re-roughened and the initial roughness was recovered (see Fig. 10 in *Schutjens and Spiers*, 1999). This example illustrates that pressure solution can continue to operate during grain boundary evolution, supporting the model choices made in Section 3.3.1.

3.7.3 Implications of the present findings for pressure solution in nature

We have established that grain boundary evolution may significantly retard pressure solution creep rates in mono-mineralic aggregates. Our models for pressure solution concurrent with grain boundary evolution have been compared with isostatic compaction data on halite, which has previously been adopted in laboratory tests as an analogue material for quartz at hydrothermal conditions (*Bos et al.*, 2000b; *Niemeijer et al.*, 2009). Although the material properties of halite are dissimilar from those of quartz, the processes involved in deformation of halite aggregates (e.g. pressure solution), have similarly been recognised to operate in quartz aggregates at the relevant conditions (*De*

Boer et al., 1977; *Heald*, 1955; *Van Noort et al.*, 2008a). This notion receives further support from the high-strain compaction tests performed on quartz by *Niemeijer et al.* (2002), reporting similar compaction trends at temperatures in the range of 400-600 °C as have been observed by *Schutjens and Spiers* (1999) in halite at room temperature conditions. Even though the process that limits the rate of pressure solution at high porosities is different for halite at room conditions than it is for quartz at hydrothermal conditions (diffusion versus dissolution, respectively; *Niemeijer et al.*, 2002; *Schutjens and Spiers*, 1999), it is expected that diffusion will become rate-limiting for both materials at low porosities (see Section 3.3.2). The models for pressure solution and grain boundary evolution derived in this study may therefore generally apply to other materials, in a laboratory setting as well as in nature.

In contrast to many laboratory tests performed on mono-mineralic aggregates, natural sediments and fault gouges are often heterogeneous in composition. Given that solid-liquid and solid-solid interface energies play an important role in controlling the structural evolution of grain boundaries, the efficiency of grain boundary evolution as envisioned in this work can be challenged. A reduced efficiency of grain boundary evolution driven by surface energy has been observed in several laboratory experiments:

- *Beeler and Hickman* (2015) observed that quartz-sapphire interfaces of compressed plano-convex lenses do not show grain contact spreading (neck growth), in contrast to quartz-quartz interfaces. Similarly, the inhibiting effect of bi-mineral interfaces was inferred from the difference in convergence rates measured in experiments conducted on halite-halite and halite-silica interfaces (*Hickman and Evans*, 1991).
- *Hickman and Evans* (1992) showed that neck growth is faster for mono-mineralic interfaces with a lower crystallographic misorientation.
- Lastly, in the compaction experiments of *Zubtsov et al.* (2004), pure halite aggregates displayed lower compaction rates than mixtures of halite and calcite, even though calcite is characterised by slower pressure solution kinetics than halite. This behaviour was attributed to a reduced efficiency of healing of halite-calcite interfaces, and correspondingly the inhibition of retardation of pressure solution as compared to pure aggregates.

These observations suggest that the potential for grain boundary evolution is reduced by the solid-liquid and solid-solid interfacial energies associated with an incompatible bi-mineral configuration, or possibly by a strong contrast in dissolution or precipitation rates of each of the minerals in contact. This has implications for the compaction behaviour of poly-mineralic aggregates in nature: relatively pure (mono-phase) aggregates may experience significant retardation in pressure solution creep rates at low porosities, whereas mixed, poly-phase aggregates may not. This effect is noticeable when comparing densification rates of single-phase aggregates with poly-phase aggregates in laboratory compaction tests (e.g. *Niemeijer and Spiers*, 2002; *Zubtsov et al.*, 2004).

The operation (or absence) of grain boundary evolution holds important implications for the time-dependent restrengthening of faults. It is generally acknowledged that faults densify during interseismic times, for which pressure solution creep is an important mechanism at in-situ conditions (*Chester and Chester*, 1998; *Evans and Chester*, 1995; *Holdsworth et al.*, 2011; *Smeraglia et al.*, 2017). The compaction of faults is thought to contribute to the restrengthening of a fault after a seismic event (*Angevine et al.*, 1982; *Sleep and Blanpied*, 1992; *Yasuhara et al.*, 2005), and so faster compaction rates would result in a larger build-up of frictional strength over a seismic cycle. If grain boundary evolution operates efficiently, compaction and frictional restrengthening by pressure solution may be severely inhibited. On the other hand, it was remarked by *Hickman and Evans* (1991) that healed interfaces exhibit significant cohesive strength, and so grain boundary evolution may contribute to the total fault strength by time-dependent cohesion, complementing restrengthening due to compaction by pressure solution. In fault gouges of poly-mineralic composition (particularly when phyllosilicates are abundant) restrengthening by compaction is promoted, but restrengthening by time-dependent cohesion may be negligible if grain boundary healing is the sole mechanism for generating cohesion. This presents opportunities for future research, and an application of the models developed in this work in the context of fault- and earthquake mechanics.

3.8 Conclusions

In this study, we have derived expressions that describe the evolution of the grain boundary structure within stressed grain contacts undergoing pressure solution. We

have focussed on the interplay between growth in asperity contact area and pressure solution creep and the ultimate cessation of pressure solution when the grain boundary fluid connectivity breaks down, in the approach to the percolation threshold. The resulting analytical relations describing the rate of pressure solution and of the increase in grain boundary solid contact area at individual grain contacts have been used to predict aggregate behaviour, assuming a uniform pack of identical grains to upscale contact behaviour to the aggregate scale. In addition, these relations have been implemented at the contact scale in a DEM framework. The compaction behaviour of granular aggregates as predicted by both modelling methods has been compared with the (only suitable) compaction experiments on NaCl conducted by *Schutjens* (1991b). From this comparison, we conclude the following:

1. Overall, grain boundary evolution involving asperity growth can explain the large reduction in pressure solution strain rates with decreasing porosity seen in experiments. The discrepancy between experimental compaction rates and predictions from analytical models that do not include grain boundary evolution (i.e. when the grain boundary structure and effective diffusivity are constant) can be fully accounted for when an evolving grain boundary structure and fluid channel constriction are considered. Moreover, analytical models that include grain boundary evolution can potentially capture the compaction behaviour equally well as the DEM simulations do, provided that an accurate relationship between contact size and porosity is used.

2. When a constant value for the grain boundary thickness (S) is assumed, the DEM model strain rates do not compare well with the full laboratory data set. Rather, model results with constant S only compare well for a single specific grain size range, suggesting that the grain size dependence is not captured properly. When S is assumed to scale with the size of the contact, corresponding to a self-affine grain boundary topography, the entire data set can be modelled with a single set of parameters. While this does not prove that S is scale-dependent, it does suggest that actively dissolving interfaces may display a fractal geometry. To further validate the model, the characteristics of such interfaces need to be better constrained.

3. The new models for pressure solution concurrent with grain boundary evolution

provide means to investigate long-term compaction behaviour of relatively pure (mono-phase) natural aggregates under in-situ conditions. However, the driving force for grain boundary evolution provided by differences in solid-solid and solid-liquid surface energy may be diminished or absent bi-mineral interfaces, so that poly-phase aggregates may not exhibit a pronounced retardation of pressure solution creep rates as seen in mono-phase aggregates. This is of particular interest to the investigation of interseismic restrengthening of gouge-filled faults, which often feature a heterogeneous mineralic composition.

Our model for pressure solution concurrent with structural evolution of the grain boundary provides new insights into the process of pressure solution, and demonstrates the relevance of explicitly considering the structure of a wetted grain contact under stress. This warrants future research into the structure dynamics and evolution of grain boundaries in stressed fluid-rock systems in greater detail.

Appendices

3.A Laboratory procedure of *Schutjens* (1991b)

In the laboratory experiments done by *Schutjens* (1991b), the sample material was prepared from a batch of analytical grade granular halite (NaCl; Merck Chemical Company) which was double-sieved to the desired grain size fractions. The samples were created by funnelling the granular halite into latex balloon membranes, which were subsequently inflated and slowly deflated to form well-rounded samples with an average diameter of 5.5 ± 0.5 cm. Next, the balloons were sealed around a stainless steel pore-fluid pipe that was terminated by a permeable end-cap, and the assembly was mounted inside a silicone oil-medium hydrostatic pressure vessel. The pressure in this vessel was servo-controlled within 0.01 MPa, and volumetric changes in the sample were measured using a system of burettes connected to the pore-fluid pipe. With this system, volumetric strain rates down to 10×10^{-9} s^{-1} could be resolved. Data was recorded manually, with 42 data points measured over the duration of the experiments. All compaction tests were carried out at room temperature conditions. First, the sample was loaded dry up to 2.15 MPa and precompacted for a duration of about 30 minutes, after which the pressure was lowered to a value of 0.05 MPa to keep the balloon membrane pressed against the sample. The pore fluid was subsequently introduced by vacuum flushing. Finally, the vessel was pressurised to a target effective pressure of 4.3 MPa, and the sample was allowed to compact over a duration of 21 days. The sample porosities were measured before and after the experiment using the Archimedes technique, and instantaneous porosities were estimated based on the

Table 3.A.1: Summary of experimental parameters reported by *Schutjens* (1991b). The sample material was sieved to the reported grain size range, and the (instantaneous) porosities were estimated based on measured volumetric changes of the sample.

Test No.	**Grain size** [μm]	**Initial porosity** [%]	**Final porosity** [%]
L1	50-75	40.2	2.3
L2	75-106	39.9	4.3
L3	106-125	39.1	3.6
L4	125-150	39.2	6.3

sample volumetric changes while it was mounted in the apparatus. A total of four experiments were conducted, and their characteristics are displayed in Table 3.A.1.

Chapter 4

An investigation into the role of time-dependent cohesion in interseismic frictional restrengthening

Martijn P. A. van den Ende, George Marketos, and André R. Niemeijer

Abstract

Earthquakes typically exhibit recurrence times that far exceed timescales attainable in a laboratory setting. To traverse the temporal gap between the laboratory and nature, the slide-hold-slide test is commonly employed as a laboratory analogue for the seismic cycle, from which the time-dependence of fault strength may be assessed. In many studies it is implicitly assumed that all fault restrengthening emanates from an increase in the internal friction coefficient, neglecting contributions from cohesion. By doing so, important information is lost that is relevant for numerical simulations of seismicity on natural faults, as well as for induced seismicity. We conduct slide-hold-slide experiments on granular halite gouge at various normal stresses to assess the time-dependence of the internal coefficient of friction, and of cohesion, independently of one another. These experiments reveal that both the internal friction coefficient and cohesion increase over time, but that these quantities do not share a common evolution, suggesting different underlying mechanisms. We propose that micro-scale cohesion results from surface-energy driven growth of asperities on grain-to-grain contacts (grain boundary evolution), which in turn contributes to the cohesive strength of the aggregate on the macro-scale. To test this hypothesis, we numerically simulate the laboratory experiments using the Discrete Element Method (DEM), incorporating pressure solution and grain boundary evolution. Overall, the DEM simulations show good agreement with the laboratory experiments. The rates of fault strengthening and cohesion development are well captured, as well as characteristic features such as the occurrence of frictional instabilities simultaneous with the development of macroscopic cohesion. Based on the laboratory and DEM results, we interpret the observed fault frictional behaviour in terms of the interplay between granular flow, pressure solution, and grain boundary evolution, through which extrapolation to natural timescales is facilitated.

4.1 Introduction

Earthquakes are among the most disruptive of natural hazards known. Owing to their destructive potential and poor predictability, earthquakes and unstable frictional sliding in general receive considerable attention in laboratory, field, and modelling studies. For the assessment of seismic hazard and risk, reliable estimates of fault strength and coseismic stress drop are of great importance. The rate at which a fault regains the frictional strength that was lost during a seismic event controls the recurrence time and the maximum strength that can be attained before the next earthquake (*Marone et al.*, 1995; *Scholz et al.*, 1986), and therefore many laboratory studies focus on the time-dependence of frictional strength (*Dieterich*, 1972; *Marone*, 1997; *Niemeijer et al.*, 2008).

A major challenge that is inherent to laboratory work is the vast contrast in spatial and temporal scales associated with typical laboratory tests and natural seismic cycles. The recurrence time for natural earthquakes may vary from days up to many hundreds of years, and densification and restrengthening by relatively slow time-dependent processes (such as pressure solution; *Angevine et al.*, 1982; *Bos and Spiers*, 2002a; *Yasuhara et al.*, 2005) become significant over those time-spans. By contrast, the laboratory-scale equivalent of earthquakes, the so-called stick-slips (*Brace and Byerlee*, 1966), commonly have interseismic periods (i.e. durations of the 'stick') of the order of several seconds to minutes, making direct comparison between laboratory and natural stick-slip cycles non-trivial.

To bridge the temporal gap between natural and laboratory interseismic periods, the time-dependent strength recovery of faults is commonly studied by conducting *slide-hold-slide* experiments (*Dieterich*, 1972). In these tests, a sample is deformed at a constant driving velocity (slide), followed by a period in which the driving motor is stopped and the shear stress supported by the sample is allowed to relax (hold). After a predetermined duration of the hold phase, active deformation is resumed (slide) and the evolution of the shear strength and porosity in response to the reactivation are monitored. This procedure attempts to simulate the seismic cycle, and can provide some insight in the frictional restrengthening of natural faults during the interseismic period. The behaviour is typically characterised by comparing the peak shear strength

of the second sliding phase with the steady-state shear strength attained during the first sliding phase. The difference between the peak and steady-state shear strength defines the restrengthening of the fault during the hold period (e.g. *Marone*, 1997), although additional measures have been proposed to quantify the restrengthening behaviour in more detail (*Chen et al.*, 2015b; *Pluymakers and Niemeijer*, 2015). By systematically varying the duration of the hold, the rate of restrengthening of the material can be estimated, from which extrapolation to natural timescales can be attempted (e.g. *Carpenter et al.*, 2014).

When considering the amount of restrengthening $\Delta\tau$ as a function of the hold time Δt, a log-linear relation is commonly assumed on the basis of the test data (i.e. $\Delta\tau \propto \log \Delta t$; *Dieterich*, 1972; *Marone*, 1997), sometimes accompanied by a cut-off at the lower hold durations (e.g. *Nakatani and Scholz*, 2004, 2006). However, *Carpenter et al.* (2014) and *Ikari et al.* (2016b) both report a strength evolution that more resembles a power-law type of restrengthening. It has been suggested by *Ikari et al.* (2016b) that the accelerated restrengthening behaviour only becomes apparent for longer hold durations, and that the classically observed log-linear relations are merely a consequence of the limited time-window of most experiments. Based on microphysical models of pressure solution, *Bos and Spiers* (2002a) argued for a strengthening rate proportional to $t^{1/2-2/3}$. A similar time-dependence of fault strength was suggested by *Hickman and Evans* (1992) based on a model for grain contact growth driven by excess surface energy. The choice of functional form has severe implications for the estimated duration over which a fault may recover its strength, which could vary by many orders of magnitude based on the chosen extrapolation strategy (*Carpenter et al.*, 2014). Furthermore, either strength evolution law (log-linear or power law) cannot hold indefinitely, as the strength of the fault zone is presumed not to exceed the strength of the intact host rock. Thus, a cut-off or a gradual reduction of restrengthening rates at even longer hold durations is anticipated, although it is presently unknown by which mechanism this occurs.

In slide-hold-slide tests, the amount of restrengthening is typically reported as a change in apparent friction coefficient, $\Delta\mu' = \Delta\tau/\sigma_n$, implicitly assuming that cohesion is negligible in magnitude compared to the applied effective normal stress. However, several studies have suggested that cohesion cannot be neglected (*Ikari and Kopf*,

2011; *Muhuri et al.*, 2003; *Tenthorey and Cox*, 2006; *Weiss et al.*, 2016), and thus needs to be considered separate from the internal coefficient of friction in the time-dependent strengthening of faults. By investigating the microphysical processes that are responsible for the time-dependence of internal friction and cohesion, the results obtained in slide-hold-slide tests can be better interpreted. A microphysically-based interpretation then facilitates the extrapolation of laboratory results to nature.

To further investigate this, we conducted a suite of experiments in which fluid-rock interactions are significant at the timescale of the experiment, and interseismic restrengthening is simulated. From these experiments, the time-dependence of the sample cohesion is estimated independently of the coefficient of friction. We then numerically simulate the laboratory slide-hold-slide tests using the Discrete Element Method, in which we incorporate the grain-scale physical processes that are thought to contribute to the time-dependent strength of the aggregate. By comparing the results of the numerical simulations with those of the real-world laboratory tests, we assess the relevance of the simulated micro-processes in the laboratory experiments, and discuss their implications for natural faults.

4.1.1 Previous work on interseismic restrengthening

Stick-slips as a mechanism for natural earthquakes was first suggested by *Bridgman* (1936), which was later elaborated on by *Brace and Byerlee* (1966). In the experiments of *Brace and Byerlee* (1966), 'jerky' motion of two sliding surfaces was observed over a wide range of conditions, and it was recognised that only a portion of the shear strength of the interface was lost during each slip event, after which strength again accumulated before being lost in the next slip event. This suggests that a (quasi-)static interface supports a higher shear stress than a dynamic interface. *Dieterich* (1972) demonstrated in a suite of hold-slide experiments that the static coefficient of friction of a number of geomaterials increased linearly with the logarithm of the hold time over the full range of hold durations (1 to 10^5 s). This log-linear relationship provided the main motivation for the formulation of an empirical framework describing the time- and velocity-dependence of friction, referred to as *rate-and-state friction* (*Dieterich*,

1979; *Ruina*, 1980, 1983), in which the internal coefficient of friction is given by (e.g. *Marone*, 1997):

$$\mu = \mu^* + a \ln \left(\frac{V}{V^*} \right) + b \ln \left(\frac{\theta V^*}{D_c} \right) \tag{4.1}$$

where V is the instantaneous sliding velocity of the fault, μ^* is a reference friction coefficient at the reference velocity V^*, a and b are (assumed) constant parameters controlling the so-called 'direct'- and 'evolution'-effect respectively. The time-dependent evolution of μ is described by the state-variable θ and characteristic slip distance D_c, which are thought to represent some microstructural state of the gouge or of the contacts in the solid framework (*Scholz*, 2002). The evolution of θ then follows from a state evolution law of a general form $\dot{\theta} = f(\theta, V)$ (e.g. *Dieterich*, 1979; *Ruina*, 1983), which controls the time-dependence of friction as observed in laboratory experiments. As indicated by *Beeler et al.* (1994) and *Marone and Saffer* (2015), the predicted rate of strengthening is proportional to b.

While the rate-and-state friction laws can describe and characterise many laboratory experiments, their physical basis remains obscure. For a more reliable extrapolation of the frictional behaviour to natural conditions, knowledge of the underlying (micro-)physics is desired. Systematic studies of the effects of initial sliding velocity (*Marone*, 1997; *Marone and Saffer*, 2015; *Niemeijer and Spiers*, 2006; *Renard et al.*, 2012), temperature (*Chen et al.*, 2015a; *Mitchell et al.*, 2013; *Nakatani and Scholz*, 2004), stress state (*Bos and Spiers*, 2002a; *Bureau et al.*, 2002; *Karner and Marone*, 2001; *Nakatani and Mochizuki*, 1996), shear strain (*Niemeijer et al.*, 2008), and fault gouge composition (*Bos and Spiers*, 2000; *Carpenter et al.*, 2016b; *Chen et al.*, 2015a) have demonstrated that the restrengthening behaviour of gouge-filled faults is affected by a large number of (potentially competing) processes. Most of these effects are generally attributed to the increase in grain-grain contact area, either through a reduction in porosity (*Bos and Spiers*, 2002a; *Yasuhara et al.*, 2005), or by creep-driven growth and indentation of contact asperities (*Beeler and Tullis*, 1997; *Dieterich and Kilgore*, 1994). These processes are thought to be thermally-activated, as faults generally restrengthen faster at elevated temperatures (*Karner et al.*, 1997; *Mitchell et al.*, 2013; *Nakatani and Scholz*, 2004). In addition to any crystal plastic deformation processes, it is commonly agreed upon that fluid-rock interactions play a key role in the mechanical evolution of the fault zone during a hold or interseismic period (*Angevine et al.*, 1982; *Carpenter*

et al., 2016a; *Chester and Chester*, 1998; *Evans and Chester*, 1995; *Yasuhara et al.*, 2005). Gouge compaction, possibly facilitated by pressure solution creep or microcracking, has been found to increase the frictional strength of the gouge during extended hold durations (*Chen and Spiers*, 2016; *Karner and Marone*, 2001; *Richardson and Marone*, 1999), and it has been proposed as a basis for velocity-weakening behaviour (*Chen and Spiers*, 2016; *Niemeijer and Spiers*, 2007).

Although fault gouge was initially classified by *Sibson* (1977) as an incohesive fault rock with random fabric, numerous experimental and field studies provide evidence that gouges can be cohesive, even at relatively shallow depths (e.g. *Boulton et al.*, 2012; *Demurtas et al.*, 2016; *Dewhurst et al.*, 2005; *Giger et al.*, 2008; *Jones et al.*, 2002; *Tenthorey and Cox*, 2006; *Tenthorey et al.*, 2003). This indicates that lithification may occur within faults over the duration of an interseismic period, but that this lithified state is lost during periods of active slip. On the timescale of a laboratory experiment, it is generally assumed that sample cohesion is negligible during most friction tests. However, it has been suggested by several authors that this assumption may not always be valid, in particular during slide-hold-slide tests (e.g. *Ikari and Kopf*, 2011; *Karner et al.*, 1997; *Muhuri et al.*, 2003; *Yasuhara et al.*, 2005). Furthermore, cohesion contributes to the overall fault strength, and may potentially affect slip stability (*Ikari et al.*, 2011; *Trütner et al.*, 2015). Since the role of sample cohesion is underappreciated in many studies, little is known about the mechanisms of cohesion build-up in gouges, the rate-controlling processes, and the total contribution of cohesion to the overall shear strength of a material.

As a candidate mechanism, it has been suggested that cementation by pressure solution creep may lead to an increase in cohesion through growth of the grain-grain contact area (*Angevine et al.*, 1982; *Yasuhara et al.*, 2005). In this work, we propose that the cohesive strength of a contact may increase through the increase in surface area of contact asperities during pressure solution creep, driven by excess surface energy (Chapter 3; *Van Noort et al.*, 2008b; *Visser*, 1999). We will refer to this process as *grain boundary evolution* (see Fig. 4.1). Pressure solution concurrent with grain boundary evolution is expected to operate at upper- to mid-crustal conditions in the presence of a chemically active pore-fluid, and both processes may contribute to the time-dependence of fault strength independently of one another.

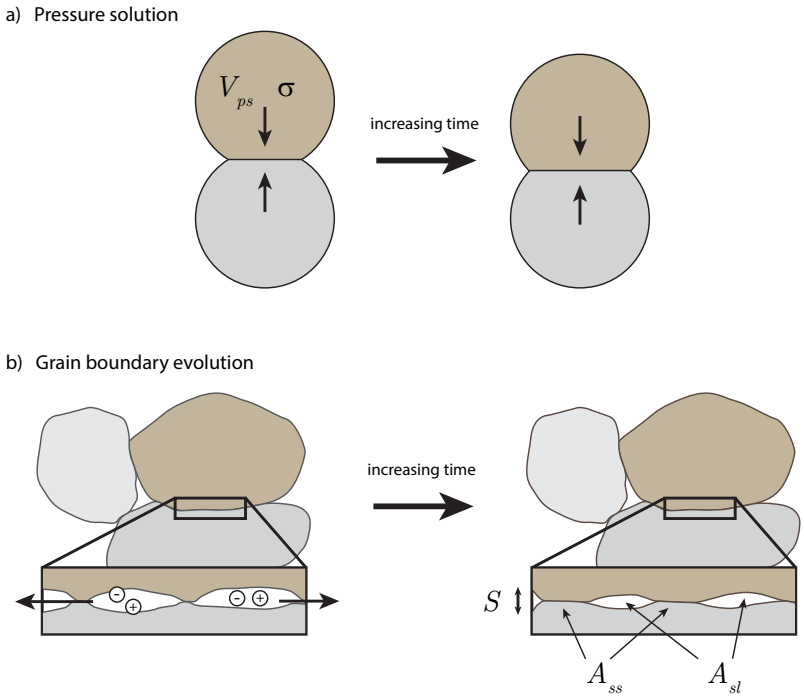

Fig. 4.1: Schematic illustrations of the fluid-rock interactions considered in this work: pressure solution and grain boundary evolution. a) Under a given grain contact stress σ, diffusive mass transfer from the grain contact into the pore space facilitates convergence at a rate $2V_{ps}$, resulting in overall densification of the aggregate; b) At steady-state pressure solution, the total volume of grain boundary occupied by contact asperities (islands) is relatively small, which allows for rapid diffusion of ionic species. When the area occupied by islands increases (i.e. when the grain boundary structure evolves), pathways for ionic diffusion are gradually obstructed and V_{ps} diminishes. Moreover, the solid-solid points of contact may support tensile stresses (cohesion). The mean width of the fluid phase in the grain boundary zone (S), and the total grain contact area occupied by islands and channels (A_{ss} and A_{sl}, respectively) are as indicated.

The frictional restrengthening is referred to by many authors as 'frictional healing' or simply 'healing'. To avoid confusion with the micro-scale process of grain boundary healing (*Van Noort et al.*, 2008b), we shall consistently use the term 'restrengthening' to refer to the increase in mechanical resistance to shear deformation. Also, we shall use the term 'cohesion' to indicate shear strength in the absence of normal stress, so that it may apply to both the macroscopic scale (sample cohesion) as well as the grain scale (particle cohesion).

4.2 Laboratory methods

4.2.1 Description of apparatus

All of the experiments reported in this study were conducted at ambient conditions in a rotary shear apparatus (Fig. 4.2), located at the High Pressure and Temperature laboratory in Utrecht, the Netherlands. In this apparatus, a 1 mm thick granular sample of synthetic gouge is enclosed by two ring-shaped toothed pistons with an inner and outer diameter of 80 mm and 100 mm respectively. The piston teeth are closely spaced and have a groove depth of 0.1 mm, and are oriented perpendicular to the direction of sliding. This artificial roughness inhibits slip on the interface between the steel and the gouge, and promotes distributed deformation. Localisation of slip, if any, occurs within the body of the gouge, rather than on the interface between the gouge and the steel (*Takahashi et al.*, 2017). Stainless steel inner and outer rings confine the sample radially to prevent extrusion of the gouge. The outer ring features two diametrically placed pore-fluid ports to allow for saturation of the sample at atmospheric fluid pressure. Inner and outer O-rings, fitted in between the pistons and the inner and outer confining rings, prevent loss of pore fluid and sample material. The sample assembly is gripped between two cylindrical forcing blocks, positioned within an Instron 1362 loading frame. The axial (normal) load applied by this frame is measured by a 100 kN Instron load cell and servo-controlled with a precision of $\sim$10 N, which corresponds to 3.5 kPa of normal stress on the sample.

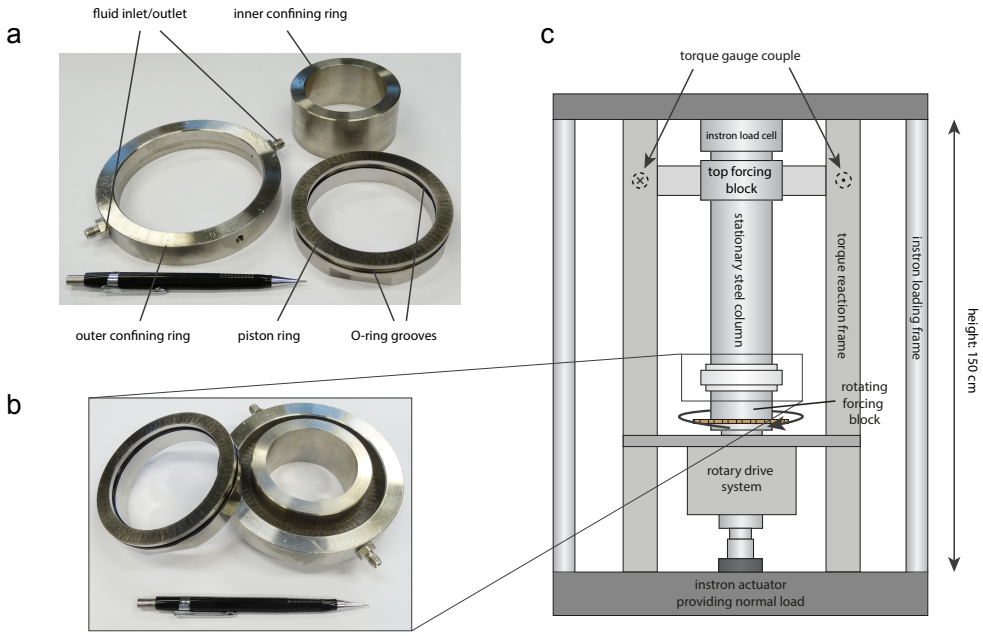

Fig. 4.2: Overview of the sample assembly and apparatus used. a) Photograph of one piston ring and the inner- and outer stainless steel confining rings. The pen for scale has a length of 14.5 cm; b) Photograph of partially assembled sample. The gouge is deposited on the piston ring that is confined by the stainless steel rings (right). The second ring (left) is placed on top of the gouge to close off the assembly; c) Schematic diagram of the rotary shear apparatus.

After application of the normal stress, the bottom forcing block is rotated with respect to the top block at a computer-controlled angular velocity by a motor-driven gear box. The range of velocities that could be attained is 1-1000 µm/s with the gear configuration used in these experiments, and the total shear displacement is in principle unlimited. The shear resistance supported by the sample as a result of shear deformation is measured by two load cells with a resolution of ∼10 kPa that are mounted in a torque couple connected to the top forcing block. Angular displacements are measured by a potentiometer with a resolution of 1 µm geared to the bottom of the rotating bottom block, and axial displacements (i.e. dilatation/compaction of the sample) are measured by two Linear Variable Differential Transformers (LVDTs), one

situated at the base of the loaded column (100 mm full scale, 1 µm resolution) and one in between the top and bottom forcing blocks (1 mm full scale, 0.1 µm resolution; referred to as 'local LVDT'). See also *Bos et al.* (2000a), *Bos and Spiers* (2000), and *Takahashi et al.* (2017). Data was acquired by a National Instruments BNC connector block (model BNC-2111) at a rate of 1000 Hz, but down-sampled to an effective rate of 1-900 Hz, which was varied manually during the experiment to capture rapid changes in the data stream (e.g. during changes in the driving velocity).

4.2.2 Sample material and preparation

Since it is expected that fluid-rock interactions play a dominant role in the frictional restrengthening of natural gouges at depth, we use analytical-grade (99.8 % pure) halite (NaCl; VWR Chemicals BV, prod. no. 27810.364) for sample material. Owing to its high solubility (0.163 m^3/m^3 at 21 °C), halite has previously been used as an analogue material for framework silicates at hydrothermal conditions (e.g. *Bos et al.*, 2000a; *Niemeijer and Spiers*, 2006; *Takahashi et al.*, 2017). The sample material was manually crushed using a mortar and pestle, and sieved to a grain size < 75 µm to obtain the desired starting grain size. During sample assembly, the gouge was carefully distributed over the bottom piston ring with a small spatula, and the layer was levelled with a smooth levelling ring. The inner and outer steel ring walls were cleaned of any remaining gouge before the top piston ring was put into place, closing off the assembly. The initial porosity was estimated by carefully weighing the sample mass and measuring the thickness of the assembly. However, during the experiment, sample material intruded into the small annular cavities between the pistons and the inner and outer confining rings, up to the level of the O-rings. Although the material did not extrude from the assembly itself, the material loss from between the pistons was sufficient to introduce a significant error in the estimate of the porosity during the experiments. Hence, we only report values of axial displacements (i.e. compaction or dilatation) relative to the start of shear deformation, which are independent of our estimates of the sample mass still present between the forcing blocks.

The pore fluid was prepared by dissolving an excess of halite in de-mineralised water. The brine was allowed to equilibrate for an hour at a temperature of 50 °C,

and was slowly cooled back to room temperature. This ensured that the brine was fully saturated, or slightly over-saturated. The brine was then contained in a 100 ml syringe, which could be readily attached to the pore-fluid system of the sample assembly. Over time, small amounts of fluid evaporated out of the syringe, producing a slight over-saturation, as evidenced by the small halite crystals forming at the bottom of the syringe.

4.2.3 Laboratory procedure

The sample assembly was loaded axially to a target load corresponding to a sample normal stress of 1, 2.5 or 5 MPa, which was varied between the different experiments. To mature the gouge and to reach a steady-state porosity more rapidly, the gouge was first sheared 'dry' (at 40-70 %RH) over a distance of 20 mm at 10 µm/s. Then, the pore-fluid was introduced by a syringe pump at a rate of 0.5 ml/min until sample saturation was achieved, after which the sample was allowed to compact for 1 hour. One of the fluid ports remained open to the atmosphere, as to maintain drained conditions while the sample compacted. Shear deformation was then re-initiated by sliding at a velocity of 10 µm/s over 20 mm of shear displacement, followed by a slide-hold-slide (SHS) sequence.

For each individually tested normal stress, a similar SHS sequence was conducted with hold durations ranging from 1 up to 40 000 s (∼11 hr), in increments of half an order of magnitude in duration. To test for sliding history effects, the SHS sequence was repeated by first step-wise increasing the hold duration from 1 s up to 10 000 s (increasing hold steps), and then reversing the sequence back down to 1 s (decreasing hold steps; see Table 4.1). Finally, the longest hold duration of 40 000 s was performed once at the end of the sequence. Between each hold phase the sample was deformed at a sliding velocity of 10 µm/s until a steady-state shear stress was achieved, which could take up to several minutes for the longer hold durations. The first experiment in this series, u472, conducted at 5 MPa normal stress, suffered from a technical failure after the first 10 000 s hold step. We consider the data from all subsequent sliding phases compromised and these are not included in the analyses presented in this work. To

compensate for the partial loss of data, a repeat experiment was conducted (u476) with hold steps of 3000, 10 000, and 40 000 s.

In addition to the procedure described above, we conducted one experiment (u480) at 5 MPa with hold durations of 10 000 and 40 000 s, in which the machine was completely unloaded prior to each reslide. This was done by first rotating the bottom forcing block back until all shear stress was removed, before removing the applied normal stress (similar to the hold-slide approach of *Ikari and Kopf* (2011)). The residual weight of the cross-head and spacer components that was supported by the sample was 0.38 kN (0.13 MPa on the sample). Then, the sample was deformed at a rate of 10 µm/s in the absence of any normal stress applied by the loading frame, so that the measured peak strength gave a near-direct measurement of the sample cohesion (shear strength in the absence of normal stress). Owing to the apparatus design, no shear deformation of the sample could occur during back-rotation other than elastic unloading, i.e. sliding on the sample was not reversed. Because of this, it is unlikely that any sample cohesion was removed by the unloading procedure, provided that the cohesive strength was sufficient to sustain elastic unloading and re-loading. Note that during the hold periods of u480, the sample was kept under the same loading conditions as the other experiments (i.e. constant normal stress, and a slowly relaxing shear stress), and that the load was manually removed only after each hold phase was concluded.

4.2.4 Data analysis

4.2.4.1 Time-dependence of friction and cohesion

In order to assess the contribution of cohesion to the overall strength of the gouge, the following data analysis procedure was adopted: first, it was assumed that during resliding following a given hold duration, the sample 'failed' macroscopically at the peak shear strength. Since the experiments were conducted at various normal stresses, Mohr-Coulomb failure envelopes of the form $\tau_{peak} = \mu\sigma_n + C_s$ could be constructed by plotting the peak shear strength τ_{peak} of the sample after a given hold duration against the applied normal stress σ_n. This was done for all normal stresses employed in the experiments, and subsequently for each hold duration. The internal coefficient of

friction μ and the sample cohesion C_s could then be obtained though linear regression. Ordinary least-squares regression was performed by the Python *StatsModels* package (*Seabold and Perktold*, 2010). This procedure was adopted for each hold duration individually, so that the time-evolution of μ and C_s could be inferred. The values of the cohesion inferred in this manner are compared to those obtained from unloading the machine (experiment u480), as to investigate the possibility that the sample failure envelope becomes nonlinear approaching the origin (e.g. *Saffer and Marone*, 2003), for which a linear failure criterion would not be an accurate description.

4.2.4.2 Localisation of shear strain

It is commonly found in laboratory friction tests that shear strain localises within a narrow region, often up to several tens of µm in thickness (*Logan et al.*, 1979; *Takahashi et al.*, 2017; *Verberne et al.*, 2014b). Even though post-mortem microstructural analysis may readily reveal any localisation features present in the sample, it is non-trivial to establish the timing of such features, and to relate the recorded mechanical response to microstructural developments, particularly when the sample experienced a complex sliding history (e.g. a multi-step slide-hold-slide sequence). Nonetheless, the tendency for localisation may be identified from the mechanical data by considering the volumetric strain response of the sample. When granular flow is confined to a narrow region in the sample, the volumetric response of the bulk of the sample will be predominantly compactive in the absence of dilatancy induced by granular flow to negate compaction by non-dilatant creep mechanisms (e.g. pressure solution or microcracking). Conversely, a continuous dilatant response hints to progressive reworking of the gouge (delocalisation).

To quantify the tendency for localisation in the laboratory experiments, we define the volumetric strain recovery parameter λ as:

$$\lambda = \frac{\Delta d}{\Delta h} \tag{4.2}$$

where Δh is the compaction measured at the end of the hold phase (relative to the start of the hold phase), and Δd is the maximum dilatancy measured from the initiation of resliding up to the start of the next hold phase (see also inset in Fig. 4.5d), so that λ represents the relative amount of compaction during the hold that is recovered during

Table 4.1: List of laboratory experiments with the applied normal stress, the range of hold durations, and indication of the hold step after which the first unstable slip event occurred. Experiment u480 was unloaded prior to resliding to get a near-direct measurement of the cohesion.

Experiment	σ_n [MPa]	**Hold steps** [s]	**Unstable after** [s]
u472	5.0	1-3-10-30-100-300-1000-3000-10 000	3000
u473	2.5	1-3-10-30-100-300-1000-3000-10 000-3000-1000-300-100-30-10-3-1-40 000	3000
u475	1.0	1-3-10-30-100-300-1000-3000-10 000-3000-1000-300-100-30-10-3-1-40 000	10 000
u476	5.0	3000-10 000-40 000	10 000
u480	5.0	10 000-40 000	-

resliding. Values of $\lambda < 1$ indicate nett compaction, which suggests that deformation is localised. A value of $\lambda > 1$ indicates nett dilatation, likely caused by reworking of dense regions of the gouge.

4.3 Numerical methods

As discussed in Section 4.1.1, it is hypothesised that the observed frictional restrengthening behaviour results from simultaneous operation of pressure solution and structural evolution of the grain boundary through a nett increase in asperity contact area. This hypothesis will be tested using the Discrete Element Method, and the effect of cohesion on restrengthening and resliding behaviour will subsequently be investigated.

4.3.1 General description of the Discrete Element Method

The Discrete Element Method (DEM; *Cundall and Strack*, 1979) is a particle-based, time-stepping numerical method for modelling discontinuous media, in which each

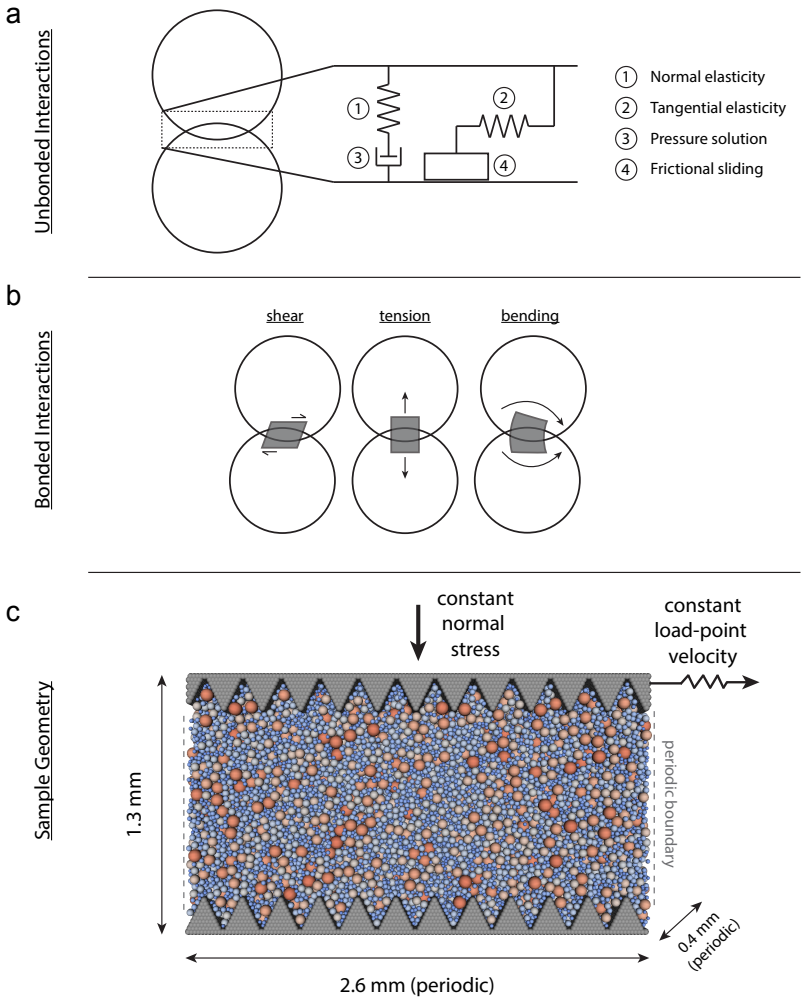

Fig. 4.3: Overview of the DEM particle interactions and sample geometry. a) Interactions of unbonded particles include normal and shear elasticity, pressure solution, and frictional sliding. No tensile forces or bending moments can be sustained; b) Interactions of bonded particles, which are complementary to those of unbonded particles. Particle bonds can deform elastically in shear, tension, and by bending. When the shear or tensile stress acting on the bond exceeds a critical value, the bond breaks; c) Side view of the three-dimensional DEM sample. The rigid pistons are displayed in gray, the particles constituting the gouge are coloured according to their diameter (in the range of 10-40 µm).

grain is modelled as a discrete particle and where individual particles interact with each other through springs at their contacts. DEM is widely adopted for studying granular mechanics, of which examples include industrial granular flows (*Cleary and Sawley*, 2002), agricultural products (*Landry et al.*, 2006), and deformation of subglacial sediments (*Damsgaard et al.*, 2013) and of fault gouges (*Guo and Morgan*, 2006; *Mair and Abe*, 2008), as well as large-scale geological features, such as fold-and-thrust belts (*Morgan*, 2015) and landslides (*Chang and Taboada*, 2009). Although DEM of samples with a large number of particles is computationally expensive, it holds a major advantage over many analytical and mesh-based techniques that it does not require a continuum description of a representative volume element. Instead, the underlying physics is defined only at the particle scale, and the macroscopic response of the system emerges spontaneously. During each time step, the following basic procedure is adopted: after identifying which particles are in contact with each other, the forces acting across each particle-particle contact are calculated through the use of a contact force-displacement law (e.g. a spring-dashpot combination). The individual particle velocities and positions are then obtained by integrating the accelerations given by Newton's second law of motion. This procedure is repeated each time step during the simulation, so that an aggregate of particles responds to external boundary conditions fully complying to Newton's laws of motion. In this way, the macroscopic mechanism of deformation can be linked to the grain-scale interactions of inter-particle contacts. These interactions are typically elastic-frictional in most studies, but here we also employ mechanics resulting from fluid-rock interactions, which are derived from the physics of a single contact.

In the DEM formulation adopted for this study, all particles are modelled as indestructible, perfect spheres. In DEM, particles are in contact when the sum of the distance between their centroids is less than the sum of their respective radii, which results in a mutual overlap of size Δx_{el} (see Fig. 4.3a). This overlap is analogous to the elastic deformation of the contact between two grains, and as such the elastic overlap results in a restoring force acting normal to the contact plane, which is approximated by a linear force-displacement relationship:

$$F_n = k_n \Delta x_{el} \tag{4.3}$$

Here, F_n is the force acting normal to the contact plane, and k_n is the normal stiffness

of the contact. Furthermore, shear forces are calculated as:

$$\vec{F}_s = \begin{cases} k_s \Delta \vec{s}_{el}, & \text{if } \left\| \vec{F}_s \right\| < \mu_p F_n \\ \mu_p F_n \frac{\Delta \vec{s}_{el}}{\|\Delta \vec{s}_{el}\|}, & \text{otherwise} \end{cases} \tag{4.4}$$

where $\vec{F}_s$ denotes the vector of the shear force that acts parallel to the contact plane, k_s denotes the shear stiffness of the contact, μ_p the inter-particle coefficient of friction, $\Delta \vec{s}_{el}$ the vector of the elastic shear displacement, and $\|\cdot\|$ denotes the Euclidean norm. The elastic shear displacement is updated incrementally as:

$$\Delta \vec{s}_{el,i+1} = \begin{cases} \Delta \vec{s}_{el,i} + \vec{V}_{rel,i} \times \Delta t, & \text{if } \left\| \vec{F}_s \right\| < \mu_p F_n \\ \mu_p \frac{F_n}{\left\| \vec{F}_s \right\|} \Delta \vec{s}_{el,i}, & \text{otherwise} \end{cases} \tag{4.5}$$

where subscript i denotes the current iteration in the simulation, $\vec{V}_{rel}$ the relative velocity vector between the two particles, and Δt the time step size. The inter-particle coefficient of friction is assumed here to be constant and particle size-independent. Furthermore, in all of the simulations reported here, it is assumed that the normal stresses are effective, i.e. $\sigma_n - P_f$, with a constant and sample-uniform pore fluid pressure $P_f \ll \sigma_n$ (or $P_f \approx 0$). This simulates drained conditions at atmospheric pressure, as is anticipated for our laboratory experiments, and is valid for relatively high porosities and/or slow deformation rates with respect to the fluid permeability of the system.

We employ the open-source software package granular LAMMPS (*Landry et al.*, 2003; *Plimpton*, 1995), which was modified by *Marketos* (2013). In addition to the contact mechanics detailed above, we also incorporate pressure solution (as described in Chapter 2 and by *Van den Ende et al.*, 2018b) and grain boundary evolution by nett growth of the contact asperities (Chapter 3). Furthermore, we propose here that the increase of solid-solid contact area (i.e. 'real' contact area) by grain boundary evolution results in grain-scale cohesion, which is simulated by a modified implementation of the PFC3D parallel-bond model (*Potyondy and Cundall*, 2004). A brief account of these particle interactions is given below.

4.3.2 DEM implementation of pressure solution

To simulate diffusion-controlled pressure solution creep at the contact scale, the implementation that is described in more detail in Chapter 2 was adopted. In this implementation, two particles in contact will dissolve at the contact and their centroids will converge at a velocity $2V_{ps}$, given by:

$$V_{ps} = Z_d \left(1 - \alpha\right) \frac{\pi F_n}{A_c^2} \tag{4.6}$$

In this formulation, Z_d is a (temperature dependent) material constant, α is the relative contact area occupied by asperities (defined in Eqn. (4.10)), and A_c is the area of contact as defined by the circular intersection of the two spherical particles. During each time increment, the total dissolved contact thickness δ is incremented by $\Delta\delta = 2V_{ps} \times \Delta t$ (factor 2 accounting for both sides of the dissolving interface). To allow for particle convergence and overall densification of the aggregate, δ is subtracted from the total particle overlap Δx_t, so that the contact normal force becomes:

$$F_n = k_n \Delta x_{el} = k_n \left(\Delta x_t - \delta\right) \tag{4.7}$$

Under a constant applied force, an increase in δ with time is accompanied by an increase in Δx_t, resulting in shortening of the inter-particle distance. In this way, creep at the contact is reproduced. Alternatively, with constant Δx_t (i.e. a constant inter-particle distance), δ increases over time through the operation of pressure solution, so that F_n decreases and the contact stress relaxes.

The kinetic constant Z_d is obtained from the theory of pressure solution for a single contact (*Lehner*, 1995; *Pluymakers and Spiers*, 2014; *Rutter*, 1976), and is written as:

$$Z_d = \frac{4(DCS)\Omega}{RT} \tag{4.8}$$

where D is the effective diffusion coefficient of the ionic species in the grain boundary interstitial fluid, C the solubility of a flat, unstressed solid interface (in m^3/m^3), S the (mean) thickness of the fluid phase in the grain boundary zone, Ω is the molar volume of the solid, R is the universal gas constant, and T is the absolute temperature

(in Kelvin). Under steady-state conditions at constant temperature, the quantities comprising Z_d can be considered to be material constants. However, under non-steady state conditions, the value of Z_d may change under the influence of an evolving grain boundary structure, as will be discussed in the next section.

4.3.3 DEM implementation of grain boundary evolution and cohesion

In most constitutive relations for pressure solution creep, a steady-state grain boundary structure is assumed to be represented by a dynamically stable island-channel network (*Ghoussoub and Leroy*, 2001; *Lehner*, 1990; *Raj*, 1982; *Schutjens and Spiers*, 1999; *Spiers and Schutjens*, 1990, e.a.; see also Fig. 4.1). This island-channel structure comprises solid-solid contact asperities (islands) and an interconnected network of interstitial fluid (channels) through which ionic diffusion occurs. It has been shown that excess surface energy stored in the grain boundary may drive a nett increase in the contact area occupied by islands (*Beeler and Hickman*, 2015; *Hickman and Evans*, 1991, 1992; *Schutjens and Spiers*, 1999), a process we will refer to as grain boundary evolution (Fig. 4.1b). Due to nett growth of the asperities, pathways for ionic diffusion become obstructed, which inhibits pressure solution creep when it is controlled by the rate of diffusion over the grain contact.

Van Noort et al. (2008b) proposed an equilibrium condition based on the competition between surface energy and elastic strain energy stored in the grain boundary, as:

$$\Delta\mu_i = \frac{2\gamma_{sl}}{S}\Delta\cos\frac{\theta}{2} - \frac{\sigma_i^2}{2E} = 0 \tag{4.9}$$

where $\Delta\mu_i$ is the chemical potential for static asperity growth, γ_{sl} is the solid-liquid surface energy, $\Delta\cos(\theta/2)$ is the mismatch between the dynamic and equilibrium dihedral angle, σ_i is the average stress supported by the asperities, and E is the Young's modulus of the material. Conceptually, the product $2\gamma_{sl}\Delta\cos(\theta/2)/S$ represents the driving force for asperity growth provided by the local surface energy, and $\sigma_i^2/(2E)$ represents the tendency for asperity contraction ('undercutting') due to the elastic strain energy stored in the asperities. The condition $\Delta\mu_i = 0$ defines an unstable

equilibrium state, dividing the two regimes of nett undercutting ($\Delta\mu_i < 0$) and nett asperity growth ($\Delta\mu_i > 0$).

However, this equilibrium condition only describes the transition from one regime to the other, but does not describe the rate of asperity growth or contraction. In Chapter 3, we developed a model for grain boundary evolution by asperity growth during pressure solution, which describes the dynamics of the grain boundary structure when $\Delta\mu_i > 0$. In this model, the rate of asperity growth is given by:

$$\frac{\mathrm{d}\alpha}{\mathrm{d}t} = \frac{8DC\,(1-\alpha)\,\Omega}{RT}\frac{\pi}{A_c}\left(\frac{2\gamma_{sl}}{S}\Delta\cos\frac{\theta}{2} + \frac{\sigma_i^2}{2E}\right) \tag{4.10}$$

Here, α is the relative contact area occupied by asperities, defined as the ratio of the total asperity area A_{ss} to the grain contact area A_c (i.e. $\alpha = A_{ss}/A_c$). The lower limit of α is determined by the elastic-plastic yield limit, which is estimated to be of the order of a few per cent for halite (*Renard et al.*, 2012; *Van Noort et al.*, 2008b).

Following procedure described in Chapter 3, we also take into account the reduction in pressure solution rates as α increases. It is expected that growth of asperities will lead to a reduction in effective diffusivity of the grain boundary zone, as a result of contraction and closure of fluid channels that enable diffusion of ionic species out of the grain boundary (see also Fig. 4.1b). Scaling of the effective diffusivity with α can be described using percolation theory (e.g. *Stauffer and Aharony*, 1992) as:

$$D = D^{eff} = D_0\left(\frac{\alpha_c - \alpha}{\alpha_c - \alpha_0}\right)^{\nu} \tag{4.11}$$

where D^{eff} is the effective diffusion constant of the grain boundary zone, α_0 is the initial value of α (roughly corresponding to the elastic-plastic yield limit of asperities), α_c is the terminal value of α corresponding to the percolation threshold, D_0 is the diffusivity when $\alpha = \alpha_0$, and ν is a constant that assumes a value of 1.16 in a (semi-)two-dimensional percolating network (*Sahimi*, 2003). As α increases over time (Eqn. (4.10)), D^{eff} decreases and pressure solution slows down. At the percolation threshold ($\alpha = \alpha_c$), $D^{eff} = 0$ and pressure solution is fully arrested. During the simulations, the value of Z_d (Eqn. (4.8)) is adjusted according to the value of D^{eff}. It is then convenient to

define a reference and instantaneous kinetic coefficient, respectively, as:

$$Z_d^0 = \frac{4\left(D_0 CS\right)\Omega}{RT} \tag{4.12a}$$

$$Z_d = \frac{4\left(D^{eff} CS\right)\Omega}{RT} = Z_d^0 \left(\frac{\alpha_c - \alpha}{\alpha_c - \alpha_0}\right)^{\nu} \tag{4.12b}$$

In addition to the effects that grain boundary evolution may have on the rate of pressure solution, we propose here that the cohesive strength of the grain contact is proportional to the total area occupied by asperities. Consequently, Eqn. (4.10) implies a time-dependence of grain-scale cohesion, and may provide a mechanism for time-dependent restrengthening of fault gouges, in addition to gouge compaction (*Chen and Spiers*, 2016). To investigate this possibility further, we implemented Eqn. (4.10) in the DEM model (see also Chapter 3). We then related the value of α to particle cohesion as follows:

1. Firstly, we modified a bond model previously added to LAMMPS (see *Marketos*, 2013) that is similar to the PFC3D parallel-bond model (Itasca Consulting Group; see *Potyondy and Cundall* (2004) for details). This contact model allows for bonding of particles and features transfer of tensile and shear forces, as well as bending moments between the two particles sharing a bonded contact (see Fig. 4.3b), and has recently been employed by *Roda et al.* (2017).

2. Then, instead of assuming a predetermined, constant size and strength of the bond, we allowed the bond size to change over time, following Eqn. (4.10). The equivalent bond area A_b is calculated as $A_b = A_{ss} = \alpha A_c$. Hence, as α evolves over time, so do the size and strength of the bond. The bond mechanics (i.e. bending and stretching) then follow from *Potyondy and Cundall* (2004), using the instantaneous bond radius $r_b = \sqrt{\alpha A_c / \pi}$ (denoted by $\bar{R}$ by *Potyondy and Cundall* (2004)).

3. Particle bonds were only created for contacts on which $\Delta\mu_i > 0$ in Eqn. (4.9), i.e. when asperity growth has initiated. The size of the bond then grows in accordance with Eqn. (4.10). Particle contacts for which $\alpha = \alpha_0$ and $\Delta\mu_i < 0$

remained unbonded, and so could not support any moments of force and tensile forces.

4. Lastly, the bond failure criteria for the normal and shear forces used here were:

$$-F_{n,b} > A_b C_p \tag{4.13a}$$

$$\left\|\vec{F}_{s,b}\right\| > \begin{cases} A_b C_p + \mu_p F_{n,b}, & \text{if } F_{n,c} > 0 \\ A_b C_p, & \text{otherwise} \end{cases} \tag{4.13b}$$

where $F_{n,b}$ and $\left\|\vec{F}_{s,b}\right\|$ respectively denote the magnitudes of the normal and shear forces acting on the bond, $F_{n,c}$ denotes the normal force acting over the entire contact, and C_p the intrinsic cohesive strength of the bond. Note that $F_{n,b}$ and $\vec{F}_{s,b}$ include contributions from bending of the bond. We took the bond tensile strength to be equal to the cohesive strength (Eqn. (4.13a)), which is only accurate up to a first-order. The exact value of C_p is presently unconstrained by laboratory experiments. However, since individual grains typically experience a state of stress that is higher than the macroscopic stress (i.e. stress intensification owing to a non-zero porosity), it can reasonably be argued that C_p is required to be larger than the macroscopic normal stress in order to contribute significantly to the macroscopic shear stress. On the other hand, the cohesion developed in a halite aggregate is expected to be substantially lower than that of bulk crystalline rocks, such as granite. In DEM simulations of the fracturing of granite samples, a value of $C_p > 150$ MPa has previously been adopted (*Potyondy and Cundall*, 2004; *Wang and Tonon*, 2009). In the absence of tight constraints on C_p, we adopt a value of 20 MPa, which gives DEM results that are in the range of the laboratory data. The macroscopic cohesion (C_s) developed in the DEM simulations scales roughly proportional to the value of C_p, so that doubling C_p would approximately double C_s in the simulations.

While two particles are bonded, pressure solution is still allowed to operate and A_c increases as a result. This assumes that asperities that are being incorporated into the newly acquired contact area grow rapidly towards the contact-average size. Since the island-channel structure is thought to represent a highly dynamic state, with islands

rapidly dissolving away and reappearing in other places, any spatial variations in α likely average out rapidly. Since A_b is calculated as $A_b = \alpha A_c$, and $\alpha \leq 1$, the size of the bond cannot exceed the size of the contact.

4.3.4 Numerical stability and scaling

For numerical stability, the time step Δt of Discrete Element Method simulations should be limited by at least the critical time step $t_c = \sqrt{m/k}$, where m is the mass of the smallest particle, and k is the highest particle stiffness (*Cundall and Strack*, 1979). In our simulations, we choose a time step $\Delta t = t_c/10$. However, when considering a gouge with particle sizes in the range of 1-100 µm, the estimated time step reduces to values that are prohibitive for simulating relatively slow time-dependent processes. Therefore, in order to achieve more reasonable computation times, we artificially increased the time step by altering the mass of the particles (a technique similar to density scaling; see *Cui and O'Sullivan*, 2006; *Ng*, 2006; *O'Sullivan et al.*, 2003) by non-dimensionalising the temporal and spatial dimensions. The minimum particle size is taken near unity with a constant mass density of 2100 kg m^{-3} (density of halite). This is equivalent to increasing the mass density of a particle much smaller in size. Time is then non-dimensionalised as:

$$t' = t\frac{Z_d^0 \sigma_n}{r^3} \tag{4.14}$$

where σ_n is the externally applied (constant) normal stress, and r is the (dimensional) particle radius. All spatial dimensions are scaled to the particle size, and measures of velocity are scaled accordingly. Note that while Z_d may vary over the course of a simulation, Z_d^0 is constant, and can therefore be used in scaling. For easy comparison with the laboratory data, all DEM simulation results are reported in their physical dimensions.

To verify the assumption of quasi-static deformation, for which our scaling procedure should not affect the macroscopic behaviour, we consider the dimensionless inertial

number of the system, defined as (*MiDi*, 2004; *Modenese et al.*, 2012):

$$I = \dot{\gamma} r \sqrt{\frac{\rho}{\sigma_n}} \tag{4.15}$$

Here, $\dot{\gamma}$ denotes the bulk shear strain rate, and ρ is the particle density. To remain within the quasi-static regime of deformation, this number should not exceed 10^{-3} (*Modenese et al.*, 2012), with typical laboratory equivalent values of I being of the order of 10^{-8}. In our simulations, we chose a degree of scaling such that $I < 10^{-4}$ during steady-state deformation. During hold periods, the sample strain rate rapidly decays as the stresses relax, and thus I is expected to decrease proportionally. In order to simulate long hold durations within reasonable computation time, we step-wise increase the degree of scaling during the hold period by increasing the value of Z_d^0 (see Eqn. (4.14)). While doing so, we ensure that $I < 10^{-4}$, as not to significantly affect our results compared to the quasi-static laboratory experiments for which we estimate $I \ll 10^{-8}$.

4.3.5 Simulation set-up and procedure

By adopting the above-described procedures, we can now attempt to simulate fault gouge restrengthening through time-dependent fluid-rock interactions, and specifically test the contribution of cohesion to gouge strength and sliding behaviour. In the following section, the procedure of simulating the laboratory experiments is detailed.

First, a cuboidal simulation domain is defined with periodic boundaries in the horizontal directions. The simulation domain is 2.6 mm in length, and 0.4 mm in width (see Fig. 4.3c). The annular geometry of the laboratory sample assembly is simulated with periodic boundaries, so that particles leaving the domain on one side re-enter and interact with particles on the opposite side. This also eliminates possible boundary effects, to which DEM is often more prone than laboratory tests, owing to the limited spatial dimensions that can be attained (*Hardin*, 1989; *Marketos and Bolton*, 2010). To constrain the particles in the vertical directions, as well as to impose constant normal stress and shear velocity boundary conditions, we generate rigid forcing blocks ('pistons') by placing particles at predefined, closely spaced positions, forming a toothed

pattern similar to the piston profile used in the laboratory set-up. These particles are then 'glued' together using the LAMMPS RIGID package, so that the collection of particles constituting one piston behaves as a single rigid object which does not deform internally. The pistons are initially situated at the top and bottom ends of the simulation domain. The bottom piston remains perfectly stationary throughout the simulations, the top piston is given two degrees of translational freedom: in the direction normal to the shear plane, a constant, servo-controlled stress is applied, and the piston can move vertically following compaction and dilatation of the simulated gouge as to maintain the target normal stress. In the direction of imposed shear, the piston is pulled by a virtual spring with constant stiffness at a predetermined horizontal velocity.

The use of a virtual spring allows us to control the effective shear stiffness of the system to be of similar magnitude as that of the laboratory set-up. In this way, we can exclude that differences in behaviour between the DEM and laboratory samples are due to differences in shear stiffness. During each time step, the forces of interaction between the piston and the simulated gouge are added to the spring force exerted by the load point to give a nett acceleration of the centre of mass of the piston. The piston velocity and displacements are obtained from integrating the acceleration. Horizontal motions of the piston perpendicular to the imposed shear direction, as well as rigid-body rotations, are inhibited. This guarantees that the piston remains perfectly aligned and horizontal at all times. The total shear traction exerted by the piston on the granular sample (F_{piston}) is calculated from the relative positions of the load point (x_{lp}) and piston (x_{piston}), and the spring stiffness (k_{spring}) as $F_{piston} = k_{spring}\,(x_{lp} - x_{piston})$.

Next, the simulated gouge is rendered by placing 30 000 particles at random locations within the volume enclosed by the two pistons, ensuring that they do not touch or overlap initially. The particle diameters are randomly sampled from a power-law distribution between 10 and 40 µm, as cataclastic fault material is known to exhibit fractal grain-size distributions (*Marone and Scholz*, 1989; *Storti et al.*, 2003). After the sample has been generated, gravity is turned on, and the simulated gouge and top piston are allowed to settle. Subsequently, a constant, servo-controlled normal stress of 5 MPa is imposed to the top piston, which transfers the load onto the gouge. During settling and loading of the sample, forces are artificially reduced ('damped')

to lower the time for the aggregate to come to rest. Once the sample has approached mechanical equilibrium, gravity and artificial damping are turned off, and pressure solution is turned on numerically, simulating instantaneous saturation of the sample with a pore fluid. The sample is then allowed to compact down to a porosity of 30 %, marking the end of the precompaction phase. Porosities are calculated based on the total mass of the particles present in the system, and the dimensions of the simulation domain, corrected for the volume occupied by the pistons.

After the precompaction phase, shear deformation is initiated by pulling the top piston with a spring whose other end moves horizontally at a rate of 10 µm/s. Sliding is continued over a duration of 100 s, during which the sample approaches a steady-state shear strength. After this first phase of sliding, the load-point velocity is set to zero and the hold phase is commenced. During the hold, the shear stress supported by the sample relaxes by slow sample creep, facilitated by pressure solution. The hold phase lasts 10^6 s in total, but snapshots of the simulation state are saved at half-decade intervals. These snapshots serve as a starting point for the next phase of sliding: for each snapshot, the simulation is reset to that particular state, and shear loading is re-initiated from that point by pulling the top piston through a spring at a rate of 10 µm/s over a duration of 50 s.

Throughout the simulations, as soon as pressure solution is activated, the grain boundary structure is allowed to evolve, and particle-particle bonds are allowed to form as described in Section 4.3.3. However, during the initial sliding and subsequent hold phase, the particle cohesion C_p is set to zero, so that the bonds have no cohesive strength (essentially equivalent to having no bonds at all). From each of the snapshots saved during the hold phase, we first run simulations of the resliding phase where the particle cohesion remains zero. These simulations serve as a benchmark for the time-dependence of shear strength in the absence of cohesion. Then, we initiate a second set of simulations from the saved snapshots where C_p is instantaneously set to a value of 20 MPa, giving the sample a macroscopic cohesive strength that depends on the average size of the asperities (i.e. the distribution of values of α) at that given moment during the simulation. In this manner, the effect of cohesion is isolated with the exact same initial state for both sets of simulations, so that the only variable is the cohesive strength that may have been attained during the hold period.

Table 4.2: Parameters used in the DEM simulations. References: a) *Spiers et al.* (1990); b) *Visser* (1999) using the approximation by *Israelachvili* (1986); c) *Lewis and Holness* (1996), assuming $\theta = 0$

Parameter	Value	Units
Number of particles	30 000	-
Particle contact stiffness	2.65×10^9	N m^{-1}
Particle friction coefficient	0.6	-
Particle density	2100	kg m^{-3}
Particle size distribution	power-law (exponent: -2.7)	
Particle diameter range	10-40	µm
Particle bond strength	20	MPa
Effective system shear stiffness	67.4	GPa m^{-1}
Applied normal stress (σ_n)	5.0	MPa
Initial simulation time step	3.76×10^{-2}	s
Kinetic constant (Z_d^0)	5.29×10^{-27}[a]	m^3 Pa^{-1} s^{-1}
Surface energy (γ_{sl})	0.2[b]	J m^{-2}
Dihedral angle mismatch ($\Delta \cos \frac{\theta}{2}$)	0.18[c]	-
Asperity Young's modulus (E)	37	GPa
Initial asperity occupation ratio (α_0)	0.1	-
Terminal asperity occupation ratio	0.7	-
Mean grain boundary fluid thickness (S)	310	nm

Details of the parameter values used in the simulations are listed in Table 4.2. These values are reported in their physical dimensions for easy comparison with laboratory parameters.

4.4 Laboratory results

A representative overview of the shear stress and compaction data (measured by the local LVDT) that is typically recorded in the SHS tests is presented in Fig. 4.4. The steady-state frictional strength of the halite sample, reported as an apparent coefficient

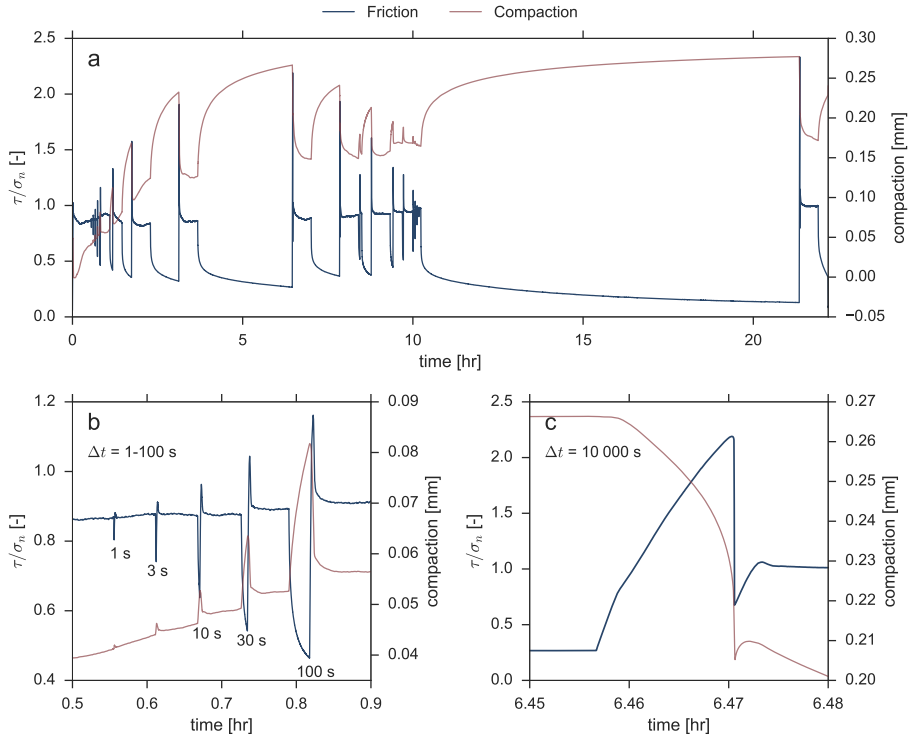

Fig. 4.4: Mechanical results from experiment u473, conducted at a normal stress of 2.5 MPa. The blue lines display the apparent coefficient of friction, τ/σ_n, the red lines display the axial displacement as recorded by the local LVDT, measuring compaction as positive. a) Overview of all of the slide-hold-slide sequences conducted in this experiment; b) Detailed view of the first five slide-hold-slides conducted. Note that resliding is stable; c) Detailed view of the resliding conducted after a hold period of 10 000 s. Note that resliding is unstable.

of friction (τ/σ_n), is initially close to but slightly lower than 0.9, but over the duration of the experiment evolves to 1.0. Overall, the steady-state apparent friction coefficient fluctuates between 0.8 and 1.0, which may be related to an uneven load distribution of the torque cells due to a non-uniform thickness of the sample, or due to slight misalignment of the piston rings. As soon as active sliding is halted (i.e. the hold starts), the shear stress relaxes rapidly, accompanied by compaction of the sample.

After the hold phase, when sliding is re-initiated, a clear peak stress is observed even for the shortest hold duration of 1 s, after which the stress evolves towards a new steady-state. During a reslide, the sample dilates until a steady-state shear stress is reached. For relatively long hold durations ($\Delta t > 3000$ s), we observe an overshoot in both the stress drop as well as in sample dilatation following the peak stress (Fig. 4.4c), which is accompanied by a clearly audible acoustic emission. We will refer to this behaviour as 'unstable' resliding. Resliding after relatively short hold durations is nominally stable and does not show show an overshoot in shear stress and dilatation (Fig. 4.4b), nor are audible acoustic emissions produced. The first occurrence of unstable sliding in each experiment is listed in Table 4.1.

The total restrengthening, expressed as an apparent coefficient of friction ($\Delta\mu' = \Delta\tau/\sigma_n$), does not obey a log-linear evolution with hold duration (Fig. 4.5a), nor can the data be represented by a power-law relation with a constant exponent (i.e. constant β in $\Delta\mu' \propto \Delta t^{\beta}$). For short hold durations ($\Delta t < 1000$ s), no effect of the imposed normal stress is observed, but for longer hold durations $\Delta\mu'$ increases faster with hold duration for lower σ_n. By contrast, the total sample compaction achieved during each hold is not systematically related to the imposed normal stress (Fig. 4.5b). In addition, there exists a clear relation between the amount of restrengthening and the amount of compaction achieved during each hold (Fig. 4.5c).

For practically all of the resliding phases in the sequence of increasing hold duration (upward pointing triangles in Fig. 4.5d), only a portion of the compaction during the hold is recovered during resliding, as indicated by $\lambda < 1$. This strongly suggests that deformation is localised during these stages of the experiments. The amount of nett compaction diminishes for longer hold durations, and turns to nett dilatation ($\lambda > 1$) for the sequence of decreasing hold duration (downward pointing triangles). However, the longest hold duration of 40 000 s that concludes the up-and-down sequence again shows near-neutral values of λ.

To estimate the amount of cohesion that was attained over time, we construct Mohr-Coulomb failure envelopes for each individual hold phase (see Section 4.2.4.1 and Fig. 4.6). The slope of this envelope represents the internal coefficient of friction, and its intercept represents the sample cohesion. Overall, the data at relatively short hold durations ($\Delta t < 1000$ s) can be captured well with a linear failure envelope (Fig. 4.6a).

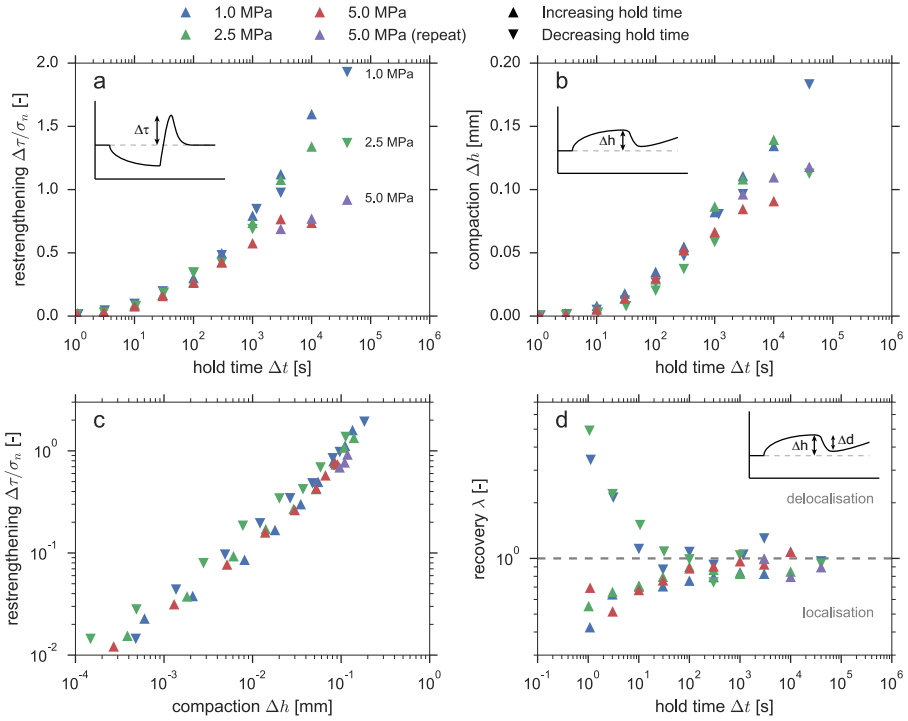

Fig. 4.5: Overview of the mechanical response of the laboratory samples. a) Frictional restrengthening, expressed as an apparent coefficient of friction $\Delta\mu' = \Delta\tau/\sigma_n$, as a function of hold duration; b) Sample compaction during the hold as a function of hold duration; c) Frictional restrengthening as a function of the compaction attained during the hold; d) Volumetric strain recovery during resliding, $\lambda = \Delta d/\Delta h$, with values < 1 suggesting localised deformation, and values > 1 suggesting delocalisation. Values of σ_n, and the direction of the slide-hold-slide sequence (increasing or decreasing hold steps) are as indicated in the legend.

For longer hold durations, the scatter of the data relative to the linear failure envelope increases, which is reflected by the uncertainty of the estimates of the internal friction and cohesion in Fig. 4.6b and c. At this point, it is unclear whether this is purely due to experimental variability, or if the assumed linear Mohr-Coulomb model does not hold for these long hold durations (e.g. due to stress-dependent time evolution of

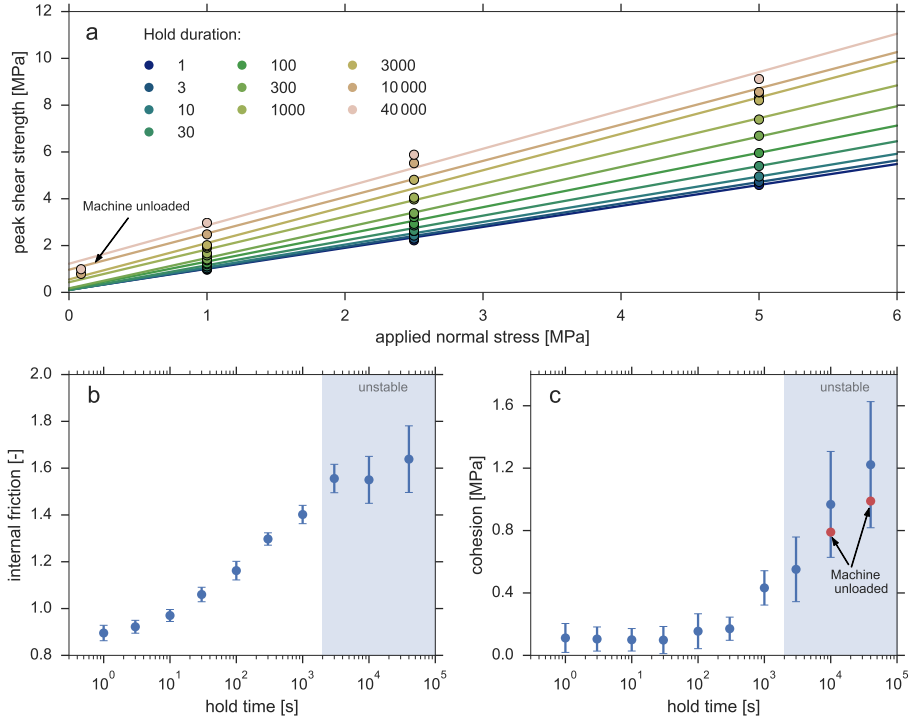

Fig. 4.6: Analysis of the time-dependence of the internal friction coefficient and sample cohesion, as estimated by fitting a Mohr-Coulomb failure envelope to the data. The slope of this linear fit represents the internal friction coefficient, the intercept represents the cohesion. a) Peak shear strength measured during resliding after each hold step, as a function of applied normal stress, and best-fit failure envelopes. Hold durations are indicated in the legend; b) Internal coefficient of friction, as inferred from the slope of the failure envelopes in panel a) as a function of hold time; c) Sample cohesion, as inferred from the intercept of the failure envelopes as a function of hold time. Measurements done while the machine was unloaded are marked in red. Error bars indicate the standard error of the parameter estimates resulting from the regression. The shaded area indicates the region of hold durations after which resliding has been oberved to be unstable.

friction and/or cohesion).

When looking more closely to the inferred internal friction (Fig. 4.6b), we find that it increases non-linearly with the logarithm of the hold duration. For relatively short hold durations (< 3000 s), the evolution is slightly concave-upwards, but for longer hold durations it plateaus (within the uncertainty of the estimate). Conversely, for hold durations < 1000 s, the inferred cohesion (Fig. 4.6c) is small compared to the frictional strength and near-constant in time, but increases rapidly for longer hold durations. The uncertainty of the estimate is relatively large for these longer hold durations, but the measurements made when the machine was unloaded (see Section 4.2.3) fall within the range of uncertainty and support the observed trend. Since the data obtained from unloading the machine are independent of the assumed Mohr-Coulomb failure model, it justifies our choice for a linear failure envelope.

4.5 Numerical results

4.5.1 Initial sliding and hold behaviour

The numerical results for the initial phase of sliding and for the hold phase are displayed in Fig. 4.7. The DEM sample reaches steady-state over a duration of 20 s, characterised by a near-constant frictional strength. The steady-state shear strength of the DEM sample is significantly lower than that of its laboratory counterpart (apparent friction of 0.4 against 0.8, respectively). This discrepancy could partly be attributed to the absence of rolling friction in the model and the convex spherical shape of the particles, as opposed to the angular, possibly concave, grain shape typical of laboratory aggregates (*Anthony and Marone*, 2005; *Guo and Morgan*, 2004; *Mair et al.*, 2002; *Mohamed and Gutierrez*, 2010). Since we are only interested in the evolution of friction and cohesion, and their underlying mechanisms, no attempts are made to match the absolute value of shear strength in the laboratory and numerical experiments.

The DEM sample shows nett dilatation prior to reaching a steady-state shear strength, but turns to nett compaction immediately after that. This behaviour is attributed to localisation, by which the bulk (spectator) region of the gouge continuously

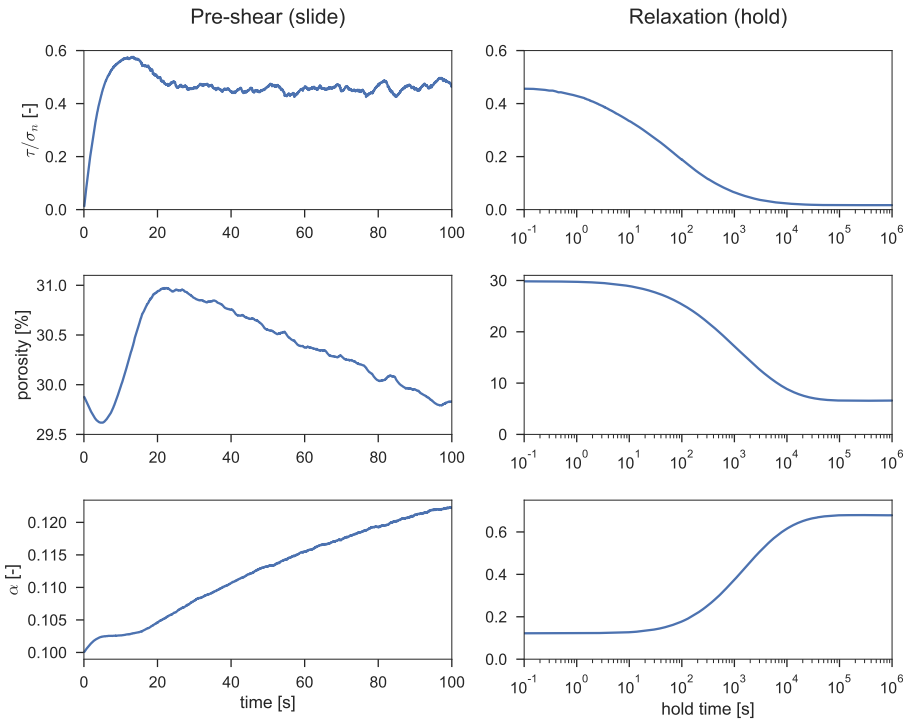

Fig. 4.7: Mechanical data from the DEM slide-hold simulations. Left panels: the apparent coefficient of friction, porosity, and bulk-averaged value of α recorded during the initial sliding phase. Right panels: the same quantities recorded during the hold phase, plotted against the elapsed time since the start of the hold. Note the use of a logarithmic horizontal axis.

compacts by pressure solution in the absence of dilatant granular flow. Similar behaviour is observed in the laboratory experiments (Fig. 4.4). Concurrent with bulk compaction of the DEM sample, we also observe an increase in α during sliding.

After sliding for 100 s, we initiate the hold phase. To be able to clearly display the evolution of shear strength, porosity, and bulk-averaged value of the relative asperity size α, we plot the results against the hold duration on a semi-logarithmic scale in Fig. 4.7. During the hold, the shear stress quickly relaxes, reaching roughly half its

initial value after 30 s, but continuing to decay for the duration of the simulation, albeit extremely slowly after 10 000 s. The relaxation of shear stress is accompanied by sample compaction down to porosities of around 6 %. By the set-up of the model, there is no lower bound on the sample porosity, but further compaction is inhibited by grain boundary evolution, which can arrest pressure solution creep at low porosities (Chapter 3; *Van Noort et al.*, 2008b). The relative size of the contact asperities (α) continuously increases during the hold phase. Prior to a hold duration of 100 s, the value of α remains close to α_0, but rapidly increases after 100 s, approaching its terminal value of $\alpha_c = 0.7$ for hold durations $> 10\,000$ s.

4.5.2 Resliding behaviour

As mentioned in Section 4.3.5, only one simulation is run that comprises the entire hold phase up to 10^6 s, with snapshots being stored at half-decade intervals. Two simulations are initiated from each snapshot, one with no particle cohesion, and one with a particle cohesion of 20 MPa. This procedure ensures that the microstructural state at initiation of sliding is identical for both simulation sets, and allows for a direct assessment of the influence of cohesion. The resliding friction results after each hold duration are reported in Fig. 4.8, showing both the simulations with and without particle cohesion. Hold durations shorter than 10 s result in a peak strength that falls within the variability of frictional resistance of the DEM sample, and could not be measured with sufficient significance. The initial apparent coefficient of friction, as measured at the end of the first sliding phase, is indicated by the horizontal dashed line. From this figure it becomes apparent that for short hold durations ($\Delta t < 10^3$ s), the difference between simulations with and without particle cohesion is small, but the difference in peak strength grows with increasing hold duration. Furthermore, as soon as the effect of cohesion becomes discernible (at about $\Delta t > 10^3$ s), the slip behaviour of the simulations with cohesion changes markedly: the resliding seems to become increasingly more unstable, as evidenced by an overshoot in the stress drop. The simulations without cohesion do not display this behaviour. All of the simulations approach a steady-state friction level that is very similar to that at the end of the initial phase of sliding, independent of the presence of particle cohesion, suggesting

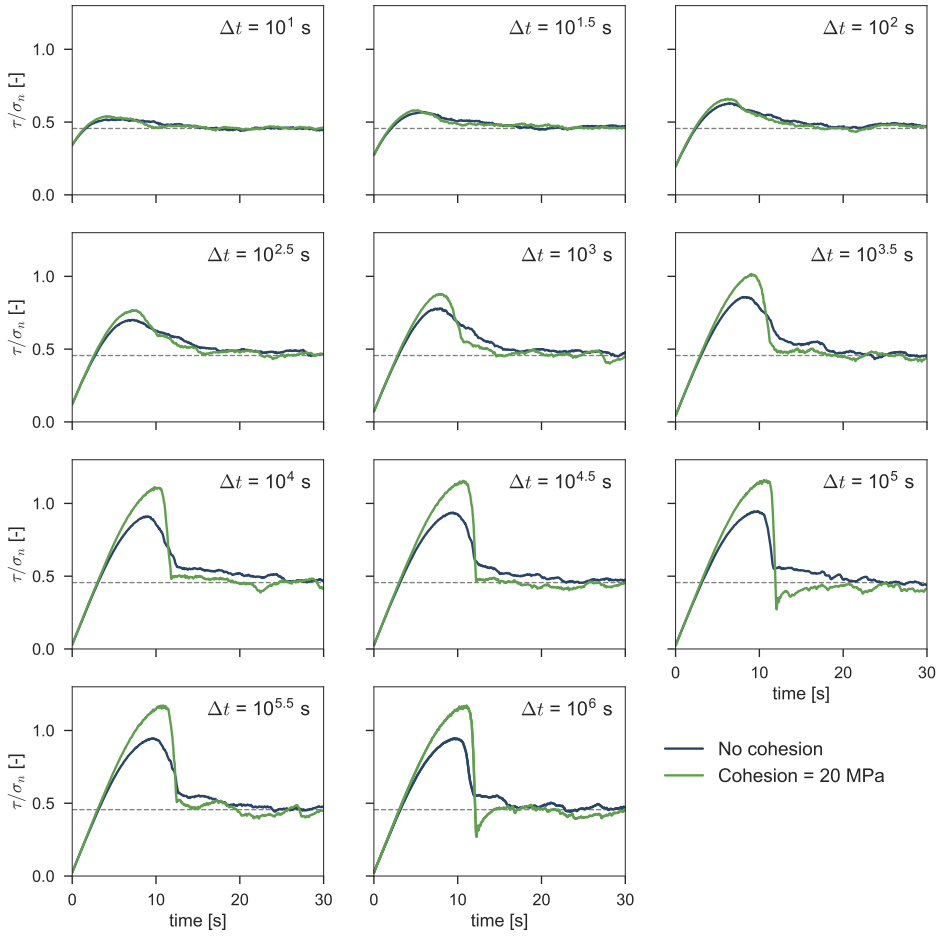

Fig. 4.8: Overview of the resliding behaviour after each hold duration, comparing the simulations with no particle cohesion to those with a particle cohesion of 20 MPa. The black dashed line indicates the apparent coefficient of friction at the start of the hold. Time on the horizontal axis is relative to the start of resliding.

that all macroscopic cohesion has been removed from the actively deforming region of the gouge upon reaching steady-state.

A more detailed overview of the shear stress and porosity data of two selected hold durations, 10^3 s and 10^5 s, is presented in Fig. 4.9. The two simulations (with and without particle cohesion) initiated after a hold of 10^3 s show the same general trends in their frictional and volumetric strain behaviour. By contrast, the two simulations initiated after a hold of 10^5 s show dissimilar behaviour: the simulation without particle cohesion exhibits stable resliding, with a continuous decay of shear stress towards steady-state, and with continuous dilatation. The simulation with particle cohesion shows unstable resliding, with an overshoot in the stress drop, as well as in the porosity, i.e. the sample compacts for a few seconds after the stress drop, before resuming dilatation. This behaviour is very similar to that observed in the laboratory experiments (Fig. 4.4), albeit not as pronounced in the DEM simulations as it is in the laboratory experiments.

4.5.3 Frictional restrengthening

In the same way as the laboratory data was treated, we define the amount of restrengthening for the DEM simulations as the peak strength recorded during resliding, minus the steady-state shear strength attained at the end of the initial sliding phase, expressed as an apparent coefficient of friction (i.e. $\Delta\mu' = \Delta\tau/\sigma_n$). The amount of frictional restrengthening for the DEM simulations with and without particle cohesion are compared with laboratory derived values for the experiments conducted at a normal stress of 5 MPa (u472 and u476) – see Fig. 4.10a. As expected from the observed resliding behaviour (Fig. 4.8), the DEM simulations that include particle cohesion gradually show more restrengthening with increasing hold duration than the simulations without cohesion. The frictional strength of both types of simulations eventually saturate for hold durations longer than 30 000 s. Overall, the DEM simulations show fair agreement with the laboratory data when cohesion is considered.

Because the DEM simulations have been conducted with and without particle cohesion, we can directly assess its effect on restrengthening by considering the difference between the simulation results. Since the simulations with and without cohesion share an identical initial state prior to resliding, we can assume that they exhibit the

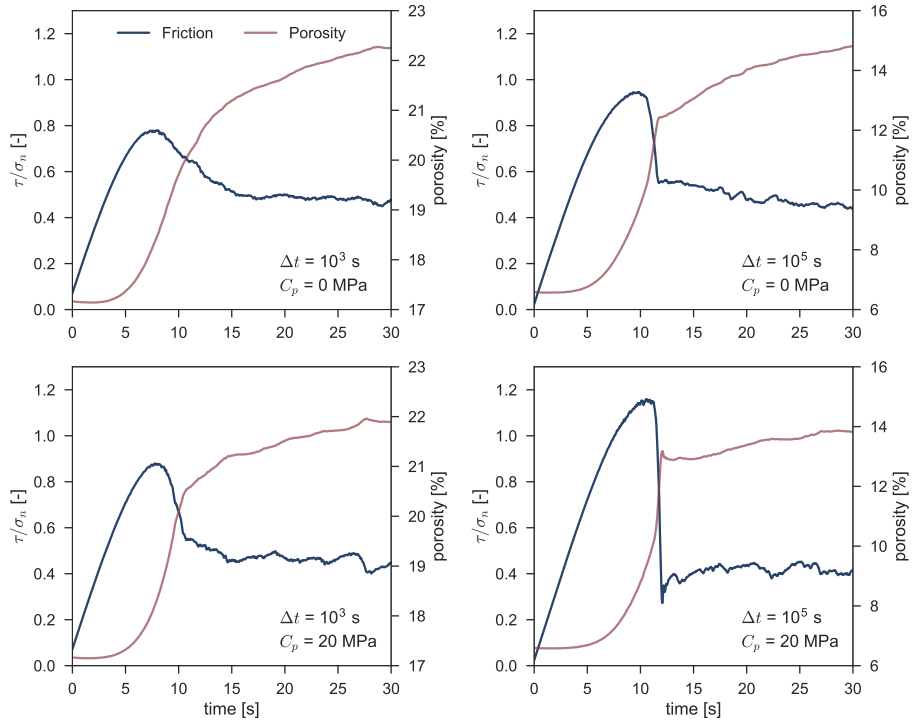

Fig. 4.9: Detailed views of the apparent coefficient of friction and porosity, for two different hold durations ($\Delta t = 10^3$ s and 10^5 s), and for the simulations with and without particle cohesion. Note different scales for the porosity data. Time on the horizontal axis is relative to the start of resliding.

same internal coefficient of friction, and that any differences in peak strength can be attributed entirely to cohesion. Thus, at each hold duration, we take the difference in peak strength of the two sets of simulations as a direct measurement of the macroscopic sample cohesion, which is plotted in Fig. 4.10b alongside the laboratory inferred values using the Mohr-Coulomb intercept method (see Fig. 4.6). Again, there is generally a good agreement between the laboratory and numerical results, showing very similar rates of increase of sample cohesion. Most notably, the sample cohesion only becomes

significant compared to the internal coefficient of friction after hold durations of 300 s, and is near-zero prior to that.

Other quantities that are considered are the amount of shear creep and compaction that were achieved over the hold period (Fig. 4.10c and d). Since pressure solution creep effectively acts as a viscous dashpot, it is expected that the shear creep rates (and corresponding shear stress relaxation) are faster for a higher initial shear stress value. Since the laboratory experiments have a steady-state shear strength that is twice that of the DEM samples, we normalise the total shear stress relaxation $\Delta\tau_c$ by the initial shear stress τ_0 prior to the hold in order to make the comparison. Furthermore, the rate of stress relaxation is sensitive to the effective stiffness of the apparatus. Since we have made no attempt to accurately match the loading stiffness in the DEM simulations with the stiffness of the apparatus used in the laboratory tests, small differences between the two may result in differences in $\Delta\tau_c$. The DEM simulations may have experienced a somewhat larger system stiffness, for it appears to achieve more relaxation for a given hold duration.

In Section 4.2.2 it was noted that the uncertainty in the absolute thickness of the sample layer prevents us from calculating porosities or sample strains from the laboratory data. The comparison of the amount of compaction in the laboratory and DEM tests is therefore done only qualitatively in Fig. 4.10d, comparing the amount of normal displacement Δh in the laboratory test with the porosity loss $\Delta\phi$ in the simulation. To a first order, these two quantities scale proportionally to the sample thickness, which allows us to compare the trends. Qualitatively, the DEM simulations and laboratory experiments show similar trends in the compaction during hold periods. While the DEM simulations show a plateau in compaction for long hold durations (i.e. DEM samples reaching their minimum porosity), it is not clear whether the laboratory data will follow a similar trajectory for longer hold durations. It is, however, expected that the sample will approach its minimum porosity for longer hold times, as compaction cannot continue indefinitely.

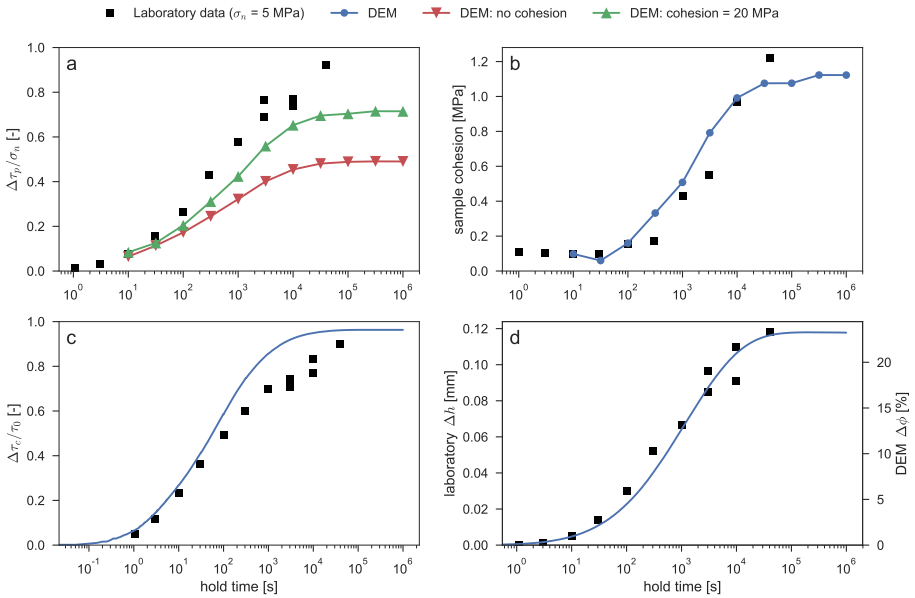

Fig. 4.10: Comparison of the restrengthening behaviour between laboratory and numerical experiments. a) Frictional restrengthening, expressed as $\Delta\tau/\sigma_n$, as a function of hold duration. The DEM simulations are conducted at a normal stress of 5 MPa, and are compared with laboratory data with the same applied normal stress; b) Total shear stress relaxation $\Delta\tau_c$ achieved during the hold period, normalised by the shear stress prior to the hold τ_0; c) Inferred cohesive strength of the sample. The laboratory values are taken from Fig. 4.6, the numerical values are obtained from the difference in peak strength between the simulations with and without particle cohesion (i.e. the difference between the two curves in panel a); d) Total compaction achieved during the hold measured in the experiments (Δh), as compared to the porosity reduction measured in the DEM simulations ($\Delta\phi$).

4.5.4 Localisation of shear strain

Similar to what is observed in the laboratory experiments, the DEM samples show pronounced dilatancy during the initial stage of resliding after a hold duration (compare Fig. 4.4 and 4.9). However, generally not all compaction that was attained during

the hold period is recovered during DEM resliding simulations. Like in the laboratory tests, we attribute this to localisation of shear strain in the DEM simulations. For the laboratory experiments, it is challenging to quantify the degree of localisation directly from the mechanical data, other than by estimating a tendency for either localisation or delocalisation based on the volumetric response of the sample. The DEM simulations, on the other hand, allow access to particle-scale quantities at any moment in time during the simulation, which facilitates the definition of a more precise measure of localisation. To do this, we consider the bulk-averaged value of α, which is calculated during the simulations as:

$$\bar{\alpha}(t) = \frac{1}{N_T} \sum^{N_T} \alpha(t) \tag{4.16}$$

where N_T is the total number of contacts present in the simulation, and $\alpha(t)$ is the instantaneous value of α for a given contact at time t. When resliding is commenced, and granular flow becomes active in the sample, particles that were initially in contact will be separated, and new contacts will form. At the onset of resliding (at $t = 0$), each particle contact will, on average, exhibit a value of α of $\bar{\alpha}(0)$. When contacts are renewed as a result of granular flow, new particle contacts will be initiated with a value of α_0. We can now decompose $\bar{\alpha}(t)$ into a population of bonded particle contacts N_b, and a population of newly formed particle contacts N_n, as:

$$\begin{aligned} \bar{\alpha}(t) &= \frac{1}{N_T} \left(\sum^{N_b} \bar{\alpha}(0) + \sum^{N_n} \alpha_0 \right) \\ &= (1 - \chi)\, \bar{\alpha}(0) + \chi \alpha_0 \end{aligned} \tag{4.17}$$

where $\chi = N_n / N_T$ reflects the number of particle contacts that have been separated by the operation of granular flow, and is therefore a measure of the degree of localisation. Rewriting Eqn. (4.17) for χ gives:

$$\chi = \frac{\bar{\alpha}(0) - \bar{\alpha}(t)}{\bar{\alpha}(0) - \alpha_0} \tag{4.18}$$

If $\chi \to 1$, all particle contacts have been separated and deformation is therefore distributed (averaged in time over the duration of resliding). A value of $\chi \ll 1$ indicates only few particles have been separated, and is suggestive for strong localisation.

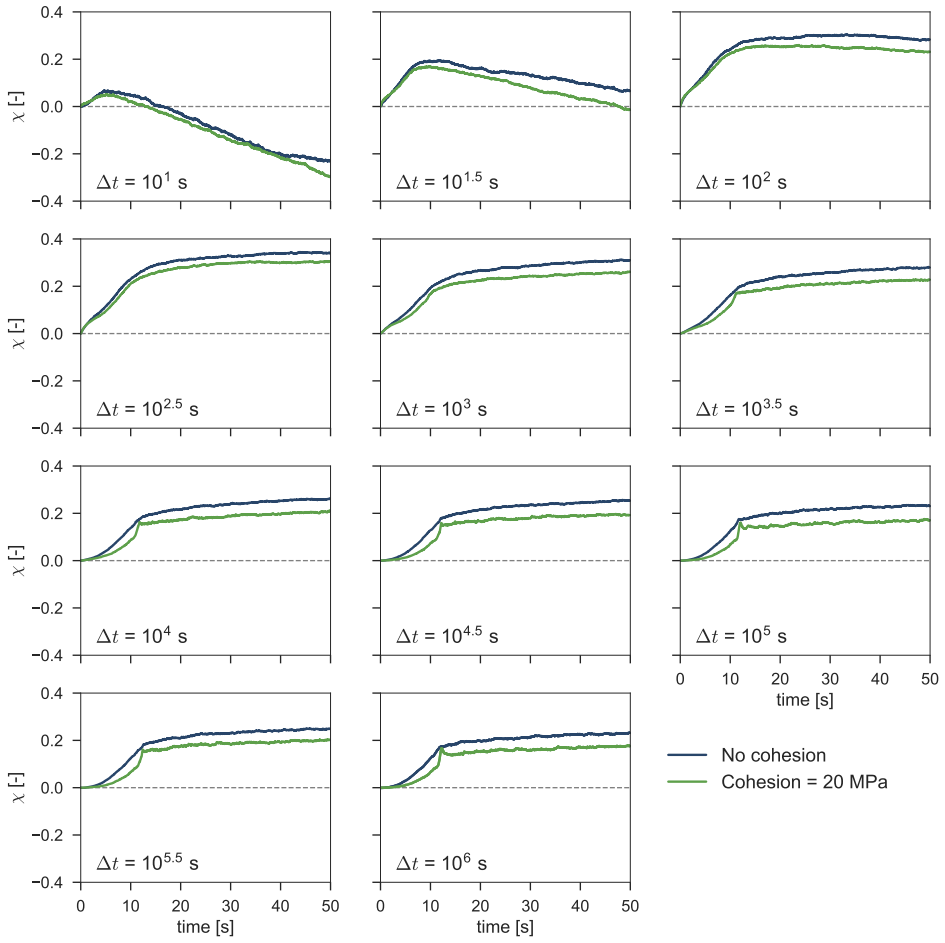

Fig. 4.11: Overview of χ (measure of localisation) calculated during resliding simulations following the hold duration as indicated in each panel. After a hold time of about 100 s, all simulations show virtually the same degree of localisation.

The procedure of assessing the degree of localisation assumes that α increases negligibly slow after forming a new contact compared to the duration of resliding, and that the total number of contacts N_T does not increase. In the case that the overall sample porosity is still high, the increase in α and sample compaction (increase in N_T) are relatively fast on the timescale of resliding (50 s), so that χ becomes negative (as can be seen in Fig. 4.11 for $\Delta t \leq 100$ s). All other resliding simulations following a hold duration $\Delta t > 100$ s all show a similar degree of localisation, with up to 20-30 % of the total number of particle contacts participating in granular flow. The simulations with cohesion systematically show lower values of χ than the simulations without cohesion, though the difference is not substantial.

4.6 Discussion

With the results presented in the previous sections, we can state that there generally exists a good agreement between the restrengthening found in laboratory experiments and in the numerical simulations. This suggests that the laboratory results can be interpreted in terms of the micro-scale physics implemented in DEM (pressure solution, granular flow, and grain boundary evolution). In this section, we will cast our interpretations into a more general framework, applicable to both laboratory and natural faults.

4.6.1 Comparison with previous work

The rate of frictional restrengthening observed in slide-hold-slide experiments conducted on (wet) granular halite is generally of the order of 0.1-0.3 decade^{-1} (*Bos and Spiers*, 2002a; *Niemeijer et al.*, 2008), being at least one order of magnitude faster than quartz at similar conditions (*Niemeijer et al.*, 2008; *Yasuhara et al.*, 2005). Our results display rates falling in a similar range, from 0.25 decade^{-1} for hold durations 1000 s or a normal stress of 5 MPa, and up to 0.5 decade^{-1} for hold durations 1000 s and a normal stress of 1 MPa (see Fig. 4.5). The rate of restrengthening cannot be captured by a single log-linear relation. Rather, the data suggest either a bi-linear (e.g. *Niemeijer et al.*, 2008; *Yasuhara et al.*, 2005) or power-law evolution (e.g. *Carpenter et al.*, 2014; *Ikari*

et al., 2016b). Furthermore, the applied normal stress (σ_n) seems to have no effect on the restrengthening behaviour for hold durations < 1000 s. For hold durations longer than 1000 s, samples subjected to lower σ_n show faster apparent restrengthening.

At first, this behaviour appears counter-intuitive, considering that all samples display a similar amount of compaction achieved for a given hold phase, as measured by the local LVDT (Fig. 4.5b). Since densification has been positively correlated to gouge strength (*Karner and Marone*, 2001; *Richardson and Marone*, 1999), it is to be expected that all samples show a similar degree of restrengthening for each hold duration. However, by expressing the frictional restrengthening in terms of an apparent friction coefficient ($\Delta\tau/\sigma_n$), it is implicitly assumed that cohesion is negligible. When this assumption is violated, the contribution of cohesion to the total shear strength is underestimated, and this underestimation increases with increasing normal stress:

$$\mu' = \frac{\mu\sigma_n + C_s}{\sigma_n} = \mu + \frac{C_s}{\sigma_n} \tag{4.19}$$

Therefore, experiments performed under low σ_n will receive a larger contribution from cohesion to the apparent friction coefficient, and will thus appear to strengthen faster for a given rate of increase of C_s. The strengthening rate observed in experiments performed at various σ_n start to diverge after a hold duration of 1000 s, which coincides with the onset of increasing C_s. The timing of this onset may be related to the time that is required to form cohesive contacts that are not immediately destroyed during the reloading after a hold period. Moreover, the equilibrium criterion proposed by *Van Noort et al.* (2008b) (Eqn. (4.9)) predicts a critical value of aggregate porosity below which asperity growth initiates, possibly explaining the observation of a rapidly increasing aggregate cohesion for hold durations longer than 300 s.

4.6.2 Localisation in laboratory and numerical experiments

The recovery of volumetric strain (λ) as calculated for the laboratory experiments, shows a decreasing tendency for nett compaction with increasing experiment duration. During a given hold phase, both the active (localised) and spectator regions in the gouge will densify, but during resliding only the active region will dilate to restore its initial gouge

porosity. A value of $\lambda < 1$ accordingly indicates that shear deformation is localised, and that compaction in the spectator regions is dominant over to the volumetric strain of the active regions in the gouge. As the spectator regions densify and compaction slows down in the approach to zero porosity, λ tends to 1 (no nett compaction). Moreover, when the volume of gouge that contributes to shear deformation increases (i.e. if shear delocalisation occurs), then gouge dilation exceeds the near-zero compaction of the spectator region, so that $\lambda > 1$.

In this view, we can interpret the volumetric strain behaviour as observed in the laboratory experiments. During initial stages of the experiments, shear deformation is localised and the spectator region compacts at a substantial rate compared to the volumetric strains in the active region, so that $\lambda \ll 1$. Over the course of the experiment, the spectator region densifies and compaction decelerates, resulting in an increase in λ, approaching a neutral value of 1. During the decreasing hold duration sequence, reworking of the gouge leads to $\lambda > 1$. These interpretations are, however, merely exhibitive. For a number of resliding phases, no steady-state sample thickness is achieved over the duration of resliding, with the sample still dilating at the moment that the next hold phase is commenced, underestimating λ. If a longer duration of resliding was chosen, the resulting trends in λ may have been different. Regardless, the frictional restrengthening of the sample ($\Delta\tau$) does not show any effects of sliding history, as similar values are obtained for both the increasing and decreasing hold duration sequences (Fig. 4.5a), which indicates that the frictional strength is insensitive to the evolution of localised regions in the gouge.

In contrast to the laboratory experiments, the DEM simulations show a clear and consistent picture for the evolution of χ after hold durations of 100 s, with each simulation indicating that 20-30 % of the initial gouge volume is reworked by granular flow. In simulations with $C_p > 0$, the values of χ are systematically lower than in simulations with $C_p = 0$, which suggests that shear deformation is somewhat more localised in cohesive aggregates. Since more mechanical work is required to separate a cohesive particle contact than for an incohesive contact, it is expected that fewer particles can be incorporated into the actively deforming region of the aggregate when the particle contacts exhibit cohesive strength.

Laboratory and natural fault gouges exhibit features that are generally not con-

sidered in DEM simulations, such as non-convex grain shapes, grain comminution, and recrystallisation. It is therefore unlikely that the microstructural results from DEM simulations are representative for real-world aggregates, and so the observations from DEM tests need to be interpreted with this in mind. Nonetheless, DEM may be used to isolate contributions from specific controlling factors (such as cohesion) on the localisation behaviour, in a way that cannot be accomplished in laboratory tests, of which the results are convoluted with contributions from various mechanisms.

4.6.3 Mechanisms for time-dependent restrengthening

In previous studies it has been inferred that pressure solution and granular flow are both dominant deformation mechanisms in halite aggregates subjected to the experimental conditions imposed in this study (*Bos et al.*, 2000a; *Niemeijer and Spiers*, 2006; *Takahashi et al.*, 2017). In our numerical simulations, these two mechanisms are the only permanent deformation mechanisms that have been implemented, which fully excludes e.g. crystal plasticity and microcracking that may have played a second-order role in the laboratory tests. Hence, for this discussion we focus entirely on strain accommodation by pressure solution and granular flow. These two mechanisms have been closely considered by *Niemeijer and Spiers* (2007) and *Chen and Spiers* (2016), and are described by a microphysical model framework which we will refer to as the *Chen-Niemeijer-Spiers* ("CNS") model. In short, the CNS model assumes that the imposed deformation is fully accommodated by parallel operation of dilatant granular flow, and non-dilatant pressure solution creep. The competition between these mechanisms controls the overall microstructural state (porosity) of the gouge, and produces a wide range of frictional behaviour (see e.g. Chapter 5; *Van den Ende et al.*, 2018a; *Verberne et al.*, 2017). We will interpret the outcomes of the laboratory and numerical experiments in this framework.

First of all, we consider the time-dependence of the internal coefficient of friction (μ). In the CNS model, the strength of an aggregate is controlled by its porosity through the average dilatancy angle $\tan\psi$ as (*Chen and Spiers*, 2016; *Niemeijer and Spiers*, 2007):

$$\mu = \frac{\tilde{\mu} + \tan\psi}{1 - \tilde{\mu}\tan\psi} \tag{4.20}$$

where $\tilde{\mu}$ is the coefficient of friction of a single grain-grain contact. For the purpose of this discussion, $\tilde{\mu}$ can be taken to be constant. The dilatancy angle describes the amount of dilatation per unit shear displacement associated with neighbour swapping and grain sliding, and is a common notion to soil mechanics (*Paterson*, 1995; *Vermeer and De Borst*, 1984). During a hold period, the gouge undergoes time-dependent compaction by pressure solution, through which $\tan\psi$ increases. As a result, the overall internal friction coefficient of the aggregate increases with time, giving rise to the observed time-dependence of friction. The maximum value of μ is achieved when the porosity reaches zero (or a small minimum value). This further implies a limit to the internal coefficient of friction that can be attained during a seismic cycle, if gouge compaction is the only restrengthening mechanism. This is clearly observed in the DEM simulations (Fig. 4.10a).

It is important to realise that in the above discussion, $\tilde{\mu}$ is taken to be constant. This is in strong contrast to previous notions that the time-dependence of fault strength stems from an intrinsic elevation of asperity contact strength through plastic creep or asperity welding (*Brechet and Estrin*, 1994; *Dieterich and Kilgore*, 1994; *Scholz*, 2002). In the view of *adhesion theory of friction* (and rate-and-state friction by association; *Putelat et al.*, 2011), the internal coefficient of friction at a macroscopic scale is directly related to the 'quality' of micro-scale asperity contacts. In our laboratory experiments, it cannot be excluded that the intrinsic friction of the grain-grain contacts increases in a manner that is envisioned by adhesion theory. However, in the DEM simulations, the particle coefficient of friction (the quality of contact) is taken to be constant, yet similar strengthening rates are observed in the numerical simulations as in the laboratory tests. In the absence of a variable contact strength in the DEM simulations with $C_p = 0$, the strengthening during a hold period can only result from an increase in the dilatancy angle, as described by the CNS model. The correspondence between the laboratory experiments, numerical simulations, and CNS microphysical model indicates that for granular gouges undergoing time-dependent compaction, asperity creep is not required to explain the observed time-dependent restrengthening.

The second mechanism for time-dependent restrengthening that is proposed in this work, is an increase in cohesion resulting from a nett increase in asperity contact size, driven by excess surface energy. This mechanism conceptually shares similarities

with adhesion theory mentioned above: the intrinsic shear strength of an individual grain contact increases by growth of contact asperities. However, in this study we interpret asperity growth to contribute to sample cohesion rather than to internal friction. Moreover, the mechanism by which asperity growth is modelled here (fluid-assisted diffusive mass transfer) is notably different from plastic creep, which is the dominant mechanism considered in adhesion theory.

Although both the internal friction coefficient and cohesion contribute to the overall shear strength of a material, it is important to distinguish between these two components when the magnitude of the effective normal stress is relevant for the problem that is considered. While at high effective normal stress the contribution of friction exceeds that of cohesion, cohesion may play a dominant role in the strengthening under relatively low effective normal stress conditions, such as shallow focus earthquakes. The stress drop associated with (induced) earthquakes in e.g. geological reservoirs may receive a significant contribution from cohesion. To assess whether or not the development of cohesion is efficient under in-situ fault conditions, it is important to consider the specific micro-mechanisms, of which the relevance in nature can be assessed independently of the laboratory results.

4.6.4 Operation of grain boundary evolution in nature

The laboratory experiments presented in this work are conducted under conditions for which grain boundary evolution and fluid-assisted asperity growth are known to operate (*Hickman and Evans*, 1991, 1992; *Renard et al.*, 2012; *Schutjens and Spiers*, 1999; *Visser*, 1999; *Zubtsov et al.*, 2004). However, it is expected that the initiation of grain boundary evolution (i.e. the balance between nett asperity growth and contraction) is controlled by the effective stress supported by the contact (Eqn. (4.9); *Van Noort et al.*, 2008b), and so it can be questioned whether or not grain boundary evolution operates in natural faults at seismogenic depths. The laboratory results obtained by *Beeler and Hickman* (2015) demonstrate that grain boundary evolution still operates in quartz-quartz interfaces at elevated temperature (up to 530 °C) and fluid pressure (up to 150 MPa), for an applied effective contact stress of at least 2 MPa. This demonstrates

that, in principle, grain boundary evolution may operate at hydrothermal conditions if the contact stress is sufficiently low.

To a first order, we can assess the effective stress at which grain boundary evolution will initiate as (*Van Noort et al.*, 2008b):

$$\sigma_{crit} = 2\alpha_0 \sqrt{E \frac{\gamma_{sl}}{S} \Delta \cos \frac{\theta}{2}} \tag{4.21}$$

where σ_{crit} is the effective normal stress acting over the grain contact. For quartz at temperatures in the range of 250-300 °C (lower seismogenic zone conditions), we take $\gamma_{sl} = 0.145$ J m^{-2} (*Hiraga et al.*, 2002), $E = 76.5$ GPa, and $\Delta \cos(\theta/2) = 0.17$ (*Holness*, 1992). When we take $\alpha_0 = 0.05$ and the value of S to lie in the range of 10-100 nm (*Nakashima*, 1995; *Van Noort et al.*, 2008b), we then obtain a range of σ_{crit} of 13.7-43.4 MPa below which grain boundary evolution may operate. At low gouge porosities, the stress intensity factor on the individual grain contacts is relatively small (of order 1), so that these values of σ_{crit} may be taken as estimates for the overall fault effective normal stress. Fluid pressures at seismogenic depths are believed to be elevated from hydrostatic, possibly approaching lithostatic values (*Rice*, 1992; *Sibson*, 1990; *Suppe*, 2014), which makes grain boundary evolution feasible even at seismogenic depth intervals. Moreover, at the above-mentioned effective stresses, a cohesive strength of 1 MPa would, if removed, correspond to a drop in apparent friction coefficient of 0.02-0.07. In the case of fault reactivation, removal of cohesion could counteract an increase in fault strength due to velocity-strengthening friction, facilitating a frictional instability even under velocity-strengthening conditions.

It should be remarked that grain boundary evolution is inhibited by a large incompatibility in lattice structure (*Beeler and Hickman*, 2015; *Hickman and Evans*, 1992; *Zubtsov et al.*, 2004), particularly for bi-mineral interfaces. It is therefore expected that grain boundary evolution is less efficient or even absent in polymineralic gouge materials. For heterogeneous gouge compositions (as commonly seen in nature; *Boulton et al.*, 2012; *Bullock et al.*, 2014; *Holdsworth et al.*, 2011), this reduces the potential for cohesion development during the seismic cycle by grain boundary evolution. However, other mechanisms, such as mineral precipitation from the pore fluid, may still be viable. Field evidence suggests that faults develop cohesion during the interseismic period

(*Boulton et al.*, 2012; *Demurtas et al.*, 2016; *Jones et al.*, 2002), and that cohesion needs to be considered regardless of the underlying mechanism.

4.6.5 Implications for the seismic cycle

We now follow the interpretations above to discuss the restrengthening and stability of natural faults. During the interseismic period fault slip rates are relatively low, and so the fault compacts by pressure solution creep and increases its strength. Simultaneously, far-field tectonic loading increases the stress on the fault. The instability (earthquake or slow slip event) occurs when the stress supported by the fault exceeds its strength, after which the fault accelerates, dilates, and weakens. For a given tectonic loading rate, the recurrence time and stress drop are therefore controlled by the rate of compaction (and the rate of cohesion development).

This leaves now three possible scenarios: in the first scenario, compaction and fault strengthening are relatively slow (compared to the tectonic loading rate). The gouge compacts during the interseismic period, but does not reach its minimum (near-zero) porosity before the next seismic event. This means that the fault continuously strengthens over time, but at a rate that, on the long-term, is lower than the tectonic stressing rate. This is a scenario that is typically considered in studies employing rate-and-state friction, where the state parameter (usually denoted by θ) and corresponding fault strength are allowed to increase indefinitely, but at a log-linear rate that is ultimately slower than the linear stressing rate.

Based on the results presented here, as well as those by previous studies (*Carpenter et al.*, 2014; *Ikari et al.*, 2016b; *Niemeijer et al.*, 2008), it cannot be excluded that faults strengthen more rapidly than the stressing rate, e.g. when considering a power-law relation with a time-exponent $n > 1$. In this second scenario, a limit to the maximum attainable fault strength (c.f. *Carpenter et al.*, 2014) is required for an earthquake to recur on a given fault patch. For granular gouges, this limit corresponds to a fully densified (i.e. minimum porosity) microstructural state, with additional grain cementation. The failure strength of a fully densified gouge must still remain at or below the failure strength of the surrounding host rock in order to achieve failure within the gouge itself (i.e. the fault must be weak relative to its surroundings; *Rice*, 1992). A

scenario of rapid restrengthening is increasingly more appropriate for faults segments at greater depth, as aggregate compaction and strengthening rates generally increase with increasing temperature and pressure (*Chen et al.*, 2015a; *Tenthorey and Cox*, 2006; *Yasuhara et al.*, 2005). It further implies that the recurrence time is one-sidedly controlled by the tectonic loading rate, as the strength of the fault has reached a constant value well before the failure stress is reached.

Lastly, a third scenario can be considered where fluid-rock interactions are slow, but tectonic loading is virtually absent (such as in an intraplate setting). In this situation, a fault remains unperturbed for an extended period of time (e.g. millions of years), over which it acquires a given amount of shear strength. If the state of stress around the fault is perturbed, for example by human subsurface activities of injection or extraction of fluids, then an instability may be triggered when the stress supported by the fault exceeds its current strength. Whether or not this instability is succeeded by subsequent events would depend on the present-day rate of restrengthening relative to the perturbed loading rate. In other words, reactivation of faults that have been inactive for long geological time periods may not necessarily lead to repeated seismic activity of similar intensity. The question of prolonged induced seismicity may be addressed by considering the strength of the fault prior to reactivation, as well as the present-day strengthening rates at in-situ conditions. Furthermore, the stress drop associated with fault reactivation likely includes loss of cohesion, which is often neglected in numerical studies of fault reactivation. To assess how much cohesion contributes to the total shear strength of a material, laboratory failure tests should be performed (e.g. *Jones et al.*, 2002).

The example scenarios above now highlight the relevance of explicitly considering the micro-mechanics of friction. On the basis of commonly used rate-and-state friction or linear slip weakening formulations, it cannot be assessed what the maximum strength of a fault will be, or how the fault will behave after reactivation. By relating the overall mechanics of a fault to the relevant micro-scale processes, hypotheses and predictions may be formulated that can be tested in a field or laboratory setting. In this study, granular flow, pressure solution, and nett asperity growth were thought to constitute the overall mechanical response of the aggregate, but other mechanisms (e.g. microcracking, mineral precipitation) could be treated in a similar fashion, and provide insight into

the restrengthening behaviour of a particular fault of interest. Adopting appropriate constitutive relations for the microphysical processes then allows for a quantitative analysis of the seismic cycle and coseismic stress drop based on physical principles (e.g. *Van den Ende et al.*, 2018a, see also Chapter 5).

4.7 Summary and conclusions

In this work, we report a suite of slide-hold-slide laboratory experiments conducted on granular halite, from which we inferred the time-dependence of the internal coefficient of friction and of the sample cohesion independently. This was done by treating the second sliding phase as a Mohr-Coulomb failure process, and measuring the peak stress as a function of the imposed normal stress. In these experiments, we found that:

- The frictional restrengthening, measured as an increase of the apparent coefficient of friction (i.e. $\Delta\mu' = \Delta\tau/\sigma_n$), increases non-linearly with the logarithm of hold time, showing a concave-up strength evolution in a semi-logarithmic representation. For hold durations > 1000 s, the restrengthening rates seem to decrease with increasing applied normal stress, which alludes to the presence of cohesion.
- Both the internal friction coefficient and sample cohesion increase with the duration of the hold phase, contributing to the overall frictional restrengthening. However, these two quantities do not share a common trend. The internal coefficient of friction increases rapidly at first, but levels off for hold durations over 3000 s. By contrast, the sample cohesion is inferred to be negligible for hold durations < 1000 s, with a rapid increase for longer durations. As a result the total shear strength (i.e. $\tau = \mu\sigma_n + C_s$) continues to increase with time.
- For long hold durations, the sample shows unstable resliding behaviour, characterised by an overshoot in stress drop and dilatation, and is accompanied by an audible acoustic emission. The occurrence of unstable resliding is correlated in time with the inferred presence of sample cohesion.

In an attempt to explain these observations, we employed the Discrete Element Method (DEM) to simulate the laboratory experiments, incorporating granular flow and pressure solution operating concurrently with structural evolution of stress grain boundaries as micro-scale mechanisms for time-dependent restrengthening. The simulations revealed that:

- For short hold durations (< 3000 s), simulations with and without time-dependent particle cohesion display the same behaviour. For longer hold durations, the addition of cohesion results in higher peak frictional strength after a given hold. Moreover, simulations with particle cohesion started to exhibit unstable resliding, characterised by the same criteria as for the laboratory experiments.
- The rate of restrengthening, as observed in the DEM simulations with cohesion, agrees well with that found in the laboratory experiments conducted under the same conditions. Also, the time-evolution of sample cohesion inferred from the DEM simulations is consistent with the laboratory experiments. This suggests that the microphysical processes responsible for the observed laboratory behaviour were captured well by the numerical simulations.

From the laboratory and numerical experiments, we conclude that time-dependent fault strengthening is facilitated by compaction by pressure solution, and by grain cementation by nett asperity growth, driven by excess surface energy stored in the grain boundary. The former mechanism is thought to be primarily responsible for the time-dependence of the internal friction coefficient, while the latter is thought to be responsible for the observed time-dependence of sample cohesion. The combined strengthening effect of these two mechanisms controls the overall frictional stability of the fault, as seen in both the laboratory experiments and the DEM simulations.

Lastly, by adopting a microphysical standpoint, laboratory observations of fault friction and restrengthening can be interpreted in terms of the grain-scale mechanisms. In this way, the challenge of extrapolating laboratory results to natural scales and conditions can be addressed. While the spatial and temporal scales typical for laboratory tests are dwarfed by those typical for natural faults, the processes that constitute the mechanical behaviour are scale-independent. The implementation of micro-mechanical

constitutive relations into numerical simulators may be used to further investigate the mechanics of frictional sliding over scales and conditions beyond those of a laboratory setting.

Chapter 5

A comparison between rate-and-state friction and microphysical models, based on simulations of fault slip

Martijn P. A. van den Ende, Jianye Chen,
Jean-Paul Ampuero, and André R. Niemeijer

Published in: *Tectonophysics* 733, 2018

doi:10.1016/j.tecto.2017.11.040

Abstract

Rate-and-state friction (RSF) is commonly used for the characterisation of laboratory friction experiments, such as velocity-step tests. However, the RSF framework provides little physical basis for the extrapolation of these results to the scales and conditions of natural fault systems, and so open questions remain regarding the applicability of the experimentally obtained RSF parameters for predicting seismic cycle transients. As an alternative to classical RSF, microphysically-based models offer means for interpreting laboratory and field observations, but are generally over-simplified with respect to heterogeneous natural systems. In order to bridge the temporal and spatial gap between the laboratory and nature, we have implemented existing microphysical model formulations into an earthquake cycle simulator. Through this numerical framework, we make a direct comparison between simulations exhibiting RSF-controlled fault rheology, and simulations in which the fault rheology is dictated by the microphysical model. Even though the input parameters for the RSF simulation are directly derived from the microphysical model, the microphysically-based simulations produce significantly smaller seismic event sizes than the RSF-based simulation, and suggest a more stable fault slip behaviour. Our results reveal fundamental limitations in using classical rate-and-state friction for the extrapolation of laboratory results. The microphysically-based approach offers a more complete framework in this respect, and may be used for a more detailed study of the seismic cycle in relation to material properties and fault zone pressure-temperature conditions.

5.1 Introduction

The destructive potential of earthquakes poses major societal challenges, and thus calls for a deep understanding of the underlying mechanics for reliable seismic hazard assessment. In order to better apprehend both natural and induced seismicity, much laboratory work is aimed at characterising the frictional behaviour of rock materials, or of their analogues. The microstructures produced by laboratory deformation tests can then be compared with those retrieved from natural outcrops to augment the interpretation of the laboratory results. Both the macroscopic mechanical behaviour and the formation of the fault zone microstructure are controlled by the micro-scale deformation mechanisms that accommodate (shear) strain (*Niemeijer and Spiers*, 2006). Thus, extrapolation of laboratory results to the spatial and temporal scales of natural faults may be facilitated through the study and quantification of micro-scale processes, provided that they operate within natural faults at the relevant pressure and temperature conditions.

Most commonly, the laboratory friction data are described in the framework of rate-and-state friction (RSF), which provides empirical relations between the measured coefficient of friction (μ), rate of deformation (V), and 'state' (θ). While some variations exist, the most widely used functional form reads (*Dieterich*, 1979; *Ruina*, 1983):

$$\mu(V,\theta) = \mu^* + a \ln\left(\frac{V}{V^*}\right) + b \ln\left(\frac{V^*\theta}{D_c}\right) \tag{5.1}$$

where μ^* is a reference coefficient of friction measured at sliding velocity V^*. The parameters a and b are proportionality constants for the magnitudes of the instantaneous 'direct' and time-dependent 'evolution' effects, respectively, and are thought to represent material properties. The characteristic slip distance D_c controls the slip distance over which the evolution towards the new steady-state takes place. The evolution of the state parameter θ is formulated either by the 'ageing law' (Eqn. 5.2a; *Dieterich*, 1979)

or 'slip law' (Eqn. 5.2b; *Ruina*, 1983):

$$\frac{\mathrm{d}\theta}{\mathrm{d}t} = 1 - \frac{V\theta}{D_c} \tag{5.2a}$$

$$\frac{\mathrm{d}\theta}{\mathrm{d}t} = -\frac{V\theta}{D_c} \ln\left(\frac{V\theta}{D_c}\right) \tag{5.2b}$$

At steady-state, both state evolution laws reduce θ to D_c/V, so that the steady-state coefficient of friction can be simply expressed as:

$$\mu_{ss}(V) = \mu^* + (a-b) \ln\left(\frac{V}{V^*}\right) \tag{5.3}$$

The parameter $(a-b)$ now describes the velocity-dependence of μ at steady-state, with positive values (i.e. $a > b$) resulting in velocity-strengthening, and negative values resulting in velocity-weakening behaviour. It has been demonstrated by *Ruina* (1983) that a material characterised by a negative $(a-b)$ is prone to frictional instabilities, i.e. stick-slip behaviour, and thus it is assumed that seismogenic fault segments exhibit a negative $(a-b)$.

Combined with Eqn. (5.2), Eqn. (5.1) yields a versatile relation that describes a wide range of laboratory data (e.g. *Blanpied et al.*, 1998; *He et al.*, 2016; *Leeman et al.*, 2015; *Marone*, 1998). Numerous experimental studies report values of RSF parameters for natural (*Boulton et al.*, 2012, 2014; *Carpenter et al.*, 2009, 2014; *Collettini et al.*, 2011; *Niemeijer et al.*, 2016; *Niemeijer and Vissers*, 2014; *Sawai et al.*, 2016; *Tesei et al.*, 2014) and synthetic gouges (*Blanpied et al.*, 1991, 1995, 1998; *Carpenter et al.*, 2009; *Chester*, 1994; *Chester and Higgs*, 1992; *Den Hartog et al.*, 2012, 2013; *He et al.*, 2013, 2007; *Ito and Ikari*, 2015; *Saffer and Marone*, 2003; *Verberne et al.*, 2015), as well as for analogue materials (*Buijze et al.*, 2017; *Leeman et al.*, 2015; *Takahashi et al.*, 2017). The RSF parameters (a, b, and D_c) obtained from laboratory experiments then serve as an input for numerical modelling studies (e.g. *Kaneko et al.*, 2017; *Lapusta and Rice*, 2003). Typical values for $(a-b)$ reported by experimental studies lie in the range of $\pm 10^{-3}$-10^{-2} (e.g. *Boulton et al.*, 2014; *Chester*, 1994; *Den Hartog et al.*, 2012, 2013; *He et al.*, 2007; *Scholz*, 2002), although much larger values have been reported up to $+0.15$ by *Blanpied et al.* (1998), and down to -0.05 by *Takahashi et al.*

(2017), −0.2 by *Buijze et al.* (2017), and −0.16 by *Fortt and Schulson* (2009). Most of these experimental studies reveal a dependence of the obtained RSF parameters on experimental conditions, including (but not limited to) ambient temperature (*Blanpied et al.*, 1991, 1995, 1998; *Chester and Higgs*, 1992; *Den Hartog et al.*, 2012, 2013; *He et al.*, 2013, 2007; *Sawai et al.*, 2016; *Verberne et al.*, 2015), deformation rate (*Carpenter et al.*, 2016a; *Collettini et al.*, 2011; *Den Hartog et al.*, 2012; *Reinen et al.*, 1992; *Tesei et al.*, 2014), imposed normal stress (*Carpenter et al.*, 2016a; *Chester*, 1994; *Sawai et al.*, 2016), and pore fluid chemistry (*Feucht and Logan*, 1990; *Hunfeld et al.*, 2017).

When considering a wide range of conditions, covered either fully or partially by each of the aforementioned studies, at least three regimes of velocity-dependence of friction can be observed: at low imposed velocities or high ambient temperatures, the gouge material is often found to exhibit velocity-strengthening behaviour with very high positive values of $(a - b)$ as compared to room temperature conditions (e.g. *Blanpied et al.*, 1998; *Den Hartog et al.*, 2012), which has been attributed to ductile or plastic creep (*Bos and Spiers*, 2002b; *Noda and Shimamoto*, 2010; *Reinen et al.*, 1992; *Shimamoto*, 1986). At intermediate velocities and temperatures, a transition is made into the velocity-weakening regime with $(a - b) < 0$ (e.g. *Blanpied et al.*, 1998; *Den Hartog et al.*, 2012; *He et al.*, 2007), characterised by an increasingly more porous and cataclastic microstructure with increasing sliding velocity (*Niemeijer and Spiers*, 2006). At high velocities or low temperatures, most gouges again exhibit (mildly) velocity-strengthening friction (e.g. *He et al.*, 2007; *Marone et al.*, 1990; *Sawai et al.*, 2016). Finally, several mechanisms have been identified to cause intense frictional weakening at coseismic slip velocities, which could be interpreted as an additional stage of velocity-weakening in the dynamic regime (see *Niemeijer et al.*, 2012; *Tullis*, 2007, and references therein). The full range of frictional behaviour that is expected to feature on large faults during the seismic cycle, from low-velocity creep to high-velocity dynamic weakening, is reported for halite by *Buijze et al.* (2017).

In spite of its inherent versatility, classical rate-and-state friction is not able to capture the full extent of frictional behaviour observed in experiments with a single set of parameters. To account for transitions from velocity-strengthening to -weakening (and vice versa), the classical RSF framework has been modified and extended, for example by coupling of the RSF equations with a creep law (*Noda*, 2016; *Noda and*

Shimamoto, 2010, 2012), or by introduction of a cut-off velocity (e.g. *Okubo*, 1989; *Shibazaki and Iio*, 2003). However, the modified RSF relations remain (mostly) empirical and do not offer a physical explanation for many experimental observations, such as the dependence of RSF parameters on the imposed normal stress, or the presence of a reactive fluid. This inhibits the extrapolation of laboratory results to the spatial- and temporal scales of natural faults. Particularly, since most experimental work focusses on the near-steady state behaviour of faults, it can be questioned whether or not the RSF parameters derived from these experiments can be applied to describe the full seismic cycle, including all of its transient features observed in nature.

As an alternative approach, microphysically-based models may provide us with a more solid basis for the extrapolation of laboratory results, since the dependence of their input parameters on thermodynamic quantities (temperature, pressure, state of stress) can be either predicted or constrained by laboratory and field observations. In recent years, several attempts have been made to derive such microphysical models and to use these to explain the seismogenic potential of faults (*Den Hartog and Spiers*, 2014; *Ikari et al.*, 2016a; *Noda*, 2008; *Perfettini and Molinari*, 2017; *Putelat et al.*, 2011; *Sleep*, 2005, and others). The microphysical models hold a major advantage over empirical models, in that their assumptions have a clear physical interpretation, so that the validity of the assumptions, and the applicability and limitations of the model can be evaluated. Moreover, some microphysical models provide a coupling with experimental or field observations through predictions pertaining to the microstructure, in addition to a predicted macro-mechanical response (e.g. *Den Hartog and Spiers*, 2014; *Niemeijer and Spiers*, 2007). However, the constitutive relations given by microphysical models are often highly simplified in order to arrive at closed-form expressions, and generally do not match the heterogeneity and geometrical complexity of natural faults.

To address the issue of upscaling, numerical seismic simulators are commonly employed. These numerical frameworks often handle non-uniform distributions of fault properties, fault slip, and stress, and are used for studying the non-steady state behaviour of natural faults. Examples include fully- and quasi-dynamic rupture propagation (*Thomas et al.*, 2014; *Zheng and Rice*, 1998), the statistics and scaling of (sub)seismic slip events (*Hillers et al.*, 2007; *Luo et al.*, 2017b), and nucleation of both slow and fast events (*Ariyoshi et al.*, 2012; *Hawthorne and Rubin*, 2013; *Kaneko*

et al., 2017; *Luo and Ampuero*, 2018; *Shibazaki and Iio*, 2003). But while the numerical simulators offer the desired complexity in terms of fault heterogeneity and geometry, they are typically based on rate-and-state friction, and are therefore limited by the aforesaid problem of extrapolation of RSF parameters beyond the scales and condition of the laboratory. Moreover, the RSF model input parameters are imposed as time-constant values, which may not necessarily be accurate, as these parameters may evolve with slip (*Mair and Marone*, 1999; *Scuderi et al.*, 2017; *Urata et al.*, 2017), or depend on slip velocity (*Collettini et al.*, 2011; *Den Hartog et al.*, 2012; *Reinen et al.*, 1992).

In an attempt to bridge the gap between the laboratory and nature, we have implemented the microphysical model formulations of *Niemeijer and Spiers* (2007) and *Chen and Spiers* (2016) ("CNS") into the seismic cycle simulator QDYN (*Luo et al.*, 2017a,b), which we will detail in this work. As a test-case, we analyse the behaviour of a crustal strike-slip fault, similar to the work of *Tse and Rice* (1986) and *Lapusta and Rice* (2003). We compare the outcomes of the microphysically-based model with the results from classical rate-and-state friction simulations, and discuss the differences between the two within a framework of upscaling laboratory results to nature. The simulations reveal that the implementation of the microphysical models results in characteristic fault slip behaviour previously ascribed to rate-and-state friction. However, the comparison between the rate-and-state based model and the microphysically-based model strongly suggests that the CNS-governed fault rheology cannot accurately be represented by classical rate-and-state friction. This implies that typical laboratory tests aimed at deriving RSF parameters may not be representative for the seismic cycle behaviour of faults exhibiting CNS microphysics (pressure solution and granular flow). The implementation of a microphysical model now offers an interpretation of simulation results in terms of material properties and thermodynamic quantities. This invites for future research into the controlling mechanisms of earthquake nucleation and rupture propagation, through the study of the underlying micro-scale processes.

5.2 Microphysical framework

For the implementation of the micro-scale physics, we have chosen the formulations of *Niemeijer and Spiers* (2007) and *Chen and Spiers* (2016) (from here on referred to as

"CNS model"), which describe the evolution of the frictional strength and microstructural state of well-matured fault gouges. The term 'friction' is here used in a general sense to describe the shear resistance of a fault. Even though superficially the functional form of the CNS constitutive relations shares little resemblance with the classical rate-and-state framework, the CNS model predictions of the transient frictional response to typical laboratory procedures (such as velocity-step tests and slide-hold-slide tests) very closely match characteristic RSF behaviour (*Chen et al.*, 2017b; *Chen and Spiers*, 2016). Furthermore, trends in experimental data for principal slip zone gouges of the Alpine Fault (obtained by *Niemeijer et al.*, 2016) can be accurately predicted by the CNS model (*Chen et al.*, 2017b, their Fig. 13), which provides some confidence that the physical processes relevant for earthquake nucleation in natural fault zones are well captured by the CNS model. The main concepts of the CNS model are summarised below.

The idealised geometry that the CNS model considers is that of a uniform layer of granular gouge, characterised by a nominal grain size d, porosity ϕ, and total thickness L (see Fig. 5.2). Optionally, the degree of localisation can be defined as a fraction λ of the total thickness L, which allows for a decomposition of the gouge body into a domain of active shear deformation (the shear band), and a spectator domain (the bulk). For the purpose of this study, we take $\lambda = 1$, which is equivalent to saying that the entire gouge layer participates in the accommodation of the imposed shear strain (see *Chen and Spiers*, 2016). A representative elementary volume defined by the above microstructural description is subjected to a constant effective normal stress σ, and shear deformation rate V_{imp} (units m s^{-1}). The deformation imposed by these boundary conditions is then accommodated within the body of the gouge by the parallel operation of granular flow (grain sliding) and a thermally-activated, time-dependent deformation mechanism. The strain rate contributions of the micro-scale deformation mechanisms as a function of the state of stress and gouge microstructural state can then be described by their respective constitutive relations, so that ultimately the shear resistance of the fault results from a combination of ductile creep and dilatant friction. In this work, we focus on the interplay between granular flow and intergranular pressure solution, a diffusive mass transfer mechanism that is commonly observed to operate in crustal faults (*Chester et al.*, 1993; *Holdsworth et al.*, 2011; *Imber et al.*, 2008). Other deformation mechanisms (stress corrosion cracking, dislocation creep, etc.) could be

incorporated in a similar fashion.

For pressure solution, we adopt a linearised flow law for dissolution controlled pressure solution creep (*Niemeijer et al.*, 2002; *Pluymakers and Spiers*, 2014):

$$\dot{\gamma}_{ps} = A_t \frac{I_s \Omega}{RT} \frac{\tau}{d} f_1(\phi) \tag{5.4a}$$

$$\dot{\varepsilon}_{ps} = A_n \frac{I_s \Omega}{RT} \frac{\sigma}{d} f_2(\phi) \tag{5.4b}$$

In these expressions, $\dot{\gamma}_{ps}$ and $\dot{\varepsilon}_{ps}$ denote the pressure solution strain rates tangential and normal to fault plane, i.e. the simple shear and uniaxial normal components of the strain rate tensor, respectively (taking compaction as $\dot{\varepsilon} > 0$). I_s denotes the (temperature-dependent) dissolution rate constant, Ω the molar volume of the solid phase, R the universal gas constant, T the absolute temperature, τ and σ are the macroscopic shear and effective normal stress, respectively (compression taken positive), and A_x is a geometric constant for the tangential (t) and normal (n) components. In this work, it is assumed that $A_t = A_n = A$, as the exact value of A_t is currently not precisely known. The evolution of the average grain contact stress is described by the porosity function $f_i(\phi)$ (*Spiers et al.*, 2004). For dissolution controlled pressure solution, this function takes the form (*Pluymakers and Spiers*, 2014):

$$f_1(\phi) = \frac{\phi_c}{\phi_c - \phi} \tag{5.5}$$

where ϕ_c is the maximum attainable (critical state) porosity of the dry gouge material (*Niemeijer and Spiers*, 2007; *Paterson*, 1995). It has been reported that this porosity function overestimates the compaction rates of low porosity aggregates, and does not accurately describe the evolution of pressure solution strain rate with porosity for $\phi < 20$ % (*Niemeijer et al.*, 2002; *Schutjens*, 1991b). *Van Noort et al.* (2008b) suggested that the discrepancy between analytical models and experimental compaction data at low porosities can be explained by considering surface-energy driven growth of grain contact asperities (i.e. structural evolution of the grain boundary; see also Chapter 3). While it is possible to include this mechanism into the above formulations, we chose to approximate this behaviour by modifying the porosity function given by Eqn. (5.5)

into:

$$f_2(\phi) = \frac{\phi - \phi_0}{\phi_c - \phi} \tag{5.6}$$

Here, ϕ_0 is a lower cut-off porosity which corresponds to the terminal porosity observed in experiments (*Niemeijer et al.*, 2002; *Schutjens*, 1991b), which could be taken as the percolation threshold for an interconnected pore network (*Van der Marck*, 1996). By using the above relation, we can approximate the rapid decay in strain rates with decreasing porosity observed in compaction experiments, without explicitly considering additional mechanisms that would otherwise complexify the implementation. As ϕ approaches ϕ_0, $\dot{\varepsilon}_{ps}$ reduces to 0, i.e. compaction by pressure solution asymptotically approaches zero, preventing $\phi \leq \phi_0$. Note that Eqn. (5.6) is only used for the densification of the gouge, i.e. compaction parallel to the fault plane normal (Eqn. (5.4b)). Since ductile shear creep by pressure solution (Eqn. (5.4a)) does not cause porosity reduction and may also operate at $\phi = \phi_0$, it is likely more appropriate to describe this process using the originally proposed porosity function (Eqn. (5.5)).

The constitutive relations for granular flow are provided by *Chen and Spiers* (2016), and read:

$$\dot{\gamma}_{gr} = \dot{\gamma}^*_{gr} \exp\left(\frac{\tau\left[1 - \tilde{\mu}^* \tan\psi\right] - \sigma\left[\tilde{\mu}^* + \tan\psi\right]}{\tilde{a}\left[\sigma + \tau \tan\psi\right]}\right) \tag{5.7a}$$

$$\dot{\varepsilon}_{gr} = -\tan\psi \dot{\gamma}_{gr} \tag{5.7b}$$

Here, the $\dot{\gamma}_{gr}$ and $\dot{\varepsilon}_{gr}$ denote the granular flow strain rates tangential and normal to fault plane, respectively, and $\tan\psi$ denotes the average dilatation angle, which can accordingly be written as $\tan\psi = 2H(\phi_c - \phi)$, H being a geometric constant (*Niemeijer and Spiers*, 2007; *Paterson*, 1995). The geometric constant H primarily depends on the grain shape and grain size distribution of the gouge, controlling the amount of dilatation that is involved in neighbour swapping and grain sliding. The magnitude of H can be predicted based on theoretical considerations, which would yield a value in the range $1/\sqrt{3}$ to $\sqrt{3}$ in 2D (*Niemeijer and Spiers*, 2007), or can be inferred from biaxial or triaxial deformation tests on sands and soils, which gives values in the range of 0.4 to 0.6 for dense sands (assuming a critical state porosity $\phi_c = 0.4$) (see *Vermeer and De Borst*, 1984). However, putting tight constrains on the exact

value of H is challenging, particularly when grain comminution operates during sliding, by which H would likely evolve. Dedicated laboratory tests and numerical simulations (e.g. employing the Discrete Element Method) could constrain this parameter further for grain size distributions relevant for natural gouges.

The micro-scale coefficient of friction of the individual grain contacts has a logarithmic velocity-dependence, which is given as $\tilde{\mu} = \tilde{\mu}^* + \tilde{a} \ln\left(\dot{\gamma}_{gr}/\dot{\gamma}^*_{gr}\right)$, with $\tilde{\mu}^*$ being the coefficient of friction at a reference grain sliding rate $\dot{\gamma}^*_{gr}$. In this form, the velocity-dependence of $\tilde{\mu}$ closely resembles the direct effect in the classical rate-and-state formulation and asperity-creep based microphysical models (e.g. *Nakatani*, 2001; *Rice et al.*, 2001). Notwithstanding this resemblance, the approach for deriving this relation is somewhat different, in that an atomic-scale jump process is considered to constitute the frictional slip at the nanometre scale of two grain contact asperities, rather than assuming deformation of an asperity through a dislocation glide or creep mechanism. Ultimately, the coefficient of logarithmic rate-dependence $\tilde{a}$ can be reduced to (*Chen and Spiers*, 2016):

$$\tilde{a} = \frac{RT}{\sigma_a \Omega_a} \tag{5.8}$$

where σ_a is the effective normal stress supported by grain contact asperities. Ω_a can be interpreted as an activation volume for the atomic-scale jump process. Classically, σ_a is taken to represent the elastic-plastic yield strength of the asperities, approximated by the material indentation hardness (e.g. *Ikari et al.*, 2016a; *Rice et al.*, 2001). However, for rock materials undergoing fluid-rock interactions, it has been convincingly demonstrated that the size of contact asperities (or 'islands') is controlled by dissolution-precipitation processes (*Beeler and Hickman*, 2015; *Hickman and Evans*, 1991; *Renard et al.*, 2012; *Schutjens and Spiers*, 1999), hence it is unlikely that σ_a of fluid-saturated gouges can be represented by the indentation hardness of a material. Furthermore, the porosity of a gouge exerts strong control on the average stress supported by each grain contact, rendering σ_a dependent on gouge porosity, strictly speaking (*Chen and Spiers*, 2016). However, during accelerating fault slip the porosity of the gouge quickly approaches the critical state porosity ϕ_c, after which the gouge porosity remains approximately constant. Additionally, since frictional heating is not considered in this work it would be unjustified to consider the effect of porosity, while ignoring the effect of frictional heat on the magnitude of $\tilde{a}$ during rapid slip. Thus, we assume for simplicity that σ_a

increases proportionally to σ, thereby ignoring contributions from the gouge porosity in elevating the average grain contact stress.

Even though the physical meaning and constituents of Ω_a are clear (see *Chen and Spiers*, 2016, for derivation and discussion), it remains non-trivial to predict its exact magnitude purely based on physical considerations. However, under the first-order assumption that $\sigma_a \propto \sigma$, $\tilde{a}$ can be written as:

$$\tilde{a} = \tilde{a}^* \frac{T}{T^*} \frac{\sigma^*}{\sigma} \tag{5.9}$$

where $\tilde{a}^*$ is an experimentally determined value measured at reference temperature T^* and normal stress σ^*. Interestingly, this makes the rate-and-state equivalent 'direct effect' not only temperature-dependent, as is often assumed (*Ikari et al.*, 2016a; *Nakatani*, 2001; *Rice et al.*, 2001), but also stress-dependent. As derived by *Chen et al.* (2017b), the equivalent RSF parameter a following a small velocity step can be approximated as $a \approx \tilde{a}\left(1 + \tan\psi_{ss}^2\right)$, where $\tan\psi_{ss}$ is evaluated at the steady-state porosity prior to the velocity step. Hence, there exists a potential for $\tilde{a}$ to decrease with depth, rather than increase when only a temperature proportionality is assumed (e.g. *Lapusta and Rice*, 2003; *Tse and Rice*, 1986), although a small contribution from $\tan\psi_{ss}$ needs to be considered to be more exact.

Having established the constitutive relations for pressure solution and granular flow, we now follow *Chen and Spiers* (2016) to use simple kinematic relations that yield a set of differential equations describing the evolution of the macroscopic shear stress and bulk gouge porosity:

$$\frac{\mathrm{d}\tau}{\mathrm{d}t} = k\left(V_{imp} - L\left[\dot{\gamma}_{gr} + \dot{\gamma}_{ps}\right]\right) \tag{5.10a}$$

$$\frac{\mathrm{d}\phi}{\mathrm{d}t} = -\left(1-\phi\right)\left(\dot{\varepsilon}_{gr} + \dot{\varepsilon}_{ps}\right) \tag{5.10b}$$

in which k is the effective stiffness (units: Pa m^{-1}) of the fault zone and surrounding medium. The instantaneous fault slip velocity V results from addition of the strain rates of granular flow and pressure solution, i.e. $V = L\left[\dot{\gamma}_{gr} + \dot{\gamma}_{ps}\right]$. What the above formulations show, is that the CNS model is modular in its design, in the sense that

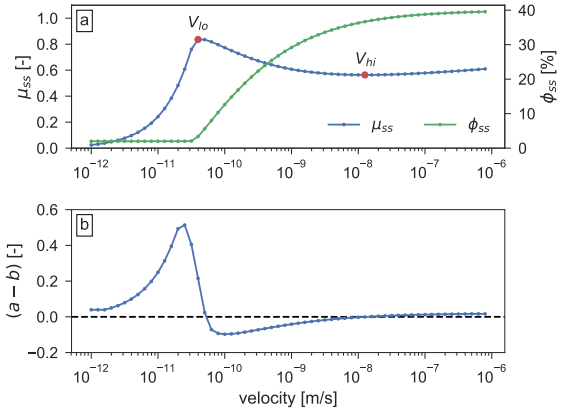

Fig. 5.1: Velocity-dependence of a) the steady-state coefficient of friction μ_{ss} and porosity ϕ_{ss}, and b) the equivalent value of $(a-b)$. The data was generated for a constant depth of 6 km and $H = 0.5$ (see Section 5.3.2.1). The points of velocity-neutrality are indicated in panel a) as V_{lo} and V_{hi}.

different (micro)physical processes can be readily incorporated within the existing model formulations. When additional deformation mechanisms are to be considered, their contributions to the total strain rate in the normal and shear directions can be simply appended in Eqn. (5.10). This offers opportunities for modelling very specific fault zone conditions and rheologies.

When the above coupled differential equations are solved for the steady-state ($\dot{\tau} = \dot{\phi} = 0$), three distinct deformation regimes emerge:

- When $\dot{\gamma}_{gr} \ll \dot{\gamma}_{ps}$ and $\dot{\varepsilon}_{gr} \ll \dot{\varepsilon}_{ps}$, the imposed deformation is fully accommodated by pressure solution creep. Since $\dot{\varepsilon}_{ps} \gg \dot{\varepsilon}_{gr}$ in this regime, compaction continues until ϕ approaches ϕ_0, so that strain is accommodated at near-zero porosity. This velocity-strengthening regime is analogous to the ductile or plastic creep regimes recognised in previous studies (*Noda and Shimamoto*, 2010; *Reinen et al.*, 1992; *Tullis and Yund*, 1987; *Verberne et al.*, 2017), and is characterised by a dense,

mylonitic gouge structure (*Bos et al.*, 2000a; *Sibson*, 1977; *Takahashi et al.*, 2017; *Zhang and He*, 2016).

- When $\dot{\gamma}_{gr}$ is of similar order as $\dot{\gamma}_{ps}$, the competition between dilatant granular flow and compaction by pressure solution results in a dynamic steady-state porosity. This steady-state porosity arises from the adverse dependencies of $\dot{\varepsilon}_{ps}$ and $\dot{\varepsilon}_{gr}$ on ϕ: with increasing ϕ, $\dot{\varepsilon}_{ps}$ increases through $f_2(\phi)$, whereas $\dot{\varepsilon}_{gr}$ decreases through a decreasing value of $\tan\psi$. Hence, at a given magnitude of $\dot{\gamma}_{gr}$, there exists a porosity for which $\dot{\varepsilon}_{ps} = -\dot{\varepsilon}_{gr}$ and so $\dot{\phi} = 0$ (defining steady-state). With increasing $\dot{\gamma}_{gr}$, a steady-state is found at increasingly higher values of ϕ, as was also observed in the experiments performed by *Niemeijer and Spiers* (2006). The strength of the gouge decreases with increasing gouge porosity (i.e. decreasing $\tan\psi$, see Eqn. (5.7a)), hence producing velocity-weakening behaviour (*Niemeijer and Spiers*, 2007).
- Finally, when $\dot{\gamma}_{gr} \gg \dot{\gamma}_{ps}$, the steady-state porosity asymptotically approaches the critical state porosity ϕ_c, with only little dilatation associated with increasing $\dot{\gamma}_{gr}$. In the absence of changes in gouge strength due to any further increase in porosity, the velocity-dependence of the gouge is controlled by rate-strengthening grain boundary friction. Characteristic microstructures for this regime reveal high porosities and abundant cataclastic features, typical for high-porosity gouges (*Niemeijer and Spiers*, 2006).

Since at steady-state $\dot{\gamma}_{gr}$ and $\dot{\gamma}_{ps}$ are related through the imposed velocity, the three deformation regimes predicted by the CNS model can be observed in a laboratory setting when a sufficiently large range of deformation rates is covered (*Buijze et al.*, 2017; *Shimamoto*, 1986). The velocity-dependence of the steady-state coefficient of friction μ_{ss} and porosity ϕ_{ss}, as well as corresponding values of $(a-b)$ as predicted by the CNS model are displayed in Fig. 5.1. At the transition from one deformation regime to the next, the velocity-dependence of the shear strength reaches neutrality, i.e. $(a-b) = 0$ in the RSF formulation. We define the transition velocities V_{lo} for the transition from ductile creep to velocity-weakening, and V_{hi} for the transition from velocity-weakening to velocity-strengthening at high imposed velocities. The absolute values of these transitional velocities are controlled by the relative rates of pressure solution and granular flow, and so depend on the (temperature-dependent) kinetics of

pressure solution, nominal grain size, and gouge composition. Thus, the main regimes of deformation shift as a function of temperature, as has also been observed in laboratory experiments (*Chester and Higgs*, 1992; *Den Hartog et al.*, 2012; *Mitchell et al.*, 2016; *Tullis and Yund*, 1987; *Zhang and He*, 2016).

5.3 Numerical methods

In essence, Eqn. (5.10) describes the behaviour of a zero-dimensional spring-block. In order to introduce further complexity and to upscale these relations to natural fault systems, we have implemented the CNS relations into the open-source boundary element code QDYN (**Q**uasi-**DYN**amic earthquake simulator; *Luo et al.*, 2017a,b, available at https://github.com/ydluo/qdyn). In the following section, we will describe the relevant details of the implementation of the CNS model into QDYN. For completeness, a concise description of the boundary element method is provided in Appendix 5.A.

5.3.1 Implementation of the microphysical model

As described in Appendix 5.A, the state of stress acting on each point on the fault is obtained through integration of a system of ordinary differential equations, which includes the time-derivative of the shear stress τ_i on the i-th fault element as:

$$\frac{\mathrm{d}\tau_i}{\mathrm{d}t} = -K_{ij}\left[V_j(t) - V_{imp}\right] - \eta\frac{\mathrm{d}V_i(t)}{\mathrm{d}t} \qquad \text{(5.A.2 revisited)}$$

where K_{ij} is a stress transfer kernel, and η is a radiation damping term. The total derivative $\mathrm{d}V_i/\mathrm{d}t$ can be decomposed into its partial derivatives as:

$$\frac{\mathrm{d}V_i}{\mathrm{d}t} = \frac{\partial V_i}{\partial \tau}\frac{\mathrm{d}\tau_i}{\mathrm{d}t} + \frac{\partial V_i}{\partial \phi}\frac{\mathrm{d}\phi_i}{\mathrm{d}t} \qquad (5.11)$$

Table 5.1: List of frequently used symbols and parameters, and their respective values.

Symbol	Description	Value	Units
A	pressure solution geometric constant	$24/\pi$	-
$\tilde{a}$	coefficient for logarithmic rate-dep. of $\tilde{\mu}$	-	-
$\tilde{a}^*$	reference value of $\tilde{a}$	3×10^{-3}	-
c_s	shear wave speed	3000	m s^{-1}
d	nominal grain size	10	µm
$\dot{\varepsilon}_{gr}$	granular flow strain rate	-	s^{-1}
$\dot{\varepsilon}_{ps}$	pressure solution strain rate	-	s^{-1}
ϕ	gouge porosity	-	-
ϕ_0	lower cut-off porosity	0.03	-
ϕ_c	critical state porosity	0.40	-
G	shear modulus	30	GPa
$\dot{\gamma}_{gr}$	granular flow shear strain rate	-	s^{-1}
$\dot{\gamma}^*_{gr}$	reference $\dot{\gamma}_{gr}$ corresponding with $\tilde{\mu}^*$	3×10^{-9}	s^{-1}
$\dot{\gamma}_{ps}$	pressure solution shear strain rate	-	s^{-1}
H	dilatancy geometric constant	0.5 and 0.2	-
η	radiation damping coefficient	0.5×10^6	Pa s m^{-1}
I_s	dissolution rate constant (T-dependent)	-	m s^{-1}
k	shear stiffness	-	Pa m^{-1}
L	thickness of the gouge layer	10^{-2}	m
$\tilde{\mu}$	grain boundary friction coefficient	-	-
$\tilde{\mu}^*$	reference grain boundary friction coefficient	0.4	-
Ω	molar volume	2.268×10^{-5}	m^3 mol^{-1}
R	universal gas constant	8.3144	J mol^{-1} K^{-1}
V	fault slip velocity	-	m s^{-1}
V_{imp}	imposed driving velocity	10^{-9}	m s^{-1}
σ	effective normal stress	-	Pa
σ^*	reference σ corresponding with $\tilde{a}^*$	50	MPa
T	temperature	-	K
T^*	reference T corresponding with $\tilde{a}^*$	353	K
τ	shear stress	-	Pa
$\tan\psi$	dilatancy angle	-	-

Substitution of (5.11) into (5.A.2) and rearrangement now gives the final system of ordinary differential equations for the CNS formulation:

$$\frac{\mathrm{d}\tau_i}{\mathrm{d}t} = \frac{-K_{ij}\left(V_j - V_{imp}\right) - \eta\frac{\partial V_i}{\partial \phi}\frac{\mathrm{d}\phi_i}{\mathrm{d}t}}{1 + \eta\frac{\partial V_i}{\partial \tau}} \tag{5.12a}$$

$$\frac{\mathrm{d}\phi_i}{\mathrm{d}t} = -\left(1 - \phi_i\right)\left(\dot{\varepsilon}_{gr,i} + \dot{\varepsilon}_{ps,i}\right) \tag{5.12b}$$

In this form, V_i is calculated for each fault element as $V_i = L_i\left(\dot{\gamma}_{gr,i} + \dot{\gamma}_{ps,i}\right)$, which yields the following partial derivatives for V:

$$\frac{\partial V}{\partial \tau} = L\left(A\frac{I_s\Omega}{dRT}f_1(\phi) + \dot{\gamma}_{gr}\left[\frac{1 - \tilde{\mu}\tan\psi}{\tilde{a}\left(\sigma + \tau\tan\psi\right)}\right]\right) \tag{5.13a}$$

$$\frac{\partial V}{\partial \phi} = L\left(\frac{\dot{\gamma}_{ps}}{\phi_c - \phi} + \dot{\gamma}_{gr}\left[\frac{2H\left(\sigma + \tilde{\mu}\tau\right)}{\tilde{a}\left(\sigma + \tau\tan\psi\right)}\right]\right) \tag{5.13b}$$

This set of equations now describes the rheology of the fault as a function of gouge material properties and microstructural state, and allows for spatio-temporal variations of the controlling parameters. In this way, we are able to predict how the fault frictional behaviour may vary with depth, and may evolve over the life-time of the seismic cycle.

In this work, we define 'steady-state' when $\dot{\tau} = \dot{\phi} = 0$ at V_{imp}. This definition also applies when V_{imp} is systematically varied between simulations, but maintained constant during each simulation, as is done to determine the steady-state shear strength as a function of load-point velocity. 'Transient' behaviour is defined as the mechanical response when $\dot{\tau} \neq 0$ or $\dot{\phi} \neq 0$ for a given fault segment.

5.3.2 Simulation procedure

5.3.2.1 Model set-up

As a first test case for the implementation of the CNS model, we set-up a crustal strike-slip model, similar to the work of *Tse and Rice* (1986), and *Lapusta and Rice* (2003) (see

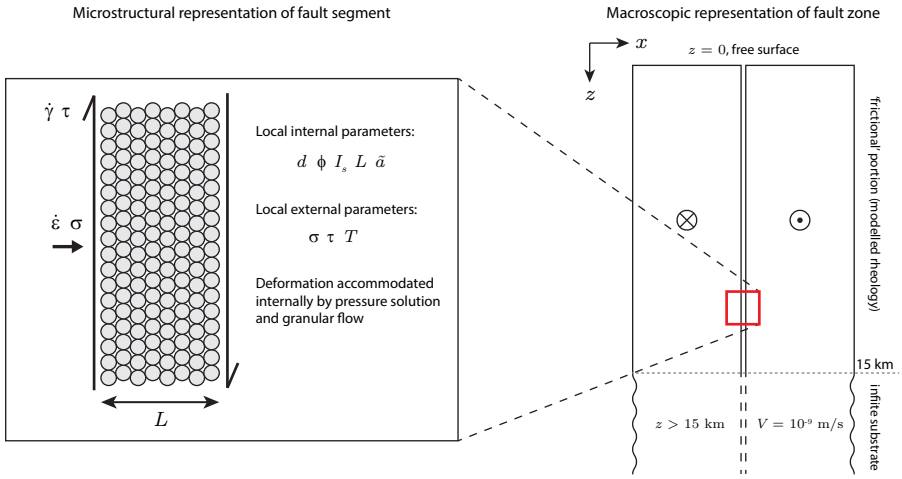

Fig. 5.2: Geometry and boundary conditions of the model set-up. The micro- and meso-scale (i.e. individual fault segment) rheology of the fault is dictated by the CNS model implementation, following the geometry of *Chen and Spiers* (2016) (left). At the macro-scale, the fault is represented as a one-dimensional vertical line that is deformed within a two-dimensional elastic medium (right). Note that in this diagram the sense of shear of the microstructural representation does not match that of the macroscopic representation.

Fig. 5.2 for a visualisation of the geometry). A one-dimensional, vertical fault, whose frictional part extends to a depth of 15 km, is embedded within a two-dimensional elastic medium that exhibits a uniform and constant shear modulus of 30 GPa. The fault is then loaded in mode III by a driving velocity of 10^{-9} m s^{-1} (≈ 30 mm yr^{-1}), which is of similar magnitude as present-day plate velocities. The fault is discretised by 8192 equal-sized segments providing a spatial resolution of 1.8 m, which proves to be sufficient for numerically stable results (see Appendix 5.B). A free surface is simulated by enforcing symmetry across a mirror plane located at the surface (e.g. *Lapusta and Rice*, 2003).

The type of fault considered here follows broadly the characteristics of a continental fault as described by *Chester et al.* (1993), exhibiting a single, discrete fault core which internally accommodates all imposed shear displacements, and where off-fault shear

strain rates (e.g. by pressure solution creep) are negligible. Other fault architectures, such as described by e.g. *Faulkner et al.* (2003) and *Kimura et al.* (2012), incorporate several principal slip zones surrounded by a creeping, phyllosilicate-rich matrix. In the present CNS formulation, such a geometry may be simulated by taking $\lambda < 1$, so that λL corresponds to the (cumulative) thickness of the fault core, and $(1 - \lambda)\, L$ corresponds to the thickness of the surrounding creeping region, where L is taken as the total width of the fault zone (which may not be well-defined). In effect, strain accommodation by the matrix reduces the strain rate imposed onto the fault core, and so has a similar effect as lowering V_{imp}. However, the aim of this work is to compare the CNS model implementation to previous work (e.g. *Lapusta and Rice*, 2003; *Tse and Rice*, 1986), motivating a simple fault structure as adopted by these authors.

In order to estimate the depth-dependency of the normal stress acting on the fault, we need to make assumptions regarding the local fluid pressure gradient. Commonly chosen depth-profiles fall into two categories: for simple analytical investigations it is often assumed that the ratio of pore fluid pressure to the total vertical stress is constant with depth, i.e. $\lambda_p = P_f/\sigma_v = \text{const}$, which results in a linear increase of effective normal stress with depth (i.e $\sigma \propto [1 - \lambda_p]\, z$). However, analyses of borehole data (*Suppe*, 2014) and theoretical considerations (*Rice*, 1992) suggest that λ_p is not a constant with depth, and that below the fluid retention depth, P_f follows a lithostatic trajectory, resulting in a constant effective normal stress below this given depth. An often cited mechanism for supra-hydrostatic pore fluid pressures is disequilibrium compaction (*Grauls*, 1997; *Morency et al.*, 2007), although the physical basis for this has yet to be fully elucidated. In a fault system that undergoes large fluid permeability changes during the seismic cycle (*Lockner et al.*, 2009; *Sibson*, 1990) it can be questioned how the effective normal stress evolves over time, and if it can be approximated by a time-constant profile. While the question of fluid pressurisation is an interesting one, we simply adopt the effective stress profile with depth-dependent λ_p of *Lapusta and Rice* (2003), based on *Rice* (1992), for easier comparison with previous work, and leave the effects of fluid pressure for future study. The fault zone temperature follows a constant geotherm of 25 K km^{-1}, with a surface temperature of 293 K (see Fig. 5.4a), and is not affected by internal heat production by fault slip (i.e. no frictional heating is considered).

Finally, the CNS model requires a number of assumptions regarding the chemical and microstructural properties of the gouge. We continue to make further simplifications by assuming a uniform and constant nominal grain size, fault zone thickness, and gouge composition. While these simplifications are not required by the CNS model implementation (fault zone structure and heterogeneity can be readily incorporated), it would likely be easier to interpret the model outcomes with fewer variables to consider. We take quartz as a main constituent for the fault zone, representing typical felsic continental upper crust (*Chester and Logan*, 1987; *Kirkpatrick et al.*, 2013; *Power and Tullis*, 1989; *Sibson*, 1977). Quartz has been shown to exhibit dissolution-controlled pressure solution creep at temperatures relevant for the upper crust, ranging from 150 to 600 °C (*Dewers and Hajash*, 1995; *Niemeijer et al.*, 2002; *Schutjens*, 1991a). We use the empirical rate equation provided by *Rimstidt and Barnes* (1980) to interpolate laboratory data of quartz dissolution in pure water as a function of absolute temperature:

$$\log_{10} k_+ = 1.174 + 2.028 \times 10^{-3} T - \frac{4158}{T} \tag{5.14}$$

The pressure solution kinetic constant I_s is then obtained as $I_s = k_+ \Omega$ (*Niemeijer et al.*, 2002), with Ω being the molar volume of quartz (2.269×10^{-5} m^3 mol^{-1}). It was noted by *Van Noort et al.* (2008a) that using the above relation may overestimate experimental compaction rates by up to one order of magnitude when dissipation by plastic deformation is neglected. Furthermore, it is known that the presence of certain cations in solution (e.g. Mg^{2+}, Ca^{2+}, Na^{+}, and Ba^{2+}) may catalyse the process of quartz dissolution (*Dove*, 1999; *Rimstidt*, 2015). Typical salinities of pore fluids present in fault zones may be higher than those of seawater (e.g. *Ohtani et al.*, 2000; *Parry*, 1998), which may accelerate quartz dissolution by over two orders of magnitude (*Rimstidt*, 2015). Moreover, the presence of phyllosilicates, as commonly found in mature fault zones (*Collettini et al.*, 2011; *Faulkner et al.*, 2003), has been convincingly demonstrated to enhance pressure solution creep by accelerating ionic diffusion rates across a grain contact (*Hickman and Evans*, 1995; *Renard et al.*, 1997). However, for the case of dissolution-controlled pressure solution (as is anticipated for quartz), phyllosilicates such as muscovite may negatively impact creep rates due to the presence of K^{+} and Al^{3+} cations released by these minerals upon dissolution (*Iler*, 1973; *Niemeijer and Spiers*, 2002).

While acknowledging these uncertainties regarding the kinetics of pressure solution in quartz, we choose to adopt Eqn. (5.14) and disregard all of the points mentioned above. Instead of attempting to accurately simulate natural faults, we focus on the comparison between the CNS model implementation and classical rate-and-state friction under identical conditions and fault zone properties. To better constrain the kinetics of pressure solution in quartz gouges, more experimental work is needed on the compaction of quartz aggregates under in-situ fault zone conditions and pore fluid chemistry.

A summary of the model input parameters and their values is given in Table 5.1.

5.3.2.2 Comparison of the CNS implementation with rate-and-state friction

In order to compare the CNS implementation with classical rate-and-state friction, we run two crustal strike-slip fault simulations following the model set-up as described in Section 5.3.2.1 above. In the first simulation (the native CNS simulation), the fault rheology is dictated by the CNS model implementation. In the second (the RSF simulation), we employ classical RSF with a single state parameter, which evolves according to the ageing law (Eqn. (5.2a)). For a direct comparison with the CNS model, the depth-dependent input parameters for this simulation (a, b, and D_c) as predicted by the CNS model need to be estimated. We will refer to these parameters as the 'equivalent' RSF parameters, without implying that these parameters injected into Eqn. (5.1) are unequivocally representative for the CNS model. The equivalent RSF parameters are obtained as follows.

For each given depth interval, a simulation is run in spring-block mode with CNS-governed fault rheology, and with the appropriate input parameters for that specific depth ($\tilde{a}$, I_s, σ, and T). The zero-dimensional, spring-block fault is then loaded at a rate $V_{imp} = 10^{-9}$ m s^{-1} with high load-point stiffness until a steady-state is reached, from which the steady-state coefficient of friction is determined as $\mu_{ss} = \tau_{ss}/\sigma$. An additional simulation is run in which a velocity-step test is simulated. In this simulation, the fault is deformed at a rate $V_0 = e^{-0.2}V_{imp}$ until steady-state is reached, followed by an instantaneous step in load-point velocity to $V_1 = e^{0.2}V_{imp}$. The simulation is stopped when the new steady-state is attained. The equivalent rate-and-state

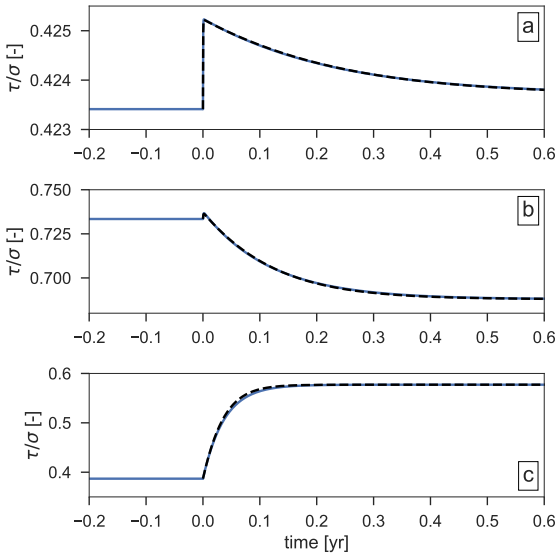

Fig. 5.3: Representative examples for the velocity-step simulations and corresponding inversion results (black dashed line), for three selected depth intervals (z) with $H = 0.5$. a) $z = 2$ km, $a = 4.5 \times 10^{-3}$, $b = 3.8 \times 10^{-3}$, and $D_c = 7.8$ mm; b) $z = 8$ km, $a = 8.2 \times 10^{-3}$, $b = 1.2 \times 10^{-1}$, and $D_c = 4.4$ mm; c) $z = 11$ km, $a = 4.8 \times 10^{-1}$, $b = 0$, and consequently D_c is undefined.

parameters are obtained from inversion of Eqn. (5.1) with the ageing state evolution law (Eqn. (5.2a); *Reinen and Weeks*, 1993) for the transient friction data resulting from this simulation, which is performed by the *SciPy* implementation of the Trust Region Reflective algorithm (*Branch et al.*, 1999; *Jones et al.*, 2001). In the simulated depth intervals where strain is fully accommodated by ductile creep, the steady-state porosity remains near $\phi_{ss} = \phi_0$, which is maintained upon a velocity-step. In these cases, no evolution effect is observed, and so the frictional response is best modelled with $b = 0$. The value of D_c for $b = 0$ is hence undefined and can therefore be arbitrarily chosen without further consequences for the RSF simulations. For depth intervals that exhibit $b \neq 0$ (i.e. where granular flow is significant), D_c results from the inversion procedure. Since the equivalent RSF parameters are velocity-dependent (*Chen et al.*,

2017b), the velocity-step size needs to be small for accurate determination of the CNS equivalent RSF parameters, hence our chosen velocity-step size is small compared to most laboratory tests (typically one order in magnitude; *Marone et al.*, 1990; *Niemeijer and Spiers*, 2006). Furthermore, owing to this velocity-dependence of the equivalent RSF parameters, the velocity at which a, b, and D_c are evaluated is of great importance. In the simulations described in this section, we have chosen to evaluate the equivalent RSF parameters at the load-point velocity, following analytical treatments of frictional instabilities in the RSF framework (e.g. *Rice and Ruina*, 1983).

The above procedure is repeated for 40 different depth intervals to obtain the depth-dependence of a, b, and D_c as resulting from the CNS model implementation. Representative simulation and inversion results at depth intervals of 2, 8, and 11 km are presented in Fig. 5.3. Since the crustal fault simulations that employ RSF require a spatial resolution that is much higher than is provided by these 40 depth intervals, the data set is resampled to the required resolution by linear interpolation, and is gently smoothed by a moving-mean filter to prevent steep gradients in the parameters. The equivalent RSF parameters then serve as an input for the RSF simulation, and should provide a direct comparison between the classical RSF and native CNS simulations. The adopted procedure also reflects typical laboratory testing procedures, in which near-steady state velocity-step tests are performed (ideally at in-situ fault zone conditions). It can be questioned whether or not these steady-state laboratory measurements of the RSF parameters can be applied to the seismic cycle, during which deformation occurs far from steady-state. Comparison between the RSF and CNS simulations could provide new insights into this problem, as the CNS model does not require steady-state rheological parameters.

5.4 Results

5.4.1 Steady-state behaviour

It is instructive to first consider the steady-state behaviour of the CNS-controlled model fault, i.e. the predicted rheology at $V = V_{imp}$. From the spring-block simulations

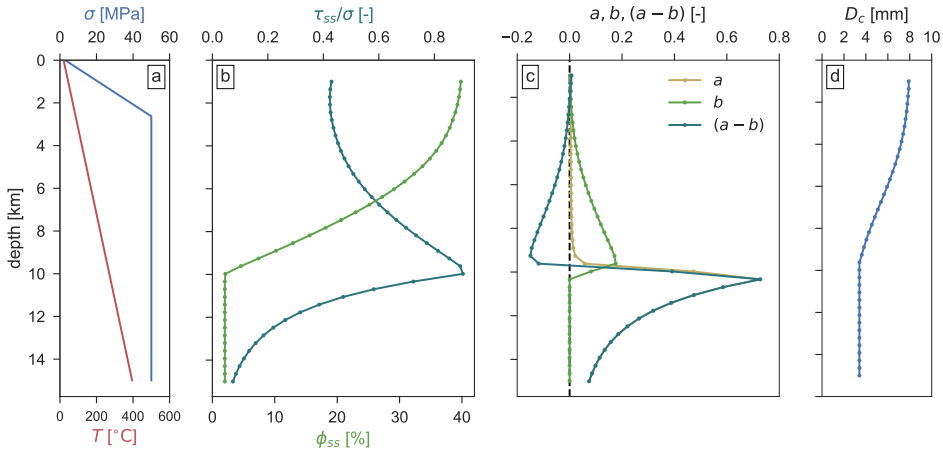

Fig. 5.4: Depth profiles of steady-state parameters for the model fault for $H = 0.5$, determined at $V = 10^{-9}$ m s^{-1}. a) Effective normal stress σ and temperature T; b) Steady-state coefficient of friction μ_{ss} and porosity ϕ_{ss}; c) Equivalent rate-and-state friction parameters a, b, and $(a - b)$. At depths > 10 km, $b = 0$ so that the curve of a overlaps with that of $(a - b)$; d) Equivalent rate-and-state parameter D_c.

described in Section 5.3.2.2, we obtain the steady-state coefficient of friction $\mu_{ss} = \tau_{ss}/\sigma$ (Fig. 5.4b) and the equivalent RSF parameters a, b, $(a-b)$ (Fig. 5.4c), and D_c (Fig. 5.4d).

The profile of $(a - b)$ in Fig. 5.4c suggests the existence of a seismogenic depth interval (i.e. potentially unstable region of the crust) between 3 and 10 km depth. Shallow depths < 3 km are characterised by mild velocity-strengthening friction due to cataclastic granular flow, consistent with laboratory tests and seismological observations (*Marone and Scholz*, 1988; *Marone et al.*, 1990). Furthermore, below the depth of 10 km, a region of strong velocity-strengthening (large positive $(a - b)$) emerges, which could be interpreted as defining the brittle-ductile transition as in the classical models of crustal rheology (*Sibson*, 1982). Note, however, that these results are specific to a given load-point velocity of $V_{imp} = 10^{-9}$ m s^{-1}, as both μ_{ss} and equivalent $(a - b)$ are velocity-dependent in the CNS formulation (*Chen and Spiers*, 2016). Hence, the depth of the seismogenic zone and the brittle-ductile transition *sensu stricto* cannot directly

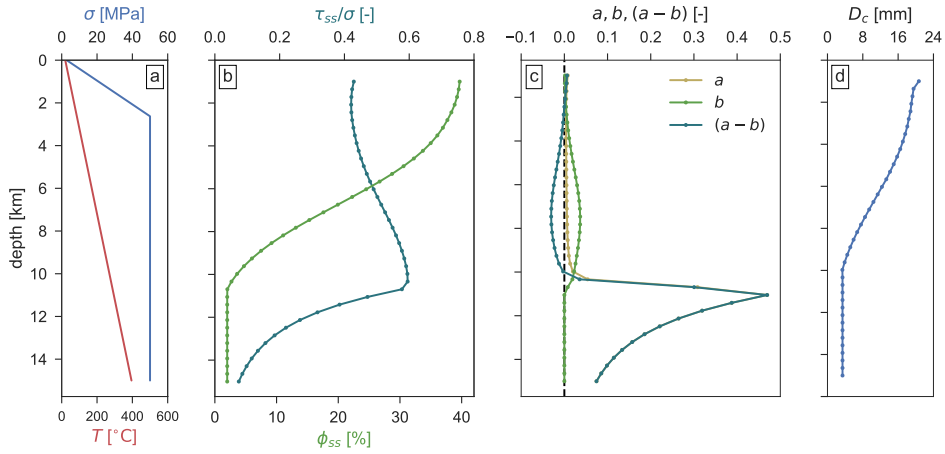

Fig. 5.5: Depth profiles of steady-state parameters for the model fault for $H = 0.2$, determined at $V = 10^{-9}$ m s^{-1}. a) Effective normal stress σ and temperature T; b) Steady-state coefficient of friction μ_{ss} and porosity ϕ_{ss}; c) Equivalent rate-and-state friction parameters a, b, and $(a - b)$. At depths > 10 km, $b = 0$ so that the curve of a overlaps with that of $(a - b)$; d) Equivalent rate-and-state parameter D_c. Note the use of different horizontal axis scales from Fig. 5.4.

be inferred based on the steady-state behaviour at a single slip velocity, as the fault slip velocity likely varies by over 10 orders of magnitude between the inter- and coseismic phases of the seismic cycle (going from $V \ll V_{imp} = 10^{-9}$ m s^{-1} during the interseismic phase to $V \approx 1$ m s^{-1} during the coseismic phase). This has important implications for the depth of earthquake nucleation and the direction of dynamic rupture propagation, as we shall demonstrate later.

Within the 'brittle' region, characterised mostly by velocity-weakening at 10^{-9} m s^{-1} (upper 10 km), the depth-dependence of the parameter b strongly controls the overall velocity-dependence of the fault, while the parameter a remains relatively small and near-constant. The large magnitude of b (up to 0.18) is not commonly observed in laboratory experiments, where typical values of the order of 10^{-3} to 10^{-2} are found (e.g. *Marone et al.*, 1990; *Tesei et al.*, 2014). However, many of these experiments are

conducted at relatively low temperature conditions, and relatively high deformation rates (in the range of 1-100 µm s^{-1}). It has been observed that fluid-rock interactions increase the magnitude of b (*Blanpied et al.*, 1998; *He et al.*, 2016), and so it is likely that b assumes larger values in regions of the crust where fluid-rock interactions occur at appreciable rates. In the limit of an infinitesimally small step-wise velocity perturbation, the value of b as predicted by the CNS model can be approximated as $b \approx H\left(\phi_c - \phi_{ss}\right)\left(1 + \tilde{\mu}^2\right)$, where ϕ_{ss} is the steady-state gouge porosity (*Chen et al.*, 2017b). This relation shows that b is expected to increase with decreasing steady-state porosity, which is achieved through time-dependent compaction by, in this case, pressure solution creep. The maximum value of b is attained when $\phi_{ss} \approx \phi_0$ (as is found at the base of the seismogenic zone) for which $b \approx H\left(\phi_c - \phi_0\right)\left(1 + \tilde{\mu}^2\right) = 0.21$. This analytical approximation corresponds well to the value obtained from the velocity-step simulations. Other mechanisms that may strongly affect the experimentally measured value of $(a - b)$ include localisation and grain comminution, which are commonly observed in experiments exhibiting velocity-weakening behaviour (*Takahashi et al.*, 2017). These mechanisms are at present not included in the CNS model formulation, and should be considered in future studies.

The large magnitude of $(a - b)$ down to -0.15 poses severe numerical challenges when attempting to perform simulations with the RSF parameters derived from Fig. 5.4. To remedy this, we have repeated the steady-state simulations for a lower value of the geometric factor $H = 0.2$ (Fig. 5.5). This effectively reduces the magnitude of $(a - b)$ (Fig. 5.5c) and increases the magnitude of D_c (Fig. 5.5d). Furthermore, H strongly controls the rate of slip weakening in response to an instantaneous velocity-step, and therefore affects the frictional stability of the fault (see Appendix 5.B, Eqn. (5.B.5)). As mentioned earlier, the values of H and ϕ_c are at present not tightly constrained for grain size distributions typical for fault gouges (e.g. power-law or log-normal; *Marone and Scholz*, 1989; *Storti et al.*, 2003). Furthermore, H and ϕ_c are expected to decrease with increasing phyllosilicate content, by lowering the dilatancy involved in granular flow and by more efficient occupation of the pore space. It has been shown in laboratory experiments that the presence of a continuous mineral foliation effectively raises $(a - b)$ towards neutral values (*Collettini et al.*, 2011), consistent with our interpretation of $\tan\psi$. We will use the equivalent RSF parameters derived from the steady-state simulations exhibiting $H = 0.2$ to perform the RSF simulation, which

is subsequently compared with the native CNS simulation for which $H = 0.2$. Then the CNS simulation with $H = 0.2$ will be compared with a CNS simulation with $H = 0.5$ (other parameters remaining constant) to evaluate the role played by H. We would like to stress the point that H and ϕ_c are purely geometrical parameters, and we anticipate no depth-dependence of these parameters in the absence of grain comminution and poro-elastic effects.

In contrast with the brittle region, the 'ductile' (steady-state) velocity-strengthening region (below 10 km depth), shows practically no variation in the microstructural state (i.e. porosity), and the velocity-step data is best represented by $b = 0$. By doing so, D_c becomes undefined, and is inconsequentially assumed to remain constant. In the ductile region of the crust, fault slip is predominantly accommodated by pressure solution creep ($\dot{\gamma}_{gr} \ll \dot{\gamma}_{ps}$ so that $V \approx L\dot{\gamma}_{ps}$), which, in the adopted formulation, acts as a linearly viscous fluid. Ignoring any contributions from state evolution ($b \approx 0$ or equivalently ϕ remaining constant near ϕ_0), the fault shear strength in this regime can be obtained directly from rewriting Eqn. (5.4a), which yields:

$$\tau \approx \frac{RTd}{AI_s\Omega}\frac{V}{L} \tag{5.15}$$

Then, by definition of $a = \partial\mu/\partial \ln(V)$ (*Rice et al.*, 2001), we obtain that in the ductile regime $a = \tau/\sigma$, which is supported by the comparison of the profiles of τ/σ and a in Fig. 5.4b and c.

Finally, the characteristic slip distance D_c is observed to vary within one order of magnitude over the entire depth range for which it could be determined. Its magnitude is significantly larger than typical laboratory measurements (commonly of the order of tens of µm; *Marone et al.*, 1990), which is directly related to the chosen thickness of the fault zone L: D_c as derived by *Chen et al.* (2017b) is proportional to L (as was also demonstrated experimentally by *Marone and Kilgore*, 1993). The value of L is chosen in this study to be constant at 1 cm, which is in the range of commonly reported values for cataclasite-rich principal slip zones (e.g. *Demurtas et al.*, 2016; *Smeraglia et al.*, 2017), although we cannot exclude the possibility that the thickness of the fault zone (or more precisely: the degree of localisation), evolves during the seismic cycle.

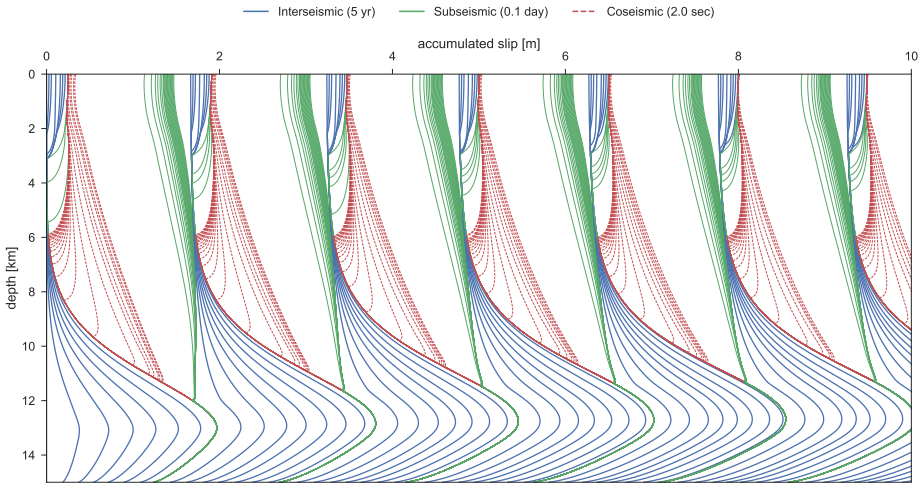

Fig. 5.6: Spatio-temporal evolution of fault slip from the CNS simulation with $H = 0.5$, relative to the slip distribution after the first seismic event. Contours of fault slip are plotted at fixed temporal intervals based on the maximum slip velocity recorded on the fault. The blue contours represent slow, interseismic creep ($V_{max} < 10^{-7}$ m s^{-1}), and are spaced every 5 years. The green contours represent subseismic (nucleation or postseismic) velocities ($10^{-7} < V_{max} < 10^{-2}$ m s^{-1}), and are spaced every 0.1 days. The coseismic stage ($V_{max} > 10^{-2}$ m s^{-1}) is represented by the red contours, which are spaced every 2 seconds.

5.4.2 Transient fault slip behaviour

The transient behaviour, i.e. the evolution of fault slip velocity during the seismic cycle, is investigated as described in Section 5.3.2. The spatio-temporal distribution of accumulated fault slip of the CNS simulation with $H = 0.5$ is presented in Fig. 5.6. In this figure, contours of fault slip are plotted at fixed temporal intervals, which are based on the maximum slip velocity V_{max} recorded over the entire fault at each given time interval. The blue contours represent slow, interseismic creep ($V_{max} < 10^{-7}$ m s^{-1}), and are spaced every 5 years. The green contours represent subseismic (nucleation or postseismic) velocities ($10^{-7} < V_{max} < 10^{-2}$ m s^{-1}), and are spaced every 0.1 days. Finally, the coseismic stage ($V_{max} > 10^{-2}$ m s^{-1}) is represented by the red contours,

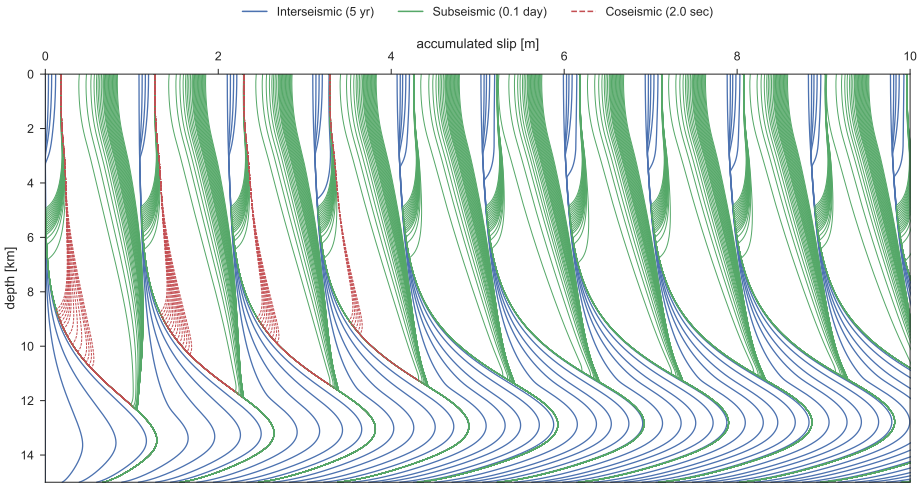

Fig. 5.7: Spatio-temporal evolution of fault slip from the CNS simulation with $H = 0.2$, relative to the slip distribution after the first seismic event. Contours of fault slip are plotted at fixed temporal intervals based on the maximum slip velocity recorded on the fault. The blue contours represent slow, interseismic creep ($V_{max} < 10^{-7}$ m s^{-1}), and are spaced every 5 years. The green contours represent subseismic (nucleation or postseismic) velocities ($10^{-7} < V_{max} < 10^{-2}$ m s^{-1}), and are spaced every 0.1 days. The coseismic stage ($V_{max} > 10^{-2}$ m s^{-1}) is represented by the red contours, which are spaced every 2 seconds.

which are spaced every 2 seconds. The slip contours are relative to the slip distribution achieved at the end of the first seismic event, which is not shown in Fig. 5.6.

In the CNS simulation, small slow slip events nucleate at shallow depths (2-3 km) that propagate down and produce stress concentrations. Once sufficient stress has been accumulated, the nucleation of a seismic event initiates at a depth of 3 km, and expands in the down-dip direction. At a depth of 6 km, the fault reaches coseismic velocities and continues to dynamically propagate down to a depth of about 11 km. The highest slip velocities are attained at depths greater than 8 km, while near the surface slip velocities remain restricted to 0.01 m s^{-1} during most events. Following a seismic event, much of the slip deficit at the surface is relieved by rapid afterslip (as indicated by the spacing between the last red and first green contour line after each

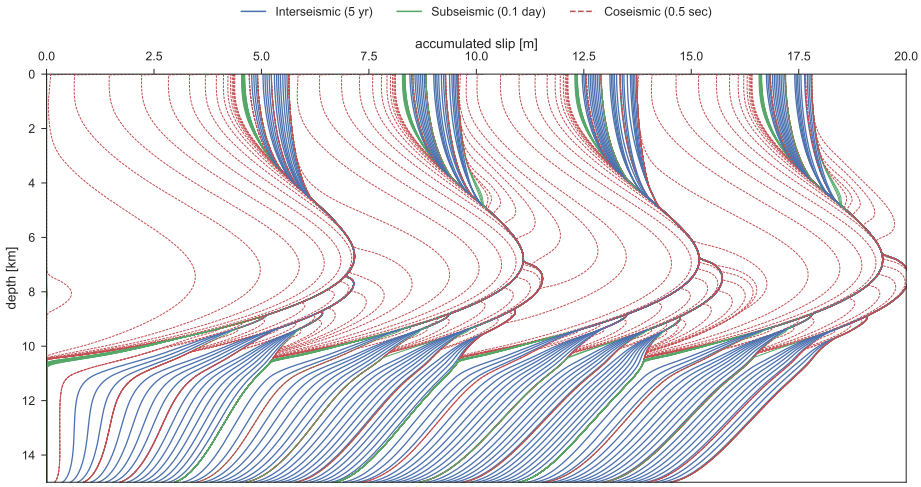

Fig. 5.8: Spatio-temporal evolution of fault slip from the rate-and-state simulation with the ageing state evolution law, relative to the start of the simulation. Contours of fault slip are plotted at fixed temporal intervals based on the maximum slip velocity recorded on the fault. The blue contours represent slow, interseismic creep ($V_{max} < 10^{-7}$ m s^{-1}), and are spaced every 5 years. The green contours represent subseismic (nucleation or postseismic) velocities ($10^{-7} < V_{max} < 10^{-2}$ m s^{-1}), and are spaced every 0.1 days. The coseismic stage ($V_{max} > 10^{-2}$ m s^{-1}) is represented by the red contours, which are spaced every 0.5 seconds. Note that a different contour interval and horizontal axis are used than in Fig. 5.6 and 5.7.

seismic event in Fig. 5.6). In the simulation with $H = 0.5$, a total of up to 1 m of afterslip is accumulated over a duration of about 1 year, which is in range of geodetical estimates of afterslip (*Marone et al.*, 1991; *Perfettini and Avouac*, 2007). The total slip accommodated within one seismic cycle is roughly 1.5 m, and so the recurrence time of the seismic events is in the range of 50 years (as also seen in Fig. 5.9). Note that the fault requires about three seismic cycles to fully settle into a repeating limit cycle.

A somewhat different picture emerges when running the same simulation with $H = 0.2$ (Fig. 5.7). In this simulation, the maximum slip velocity recorded over the entire fault is much lower in value (up to 0.01 m s^{-1}), and the imposed deformation within the brittle region is predominantly accommodated by episodic slow slip. The

recurrence time between the slow slip events is only about half of the recurrence time seen when $H = 0.5$. Despite this difference, the depth of nucleation, propagation direction, and maximum down-dip extent of the rupture are still comparable between both simulations.

The RSF-based simulations are performed with the equivalent parameters obtained for $H = 0.2$ and $V_{imp} = 10^{-9}$ m s^{-1}, and so the RSF results presented in Fig. 5.8 should be compared with the CNS results of Fig. 5.7. When doing so, we find that the slip behaviour is rather dissimilar from the CNS-based simulations. First of all, the RSF simulation shows large seismic events, producing up to 6 m of coseismic slip in some of the larger events. Additionally, a number of smaller seismic events nucleate at the base of the seismogenic zone (near a depth of 10 km). Within the brittle region, interseismic and postseismic creep are virtually absent, and most of the surface slip is produced at coseismic slip rates. The down-dip extent of the rupture is strongly confined to the boundary with the velocity-strengthening region, and does not traverse this boundary.

The depth-averaged friction at which the fault operates (defined as $\bar{\mu} = \frac{1}{N}\sum \tau_i/\sigma_i$, where N is the number of fault segments), is shown in Fig. 5.9a. For comparison, the steady-state values of friction, measured at $V = 10^{-9}$ m s^{-1}, are indicated by the horizontal dashed lines. Although both the CNS simulations operate at a very similar apparent friction during their respective seismic cycles, their steady-state friction values differ by about 0.06 units of friction. The CNS simulation with $H = 0.2$ operates more closely to its steady-state value than the simulation with $H = 0.5$, or the RSF simulation.

5.5 Discussion

In the following section, we shall discuss some distinctive features of the various simulations, and make the comparison between them. The discussion will be hosted mostly within a conceptual framework of classical rate-and-state friction, as to build upon previous experience gained from RSF-based studies. Note, however, that the 'measured' RSF constitutive parameters are taken as time-constants (i.e. independent

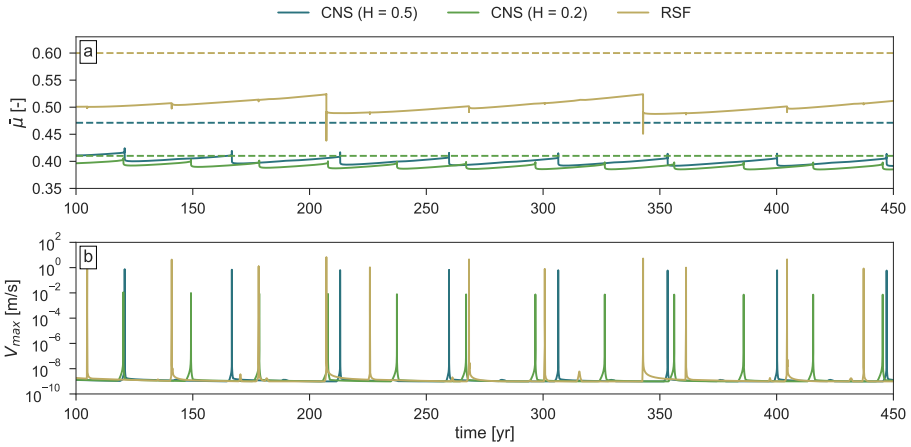

Fig. 5.9: a) Time series of the depth-averaged friction coefficient $\bar{\mu}$ at which the fault operates. Solid lines represent the average friction measured during the seismic cycle simulations, dashed lines represent the depth-averaged friction at steady-state ($V = 10^{-9}$ m s^{-1}); b) Time series of the maximum slip velocity V_{max} recorded over the entire fault.

of velocity and state), while the equivalent RSF parameters for the CNS model are dependent on e.g. velocity, stress, and porosity (i.e. 'state'). This inhibits a one-to-one comparison between the results produced in CNS- and RSF-based simulations, and solicits for the development of a new framework based on microphysical concepts.

5.5.1 Velocity-dependence of friction

Before discussing the seismic cycle behaviour of the CNS and RSF simulations, we will first discuss the steady-state behaviour of the CNS model. The velocity-dependence of friction as predicted by the CNS model will play a central role in the comparison between the CNS and RSF simulations, and so it would be informative to first point out a number of key features.

Fig. 5.1 shows the steady-state coefficient of friction and gouge porosity as a function

of the imposed velocity, as well as the corresponding values of $(a-b)$, generated with the CNS model parameters for a depth of 6 km and $H = 0.5$. Qualitatively, the shape of these profiles is similar to the depth profiles of μ_{ss} and $(a-b)$ as shown in Fig. 5.4, with the lowest slip velocities corresponding with the greatest depth or highest temperature, and vice versa. The frictional response of a fault obeying the CNS rheology is the result of the relative rates of granular flow and (thermally-activated) pressure solution creep. Hence, an increase in temperature has a similar effect on the magnitude of μ_{ss} and $(a-b)$ as does a decrease slip velocity, producing similar profiles (see also *Niemeijer and Spiers*, 2007, their Fig. 10). This trade-off between temperature and velocity has been reported in laboratory studies (*Chester and Higgs*, 1992; *Den Hartog et al.*, 2012; *Mitchell et al.*, 2016; *Niemeijer et al.*, 2016), providing experimental support for the trends in rheology predicted by the CNS model.

It is apparent from Fig. 5.1b that $(a-b)$ itself is non-monotonically velocity-dependent for any given depth interval. When performing velocity-step tests, either experimentally or numerically (as we have done to obtain the equivalent RSF parameters), a point-measurement is made of the steady-state coefficient of friction and RSF parameters near the given load-point velocity (10^{-9} m s^{-1} in our case, but 10^{-6}-10^{-4} m s^{-1} are commonly chosen laboratory values). For small deviations from the steady-state velocity, i.e. for small velocity step amplitudes, the values of the obtained $(a-b)$ accurately represent the steady-state velocity-dependence ($\mathrm{d}\mu_{ss}/\mathrm{d}\ln V$, proportional to the slope of μ_{ss} in Fig. 5.1a). However, for large deviations, such as attained during the interseismic period ($V \ll V_{imp}$) or during the coseismic phase ($V \gg V_{imp}$), the RSF parameters obtained at V_{imp} no longer capture the rheology of the fault zone. In other words, the tangent line at any point in Fig. 5.1a is no accurate representation of $(a-b)$ at larger distances from that point, and $(a-b)$ cannot be taken as a constant when considering wide velocity ranges. This feature has been recognised in laboratory experiments (see above references), but is underappreciated in modelling studies as the velocity-dependence of the RSF parameters is difficult to predict based on laboratory observations alone. The use of a microphysical model facilitates incorporation of this complex velocity-dependence of friction.

To illustrate the effect of sliding velocity on the frictional response of our model strike-slip fault, we have re-drawn the steady-state depth profiles of μ_{ss} and $(a-b)$ as

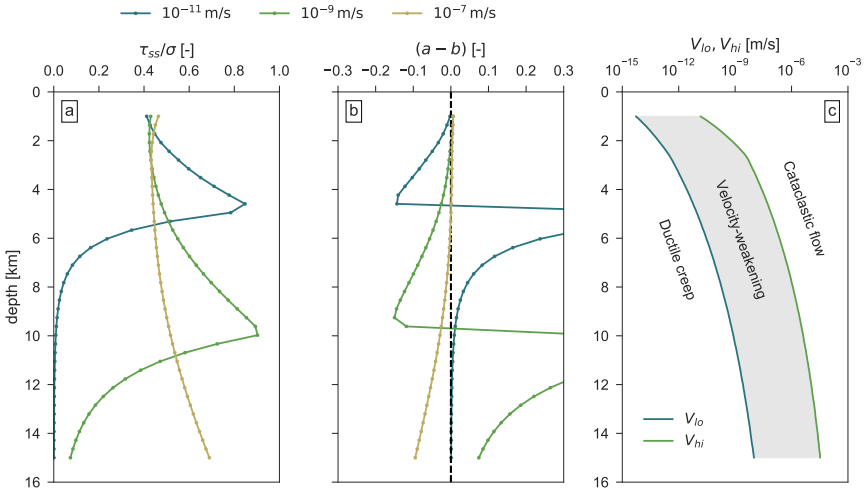

Fig. 5.10: Steady-state depth-profiles of a) steady-state coefficient of friction, and b) $(a-b)$, generated for imposed velocities of 10^{-11}, 10^{-9} (see legend), and 10^{-7} m s^{-1}, and $H = 0.5$. Panel c) shows the transitional velocities V_{lo} and V_{hi}, at which $(a-b) = 0$ (see Fig. 5.1), delineating the depth-dependence of the three main deformation regimes.

shown in Fig. 5.4 for three different imposed velocities, 10^{-11}, 10^{-9}, and 10^{-7} m s^{-1}, see Fig. 5.10. In this figure it can be observed that, while the general trends in the profiles of μ_{ss} and $(a-b)$ remain, the region in which $(a-b)$ is at a minimum shifts towards more shallow depths for lower fault slip velocities (and vice versa for higher slip velocities). For the profile of $V = 10^{-7}$ m s^{-1}, the transition of velocity-weakening to ductile creep occurs at a depth greater than shown in Fig. 5.10. The same observation can be made when considering the depth-dependence of the transitional velocities V_{lo} and V_{hi} (Fig. 5.10c), which delineate the three main deformation regimes. Moreover, during interseismic times, where $V \ll V_{imp}$ for locked fault segments in the seismogenic zone, the fault is expected to deform by ductile creep even in the 'brittle' region at intermediate depths, albeit at $V \ll V_{imp}$. If a given fault segment creeps at a rate lower than V_{lo} (blue line in Fig. 5.10c), shear stress will increase from the accumulating slip deficit, and so the creep rates increase following Eqn. (5.4a) up to V_{lo}. At slip

rates higher than V_{lo}, granular flow is expected to contribute to the total slip velocity, by which the fault enters the velocity-weakening regime at that particular depth, and accelerated slip is anticipated. From a stability perspective, V_{hi} can be considered a stable fixed point, whereas V_{lo} can be considered a half-stable fixed point.

5.5.2 Comparison of the RSF simulation with previous work

As a brief verification of the numerical method, we qualitatively compare our RSF simulation (based on CNS-derived parameters) with previous work by *Lapusta and Rice* (2003). In their simulations, values of $(a - b)$ were chosen to have a minimum value of -0.004 in the velocity-weakening region, about one order of magnitude smaller in absolute value than employed in this study ($(a - b) = -0.03$ for $H = 0.2$). Subsequently, the coseismic slip produced by the larger events in *Lapusta and Rice* (2003) is smaller than presented in this work, which we attribute to the difference in magnitude of $(a - b)$. The parameter values chosen by *Lapusta and Rice* (2003) were based on the experimental work of *Blanpied et al.* (1995, 1998) conducted on simulated granite gouges at hydrothermal conditions. The differences between the parameter values measured in the experiments and predicted by the CNS model are substantial, but it should be remarked that the gouge composition (poly-mineralic granite versus mono-mineralic quartz) prevents a direct comparison. Moreover, the observed trends in $(a - b)$ are qualitatively very similar, with a low-temperature velocity-strengthening region, an intermediate-temperature velocity-weakening region, and a very strong velocity-strengthening region at the highest temperatures (*Blanpied et al.*, 1998, their Fig. 7d). Dedicated laboratory tests and model analyses thereof should provide for a more detailed comparison with and validation of the CNS model. As mentioned earlier, the aim of this work is not to accurately simulate the rheology of a particular fault system. Rather, a direct comparison is made between the CNS model implementation and equivalent RSF simulations.

An important finding in the work of *Lapusta and Rice* (2003) is that for smaller values of D_c (maintaining constant $(a - b)$), the depth of nucleation migrates towards the base of the seismogenic zone, chosen there to lie near 14 km depth. Additionally, smaller magnitude events would nucleate near the base of the seismogenic zone and

would produce a non-repetitive sequence of larger and smaller seismic events. The results of *Lapusta and Rice* (2003) are best interpreted through consideration of a characteristic length scale "L_∞" introduced by *Rubin and Ampuero* (2005):

$$L_\infty \approx \frac{1}{\pi}\left(\frac{b}{b-a}\right)^2 L_b \tag{5.16a}$$

$$L_b = \frac{D_c G}{b\sigma} \tag{5.16b}$$

The use of L_∞ as the characteristic length scale is valid for the ageing state evolution law and with a/b close to but smaller than 1, as adopted in *Lapusta and Rice* (2003). Smaller values of D_c reduce the magnitude of L_∞, allowing for smaller seismic events to nucleate, in the case of *Lapusta and Rice* (2003) for a $D_c < 2$ mm. For $a \ll b$, as is the case in the RSF simulation presented in this study, the use of L_b would be more appropriate for a RSF framework in conjunction with the ageing law. In our RSF simulation, the large value of b offsets the relatively large value of D_c (up to 20 mm) to result in a characteristic length scale L_b that is sufficiently small to nucleate minor seismic events, similar to the simulations of *Lapusta and Rice* (2003).

Apart from the slip displacements achieved during the larger seismic events, the RSF simulation results presented here are qualitatively very similar to those of *Lapusta and Rice* (2003), and so we will now focus our attention on comparing the RSF simulation with the native CNS simulations.

5.5.3 Event magnitude and frictional stability

The most apparent difference between the native CNS simulations and the RSF simulation, is that both the maximum slip velocity and slip distance attained during a (sub-)seismic event are much larger in the RSF simulation, even though the relevant RSF parameters have been derived directly from the CNS near-steady state behaviour. This first of all shows that the steady-state behaviour predicted by the CNS model is not directly representative for transient, seismic cycle behaviour. The discrepancies between steady-state and transient behaviour mainly result from the velocity-dependence of the gouge porosity and frictional strength of CNS-controlled faults. At each depth

interval, the RSF parameters have been determined near the steady-state velocity V_{imp}. Particularly in the deeper sections of the brittle region (between 8 and 10 km), the estimated values of $(a-b)$ are strongly negative, and represent the maximum rate of velocity-weakening. However, as is apparent from Fig. 5.1, equivalent values of $(a-b)$ for the CNS model are expected to approach zero and turn positive as the fault accelerates towards coseismic slip velocities, mostly due to a decrease in magnitude of b (*Chen et al.*, 2017b). This is in strong contrast with the assumed constant values of a and b in the RSF simulation, which are representative only at $V = 10^{-9}$ m s^{-1}. It is expected that as $(a-b)$ approaches zero, the driving potential for accelerating slip vanishes. In other words, the fault stabilises as it accelerates, and so a larger initial potential for a frictional instability (i.e. more negative $(a-b)$, or larger perturbation from steady-state) is required for the development of a seismic event. This is also apparent in the differences between the two CNS simulations: in the initial simulation with $H = 0.5$ and $(a-b)$ in the range of -0.15, seismic slip velocities close to 1 m s^{-1} are achieved, whereas in the simulation with $H = 0.2$ and minimum $(a-b) = -0.03$, fault slip velocities do not exceed 0.01 m s^{-1}, and the events produced in this simulation would likely be considered slow slip events rather than fast earthquakes.

This transition from velocity-weakening at slow (interseismic) velocities to velocity-strengthening at higher (coseismic) velocities can be effectively simulated by a modified formulation of Eqn. (5.1) (*Okubo*, 1989):

$$\mu(V,\theta) = \mu^* - a\ln\left(\frac{V_c^*}{V} + 1\right) + b\ln\left(\frac{V_c\theta}{D_c} + 1\right) \tag{5.17}$$

where V_c^* and V_c are predefined cut-off velocities, so that at $\mathrm{d}\mu_{ss}/\mathrm{d}\ln(V) = (a-b)$ for $V \ll V_c$, and $\mathrm{d}\mu_{ss}/\mathrm{d}\ln(V) = a$ for $V_c \ll V \ll V_c^*$. For the purpose of this discussion, the role of V_c^* can be ignored. It has been shown by *Shibazaki and Iio* (2003) that such a modification facilitates the nucleation and propagation of slow slip transients for appropriate values of V_c. Hence, the small magnitude seismic events and slow slip transients produced in the CNS simulations can indeed be attributed to the transition from velocity-weakening to -strengthening, and is not a unique feature of the adopted fault rheology. This also offers perspectives for studying natural slow slip events using the CNS model formulation, as the transition from velocity-weakening to -strengthening emerges spontaneously from the underlying physical mechanisms.

5.5.4 Rupture nucleation

In a homogeneously stressed medium, nucleation of a frictional instability is expected to occur near the location of the smallest nucleation length scale (h_{nucl}). In the classical RSF framework with velocity-independent values of a and b, h_{nucl} can be estimated as L_b (Eqn. 5.16b) for $a \ll b$ (see Eqn. (5.B.6) and (5.B.7) in Appendix 5.B). Indeed, from Fig. 5.8 it is apparent that in the RSF simulation, nucleation of both small and large events occurs near the base of the seismogenic zone, where h_{nucl} assumes its smallest values. However, in the CNS simulation with $H = 0.5$ (Fig. 5.6), small slow slip events develop at shallow depths ($\sim$2 km), with no apparent surface expression. At the depth at which the slow slip events arrest, stress is concentrated and facilitates nucleation of a larger event. In the simulation with $H = 0.2$, the small slow slip events are absent, and nucleation of larger slow slip events initiates at 4 km with no precursory events. The size of the nucleation patch is generally large when compared to the RSF simulation. These observations suggest that near the moment of nucleation, the equivalent value of h_{nucl} is large in magnitude. As discussed in Section 5.5.3, the equivalent values of D_c, a, and particularly b depend on the instantaneous slip velocity and gouge porosity, and so h_{nucl} can no longer be represented by a constant value of L_b. The reduction of $(a - b)$ with increasing velocity, or more precisely, the reduction of b with increasing porosity cause h_{nucl} to grow, and the nucleation size to increase before coseismic velocities are attained. The slowly accelerating nucleation front in Fig. 5.6, propagating several kilometres before accelerating dynamically, attests to this. The larger nucleation size also explains the absence of the smaller seismic events in the CNS model, in contrast with the RSF simulation and those of *Lapusta and Rice* (2003). For a more accurate estimation of the nucleation length scales in the CNS simulations, an in-depth analysis of the fracture energy needs to be performed. We leave this analysis for future study, but a first-order estimate of the fracture energy for a large velocity-step is provided in Appendix 5.B.

A more detailed view of the process of nucleation and arrest of an accelerated slip event is presented in Fig. 5.11. In this figure, snapshots of fault slip velocity are plotted against a selected depth range for the fifth event produced by the CNS simulations with $H = 0.5$ and $H = 0.2$. These snapshots are spaced at a fixed number of time steps (which are of variable duration, depending on the rate of change of τ and ϕ), rather

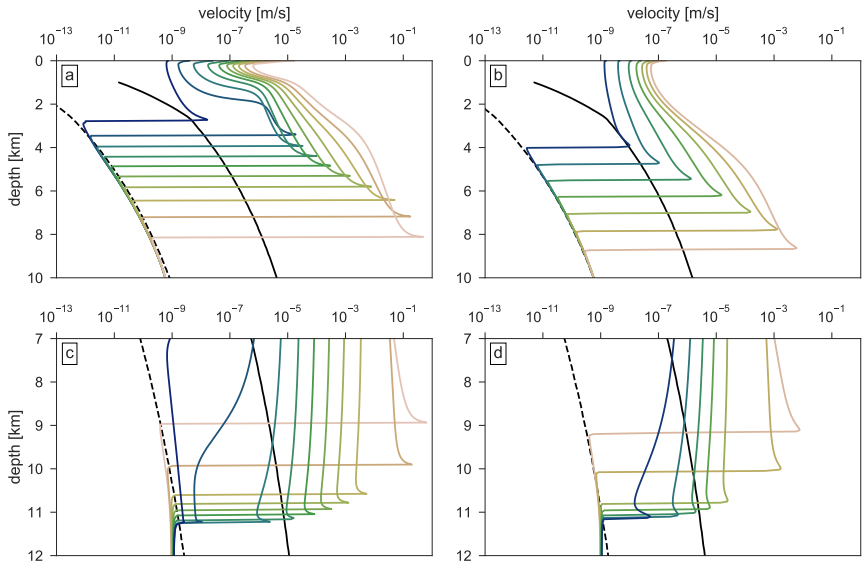

Fig. 5.11: Snapshots of fault slip velocity versus depth for the fifth event produced in the CNS simulations with $H = 0.5$, and $H = 0.2$. a) and b): Nucleation of the event for $H = 0.5$ and $H = 0.2$, respectively, with snapshots plotted up to the maximum slip velocity attained during the event. The first snapshot is coloured in dark blue, with subsequent snapshots increasing in brightness; c) and d): Arrest of the rupture in the ductile creep region for $H = 0.5$ and $H = 0.2$, respectively, with snapshots plotted from the moment of the maximum slip velocity onwards (subsequent contours are coloured with decreasing brightness); The snapshots are not equally spaced in time, as to clearly visualise both the nucleation, peak velocity, and arrest. The black solid and dashed lines indicate the transitional velocities V_{hi} and V_{lo}, respectively.

than at fixed time intervals, in order to clearly visualise the details of the rupture. For reference, the transitional velocities V_{hi} and V_{lo} are plotted as black solid and dashed lines, respectively. In Fig. 5.11a and b, snapshots of the nucleation process are plotted up to the maximum velocity attained during the event, for $H = 0.5$ and $H = 0.2$, respectively. In Fig. 5.11c and d, snapshots of the rupture arrest are plotted from the moment of maximum slip velocity up to the moment of arrest, for $H = 0.5$ and $H = 0.2$, respectively. The propagation velocity of the crack tip (V_{prop}) and slip

velocity behind the crack tip (V_{max}) are plotted in Fig. 5.12 against the depth at which the crack tip is situated, and as a function of nucleation time ($t_f - t$ where t_f is an arbitrarily chosen moment in time).

Fig. 5.11a shows that for the CNS simulation with $H = 0.5$, nucleation occurs near the transition of cataclastic flow to velocity-weakening, i.e. near the depth interval where $V_{hi} = V_{imp} = 10^{-9}$ m s^{-1}. At the moment of nucleation, fault slip at the nucleation front accelerates from 10^{-9} to 10^{-5} m s^{-1} over a short depth range of less than 1 km, then decelerates, stabilises, and continues to accelerate at a steady rate (as seen more clearly in Fig. 5.12a). From thereon, the nucleation zone expands aseismically over a distance of 2 km before reaching coseismic slip velocities. In the simulation with $H = 0.2$, the initial deceleration is absent, and the acceleration of fault slip is more gentle so that much lower slip velocities are attained (less by two orders of magnitude). Also note that at the moment of nucleation, the majority of the seismogenic (locked) zone creeps at a rate V_{lo} as anticipated in Section 5.5.1, indicating that the fault is critically stable.

Owing to the coupling with elasticity, the fault slip velocity and down-dip propagation velocity of the rupture tip are interrelated. Following *Ida* (1973) and *Ampuero and Rubin* (2008), this relation can accordingly be written as:

$$V_{prop} = \alpha V_{max} \frac{G}{\Delta\tau_{p\text{-}r}} \tag{5.18}$$

where V_{prop} is the rupture propagation velocity, V_{max} is the maximum slip velocity attained in the near-tip region, α is a shape factor of order 1 (*Hawthorne and Rubin*, 2013), and $\Delta\tau_{p\text{-}r}$ is the drop in shear stress between the rupture tip ('peak') and the residual stress. Generally, the frictional strength of a fault in the velocity-weakening and cataclastic flow regimes can be described as (*Chen and Spiers*, 2016):

$$\tau = \frac{\tilde{\mu} + \tan\psi}{1 - \tilde{\mu}\tan\psi}\sigma \tag{5.19}$$

For a sufficiently long recurrence time in which $\phi \to \phi_0$, and with negligible porosity evolution ahead of the advancing rupture front, the peak strength of a given fault

segment predicted by the CNS model is:

$$\tau_p = \frac{\tilde{\mu}_{max} + \tan\psi_0}{1 - \tilde{\mu}_{max}\tan\psi_0}\sigma \tag{5.20}$$

where $\tilde{\mu}_{max}$ is the grain-boundary coefficient of friction evaluated at V_{max}, and $\tan\psi_0 = 2H(\phi_c - \phi_0)$. The residual shear strength of the fault is obtained by evaluation of Eqn. (5.19) at the steady-state up-step velocity and porosity. At nucleation slip velocities the porosity behind the rupture tip is approximated by $\phi \approx \phi_c$, so that $\tau_r \approx \tilde{\mu}_{max}\sigma$. Hence, $\Delta\tau_{p\text{-}r}$ can be estimated as:

$$\Delta\tau_{p\text{-}r} \approx \frac{\tan\psi_0\left[1 + \tilde{\mu}_{max}^2\right]}{1 - \tilde{\mu}_{max}\tan\psi_0}\sigma \tag{5.21}$$

Since $\tilde{\mu}$ only has a minor depth- and velocity-dependence (varying by only 0.05 in absolute value over 4 orders of velocity change), the magnitude of $\Delta\tau_{pr}$ is practically constant with depth for the chosen distribution of model parameters ($\tan\psi_0$ and σ are constant below 3 km). By insertion of Eqn. (5.21) into (5.18), we obtain a relation between V_{prop} and V_{max}. This relation is tested by comparison with the measured values of V_{max} and V_{prop} for $\alpha = 1$, and is found to provide a near-exact match. In Fig. 5.12, V_{max} and V_{prop}, as well as the predicted V_{prop} based on Eqn. (5.18), are plotted against depth and against the nucleation time $t_f - t$.

A profound feature of the simulation with $H = 0.5$ (Fig. 5.12a) is the initial rupture deceleration phase, followed by a brief period of steady propagation of the rupture front. These phases are absent in the simulation with $H = 0.2$ (Fig. 5.12b), where only acceleration is observed. Similar behaviour has been observed in classical RSF simulations performed by *Kaneko and Ampuero* (2011), where two converging rupture fronts produced a stress concentration at the point of coalescence, after which nucleation expanded bilaterally. During this second phase of nucleation, the rupture and slip velocities initially decelerated towards a steady rate before accelerating again towards their final values. Likewise, in the simulation with $H = 0.5$, a small slow slip event prior to nucleation of the main event yields a residual stress concentration upon arrest. The main event then nucleates from this perturbation, resulting in a phase of deceleration and steady slip similar to the observations of *Kaneko and Ampuero* (2011). These authors also provide a theoretical basis for the observed behaviour based on fracture

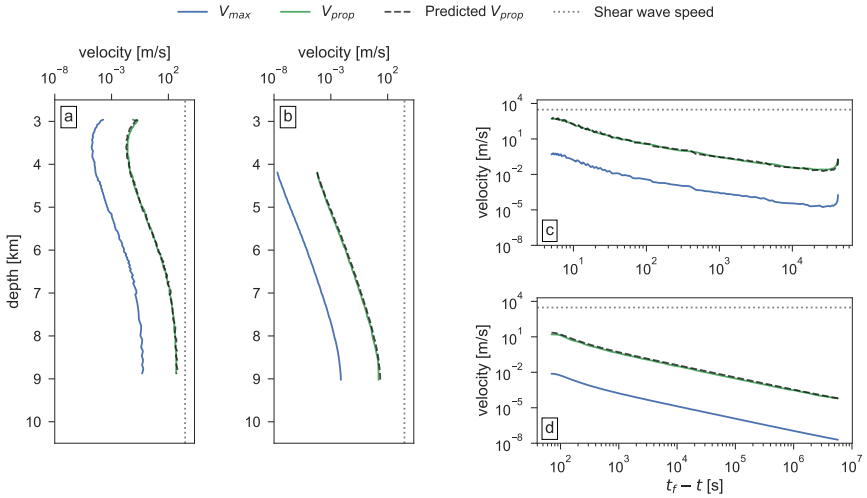

Fig. 5.12: Recorded slip velocity V_{max} and propagation velocity V_{prop} at the crack tip, as the rupture front propagates down-dip. Panels a) and c) correspond with Fig. 5.11a ($H = 0.5$), panels b) and d) correspond with 5.11c ($H = 0.2$). t_f in panels c) and d) is arbitrarily chosen as to remove non-linearities at small $t_f - t$. The dashed line in each panel represents the predicted V_{prop} based on Equations (5.18) and (5.21), the gray dotted line indicates the shear wave speed (3000 m s^{-1}).

mechanics. In the simulation with $H = 0.2$, no slow slip event and accompanying stress concentration is observed, and the nucleation front accelerates monotonically.

Another interesting result obtained for CNS simulations is the evolution of V_{prop} with the nucleation time $t_f - t$ (Fig. 5.12c and d). For classical RSF analyses and simulations, it has been found that $V_{prop} \propto (t_f - t)^{-1}$ (e.g. *Ampuero and Rubin*, 2008; *Dieterich*, 1992; *Noda and Lapusta*, 2013). This is observed for both the CNS simulations, as evidenced by the exponent of -1 in the double-logarithmic plots, up to the moment at which the maximum slip velocity is approached. The choice for t_f is arbitrarily made, and is taken here as a free ('fitting') parameter. For the RSF framework, t_f can be expressed in terms of the governing RSF parameters (*Rubin and Ampuero*, 2005), which in the CNS formulation are dependent on the slip velocity. In

spite of this, V_{prop} is still found to be proportional to $(t_f - t)^{-1}$ in the CNS simulations, alluding a more general basis for this feature.

Apart from the initial deceleration phase in the simulation with $H = 0.5$, the nucleation patterns of both CNS simulations are qualitatively very similar, suggesting that the underlying mechanisms for nucleation of slow and fast slip events are similar. In the simulation with $H = 0.5$, the seismogenic zone is sufficiently large for the rupture to propagate dynamically below a depth of 8 km. In the simulation with $H = 0.2$, the nucleation length is likely of similar size as the extent of the seismogenic zone, so that only slow slip events are produced, and the rupture is terminated before the phase of dynamic propagation is reached (*Kaneko et al.*, 2016).

5.5.5 Rupture arrest

Figures 5.1 and 5.10 also provide insight into the down-dip extent of the rupture in the CNS simulations. In the RSF simulation, the rupture is effectively arrested at the down-dip end of the velocity-weakening region by the large positive value of $(a - b)$, which forms a barrier to accelerated slip. In the CNS formulation, the predicted large values of $(a - b)$ at low velocities (or high temperatures) arise from ductile creep facilitated by pressure solution. In Fig. 5.1, the regime of ductile creep appears in the velocity range up to $V_{lo} = 5 \times 10^{-11}$ m s^{-1}, accompanied by large positive values of $(a - b)$. At intermediate velocities from 10^{-10} to 10^{-8} m s^{-1}, the competition between compaction induced by pressure solution and dilatant granular flow results in velocity-weakening behaviour. Hence, a sufficiently large perturbation in velocity or shear stress could trigger a transition from the low-velocity creep regime into the velocity-weakening regime. As a rupture front approaches the down-dip ductile region, the velocity perturbation could render parts of the initially velocity-strengthening region unstable and allow for continued rupture propagation across the brittle-ductile transition. This model prediction is consistent with the findings of pseudotachylyte veins within mylonite zones (e.g. *White*, 2001), indicating that the dynamic rupture propagated at least partly within ductile creeping regions. Similar results were obtained by *Shimamoto and Noda* (2014) with an extension of the RSF framework, motivated

by laboratory observations to include low-velocity plastic creep and a transition into (frictional) velocity-weakening (*Noda and Shimamoto*, 2010).

Fig. 5.11c and d show the details of rupture arrest, in which contours of fault slip velocity are plotted against depth. In the CNS simulation with $H = 0.5$ (Fig. 5.11c), the dynamic rupture decelerates from a depth of 9 km onwards, and is arrested at a depth greater than 11 km. From the steady-state simulations, the brittle-ductile transition is expected to occur near a depth of 10 km, below which deformation is accommodated by steady fault creep at a rate of V_{imp}. In this region, the stress ahead of the rupture can be estimated from Eqn. (5.15). The stress behind the rupture tip can still be approximated as $\tilde{\mu}_{max}\sigma$, so that the total stress drop is given by:

$$\Delta\tau = \frac{RTd}{AI_s\Omega}\frac{V_{imp}}{L} - \tilde{\mu}_{max}\sigma \tag{5.22}$$

Owing to the minor depth- and velocity-dependence of $\tilde{\mu}$, the depth-variation of $\Delta\tau$ in the ductile region is primarily controlled by the kinetics of pressure solution, so that $\Delta\tau$ decreases with depth. Based on fracture mechanics theory, *Ampuero et al.* (2006) argued that a rupture is arrested when the energy release rate of a crack decreases below the fracture energy. For a steeply decreasing $\Delta\tau(z)$, the depth of rupture arrest roughly equals the depth where $\Delta\tau \leq 0$, which lies at a depth of 11 km in our simulations. Similar reasoning for the down-dip extent of dynamic ruptures was put forward by *Brantut and Platt* (2017) and *Shimamoto and Noda* (2014). Since $\Delta\tau$ is independent of H, the same depth of rupture arrest is expected for both of the CNS simulations, as is evident from comparison of Fig. 5.11b and d. However, the extent of the rupture over which coseismic velocities are maintained likely still depends on H, as the fracture energy for the rupture depends on the magnitude of H. Furthermore, if the steady-state shear strength of the ductile region decays less rapidly with depth (e.g. owing to a lower geothermal gradient, or different deformation mechanisms operating), the extent to which the rupture propagates into the ductile region increases, and the rupture may penetrate a significant distance into regions with $\Delta\tau < 0$ before the energy release rate drops below the fracture energy (*Ampuero and Ben-Zion*, 2008). Notably, if the shear strength of the ductile region is to remain constant, as would be expected for an along-strike fault segment with no lateral temperature or compositional variations, the ductile velocity-strengthening regions would offer little resistance to the propagation of

a dynamic rupture, allowing for continued rupture as long as $\Delta\tau > 0$.

Using a classical RSF numerical framework, *Kaneko et al.* (2010) investigated the efficiency of rupture arrest of an impeding, velocity-strengthening patch enclosed by two seismogenic, velocity-weakening patches. The authors observed that the probability of a rupture propagating from the first seismogenic patch to the second is strongly related to the resistance offered by the enclosed velocity-strengthening patch. This resistance could be approximated as $C \approx 20\,(a-b)_{vs}\,\sigma D_{vs}$, with constant $(a-b)_{vs} > 0$, and D_{vs} denoting the length of the patch. The CNS model predicts two distinct regimes of steady-state velocity-strengthening: one ductile creep regime at low velocities $V < V_{lo}$ (or high temperatures), and one high-porosity, cataclastic regime at high velocities $V > V_{hi}$ (or low temperatures; see Fig. 5.1). In the cataclastic velocity-strengthening regime, $(a-b)$ is mildly increasing with velocity, and so if the velocity-strengthening patch as considered by *Kaneko et al.* (2010) is interpreted to operate in the cataclastic regime, the conclusions drawn by these authors are expected to be maintained by the CNS model. However, in the geological setting envisioned by *Kaneko et al.* (2010), i.e. a segment on a subducting plate interface at seismogenic depths, it is more likely that the velocity-weakening patches ('asperities') are embedded as lenses within a low-porosity, ductily or plastically deforming host material (*Fagereng and Sibson*, 2010; *Kimura et al.*, 2012). As discussed above, a sufficiently large perturbation in either stress or velocity could potentially trigger unstable slip within the velocity-strengthening matrix, facilitating continued rupture even for large positive values of $(a-b)$, as long as the total stress drop $\Delta\tau > 0$. Thus the scaling between the probability of continued rupture, asperity size, and asperity spacing needs to be re-evaluated for a CNS-type rheology. Similar considerations need to be made when dynamic weakening mechanisms operate within inherently velocity-strengthening regions, as was shown by *Noda and Lapusta* (2013).

5.5.6 Modes of fault slip

In classical RSF, slow slip transients have successfully been produced in cases where the nucleation length scale was sufficiently large with respect to the fault's spatial dimensions (*Hawthorne and Rubin*, 2013; *Kaneko et al.*, 2016; *Rubin*, 2008, see also

laboratory evidence by *Leeman et al.* (2016)). In our RSF simulation, where h_{nucl} is particularly small, very little creep is observed outside of the ductile region. In the upper 10 km of the fault, deformation is predominantly accommodated by coseismic slip. This is in strong contrast with the CNS simulations, which feature a mixture of inter-, co-, and postseismic slip on the brittle portion of the fault. Particularly in the CNS simulation with $H = 0.2$, slow slip transients are the dominant mode of slip. This behaviour is readily understood from the velocity-dependence of friction and $(a - b)$ predicted the CNS model (Fig. 5.1). CNS-governed faults may exhibit a host of deformation modes (ductile creep, stick-slip, and high porosity steady sliding) depending on the instantaneous gouge porosity and rate of deformation. Following a slip event, the porosity on a given section of the fault will be high, which facilitates rapid rates of granular flow and pressure solution, and the fault will deform at a rate $V > V_{imp}$. In segments that are identified as velocity-weakening at V_{imp}, the fault strengthens as the gouge densifies and the rate of fault slip diminishes, so that a transition is made back into the velocity-weakening regime where $V < V_{imp}$ (i.e. the fault returns to its 'locked' state). In shallow parts of the crust (e.g. upper 3 km in Fig. 5.6), no transition is made into the velocity-weakening regime as the porosities remain high owing to much lower compaction rates, and the fault continues to produce creep during the interseismic phase. Over the duration of a seismic cycle, faults may accumulate significant amounts of subseismic slip, even in seismogenic segments.

The degree of coupling of the individual fault segments can be quantified following the definition of interseismic coupling (ISC; *Kaneko et al.*, 2010), which is the ratio of slip deficit accumulated during the interseismic period over the imposed (or long-term) slip $V_{imp}\Delta t$. An ISC value of 1 implies full coupling, i.e. all slip being accommodated by non-interseismic slip, which in our models comprises of both coseismic slip, afterslip, and slip accommodated during nucleation. To be more precise, we define ISC as:

$$\mathrm{ISC} = 1 - \frac{\int V \mathrm{d}t_{int}}{V_{imp}\Delta t} \tag{5.23}$$

where t_{int} is the interseismic time during which the local slip velocity is less than 10^{-7} m s^{-1}. In this way, the value of ISC can be determined for each fault segment individually to produce a depth-profile of ISC (Fig. 5.13). When comparing the ISC of the RSF simulation with those of the CNS simulations, it becomes apparent that the

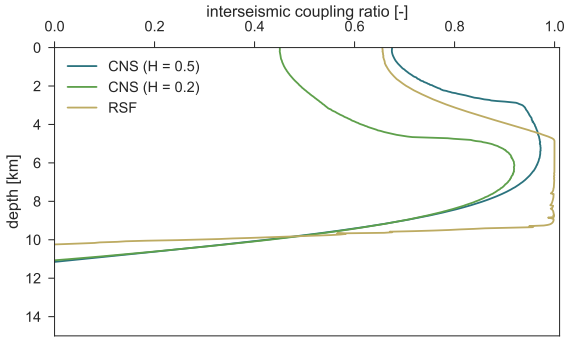

Fig. 5.13: Depth-profiles of the interseismic coupling ratio (ISC), defined as the cumulative sum of non-interseismic slip $V > 10^{-7}$ m s^{-1} over $V_{imp}\Delta t$, for all three simulations. An ISC of 1 indicates full coupling, a value of 0 indicates no coupling.

coupling predicted by the RSF simulation is stronger, and more clearly bounded at the down-dip extent of the locked patch. By contrast, both the CNS simulations show more gradual transitions in their degree of coupling, and generally predict less strong coupling than the RSF simulation. The operation of pressure solution creep in the CNS simulations relieves a portion of accumulated slip deficit within the seismogenic zone, particularly at the down-dip extent of the seismogenic zone (see also Fig. 5.11a), resulting in lower ISC values. Interestingly, the region of strongest increase in ISC values also coincides roughly with the depth of nucleation of all simulations (at 10 km for the RSF simulation, and at 3 and 5 km for the CNS simulations with $H = 0.5$ and $H = 0.2$, respectively).

As pointed out earlier, the CNS model predicts steady-state, velocity-strengthening fault slip both at very low and high rates of deformation, or alternatively, at low and high temperatures (since the mode of deformation is controlled by the relative rates of $\dot{\gamma}_{gr}$ and temperature-dependent $\dot{\gamma}_{ps}$). This suggests that the presence of steady fault slip at the surface does not necessarily imply low-porosity, ductile creep in a classical sense. Instead, the observed steady creep may well be hosted within high-porosity cataclasites that show little evidence of ductile or crystal plastic deformation mechanisms. The

micro-mechanical predictions from the CNS formulation for this regime match the general interpretation of (secondary) 'brittle creep' (*Perfettini and Avouac*, 2004), i.e. rate-strengthening cataclastic flow, that has previously been analysed in the context of postseismic afterslip and aftershock activity (*Marone et al.*, 1991; *Perfettini and Avouac*, 2007). In deeper sections of the fault, afterslip and steady creep are accommodated by pressure solution creep, which exhibits a linear viscous rheology at constant (zero) porosity. However, the incorporation of other (high-temperature) creep mechanisms, such as dislocation creep, could result in predominantly power-law rheology at greater depths. For a more in-depth investigation of postseismic creep phenomena, such mechanisms need to be considered, as much evidence points towards a power-law type of rheology operating in the lower crust and upper mantle (e.g. *Bürgmann and Dresen*, 2008; *Montési*, 2004).

5.5.7 The role of dynamic weakening processes and frictional heating

One important feature that is currently absent in both the CNS and RSF simulations employed in this study, is high-velocity dynamic weakening. At high slip velocities and accelerations, heat production by frictional sliding induces numerous thermally-assisted processes, including flash weakening (*Rice*, 2006), thermochemical pressurisation (*Mase and Smith*, 1985; *Platt et al.*, 2015), melt lubrication (*Hirose and Shimamoto*, 2003; *Nielsen et al.*, 2008), and gouge graphitisation (*Kuo et al.*, 2014). Which (combinations) of these mechanisms operate within faults strongly depends on gouge composition and fault zone transport properties, but generally speaking any of these mechanisms has the potential of dramatically reducing the fault's resistance to slip, allowing the fault to operate at extremely low shear stress (*Tullis*, 2007). It has been shown in several numerical studies that incorporation of dynamic weakening mechanisms strongly affects the magnitude of maximum slip velocity and seismic moment (*Noda and Lapusta*, 2010, 2013; *Thomas et al.*, 2014). For the case of the CNS simulations presented in this work, it is expected that coseismic slip velocities are intensified by dynamic weakening, possibly producing more coseismic slip at or near the surface (c.f. *Noda and Lapusta*, 2013).

More importantly, dynamic weakening mechanisms allow the fault to operate at low shear stresses. Recall from Section 5.5.5 that the maximum down-dip extent of the rupture is controlled by the total stress drop $\Delta\tau$, which reduces to zero as the stress ahead of the rupture decays with depth, while maintaining a near-constant residual strength behind the rupture tip. When the rupture grows to a size that is sufficiently large to attain coseismic velocities, the activation of dynamic weakening induces a larger stress drop and facilitates extended rupture depths (*Brantut and Platt*, 2017). Continuing this reasoning, a critical length scale for down-dip rupture propagation it is anticipated: when the length scale for nucleation of a dynamic event is of similar size as the extent of the seismogenic zone (as is the case for the CNS simulation with $H = 0.2$), no coseismic velocities are attained before the rupture is arrested in the ductile region. Conversely, when the nucleation length is small enough with respect to the dimensions of the fault, coseismic velocities can be attained and dynamic weakening mechanisms can be triggered, strongly promoting extended rupture. Based on the two CNS simulations presented here, it is expected that this threshold length scale depends on H, rendering the down-dip extent of the rupture sensitive to H (and other parameters that affect h_{nucl}) when dynamic weakening is considered.

In addition to triggering of dynamic weakening mechanisms, frictional heating may further affect the fault rheology by enhancing the rates of pressure solution as a result of a locally perturbed geotherm. For many gouge compositions, an increase in ambient temperature would likely result in enhanced pressure solution creep rates, as the solubility and ionic diffusivity of many materials monotonically increase with temperature (e.g. *Dewers and Hajash*, 1995; *Spiers et al.*, 2004; *Van Noort et al.*, 2008a). Increased pressure solution creep rates may temporarily result in enhanced rates of afterslip. Since the perturbation of the geotherm is likely confined to the vicinity of the rupture patch, residual stress concentrations at the arrested rupture tip may be relieved by this enhanced creep. One notable exception to this is calcite, which is expected to obey a non-monotonous temperature-dependence of diffusion-controlled pressure solution rates (*Verberne et al.*, 2014a; *Zhang et al.*, 2010). Residual heat produced by a seismic event may thus result in a complex spatio-temporal distribution of fault creep and frictional stability of calcite-rich gouges. We leave further investigation into the CNS-governed behaviour of carbonates for future studies.

5.5.8 Implications and outlook

From simple spring-block analyses, it can be shown that laboratory friction data is well represented by the CNS microphysical model, and that for small-amplitude velocity-step tests the CNS model closely resembles rate-and-state friction transients (*Chen and Spiers*, 2016). The linearised approximations of the equivalent RSF parameters a, b, and D_c can accurately relate the CNS framework to classical RSF for small perturbations of velocity and state (*Chen et al.*, 2017b). The procedure adopted in this study to obtain the equivalent RSF parameters from the CNS model implementation resembles typical laboratory procedures (i.e. velocity-step tests, ideally conducted at in-situ PT-conditions), yet the resulting transient behaviour produced in the RSF simulation does not correspond to the native CNS model from which the RSF parameters have been derived. This has the following implication for the extrapolation of laboratory results to nature: when laboratory faults that obey CNS-type behaviour (i.e. gouges accommodating deformation by granular flow and pressure solution at appreciable rates) are characterised by classical rate-and-state friction, then the parameters resulting from that characterisation are only accurate at the steady-state sliding velocities that were employed in the laboratory test. At deformation rates and timescales that deviate from the laboratory test conditions, it is likely that the derived parameters no longer describe the transient mechanical response of a fault, and so it is unjustified to use rate-and-state friction as a means for extrapolation of laboratory results to natural scales and conditions.

Instead, using microphysically-based models may offer an alternative for the interpretation of laboratory results, so that the mechanics of natural faults can be represented more accurately. The implementation of microphysical models into (existing) seismic cycle simulators can be used to study the non-steady state behaviour of faults that are heterogeneous in both composition and state of stress. The rheological complexity associated with this new class of numerical models is a requirement for capturing the complexity exhibited by natural fault systems. While the microphysical models pose new challenges, they also offer opportunities for understanding the mechanics of rock friction at a more fundamental level by connecting laboratory, numerical, and field studies.

5.6 Conclusions

In this study, we compare the outcomes of seismic cycle simulations that are based on classical rate-and-state friction (RSF) with those based on an implementation of the CNS (*Chen-Niemeijer-Spiers*) microphysical model. From the comparison of the two classes of models, we conclude the following:

- The implementation of the CNS microphysical model is capable of producing seismic cycle transients that have classically been ascribed to rate-and-state friction.
- By simulating laboratory velocity-step tests using the CNS model implementation, the equivalent rate-and-state friction parameters a, b, and D_c can be obtained for near-steady state deformation. However, rate-and-state friction simulations performed with these parameters predict a seismic cycle evolution that is dissimilar from the native CNS model simulations.
- Many of the features of the CNS simulations and differences with the RSF simulation, such as the relatively small event magnitude, the extent of the rupture, and occurrence of slow slip events, can be explained by the predicted velocity-dependence of $(a - b)$. In particular, the transitions between the main deformation regimes play a pivotal role in the rupture nucleation and arrest.
- Owing to the strong velocity-dependence of its rheological properties, we argue that a CNS-governed fault (undergoing deformation by pressure solution and granular flow) cannot be readily described by assumed constant RSF parameters, and that laboratory results of the RSF parameters are only valid for the conditions under which they were obtained.

As is commonly the case, the applicability of the microphysical model employed in this study is bounded by the validity of its assumptions and the quality of the input parameters. However, since this type of models offers a clear physical interpretation of both its assumptions and parameters, firm assessments can be made regarding the accuracy of the model predictions, and dedicated laboratory experiments can

be designed to constrain the model parameters to a sufficient degree. Hence, when implemented within numerical frameworks, microphysical models hold potential for improving our understanding of fault rheology and earthquake mechanics through the study of micro-scale processes.

Appendices

5.A Description of the boundary element method

Within our earthquake cycle modelling framework, we presume the existence of a fault with fixed, known geometry that is embedded within a linearly elastic medium. Slip occurs on this prescribed fault surface, and represents the integral of inelastic strain across the width of the fault zone, though the spatial distribution of deformation at a scale smaller than the fault zone width is not explicitly modelled. The mechanics of the fault is only modelled explicitly up to a given depth. In the upper, frictional portion, the fault rheology is governed by a friction law. In the remaining, deeper part of the fault, steady slip is prescribed at a rate V_{imp}, accumulating slip as $d_{imp} = V_{imp} \times t$. This lower 'substrate' of the fault is assumed to extend down into infinity.

To obtain the shear stress at a given point on the frictional part of the fault, we adopt the quasi-dynamic approximation (*Rice*, 1993):

$$\tau(x,t) = -\mathcal{K}\left[d - d_{imp}\right](x,t) - \eta V(x,t) \tag{5.A.1}$$

The first term on the right hand side represents the static elastic stress induced by slip elsewhere on the fault, which involves a linear functional $\mathcal{K}[d]$, for which analytical expression are available if the model geometry is simple, e.g. a homogeneous elastic half-space. The second term on the right hand side represents the stress drop due to seismic wave radiation in the direction normal to the fault plane. The parameter η is a

damping factor that assumes a value of $G/2c_s$, with G being the shear modulus, and c_s the shear wave speed (*Rice*, 1993). By employing radiation damping, unbounded limit cycle growth accompanied with unrealistic fault slip velocities is inhibited. The radiation damping representation would be exact if slip were spatially uniform, in which case seismic waves would only be radiated in the direction normal to the fault plane (see *Ampuero et al.*, 2002).

The frictional part of the fault surface is decomposed into a mesh of N non-overlapping elements, and slip is assumed to be uniform inside each element. The following discrete version of Eqn. (5.A.1) is then obtained:

$$\tau_i(t) = -K_{ij}\left[d_j(t) - d_{imp}\right] - \eta V_i(t) \tag{5.A.2}$$

Here, the Einstein summation convention is adopted. The above equation involves the computation of a stress transfer kernel, a matrix whose coefficient K_{ij} represents the shear stress induced on the i-th fault element by a unitary slip on the j-th fault element. The kernel can be computed via existing formulas, e.g. Okada formulas for rectangular elements in a 3D elastic half-space (*Okada*, 1985). QDYN employs the spectral approach in finite-size domains introduced by *Cochard and Rice* (1997), together with efficient evaluation of stresses as a convolution via FFT. An alternative form of the equations, more convenient for numerical implementation, is obtained by temporal differentiation of (5.A.2):

$$\frac{\mathrm{d}\tau_i}{\mathrm{d}t} = -K_{ij}\left[V_j(t) - V_{imp}\right] - \eta\frac{\mathrm{d}V_i(t)}{\mathrm{d}t} \tag{5.A.3}$$

When the fault rheology is governed by the RSF framework, it is customary to partition $\mathrm{d}\tau_i/\mathrm{d}t$ into partial derivatives with respect to V and θ, so that Eqn. (5.A.3) can be rewritten explicitly for $\mathrm{d}V_i/\mathrm{d}t$. Complemented with a state evolution law (e.g. Eqn. (5.2)), this system of ordinary differential equations (ODE) can be rearranged and solved in the form:

$$\frac{\mathrm{d}\mathbf{X}}{\mathrm{d}t} = \mathbf{F}(\mathbf{X}, t) \tag{5.A.4}$$

where $\mathbf{X}(t)$ is a vector comprising the collection of $V_i(t)$ and $\theta_i(t)$ variables on all fault elements. This system is then solved by a standard, explicit ODE solver with adaptive time stepping. In the CNS model formulation, as described in Section 5.3.1, it

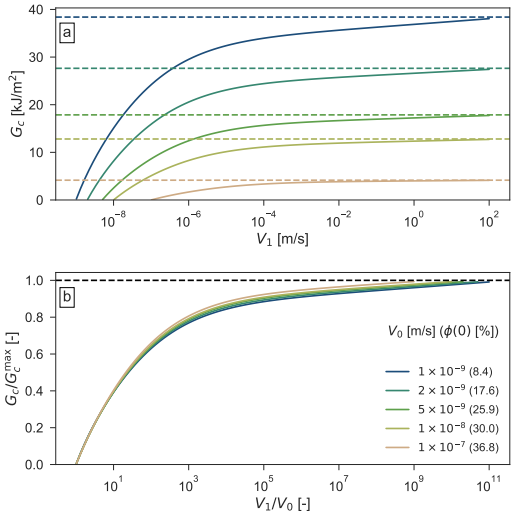

Fig. 5.B.1: The fracture energy G_c predicted for the CNS model, as obtained from numerical integration. a) Magnitude of G_c as a function of the up-step velocity V_1; b) Ratio of G_c to the analytical upper bound G_c^{max} as a function of the velocity-step size V_1/V_0. The analytical upper bounds are plotted as dashed horizontal lines.

is required to solve for $\tau_i(t)$ rather than $V_i(t)$, and $\theta_i(t)$ is replaced by $\phi_i(t)$, following Eqn. (5.12). The vector $\mathbf{X}(t)$ now contains $\tau_i(t)$ and $\phi_i(t)$, and the local fault slip velocity V_i is calculated as $V_i = L_i\,(\dot{\gamma}_{gr,i} + \dot{\gamma}_{ps,i})$.

5.B Slip weakening and characteristic length scale

In the classical rate-and-state friction framework, much work focuses on the analysis of characteristic length scales, such as the nucleation length and process zone width (*Ampuero and Rubin*, 2008; *Rice and Ruina*, 1983; *Rubin and Ampuero*, 2005). These are generally obtained by comparison of the fault stiffness with the critical stiffness, or the rate of fault weakening with increasing fault slip. For the derivation of the

characteristic length scale for the CNS formulation, we analyse the weakening rate of a fault that accommodates shear strain through granular flow, and that is subjected to an instantaneous velocity-step $V_0 \rightarrow V$ in an infinitely stiff medium.

We first consider the rate of frictional weakening, decomposed into partial derivatives of porosity and velocity:

$$\frac{\mathrm{d}\tau}{\mathrm{d}x} = \frac{1}{V}\left(\frac{\partial\tau}{\partial\phi}\frac{\mathrm{d}\phi}{\mathrm{d}t} + \frac{\partial\tau}{\partial V}\frac{\mathrm{d}V}{\mathrm{d}t}\right) \tag{5.B.1}$$

For an infinitely stiff medium, $\mathrm{d}V/\mathrm{d}t = 0$. Outside of the ductile creep regime (i.e. $\dot{\gamma}_{gr} \gg \dot{\gamma}_{ps}$), the frictional strength of the fault is given by *Chen and Spiers* (2016):

$$\tau = \frac{\tilde{\mu} + \tan\psi}{1 - \tilde{\mu}\tan\psi}\sigma \tag{5.B.2}$$

Hence, $\partial\tau/\partial\phi$ can be accordingly written as:

$$\frac{\partial\tau}{\partial\phi} = -2H\sigma\frac{1+\tilde{\mu}^2}{\left(1-\tilde{\mu}\tan\psi\right)^2} \tag{5.B.3}$$

Combined with Eqn. (5.10b) for $\mathrm{d}\phi/\mathrm{d}t$, the slip weakening rate can now be obtained as:

$$\frac{\mathrm{d}\tau}{\mathrm{d}x} = \frac{2H\sigma}{V}\frac{1+\tilde{\mu}^2}{\left(1-\tilde{\mu}\tan\psi\right)^2}\left(1-\phi\right)\left(\dot{\varepsilon}_{ps} - \tan\psi\frac{V}{L}\right) \tag{5.B.4}$$

The minimum nucleation length (i.e. fastest weakening rate) is obtained when $\phi \approx 0$, at which point $\dot{\varepsilon}_{ps} \ll \tan\psi V/L$, so that the above relation can be further simplified to:

$$\frac{\mathrm{d}\tau}{\mathrm{d}x} = -\frac{4H^2\phi_c\sigma}{L}\frac{1+\tilde{\mu}^2}{\left(1-2\tilde{\mu}H\phi_c\right)^2} \tag{5.B.5}$$

Finally, by equating the critical stiffness k_{cr} to the stiffness of an elastic crack G/h, G being the effective shear modulus and h the crack length, we solve for the minimum crack length h_{cr} which could facilitate a frictional instability:

$$h_{cr} = \frac{GL}{4H^2\phi_c\sigma}\frac{\left(1-2\tilde{\mu}H\phi_c\right)^2}{1+\tilde{\mu}^2} \tag{5.B.6}$$

By inserting analytical expressions for b and D_c as given by *Chen et al.* (2017b) into Eqn. (5.B.6), we obtain the familiar result for the crack process zone width (*Rubin and Ampuero*, 2005):

$$h_{cr} = \frac{D_c G}{b\sigma} = L_b \tag{5.B.7}$$

For numerically stable simulations, the spatial resolution Δx should be smaller than h_{cr}. In the simulations with $H = 0.5$ and $H = 0.2$, h_{cr} assumes values of 9.1 and 70.8 m, respectively, which are both sufficiently large compared to $\Delta x = 1.8$ m to ensure a well-resolved rupture process zone.

Alternatively, instead of assuming the end-member case for which $\phi = 0$, one could integrate Eqn. (5.10b) over slip distance x to obtain the weakening curve $\tau(x)$, from which the fracture energy can be derived. When we maintain the assumption that $\dot{\varepsilon}_{ps} \ll \tan\psi V/L$, which is valid for $\phi > 0$ when V is relatively high, integration from $\phi(0)$ to ϕ yields:

$$\phi(x) = \frac{\exp\left(-2H\frac{x}{L}\left[1-\phi_c\right]\right) - \phi_c\frac{1-\phi(0)}{\phi_c-\phi(0)}}{\exp\left(-2H\frac{x}{L}\left[1-\phi_c\right]\right) - \frac{1-\phi(0)}{\phi_c-\phi(0)}} \tag{5.B.8}$$

Substitution of $\phi(x)$ into Eqn. (5.B.2) gives the evolution of $\tau(x)$, from which the fracture energy G_c can be derived as:

$$\begin{aligned} G_c &= \int_0^\infty \left[\tau(x) - \tau(\infty)\right] \mathrm{d}x \\ &= \frac{\left(1+\tilde{\mu}^2\right) L\sigma}{1-2H\tilde{\mu}\left(\phi_c - 1\right)} \ln\left(\frac{1-\phi(0)}{1-\phi_c}\frac{1}{1-\tilde{\mu}\tan\psi_0}\right) \end{aligned} \tag{5.B.9}$$

where $\tan\psi_0 = 2H\left(\phi_c - \phi(0)\right)$. The initial condition $\phi(x=0)$ can be obtained from steady-state solutions (see *Chen et al.*, 2017b), although it can be expected that $\phi(0) \approx \phi_0$ for 'locked' seismogenic patches experiencing long interseismic durations. The grain boundary friction coefficient $\tilde{\mu}$ is evaluated at the up-step velocity, adding a minor velocity-dependent contribution to G_c.

Ignoring the operation of pressure solution is mathematically equivalent to assuming that $V \to \infty$. This makes G_c largely independent of V, and only provides an upper bound to the fracture energy. Exact evaluation of G_c for arbitrary velocity-step

amplitudes is possible but impractical when no other approximations are made. Instead, we evaluate G_c numerically to get a more accurate estimate. This is done for various initial velocities V_0 and corresponding steady-state porosities $\phi(0)$ (see Fig. 5.B.1). Larger values of V_0 and subsequently $\phi(0)$ are predicted by Eqn. (5.B.9) to result in lower values of the analytical upper bound G_c^{max}. Indeed, from numerical integration we obtain that G_c approaches G_c^{max} for larger magnitudes of the up-step velocity V_1, and that G_c^{max} decreases with increasing $\phi(0)$ (Fig. 5.B.1a).

When the numerically obtained values for G_c are normalised to its corresponding upper bound, and plotted against the magnitude of the velocity-step V_1/V_0, the data converge to a single curve (Fig. 5.B.1b). For small velocity-steps (smaller than a factor of 10), no effect of the initial velocity is apparent. For larger velocity-steps, there is a small but noticeable effect of V_0, with higher initial velocities (and porosities) resulting in a larger G_c/G_c^{max} for a given velocity-step size. The general trends, however, remain.

Chapter 6

Microphysical mechanisms behind giant earthquakes and seismic supercycles

Martijn P. A. van den Ende, Jianye Chen,
Jean-Paul Ampuero, and André R. Niemeijer

Submitted to: *Nature Geoscience*

Abstract

Field observations suggest that natural fault zones are commonly heterogeneous in their composition, exhibiting alternations of frictionally stable and unstable materials (defined nominally to a reference plate velocity). This complexity prevents a simple interpretation of seismological observations based on laboratory results. To relate laboratory and field observations, we investigate the seismic cycle behaviour of heterogeneous faults of which the rheology is governed by a microphysical model for fault rock deformation. In particular, we focus on the occurrence of frictional instabilities in which the entire fault fails in a single event ('T-instabilities'), rupturing through both nominally stable and unstable fault segments (defined relative to the plate convergence rate), as opposed to instabilities that rupture only a part of the fault. A model T-instability may be analogous to giant ($M_w > 9$) earthquakes occurring in major subduction zones, and so uncovering the processes that govern this type of events may provide useful insights for seismic hazard assessments. The mechanics behind T-instabilities are first investigated in a simplified system of a nominally velocity-weakening asperity embedded in a nominally velocity-strengthening matrix. We subsequently study the occurrence of T-instabilities in more complex heterogeneous fault systems, in which the fault zone geometry and microphysics are based on geological observations of exhumed faults and laboratory interpretations of friction. We find that the emergence of T-instabilities in these simulations is governed by a rheological transition that occurs within nominally stable segments of the fault, rendering large parts (or the entirety) of the fault unstable and causing initially stable segments to propagate dynamic ruptures rather than arresting them. In turn, this rheological transition is driven by an accumulating slip deficit which raises the average stress on the fault near a critical level at which the transition occurs. This makes T-instabilities time-predictable on the basis of the seismic moment accumulation rate. T-instabilities in the model are thought to be analogous to giant earthquakes in nature, and so the proposed mechanism for T-instabilities offers a microphysical interpretation for the origin of multi-segment ruptures and megathrust earthquakes.

6.1 Introduction

One major question in seismic hazard assessments, is that of periodicity and predictability of earthquakes. On the timescale of instrumental recordings, seismic events tend to occur quasi-randomly in time and space, reflecting a stochastic origin and making them unpredictable based on the statistics of past events. The failed prediction of the seemingly periodic Parkfield sequence (*Bakun et al.*, 2005) attests to this. Great earthquakes (with moment magnitudes $M_w > 8.0$) are of particular interest in the assessment of hazard and risk, but exhibit recurrence times up to several hundreds of years, far exceeding our instrumental time-span.

Over the last two decades or so, innovative techniques in palaeoseismology have substantially expanded our catalogue of (pre)historic seismic events, with recorded events dating back over 10 000 years (*Benedetti et al.*, 2013; *Clague*, 1997; *Goldfinger et al.*, 2012; *Ratzov et al.*, 2015; *Sieh et al.*, 2008). The improved catalogue completeness, and accuracy of dating methods and seismic moment estimates, have led to numerous reports of supercycle behaviour, in the form of periodic earthquake clustering (*Benedetti et al.*, 2013; *Philibosian et al.*, 2017; *Ratzov et al.*, 2015; *Sieh et al.*, 2008) or occurrence of anomalously large events ('superimposed cycles'; *Goldfinger et al.*, 2013; *Mannen et al.*, 2018; *Satake*, 2015). Furthermore, millenary recurrence of $M_w \geq 9.0$ earthquakes has been anticipated for the Main Himalayan Thrust and Japan Trench regions on the basis of geodetic estimates of moment accumulation rates (*Satake and Fujii*, 2014; *Stevens and Avouac*, 2016). In estimating the recurrence interval and magnitude of such megathrust events, it is assumed that all earthquakes follow a Gutenberg-Richter distribution. However, 'non-characteristic' earthquakes as preserved in palaeoseismic records may not follow well-behaved frequency-magnitude relations (*Satake and Atwater*, 2007), hampering assessments based on catalogue statistics.

To further the understanding of great ($M_w > 8.0$) and giant ($M_w > 9.0$) earthquakes, statistical correlations have been sought between subduction plate properties (relative velocity, slab bending, interface width, etc.) and the occurrence of megathrust events (*Heuret et al.*, 2011). Although certain trends have been discerned, e.g. between plate age and maximum earthquake size (*Ruff and Kanamori*, 1980), or plate velocity and seismicity rate (*Ide*, 2013), the correlations often suffer from outliers, sizeable

uncertainties, and/or a large spread in the data. It seems, however, that most subduction fault segments are intrinsically capable of generating great or giant earthquakes of which the ruptures span a large portion, if not all, of their plate interfaces (*Kagan*, 1997; *McCaffrey*, 2008). Palaeoseismic and instrumental recordings of great earthquakes include Cascadia, Kuril Islands, Japan Trench, Sunda Arc, Nankai Trough, Chile, and others regions. Some of these regions exhibit high seismicity rates (Japan Trench, Sumatra; *Satake*, 2015; *Sieh et al.*, 2008), while others are currently quiescent except for episodic slow slip (Cascadia; *Gomberg*, 2010) and deep tremor (Nankai; *Obara*, 2002), or generally have low levels of background seismicity (Andaman, Chile Maule; *Ide*, 2013). In spite of these large contrasts in seismic character, the seemingly universal appearance of great earthquakes in all subduction settings (*McCaffrey*, 2008), is suggestive of a common underlying mechanism.

Much of our knowledge of the behaviour of faults comes from laboratory observations and corresponding interpretations (e.g. *Blanpied et al.*, 1998; *He et al.*, 2013, 2016; *Marone et al.*, 1990). Most commonly, laboratory friction tests are conducted on bare rock-rock interfaces or fault gouges of uniform composition (i.e. no spatial variation in fault rock material). However, numerous field studies have shown that natural faults are spatially heterogeneous in both their composition and structure (*Collettini et al.*, 2011; *Fagereng*, 2011; *Rowe et al.*, 2011). For example, exhumed mature fault zones often include lenses of competent material embedded in a less-competent matrix, up to scales of several metres or more (*Fagereng*, 2011; *Fagereng and Sibson*, 2010; *Kimura et al.*, 2012; *Niemeijer and Vissers*, 2014). At a smaller (up to centimetre) scale, similar features are observed in drill core materials retrieved in drilling campaigns (e.g. *Bradbury et al.*, 2011; *Holdsworth et al.*, 2011; *Kirkpatrick et al.*, 2015). This highlights a fundamental limitation of laboratory experiments to capture the behaviour of heterogeneous natural fault systems, as the size of test samples falls in the range of millimetres to centimetres. On occasion, in experimental studies where heterogeneity was simulated by juxtaposition of different fault rock materials (*Carpenter et al.*, 2014), significant differences in frictional behaviour are observed, further underlining the relevance for studying heterogeneous systems.

In an attempt to upscale the laboratory results in space and time to nature, (numerical) models of fault friction are often employed (e.g. *Hillers et al.*, 2007; *Lapusta*

et al., 2000; *Liu and Rice*, 2009; *Tse and Rice*, 1986). In particular, modelling of fault frictional behaviour and the seismic cycle is conducted in the rate-and-state friction framework, which provides an empirical description of the magnitude of the coefficient of friction μ as a function of fault slip velocity V and 'state' θ. The original formulation, as proposed by *Dieterich* (1979) can be written as:

$$\mu(V,\theta) = \mu^* + a \ln\left(\frac{V}{V^*}\right) + b \ln\left(\frac{V^*\theta}{Dc}\right) \tag{6.1}$$

where μ^* is a reference coefficient of friction obtained at a reference velocity V^*, a and b are proportionality constants for the instantaneous 'direct' and time-dependent 'evolution' effects, respectively, and D_c is a characteristic slip distance over which the fault evolves towards its new steady-state. The time-dependence of the state parameter θ is described by a state evolution law that takes the general form $\mathrm{d}\theta/\mathrm{d}t = f(V,\theta,...)$. When $a > b$ (or $(a-b) > 0$) the fault is velocity-strengthening, whereas the converse indicates velocity-weakening. In this framework, spontaneous frictional instabilities (i.e. accelerated slip above the driving velocity, such as stick-slips earthquakes) can be generated when $(a-b) < 0$ (i.e. the fault is velocity-weakening). For a given material, and under a given set of experimental conditions, a, b, and D_c may be constrained by laboratory friction tests (e.g. *Blanpied et al.*, 1995, 1998; *He et al.*, 2016). These values are then typically taken as time-constants by numerical studies. However, the empirical nature of rate-and-state friction limits its predictive capabilities to the range of conditions and spatial or temporal scales that are attainable in a laboratory setting.

Alternatively, microphysical models allow for interpretation of their parameters in terms of thermodynamic or material quantities, such as the fault temperature, nominal grain size, or solubility of the solid phase (see e.g. *Chen and Spiers*, 2016; *Den Hartog and Spiers*, 2014). This facilitates extrapolation of laboratory results to natural scales and conditions, with an independent assessment of the validity of the model outcomes. Recently, *Van den Ende et al.* (2018a) (see also Chapter 5) demonstrated how the implementation of a particular microphysical model, the *Chen-Niemeijer-Spiers* model (from here on referred to as the 'CNS' model; *Chen and Spiers*, 2016; *Niemeijer and Spiers*, 2007), into the seismic cycle simulator QDYN (*Luo et al.*, 2017a) could produce a range of fault slip behaviours previously ascribed only to rate-and-state friction, while having a direct physical underpinning. In its essence, the CNS microphysical

model considers the interplay between a time-dependent compaction mechanism, such as pressure solution creep, and dilatant granular flow. The CNS model predictions for granular gouges are supported by a wide range of laboratory observations, and are readily understood in terms of micro-scale observable quantities (such as nominal grain size or slip zone thickness). In this work, we continue to use the implementation described in Chapter 5 and by *Van den Ende et al.* (2018a) to examine the behaviour of heterogeneous faults, and to investigate the mechanisms behind giant earthquakes and seismic supercycles from a microphysical standpoint. We discuss the model outcomes in relation to previous insights gained from rate-and-state friction, and describe how the microphysical model approach can contribute to our understanding of earthquake mechanics and the seismic cycle.

6.2 Key observations

Owing to the enormous spatial and temporal scales inherent to faults and earthquakes, relevant observations need to be sourced from a range of scientific disciplines. By combining key observations from various fields, a broader picture may emanate that includes important model constraints and hypotheses to be tested. We review these observations in the following sections.

6.2.1 (Palaeo)seismological and geodetic observations of earthquake recurrence

Since our instrumental record of seismic events covers only a period of about 100 years in most places, the statistical basis for forecasting great and giant earthquakes is slim. Palaeoseismology aims to complement the instrumental catalogue by considering written accounts of historical earthquakes, as well as geological evidence in the form of e.g. dated deep-sea turbidites (*Goldfinger et al.*, 2012; *Ratzov et al.*, 2015), estuarine and tsunami deposits (*Cisternas et al.*, 2005), coral microatoll growth (*Philibosian et al.*, 2017; *Sieh et al.*, 2008), and cosmogenic isotope measurements on exposed fault scarps (*Benedetti and van der Woerd*, 2014). While the absolute timing and magnitude

of geologically recorded events are not as precise as written accounts and instrumented events, they offer means for studying the occurrence of great earthquakes that date back thousands of years. Examples of well-studied areas of (palaeo)seismic activity include Cascadia (*Clague*, 1997; *Goldfinger et al.*, 2003, 2012; *Nelson et al.*, 2006), the Sunda Arc (*Philibosian et al.*, 2017; *Sieh et al.*, 2008), and the Japan and Kuril Trenches (see *Satake*, 2015, for a review), which have geologically documented several tens of earthquakes. Furthermore, cycles of earthquake clusters (*Philibosian et al.*, 2017; *Ratzov et al.*, 2015; *Schlagenhauf et al.*, 2011) and exceptionally large (anomalous) events (*Goldfinger et al.*, 2013, 2012; *Mannen et al.*, 2018) have been identified to recur on timescales of several hundreds of years, much larger than the average recurrence time of decades for regular earthquakes.

In addition to palaeoseismological studies, geodetic studies have inferred the existence of giant earthquakes for the Main Himalaya Thrust (*Stevens and Avouac*, 2016) and Japan Trench (*Satake and Fujii*, 2014) regions. In these studies, the present day convergence rates have been compared to (palaeo)seismological estimates of yearly moment release rates by seismic events, concluding that $M_w > 9$ earthquakes with a recurrence time of 700-800 years are required to close the slip budget. Similarly, a great earthquake is anticipated for the presently aseismic Cascadia subduction region based on geodetic observations of plate interlocking (*Dragert and Hyndman*, 1995), in accordance with palaeoseismological observations that suggest a 500-year recurrence time for great earthquakes (on average; *Clague*, 1997; *Goldfinger et al.*, 2012).

As seismic event catalogues suffer from incompleteness, physically-oriented arguments have been put forward to regionally constrain the expected maximum magnitude of earthquakes, for instance by correlating seismicity with subducting plate properties. A classical example is given by *Ruff and Kanamori* (1980), who found correlations between the maximum instrumentally recorded magnitude, and plate age and convergence rate. By relating the independent quantities to the geometry and thermal structure of the subduction thrust, a multiple physical mechanisms for the upper limit of earthquake magnitudes has been proposed (*Heuret et al.*, 2011; *Schellart and Rawlinson*, 2013). In later years, mounting evidence opposed the apparent relation between plate age and maximum earthquake magnitude (*McCaffrey*, 1997; *Pacheco et al.*, 1993; *Stein and Okal*, 2007), with the 2004 Sumatra-Andaman and 2011 Tohoku-Oki $M_w > 9$ events

severely challenging a causal relation. Although there exists a risk of over-interpretation, statistical correlations may still provide the necessary constraints for understanding the apparent variability in seismic character between various subduction zones (and faults in general). For instance, based on instrumental records it was observed by *Ide* (2013) that regions of low background seismicity (i.e. few earthquakes, corrected for aftershock sequences) are more likely to generate a giant earthquake than regions of high seismicity rates. While the statistical significance of such observations can be questioned (e.g. *McCaffrey*, 2008), at the very least it demonstrates that present-day seismically quiescent regions (Nankai, Cascadia, Alaska, Chile Maule) may generate giant earthquakes, which raises the question whether or not regular and giant earthquakes are governed by the same mechanisms.

In the commonly observed Gutenberg-Richter distribution of earthquake magnitudes (*Gutenberg and Richter*, 1944, 1956), quasi-periodically recurring events of similar size can be taken as 'characteristic' earthquakes, from which the recurrence times of larger, less frequent events can be estimated. Optionally, a tapered Gutenberg-Richter distribution can be defined to include a corner magnitude that is commonly thought to represent the maximum possible magnitude for that region (see *Kagan and Jackson*, 2013). It was noted by *Kagan* (1997) that all subduction zones share statistically similar maximum magnitude parameters, implying a corner magnitude of $M_{w,c} > 9.4$ for major subduction regions (*Kagan and Jackson*, 2013). This suggests that each subduction zone is capable of generating giant earthquakes, provided that its seismogenic zone is sufficiently large (*Weng and Yang*, 2017). A more physically established method is seated on the principle of seismic moment conservation, where any deficits in the overall slip budget are balanced by seismic events outside of the existing catalogue (*Kagan and Jackson*, 2013; *Satake and Fujii*, 2014; *Stevens and Avouac*, 2016). This approach relies heavily on catalogue completeness and estimates of the coupling coefficient (amount of coseismic slip versus creep), but offers physical rather than statistical constraints on event magnitudes and recurrence times. Nevertheless, both methods assume that the earthquake size distribution follows a (modified) Gutenberg-Richter relation, which implies a purely stochastical nature of earthquake occurrence (*Satake*, 2015). Contrarily, if great and giant earthquakes merely serve to close the slip budget, then they do not occur randomly in time, but rather are related to moment accumulation and release rates by regular earthquakes. The inference of long-term earthquake cycles seem to

further underline this (*Goldfinger et al.*, 2013; *Moernaut et al.*, 2018; *Schlagenhauf et al.*, 2011; *Sieh et al.*, 2008). Moreover, long-term seismic moment conservation driving great earthquakes can be regarded as a physical mechanism that differs from that of regular earthquakes, as suggested above.

The above observations can now be summarised to describe the existence of long-term (multi-century to millennial) earthquake cycles, emerging as clusters of earthquakes or as anomalously large events occurring within a sequence of regular earthquakes. These cycles, and giant earthquakes in general, occur universally in both seismically active and seismically quiet regions, suggesting that the mechanism behind giant earthquakes is shared between various subduction zones, but being somehow different from that of regular earthquakes. One possible mechanism for this, as mentioned above, is the requirement that a fault's global slip budget be closed over geological times. In turn, this implies that giant earthquakes do not occur randomly in time, and so may not follow a well-established Gutenberg-Richter relation in the same way that conventional earthquakes do. Such hypotheses are testable with numerical seismic cycle models, provided that the model fault rheology and structure are representative for natural faults on which great and giant earthquakes occur.

6.2.2 Structure and composition of heterogeneous fault zones

While seismological and geodetical methods lack the resolution to resolve sufficient details of a fault zone architecture relevant for the set-up of our numerical model, exhumed fault zones may serve as field analogues for the in-situ structure of seismogenic faults. We therefore briefly review a number of field observations that contribute to our understanding of 'asperities' at a metre scale, and that will be used to set-up a model fault that is geologically sensible. The fault rock and architecture terminology adopted here does not strictly follow any particular classification (e.g. *Sibson*, 1977; *Woodcock and Mort*, 2008), and descriptions such as 'gouge' and 'slip zone' loosely refer to textures and structures resulting from discontinuous strain accommodation.

In characterising a typical fault zone structure, the Punchbowl fault (*Chester et al.*, 1993; *Chester and Logan*, 1987) is commonly taken as a model for mature crustal faults. However, fault core architectures may strongly vary under influence of the protolith

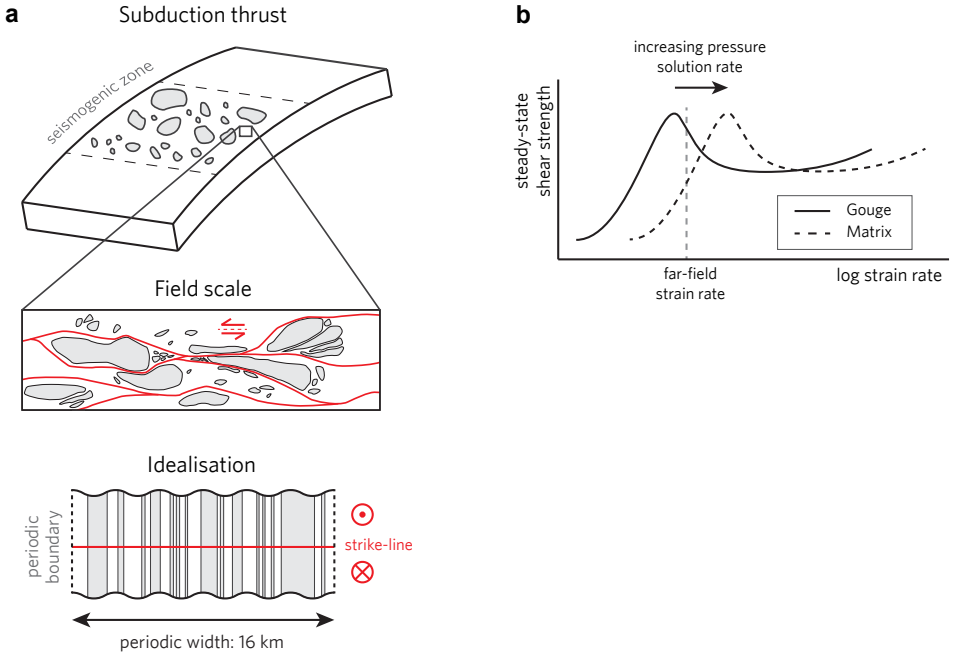

Fig. 6.1: a) Visual representation of the model fault. The fault structure as envisioned in this work is based on field reports of exhumed faults (e.g. *Fagereng*, 2011), featuring boudinaged lenses of competent material embedded in a phyllonitic matrix. For the model implementation, this is idealised by assuming a cross-fault averaged structure, so that the problem is reduced to one dimension; b) Schematic diagram of the steady-state shear strength, as predicted by the CNS model. The distinction between the phyllonite matrix and the cataclastic gouge is made by a contrast in pressure solution kinetics, with the phyllonite exhibiting faster pressure solution rates than the gouge. This effectively induces a lateral shift of the steady-state curve of the phyllonite towards higher strain rates. At a given far-field (imposed) strain rate, the phyllonite is velocity-strengthening, whereas the gouge is velocity-weakening (at steady-state).

(*Bullock et al.*, 2014; *Faulkner et al.*, 2010): faults cross-cutting predominant quartzo-feldspathic, carbonaceous, or crystalline lithologies often accommodate strain within a single, straight and narrow fault core, no more than a few metres in width, surrounded by a damage zone (*Chester et al.*, 1993; *De Paola et al.*, 2008; *Faulkner et al.*, 2010; *Fondriest et al.*, 2012). Shear strain within the fault core itself is typically localised in

millimetre to centimetre wide principal slip zones, with an additional hierarchical level of localisation (the principal slip surface) at the micrometre scale.

Conversely, phyllosilicate-bearing or mixed lithology fault zones are characterised by multiple fault cores, spatially distributed within up to a kilometre-wide zone (*Faulkner et al.*, 2003; *Jefferies et al.*, 2006; *Rowe et al.*, 2011). Exhumed tectonic mélanges feature boudinaged lenses of competent material (such as dolomite, quartz, chert, or basalt) embedded in a less-competent, phyllosilicate-rich matrix, enclosed or cross-cut by a number of undulating fault strands (*Collettini et al.*, 2011; *Fagereng*, 2011; *Faulkner et al.*, 2003; *Kimura et al.*, 2012; *Niemeijer and Vissers*, 2014; *Rowe et al.*, 2011, see also Fig. 6.1a). The phyllonite matrix typically displays distributed deformation with a pervasive, well-developed foliation and abundant pressure solution seams, suggesting that pressure solution is a dominant deformation mechanism (*Fagereng*, 2011; *Kimura et al.*, 2012). By contrast, thin (mm-cm thick) layers of gouge or ultracataclasite bounding the competent lenses evidence localised deformation (*Faulkner et al.*, 2003; *Kimura et al.*, 2012). The numerous cataclastic features (grain comminution, fracturing, polished and striated surfaces) hosted within the localised slip zones and competent blocks are accompanied by evident dissolution/precipitation textures, indicating that pressure solution occurs broadly contemporaneously with granular flow over the course of a seismic cycle (*Bullock et al.*, 2014; *Hadizadeh et al.*, 2012; *Holdsworth et al.*, 2011; *Jefferies et al.*, 2006; *Smeraglia et al.*, 2017, and others).

An important question that has been raised (and addressed) by *Imber et al.* (2008), is how frictional instabilities nucleate when the phyllonitic matrix displays predominantly velocity-strengthening (i.e. frictionally stable) behaviour (*Collettini et al.*, 2011; *Moore and Lockner*, 2007; *Niemeijer and Vissers*, 2014). One possible solution that *Imber et al.* (2008) put forward, is that instabilities nucleate from embedded lenses or competent blocks, which may cause local stress concentrations and subsequent brittle failure (*Faulkner et al.*, 2003; *Niemeijer and Spiers*, 2005). Alternatively, it has been hypothesised (e.g. by *Fagereng and Sibson*, 2010) that the spatial distribution of competent lenses embedded in an incompetent matrix leads to local variations in strain rate, causing embrittlement of the matrix in regions where lenses are volumetrically more abundant and strain rates are locally high. This hypothesis seems to be supported further by field measurements of the size distribution of these lenses (or phacoids),

which tend to follow a power-law distribution, in relation to the mode of deformation. It was found by *Fagereng* (2011) that a phacoid size distribution characterised by a (2D) fractal dimension D larger than about 1.4 (dominated by numerous small phacoids) is indicative for predominantly distributed deformation, whereas outcrops exhibiting values of D smaller than 1.4 (dominated by several large phacoids) display mostly localised deformation. In addition, since localisation and brittle deformation in tectonic mélanges seems most intense on the boundaries between matrix and lenses (*Faulkner et al.*, 2003; *Kimura et al.*, 2012; *Niemeijer and Vissers*, 2014), it is likely that these slip zones incorporate material from the competent and possibly velocity-weakening lenses, inheriting the frictional properties of the lens materials (*Collettini et al.*, 2011; *Niemeijer and Vissers*, 2014).

It is commonly observed that earthquakes follow a fractal frequency-magnitude distribution (*Heuret et al.*, 2011), and it has been proposed that the fractal Gutenberg-Richter distribution arises from a fractal distribution in asperity size (*Lay and Kanamori*, 1981; *Seno*, 2003). Indeed, typical frequency-magnitude distributions have been reproduced in numerical studies exploring the effect of spatially fractal heterogeneities in stress or frictional properties (*Hillers et al.*, 2006, 2007; *Ide and Aochi*, 2005; *Norbeck et al.*, 2016). However, the relation between the size of an earthquake and the size of individual seismogenic asperities is not directly evident, as an asperity in a seismological sense does not necessarily correspond to a single geological feature with geometrical or compositional contrast. At a metre scale, seismogenic asperities can be defined by mechanically competent lenses embedded in an incompetent matrix (*Fagereng and Sibson*, 2010; *Kimura et al.*, 2012), which have been observed to follow a fractal distribution in size (*Fagereng*, 2011). At a larger (up to kilometre) scale, it has been proposed that seamounts may act as seismogenic asperities (*Cloos*, 1992), particularly since basaltic rocks often display velocity-weakening behaviour (*He et al.*, 2007; *Tsutsumi and Shimamoto*, 1997). On the other hand, there exists compelling evidence that seamounts induce distributed deformation rather than large seismic events that would normally be associated with an asperity of such dimensions (*Wang and Bilek*, 2011), and it has been suggested that the 1982 M_w 7 Daiichi-Kashima event ruptured outward, away from the edge of a seamount, rather than inward (*Mochizuki et al.*, 2008). These examples show that a seismological asperity does not always have an immediately clear physical representation.

6.2.3 Results from rate-and-state based modelling studies

There exists a multitude of modelling studies based on rate-and-state friction (RSF; e.g. *Hillers et al.*, 2006, 2007; *Lapusta and Rice*, 2003; *Rice*, 1993; *Tse and Rice*, 1986) that incorporate a depth-variation of constitutive parameters a and b based on the experimental work of *Blanpied et al.* (1995, 1998). In these studies, the spatial heterogeneity in frictional properties arises from an increasing fault temperature with depth, induced by a smooth and continuous geotherm. The fault itself is assumed to be homogeneous in composition (granitic). However, it is recognised by seismological and geodetic studies that heterogeneous fault properties cannot be explained purely by thermal gradients, as evidenced by e.g. the occurrence of along-strike (constant temperature) variations in interseismic coupling and seismic signature (*Barbot et al.*, 2012; *Bürgmann et al.*, 2005; *Thomas et al.*, 2017; *Wallace et al.*, 2009). In particular, isolated velocity-weakening asperities loaded by a creeping velocity-strengthening matrix are commonly believed to produce (micro-)seismicity at seismogenic depths. These observations hint at a discontinuous, compositional fault heterogeneity, which receives strong support from field studies (see references in Section 6.2.2).

The simplest scenario, i.e. the interaction between a single seismogenic asperity and its frictionally stable surroundings has been studied extensively, e.g. by *Boatwright and Cocco* (1996), *Kaneko and Ampuero* (2011), *Noda et al.* (2013a), *Noda and Hori* (2014), *Skarbek et al.* (2012), *Tinti et al.* (2005), and others. Generally, it is found that dynamic ruptures are arrested by velocity-strengthening fault materials, and that the extent to which the rupture penetrates into the velocity-strengthening matrix is controlled by the fracture energy (*Ampuero and Ben-Zion*, 2008), and is reduced by a diminishing stress drop (*Brantut and Platt*, 2017) or by a large contrast in D_c (*Bizzarri et al.*, 2001; *Tinti et al.*, 2005). However, dynamic ruptures may still propagate between two velocity-weakening asperities separated laterally by a velocity-strengthening region, provided that the resistance or size of the velocity-strengthening region is sufficiently small (*Kaneko et al.*, 2010; *Tinti et al.*, 2005). In such a double asperity geometry (i.e. two velocity-weakening asperities separated by a velocity-strengthening region), *Kaneko et al.* (2010) found that the probability that a dynamic rupture traversed from one asperity to the next was roughly proportional to the non-dimensional barrier efficiency of the velocity-strengthening patch. Beyond a critical value of the barrier efficiency,

practically no ruptures could propagate through the velocity-strengthening region. Furthermore, the probability of a two-segment rupture was directly proportional to the degree of interseismic coupling, which offers a handle on improving seismic hazard assessments based on geodetic data.

Closely related to the probability of multi-segment ruptures is the concept of a total instability (or 'T-instability'; *Luo and Ampuero*, 2018). For a fault with a given spatial distribution of velocity-weakening and -strengthening materials, one can speculate the existence of a threshold composition for which the fault behaves either stable, controlled by the velocity-strengthening segments, or unstable, controlled by the velocity-weakening segments. It was found by *Skarbek et al.* (2012) that for a heterogeneous model fault, there exists a continuous spectrum from stable creep to fast, dynamic sliding with increasing percentage of velocity-weakening material present in the fault. *Dublanchet et al.* (2013) investigated the behaviour of a model fault covered with isolated, critically-stressed asperities, and observed a critical density of asperities above which the asperities started to display increasingly more interaction (i.e. rupture concurrently). This asperity density was subsequently related to the $(a - b)$ value of the velocity-strengthening matrix, being a measure of the barrier strength of the matrix to sustained dynamic rupture (e.g. *Tinti et al.*, 2005). The interaction between asperities was investigated further by *Luo and Ampuero* (2018) and *Yabe and Ide* (2017), who distinguished between (partial) P-instabilities for instabilities confined to a single asperity, and (total) T-instabilities for instabilities that rupture the entire fault. The sharp transition from the regime dominated by P-instabilities to a regime dominated by T-instabilities was found to be controlled by as many as seven independent dimensionless quantities, and the boundary between the two regimes was predicted based on linear stability analysis (extending the analysis of *Skarbek et al.* (2012)). The analytical and numerical results of *Luo and Ampuero* (2018) are consistent with the findings of *Kaneko et al.* (2010) that the probability of a two-segment rupture decreases with increasing barrier efficiency. In the simulations of *Kaneko et al.* (2010), the occurrence of a two-segment rupture can thus be interpreted as a T-instability following the definition of *Luo and Ampuero* (2018), and may find its natural counterpart in large, multi-asperity and multi-segment ruptures (such as great megathrust earthquakes).

In the rate-and-state friction studies cited above, the constitutive parameters a, b, and D_c are all assumed to reflect material properties, and are taken as time-constants. However, as observed in many laboratory studies, these parameters are likely controlled by time-dependent quantities, such as slip velocity and gouge porosity (*Carpenter et al.*, 2016a; *Chen et al.*, 2015a; *Den Hartog et al.*, 2012; *Reinen et al.*, 1992; *Tesei et al.*, 2014). By comparing the RSF-based seismic cycle simulations with microphysically-based simulations, *Van den Ende et al.* (2018a) showed that rate-and-state friction cannot reproduce the seismic cycle behaviour predicted by the microphysical model, which is directly related to the assumed constant values of the RSF constitutive parameters (see also Chapter 5). Since experimental work clearly shows that RSF parameters depend on velocity (and therefore are time-dependent; see references above), different outcomes are anticipated when investigating the effects of heterogeneity on fault rheology with a microphysically-based seismic cycle simulator. Most importantly, it was argued in Chapter 5 (as well as by *Niemeijer and Spiers*, 2007) that a material exhibiting steady-state ductile creep can become unstable in response to a sufficiently large perturbation in stress, enforcing a transition from stable velocity-strengthening to unstable velocity-weakening. Such a transition has previously been simulated by linking a general flow law to the classical RSF formulations (*Shimamoto and Noda*, 2014), enforcing a transition from plastic flow to rate-and-state friction behaviour with increasing velocity. However, in the CNS formulation this transition spontaneously emerges in a self-consistent manner, and allows triggered frictional instabilities to nucleate in velocity-strengthening regions, which could play a central role in multi-asperity and multi-segment ruptures.

6.3 Approach and objectives of the present study

Before discussing the details of the numerical model and simulation procedures, we will first extract essential fault zone characteristics from the field observations discussed in Section 6.2.2 to set-up a general framework for our model approach. We will then specify the aims of this study based on the results and open questions discussed in Sections 6.2.1 and 6.2.3.

6.3.1 General model framework

As mentioned in Section 6.2.2, pressure solution and cataclastic granular flow have been recognised as dominant deformation mechanisms operating within a phyllonitic matrix and localised slip zones. So in order to realistically simulate a spatially heterogeneous fault zone segment, following the characteristics described in Section 6.2.2, the model fault rheology needs to be based on constitutive relations for pressure solution and granular flow. Such relations have been derived from microphysical considerations, e.g. by *Bos and Spiers* (2002b), *Niemeijer and Spiers* (2007), and *Den Hartog and Spiers* (2014). The differences between these microphysical models stem mainly from their assumed model microstructure, and the grain-scale interactions that were envisioned to constitute the mechanical behaviour. For the purpose of the present study, we chose to adopt the extended model formulations of *Niemeijer and Spiers* (2007) and *Chen and Spiers* (2016) (the 'CNS' model; see Section 6.4.1 for a description). In Chapter 5, this microphysical model formulation was implemented into the seismic cycle simulator QDYN (*Luo et al.*, 2017a; *Van den Ende et al.*, 2018a), and a detailed study was performed of the seismic cycle behaviour of a crustal strike-slip model fault, uniformly composed of quartz gouge. We note that the assumed microstructure of the CNS model is not fully compatible with the microstructure of a typical phyllonite (see e.g. *Jefferies et al.*, 2006). However, the CNS model microstructure corresponds well to what is anticipated for the localised, cataclastic gouges surrounding competent blocks (*Collettini et al.*, 2011), which are thought to host nucleation of seismic slip. Aware of the limitations of the chosen formulation, we will interpret the outcomes of the model with care and discuss possible deficiencies where relevant.

One important feature of the CNS model is that it predicts a progression from non-dilatant ductile creep to dilatant granular flow with increasing fault slip velocity, which marks the transition from strong velocity-strengthening to velocity-weakening behaviour. The predicted velocity-dependence of shear strength is drawn schematically in Fig. 6.1b, where the steady-state shear stress is plotted as a function of the imposed shear strain rate. In this work, we distinguish between two types of fault rock, following the descriptions in Section 6.2.2: on the one hand we have the phyllonitic matrix (or simply 'matrix'), which shows predominantly ductile deformation, and on the other hand we have the localised, cataclastic gouges (or simply 'gouges'). Since the

gouges are mostly situated at the boundaries between the phyllonite matrix and the competent lenses, we also refer to the cataclastic gouges as 'asperities', in analogy to the seismological description for competent and potentially seismogenic sites in a fault zone. The distinction between the two rock types is made here through the kinetics of pressure solution. This reflects a compositional variation, in which the matrix is assumed to exhibit faster rates of pressure solution than the gouge. As is illustrated in Fig. 6.1b, a faster rate of pressure solution effectively results in a lateral shift of the stress-strain rate curve towards higher strain rates, so that the matrix will accommodate a larger portion of the imposed strain rate by ductile creep relative to the gouge (see also *Niemeijer and Spiers*, 2007, their Fig. 10).

The lateral position of the stress-strain rate curve in Fig. 6.1b depends strongly on the pressure solution kinetics, nominal grain size, fault temperature, and effective normal stress. These parameters are not well constrained for a seismogenic fault segment at depth. However, the fault rheology is not uniquely defined by any particular value of these parameters, and so we can chose a combination of the parameters above that satisfies the scenario in which we have potentially seismogenic asperities embedded in a predominantly ductile phyllonitic matrix. This amounts to stating that the model fault segment is situated at a particular depth interval with the pressure and temperature conditions favourable for nucleation of a frictional instability. Alternatively, we could rescale (non-dimensionalise) the horizontal axis of Fig. 6.1b by the rate of pressure solution, using the four quantities above in the rescaling procedure. Fig. 6.1b also reveals a peculiar model prediction regarding the distinction between strain rate embrittlement of the phyllonite (*Fagereng and Sibson*, 2010), and compositional variations (*Collettini et al.*, 2011; *Niemeijer and Vissers*, 2014) as being responsible for nucleation of unstable fault slip: by discriminating the phyllonite matrix from the cataclastic gouge through its faster pressure solution kinetics (i.e. compositional variation), we perform a lateral shift of the phyllonite steady-state strength curve towards higher strain rates. This is essentially identical to imposing a strain rate to the phyllonite matrix that is lower in regions of the fault zone that have a lower abundance of competent lenses, or equivalently imposing a strain rate that is higher in between two closely-spaced lenses. In other words, our model definition of a compositional variation (*Collettini et al.*, 2011; *Niemeijer and Vissers*, 2014) is rheologically indistinguishable from strain rate embrittlement (*Fagereng and Sibson*, 2010).

Lastly, simplifications have to be made regarding the architecture of the fault in order to reduce the highly complex fault zone structure to one that is numerically feasible (see Fig. 6.1a). First, we consider only a cross-sectional fault area spanned by the along-strike and normal directions of the fault zone. Then, we assume that the averaged fault behaviour at a given point along-fault can be represented by the behaviour of one of the end-member types of fault rock defined above (i.e. the matrix or the gouge), so that the fault structure reduces to a one-dimensional line parallel to the strike line. This may seem as an unjustifiable over-simplification, but it can be warranted by considering the following: deformation within the fault zone is accommodated on a large number of fault strands, and if the spatial distribution of competent lenses and phyllonitic matrix is random, then each fault strand will (on average) encounter a statistically similar distribution of lenses and matrix. Furthermore, a rupture nucleating at a given location on the fault follows a largely planar trajectory, with a long wavelength compared to the amplitude of the undulation, so that it likely will follow a single fault strand. The dynamics of the fault in terms of its seismogenic potential and slip can thus be investigated by 'selecting' one fault strand that would host a frictional instability and subsequent dynamic rupture. One important drawback of this procedure is that the chosen thickness of a single slip zone is not representative for the thickness of the entire fault zone, and so the strain rate accommodated within that slip zone cannot be obtained. However, in the manner in which the fault temperature, normal stress, etc. are chosen (i.e. the 'normalisation' procedure), the absolute value of the average strain rate (far-field driving velocity divided by the cumulative thickness of all deforming regions) becomes irrelevant. For instance, if the proposed homogenisation procedure would systematically underestimate the strain rate accommodated by each fault strand, then one would simply have to consider a different temperature (i.e. depth) range to nucleate seismic slip.

6.3.2 Aims of this study

Based on the field and numerical observations reported in Section 6.2, we establish the following scope for this work:

1. Since the CNS model exhibits more complex mechanics than classical rate-and-state friction in terms of the velocity- and time-dependence of friction, we will first investigate the behaviour of a single (periodic) seismogenic asperity embedded in a phyllonitic matrix. In this highly simplified geometry, the mechanics behind T-instabilities as predicted by the CNS model can be elucidated in an intuitive way, and can be compared with the work of *Luo and Ampuero* (2018).

2. As an intermediate step between the single-asperity system and random heterogeneous faults, we briefly verify the mechanics of single-asperity T-instabilities in a system defined by two seismogenic asperities separated by a matrix.

3. We then proceed to explore the behaviour of a fault with a geometry described in Section 6.3.1, i.e. exhibiting a fractal asperity size distribution. In this highly complex system, we interpret the observed seismic character based on the mechanics of T-instabilities, as uncovered in the simplified single and double asperity systems.

4. The model outcomes are compared with previous rate-and-state based numerical studies, as to identify similarities and differences between the two methods. Moreover, the model results are put in the context of (palaeo)seismological and geodetic observations, to establish whether the microphysical model can explain the behaviour of natural faults.

The ambition of this paper is not to make precise predictions for one particular fault zone, but rather to establish a more general theory for the occurrence of supercycles and giant earthquakes, and to provide directions for future study using a microphysically-based approach.

6.4 Numerical methods

6.4.1 Description of the microphysical model

The derivation of the CNS model, and its implementation into QDYN are described in detail in *Niemeijer and Spiers* (2007), *Chen and Spiers* (2016), and Chapter 5. Some

key concepts of this model are recited here.

The CNS model geometry is based on the microstructural observations provided by *Niemeijer and Spiers* (2006), and considers a granular gouge layer of uniform thickness h, characterised by a nominal grain size d and porosity ϕ. A representative volume element is subjected to an effective normal stress σ and deformation rate V_{imp}, which is accommodated internally by parallel operation of granular flow (grain rolling and sliding), and one or more thermally-activated, time-dependent deformation mechanisms. Following previous work (*Chen and Spiers*, 2016; *Niemeijer and Spiers*, 2007; *Van den Ende et al.*, 2018a), and based on the observations summarised in Section 6.2.2, we take intergranular pressure solution as the sole time-dependent compaction mechanism, ignoring other mechanisms such as stress corrosion cracking (*Atkinson*, 1984; *Brantut et al.*, 2013). The constitutive relation for the rheology of the fault then results from the individual constitutive relations for granular flow and pressure solution, which are dependent on the instantaneous state of stress and gouge porosity.

From geological observations, it is clear that pressure solution creep operates at significant rates in fault rocks, though it is presently unclear which mechanism (dissolution, diffusion, or precipitation) is rate-limiting. In absence of such constraints, we adopt a flow law for dissolution-controlled pressure solution creep that has previously been used for describing laboratory compaction data of pure quartz aggregates (*Niemeijer et al.*, 2002; *Van Noort et al.*, 2008a). This constitutive relation reads (*Niemeijer et al.*, 2002; *Pluymakers and Spiers*, 2014):

$$\dot{\gamma}_{ps} = A\frac{I_s\Omega}{RT}\frac{\tau}{d}f_1(\phi) \tag{6.2a}$$

$$\dot{\varepsilon}_{ps} = A\frac{I_s\Omega}{RT}\frac{\sigma}{d}f_2(\phi) \tag{6.2b}$$

Here, $\dot{\gamma}_{ps}$ and $\dot{\varepsilon}_{ps}$ are the strain rates in the fault tangential and normal directions, respectively, A is a geometric factor accounting for the grain shape, I_s is the dissolution rate constant, Ω is the molar volume, R is the universal gas constant, T is the absolute temperature, and τ and σ are the macroscopic shear and effective normal stress, respectively. The evolution of the grain-grain contact area (and grain contact stress) with porosity ϕ is described by the porosity function $f_i(\phi)$ (*Spiers et al.*, 2004). For

dissolution controlled pressure solution creep, this function takes the following form (Chapter 5; *Pluymakers and Spiers*, 2014):

$$f_1(\phi) = \frac{\phi_c}{\phi_c - \phi} \tag{6.3a}$$

$$f_2(\phi) = \frac{\phi - \phi_0}{\phi_c - \phi} \tag{6.3b}$$

where ϕ_0 is a lower cut-off porosity corresponding to the percolation threshold for an interconnected pore network of 3 % (*Van der Marck*, 1996), and ϕ_c is the maximum attainable porosity of a purely dilatant gouge material, referred to here as the 'critical state' porosity (*Niemeijer and Spiers*, 2007; *Paterson*, 1995). Typically, a porosity function similar to $f_1(\phi)$ is used in analytical models for intergranular pressure solution that employ a porosity function (*Pluymakers and Spiers*, 2014; *Spiers et al.*, 2004). However, in laboratory compaction tests it has been observed that microphysical model predictions for compaction by pressure solution overestimate experimentally measured strain rates at low porosities (< 20 %), sometimes by several orders of magnitude (*Niemeijer et al.*, 2002). While the physical mechanisms behind this discrepancy are yet to be fully identified, the trends in the experimental data can be approximated by the modified porosity function $f_2(\phi)$, which asymptotically reduces $\dot{\varepsilon}_{ps}$ to zero for $\phi \to \phi_0$. Furthermore, this ensures that $\phi > \phi_0$ at all times, preventing negative porosities that are physically unrealistic. By contrast, shear creep accommodated by pressure solution does not involve volume changes (i.e. porosity reduction), so it is expected that $\dot{\gamma}_{ps} > 0$ even for $\phi = \phi_0$. A functional form like $f_1(\phi)$ is therefore more likely to describe shear creep by pressure solution, as is adopted for this study.

The constitutive relations for granular flow, as derived by *Chen and Spiers* (2016) are given as follows:

$$\dot{\gamma}_{gr} = \dot{\gamma}^*_{gr} \exp\left(\frac{\tau\left[1 - \tilde{\mu}^* \tan\psi\right] - \sigma\left[\tilde{\mu}^* + \tan\psi\right]}{\tilde{a}\left[\sigma + \tau \tan\psi\right]}\right) \tag{6.4a}$$

$$\dot{\varepsilon}_{gr} = -\tan\psi \dot{\gamma}_{gr} \tag{6.4b}$$

In these relations, $\dot{\gamma}_{gr}$ and $\dot{\varepsilon}_{gr}$ denote the granular flow strain rates tangential and

normal to the fault plain, respectively, and $\tan\psi$ denotes the average grain-grain dilatation angle, which can be written as $\tan\psi = 2H\,(\phi_c - \phi)$, where H is a geometric constant of order 1 (*Niemeijer and Spiers*, 2007; *Paterson*, 1995). The microscopic coefficient of friction of grain-grain contacts is given by *Chen and Spiers* (2016) as $\tilde{\mu} = \tilde{\mu}^* + \tilde{a}\ln\left(\dot{\gamma}_{gr}/\dot{\gamma}^*_{gr}\right)$, $\tilde{\mu}^*$ being a reference value of $\tilde{\mu}$ evaluated at $\dot{\gamma}^*_{gr}$, and $\tilde{a}$ being the coefficient of logarithmic rate-dependence of $\tilde{\mu}$. Note that $\tilde{a}$ cannot generally be taken as a constant, but instead depends on the bulk gouge porosity and the (possibly time-dependent) nanometre-scale grain boundary structure (see *Takahashi et al.*, 2017; *Van den Ende et al.*, 2018a). However, for the purpose of this study, we assume a constant value of $\tilde{a}$.

With the above constitutive relations for the relevant deformation mechanisms, the evolution of the macroscopic shear stress and gouge porosity of a zero-dimensional (spring-block) fault can be expressed in the following set of differential equations (*Chen and Spiers*, 2016):

$$\frac{\mathrm{d}\tau}{\mathrm{d}t} = k\left(V_{imp} - h\left[\dot{\gamma}_{gr} + \dot{\gamma}_{ps}\right]\right) \tag{6.5a}$$

$$\frac{\mathrm{d}\phi}{\mathrm{d}t} = -\left(1-\phi\right)\left(\dot{\varepsilon}_{gr} + \dot{\varepsilon}_{ps}\right) \tag{6.5b}$$

in which k is the effective shear stiffness (units: Pa m^{-1}) of the fault. In Eqn. (6.5a), the instantaneous fault slip velocity V is obtained from the addition of the strain rates of granular flow and pressure solution (i.e. $V = h\left[\dot{\gamma}_{gr} + \dot{\gamma}_{ps}\right]$).

One important characteristic to note, is that the steady-state velocity-dependence of friction, i.e. a material being velocity-strengthening or -weakening, changes with velocity (see Fig. 6.1b). As a result, classical rate-and-state friction is only comparable to the CNS model near steady-state conditions (*Chen et al.*, 2017b). With increasing departure from steady-state, both model frameworks predict different frictional behaviour, as is notably seen in seismic cycle simulations (Chapter 5; *Van den Ende et al.*, 2018a). Hence, to avoid ambiguities in comparing CNS results with previous work using rate-and-state friction, we will refer in this work to velocity-strengthening or -weakening behaviour as the frictional rate-dependence evaluated at the imposed (far-field) driving velocity.

6.4.2 Description of the boundary element method

To model spatio-temporal variations of fault slip, we employ the boundary element code QDYN (*Luo et al.*, 2017a). This seismic cycle simulator originally utilises rate-and-state friction to describe the model fault rheology, but it has been extended in Chapter 5 to include the CNS microphysical model as described above in Section 6.4.1. Regardless of the underlying rheological model, the shear stress at point i on the fault is obtained using the quasi-dynamic approximation (*Rice*, 1993):

$$\tau_i(t) = -K_{ij}\left[d_j(t) - d_{imp}\right] - \eta V_i(t) \tag{6.6}$$

Here, K_{ij} is a stress transfer kernel whose coefficients represent the shear stress induced on the i-th fault element by unitary slip on the j-th fault element, d_j is the total fault slip on the j-th fault element, and d_{imp} is the far-field displacement, accumulating as $d_{imp} = V_{imp} \times t$. Radiation damping due to seismic wave radiation normal to the fault plane is accounted for by the last term on the right-hand side, in which the damping factor η assumes a value of $G/2c_s$, with G being the shear modulus of the homogeneous elastic medium, and c_s the shear wave speed (*Rice*, 1993). The stress transfer kernel K_{ij} is computed using a '2.5D' approximation for infinite one-dimensional faults embedded in two-dimensional homogeneous media (see *Luo and Ampuero*, 2018). For numerical implementation, Eqn. (6.6) is differentiated with respect to time to give:

$$\frac{\mathrm{d}\tau_i}{\mathrm{d}t} = -K_{ij}\left[V_j(t) - V_{imp}\right] - \eta\frac{\mathrm{d}V_i(t)}{\mathrm{d}t} \tag{6.7}$$

The fault slip velocity $V(t)$ is obtained as a function of stress and porosity as $V = h\left[\dot{\gamma}_{gr} + \dot{\gamma}_{ps}\right]$ (see Section 6.4.1). The acceleration term on right hand side of (6.7) is

then decomposed in its partial derivatives as:

$$\frac{\mathrm{d}V}{\mathrm{d}t} = \frac{\partial V}{\partial \tau}\frac{\mathrm{d}\tau}{\mathrm{d}t} + \frac{\partial V}{\partial \phi}\frac{\mathrm{d}\phi}{\mathrm{d}t} \tag{6.8a}$$

$$\frac{\partial V}{\partial \tau} = h\left(A\frac{I_s\Omega}{dRT}f_1(\phi) + \dot{\gamma}_{gr}\left[\frac{1-\tilde{\mu}\tan\psi}{\tilde{a}\left(\sigma+\tau\tan\psi\right)}\right]\right) \tag{6.8b}$$

$$\frac{\partial V}{\partial \phi} = h\left(\frac{\dot{\gamma}_{ps}}{\phi_c-\phi} + \dot{\gamma}_{gr}\left[\frac{2H\left(\sigma+\tilde{\mu}\tau\right)}{\tilde{a}\left(\sigma+\tau\tan\psi\right)}\right]\right) \tag{6.8c}$$

Note that these partial derivatives are given specifically for the assumed porosity functions (Eqn. (6.3)). Substitution of (6.8) into (6.7), and rearrangement gives:

$$\frac{\mathrm{d}\tau_i}{\mathrm{d}t} = \frac{-K_{ij}\left[V_j - V_{imp}\right] - \eta\frac{\partial V_i}{\partial \phi}\frac{\mathrm{d}\phi_i}{\mathrm{d}t}}{1+\eta\frac{\partial V_i}{\partial \tau}} \tag{6.9a}$$

$$\frac{\mathrm{d}\phi_i}{\mathrm{d}t} = -\left(1-\phi_i\right)\left(\dot{\varepsilon}_{gr,i} + \dot{\varepsilon}_{ps,i}\right) \tag{6.9b}$$

These equations are of the general form $\dot{\mathbf{X}} = \mathbf{F}(\mathbf{X}, t)$, with $\mathbf{X}(t)$ being a vector containing the collection of $\tau_i(t)$ and $\phi_i(t)$ variables on all fault elements. This system of ordinary differential equations is solved by the $4(5)^{\text{th}}$-order Runge-Kutta-Fehlberg method with adaptive time stepping (*Fehlberg*, 1969; *Shampine et al.*, 1976).

6.4.3 Simulation procedures

6.4.3.1 Single- and double-asperity faults

In the most simple case, we consider a one-dimensional, periodic fault of length L incorporating one region with velocity-strengthening properties (the phyllonite matrix), juxtaposed to a region of length L_a with velocity-weakening properties (the asperity), similar to the geometry adopted by *Luo and Ampuero* (2018). We define the fraction of fault length occupied by the asperity as $f = L_a/L$. The fault is then loaded at $V_{imp} = 10^{-9}$ m s^{-1} (≈ 30 mm yr^{-1}), under a constant and uniform effective normal stress of $\sigma = 50$ MPa. Both patches exhibit identical rheological parameters, except for

Table 6.1: List of frequently used symbols and parameters, and their respective values (if applicable). "var." indicates that the quantity is varied between simulations, with a reference value as indicated.

Symbol	Description	Value	Units
$\tilde{a}$	coefficient for logarithmic rate-dependence of $\tilde{\mu}$	0.006	-
c_s	shear wave speed	3000	$\mathrm{m\ s^{-1}}$
$\dot{\varepsilon}_{gr}$	granular flow strain rate	-	$\mathrm{s^{-1}}$
$\dot{\varepsilon}_{ps}$	pressure solution strain rate	-	$\mathrm{s^{-1}}$
f	asperity occupation ratio	0.5, var.	-
ϕ	gouge porosity	-	-
ϕ_0	lower cut-off porosity	0.03	-
ϕ_c	critical state porosity	0.30	-
G	shear modulus	30	GPa
$\dot{\gamma}_{gr}$	granular flow shear strain rate	-	$\mathrm{s^{-1}}$
$\dot{\gamma}^*_{gr}$	reference $\dot{\gamma}_{gr}$ corresponding with $\tilde{\mu}^*$	3×10^{-9}	$\mathrm{s^{-1}}$
$\dot{\gamma}_{ps}$	pressure solution shear strain rate	-	$\mathrm{s^{-1}}$
h	thickness of the gouge layer	10^{-2}	m
H	dilatancy geometric constant	0.4	-
η	radiation damping coefficient	0.5×10^6	$\mathrm{Pa\ s\ m^{-1}}$
$\tilde{\mu}$	grain boundary friction coefficient	-	-
$\tilde{\mu}^*$	reference grain boundary friction coefficient	0.4	-
V	fault slip velocity	-	$\mathrm{m\ s^{-1}}$
V_{imp}	imposed driving velocity	10^{-9}	$\mathrm{m\ s^{-1}}$
W/L	amplitude-wavelength ratio of periodic faults	10	-
σ	effective normal stress	50	MPa
τ	shear stress	-	Pa
$\tan\psi$	dilatancy angle	-	-
Z_{ps} (gouge)	pressure solution kinetic parameter	5×10^{-16}	$\mathrm{Pa^{-1}\ s^{-1}}$
Z_{ps} (matrix)	pressure solution kinetic parameter	var.	$\mathrm{Pa^{-1}\ s^{-1}}$

Table 6.2: List of frequently used symbols and parameters for specific simulations, and their respective values (if applicable). "var." indicates that the quantity is varied between simulations, with a reference value as indicated.

Symbol	Description	Value	Units
	Single- and double-asperity simulations		
L	length of periodic fault	300	m
N	number of fault elements	1024	-
Z_{ps} (matrix)	pressure solution kinetic parameter	(3 or 4)$\times 10^{-15}$	$\mathrm{Pa}^{-1}\ \mathrm{s}^{-1}$
	Heterogeneous fault simulations		
D	fractal dimension of size distribution	1, var.	-
L	length of periodic fault	16	km
N	number of fault elements	8192	-
x_{max}	maximum size distribution width	16	km
x_{min}	minimum size distribution width	3.91	m
Z_{ps} (matrix)	pressure solution kinetic parameter	3×10^{-15}	$\mathrm{Pa}^{-1}\ \mathrm{s}^{-1}$

the kinetics of pressure solution, through which we distinguish between the phyllonite matrix and the cataclastic gouge – see Table 6.1. The kinetic and thermodynamic constants as appearing in Eqn. (6.2) are combined into a single parameter Z_{ps}, given by:

$$Z_{ps} = \frac{A}{d}\frac{I_s \Omega}{RT} \tag{6.10}$$

so that $\dot{\gamma}_{ps} = Z_{ps}\tau f_1(\phi)$ and $\dot{\varepsilon}_{ps} = Z_{ps}\sigma f_2(\phi)$. For the gouge, Z_{ps} is maintained constant throughout the various simulations at 5×10^{-16} Pa^{-1} s^{-1}. For the matrix, Z_{ps} is chosen as 3×10^{-15} Pa^{-1} s^{-1} for a reference set of simulations. A second set of simulations is run with identical parameters, in which $Z_{ps} = 4 \times 10^{-15}$ Pa^{-1} s^{-1}, to investigate the effect of enhanced creep rates and contrasting rheology. We will refer to this simulation geometry as a single-asperity fault, though it is more accurate to describe this geometry as an infinite, regular array of asperities, owing to the adopted periodic boundary conditions.

While this simplified geometry is not directly representative for (randomly) heterogeneous faults, it exemplifies the interaction between the matrix and the asperity

in a transparent way, which will make the emergence of T-instabilities more comprehensible. As a next step towards heterogeneous systems, we subsequently set-up a periodic fault exhibiting two potentially seismogenic asperities equally spaced in both (periodic) directions: one small asperity of size L_a, and one large asperity of size $2L_a$, so that $f = 3L_a/L$. In this double-asperity system, we repeat a number of simulations performed previously with a single asperity, to verify that our hypotheses hold in more complex geometries.

6.4.3.2 Heterogeneous faults

By employing a microphysical model that contains microstructural information, one can closely relate the model fault geometry to field and laboratory observations. In this work, guided by numerous field reports, we define heterogeneity through spatial variations in pressure solution kinetics, which reflect contrasts in fault rock composition or spatial variations in strain rate (see Section 6.3.1). Following *Fagereng* (2011), we assume that competent lenses (the asperities) obey a power-law distribution in size, i.e.:

$$N(x) \propto x^{-D} \tag{6.11}$$

where $N(x)$ is the number of asperities of size x or greater, and D is the fractal dimension (or power-law exponent). Our procedure adopted to generate an asperity size distribution that obeys the above relation is described in Appendix 6.A. Following this procedure, we obtain a fault structure that is consistent with our interpretation of the field observations summarised in Section 6.2.2 (see Fig. 6.1a). This fault geometry is projected onto a one-dimensional periodic fault, and the fault is subjected to the same conditions as employed in the single-asperity simulations ($V_{imp} = 10^{-9}$ m s^{-1} and $\sigma = 50$ MPa). The total extent of the fault ($L = 16$ km) is discretised evenly into $N = 8192$ fault elements, each of size $\Delta x = 1.95$ m. This mesh resolution is sufficiently small to resolve the rupture process zone, which has an estimated width of 21.45 m for the chosen set of parameters (see Chapter 5, Appendix 5.B).

It has been observed that pressure solution kinetics are accelerated in the presence of phyllosilicates (e.g. *Hickman and Evans*, 1995). The enhanced pressure solution rates in phyllonites can reasonably be argued by the large abundance of phyllosilicates in

the matrix that are thought to accelerate diffusive mass transfer rates (*Bjørkum*, 1996; *Hickman and Evans*, 1995; *Renard et al.*, 2001). This reasoning holds for diffusion-controlled pressure solution creep, or in the case that the kinetics of diffusion and dissolution are of similar magnitude (*Bernabé and Evans*, 2007; *Lehner and Leroy*, 2004). Moreover, the chemistry of the pore fluid is known to exert strong controls on the rate of quartz dissolution, either enhancing (*Dove*, 1999; *Rimstidt*, 2015) or retarding (*Iler*, 1973) interface reaction rates depending on the presence of ionic species in the pore fluid. As mentioned in Section 6.4.1, it is unclear which mechanism limits the rate of pressure solution under in-situ thermodynamic and chemical conditions. However, field observations suggest that pressure solution rates are faster in the matrix than in the gouge, so for the kinetics of pressure solution Z_{ps}, we adopt values of 5×10^{-16} and 3×10^{-15} Pa^{-1} s^{-1} for the asperity and matrix, respectively. A value of $Z_{ps} = 3 \times 10^{-15}$ Pa^{-1} s^{-1} corresponds to theoretical estimates of Z_{ps} for mono-mineralic quartz at 250 °C and a grain size of 5 µm (*Niemeijer et al.*, 2002).

The simulation is then run for at least 2000 years, a time span over which all possible fault slip behaviour is expected to be displayed. In the case that the fault exhibits unstable slip (i.e. slow slip or earthquakes), we generate an event catalogue as described in Appendix 6.B. Owing to the finite simulated fault length ($L = 16$ km), the model outcomes will unavoidably be affected by the realisation of the asperity distribution in the form of clustering and repeating events controlled by the local density of asperities. Therefore, the heterogeneous fault simulations are repeated with identical model parameters, but with a different random asperity distribution that has similar statistical properties as the first simulation set. We will refer to these two sets as Set 1 and Set 2, and consider the differences between them as stochastic noise. For the purposes of this study, we do not perform a detailed statistical analysis of the model results, as we only consider general trends as a basis for our interpretations and hypotheses.

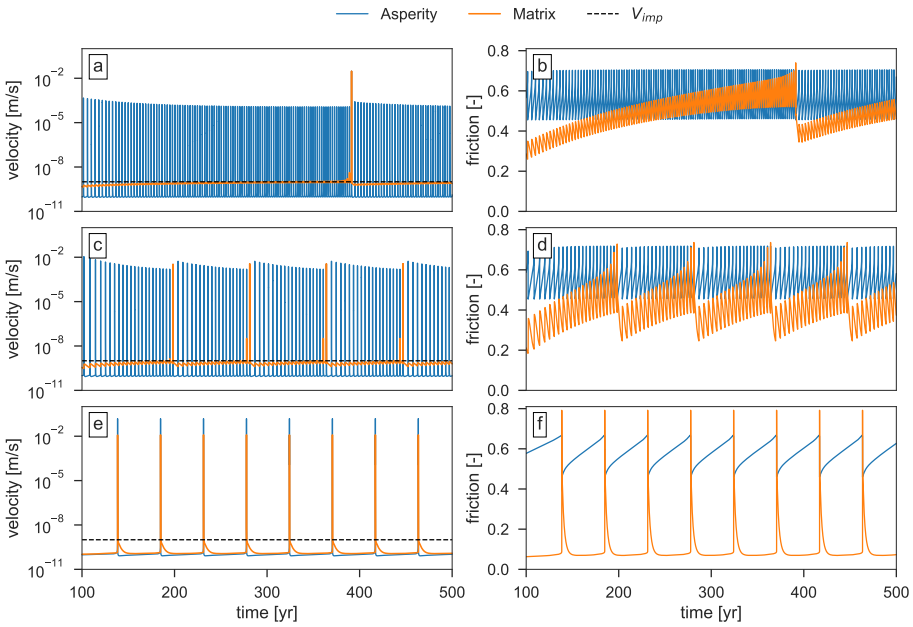

Fig. 6.2: Time series slip velocity and friction coefficient for exemplary single-asperity simulations, with $Z_{ps} = 3 \times 10^{-15}$ Pa^{-1} s^{-1}. Quantities are measured at the centre of the asperity and matrix patches. a) and b) $f = 0.5$. Only one T-instability is observed over the simulated period of 500 years; c) and d) $f = 0.6$. Several T-instabilities are observed; e) and f) $f = 0.8$. Each P-instability in the velocity-weakening asperity induces a T-instability.

6.5 Results

6.5.1 Single- and double-asperity faults

To illustrate characteristic behaviour of a single-asperity fault, we have plotted in Fig. 6.2 time series of slip velocity and friction (shear stress over normal stress) recorded at the midpoints of the asperity and matrix patches, for three different values of f. The single asperity exhibits unstable sliding in periodic stick-slip events constrained by the

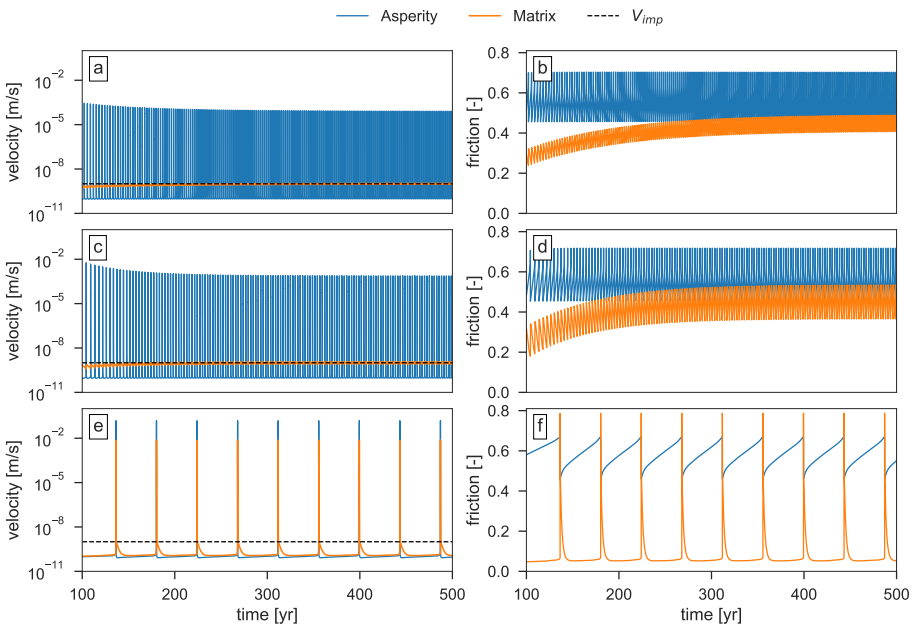

Fig. 6.3: Time series slip velocity and friction coefficient for exemplary single-asperity simulations, with $Z_{ps} = 4 \times 10^{-15}$ Pa^{-1} s^{-1}. Quantities are measured at the centre of the asperity and matrix patches. a) and b) $f = 0.5$. No T-instability is observed over the simulated period of 500 years, and the stress on the matrix asymptotically approaches a long-term constant value; c) and d) $f = 0.6$. No T-instability is observed, although the stress perturbation experienced by the matrix is larger than seen in the simulation with $f = 0.5$; e) and f) $f = 0.8$. Each P-instability in the velocity-weakening asperity induces a T-instability.

dimensions of the asperity (P-events). However, after a critical number of consecutive P-events, the fault ruptures over its entire length (T-event), as indicated by an abrupt peak in slip velocity and corresponding drop in stress, experienced at the centre of the matrix patch. For $f = 0.5$ (Fig. 6.2a and b), this behaviour is seen only once over the duration of the simulation, but will reoccur for longer simulated times. For $f = 0.6$ (Fig. 6.2c and d), T-events are more frequent and appear periodically. Lastly, for $f = 0.8$ (Fig. 6.2e and f), each subsequent P-event immediately triggers a T-event.

A striking feature of Fig. 6.2 is that, following a P-event, the matrix sustains a measurable perturbation in stress. On a timescale much longer than the recurrence time of a P-event, incremental slip in the asperity and far-field tectonic loading both contribute to raising the stress supported by the matrix. When the stress at the centre of the matrix patch reaches a critical level similar to the peak stress of the asperity stick-slips, the matrix patch becomes unstable and the entire fault ruptures in a T-event.

The effect that matrix Z_{ps} has on the fault dynamics is demonstrated in Fig. 6.3, displaying single-asperity simulation results with faster matrix pressure solution kinetics ($Z_{ps} = 4 \times 10^{-15}$ Pa^{-1} s^{-1}). In contrast to the previous simulation set, no T-instabilities are observed for $f = 0.5$ and 0.6. Instead, the long-term average stress supported by (and strain rate of) the matrix asymptotically approaches a constant value. For $f = 0.6$, the stress perturbation induced by the asperity is larger than for $f = 0.5$, yet is insufficient to trigger a T-instability. For this value of Z_{ps} the combined loading by the asperity and V_{imp} results in a steady-state (average) level of stress supported by the matrix that is below the critical value.

A fault containing two asperities shows similar behaviour as the single-asperity fault, where P-instabilities nucleating from both asperities perturb the matrix until a T-instability is generated (see Fig. 6.4). The larger asperity imposes larger stress perturbations than the smaller asperity, but has a longer recurrence time than the smaller asperity. This longer recurrence time may allow the stress perturbation in the matrix to (partially) relax away by creep. Moreover, the maximum slip velocity attained during a T-instability can be orders of magnitude higher than the slip velocities attained during P-events in each asperity (e.g. Fig. 6.4c).

A more illustrative way to visualise fault slip behaviour and the emergence of T-instabilities, is by considering the spatio-temporal variation in fault slip rates, as exemplified for the double-asperity system by Fig. 6.5. In this figure, slip velocities are plotted as filled contours against the along-strike position and accumulated slip (as an alternative measure of time), with the fill colours indicating the local slip velocity in units of m s^{-1}. The locations of the asperities are indicated by the black bars at the top of the figure. These asperities produce numerous P-instabilities identified by a 'layered' pattern of brighter colours, with the occasional occurrence of a T-instability

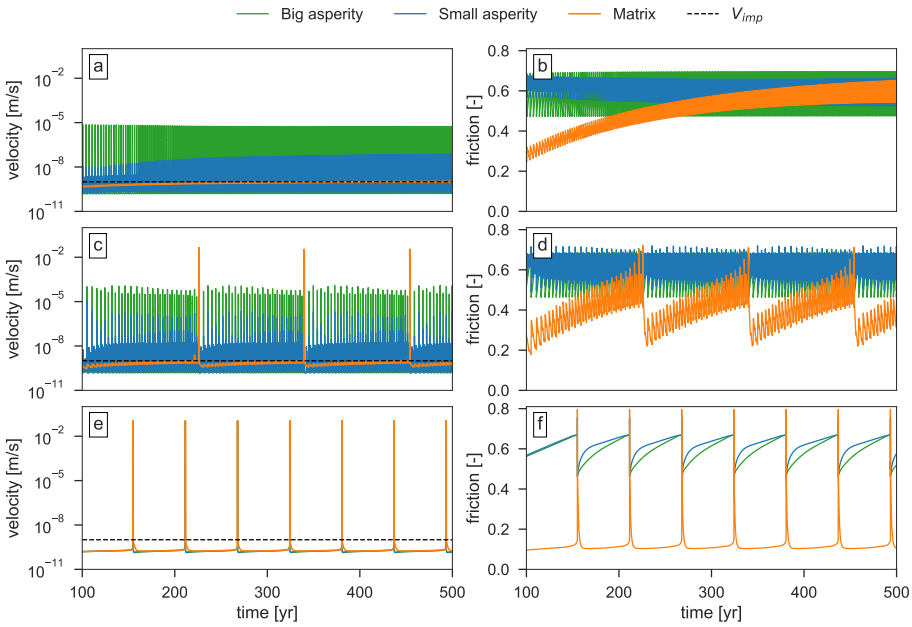

Fig. 6.4: Time series slip velocity and friction coefficient for the double-asperity simulations, with $Z_{ps} = 3 \times 10^{-15}$ Pa^{-1} s^{-1}. Quantities are measured at the centre of each asperity and matrix patches. a) and b) $f = 0.5$. No T-instabilities are observed over the simulated period of 500 years, although the stress supported by the matrix approaches the critical value. A T-instability is likely imminent for longer simulation times; c) and d) $f = 0.6$. Several T-instabilities are observed, with each asperity contributing to stress increments on the matrix; e) and f) $f = 0.8$. Each P-instability in the larger velocity-weakening asperity induces a T-instability.

identified as the fault-spanning rupture associated with high slip velocity and large total displacement.

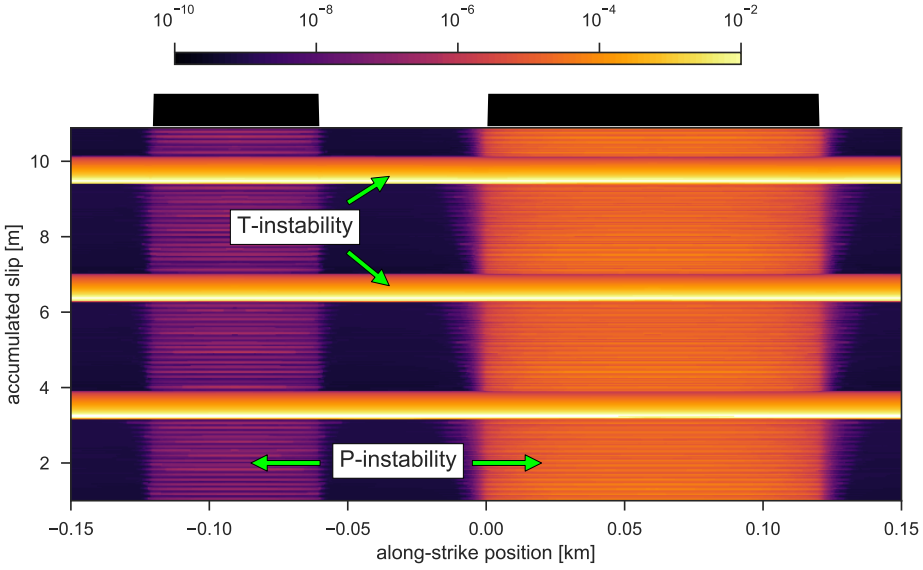

Fig. 6.5: Filled contour maps of fault slip velocity (in m s^{-1}) for the double-asperity simulation with $f = 0.6$. P- and T-instabilities are identified as brightly coloured regions that traverse the map partially and entirely, respectively. Note that there are numerous P-instabilities leading up to a single T-instability. The locations of the two asperities are indicated by the black bars below the colour bar at the top of the figure.

6.5.2 Heterogeneous faults

6.5.2.1 Seismic character

As anticipated, the simulations with randomly heterogeneous faults show complex slip behaviour controlled by the spatial and size distributions of asperities that litter the fault. This behaviour is visualised in Fig. 6.6 for simulation Set 1 by filled contour maps of the slip velocity as a function of the along-strike position and accumulated slip, for three simulations characterised by asperity distribution exponents (D) of 1, 1.5, and 2, all exhibiting an asperity occupation ratio of $f = 0.5$. For reference,

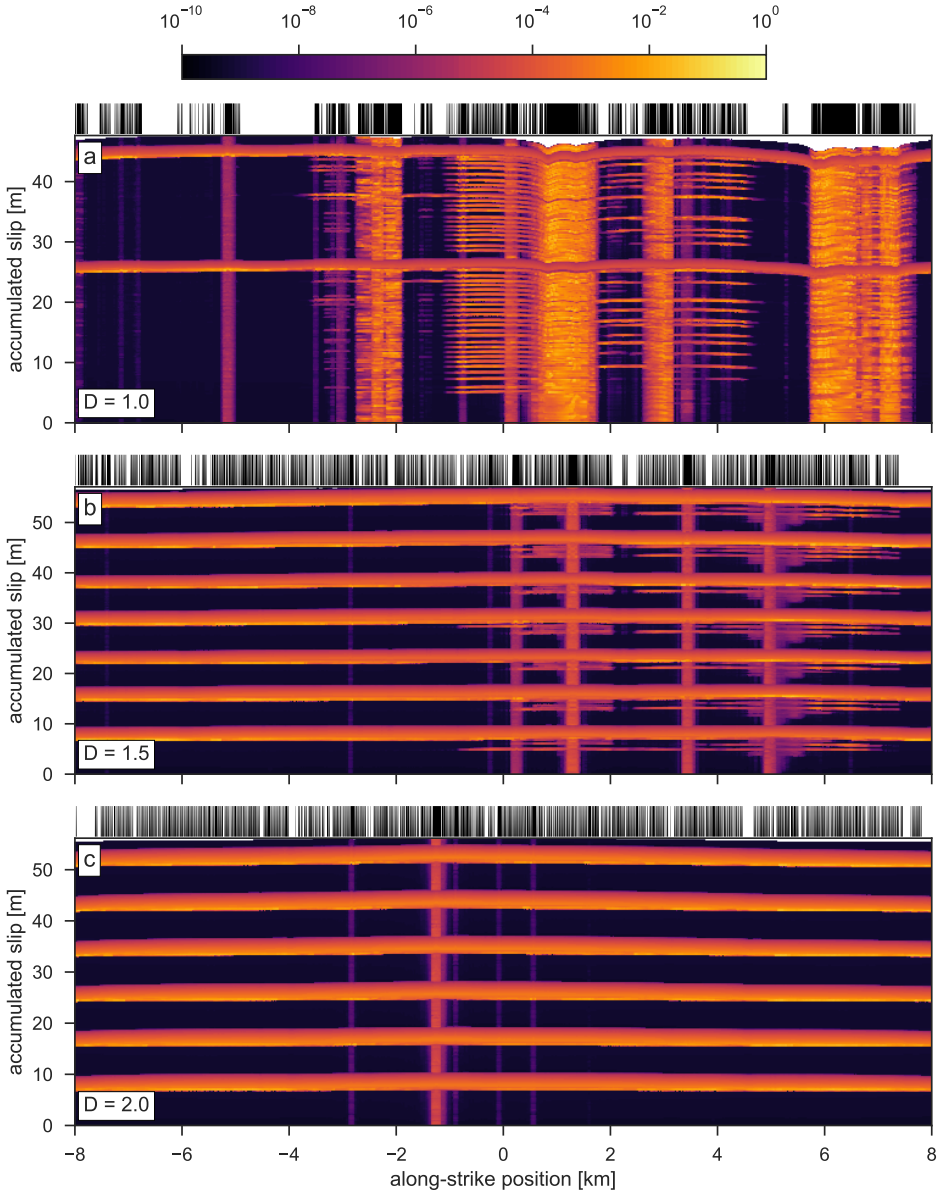

Fig. 6.6: (Caption on page 262)

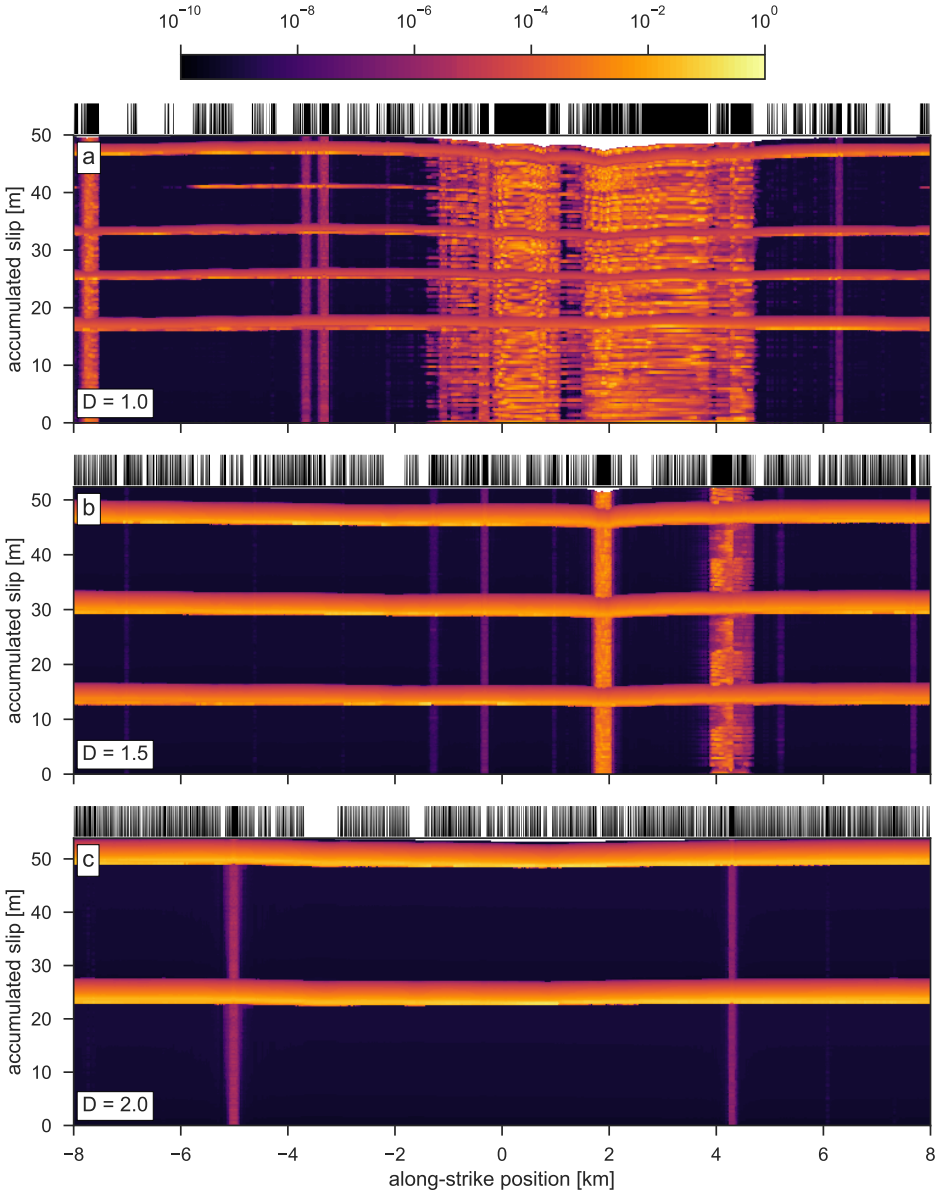

Fig. 6.7: (Caption on page 262)

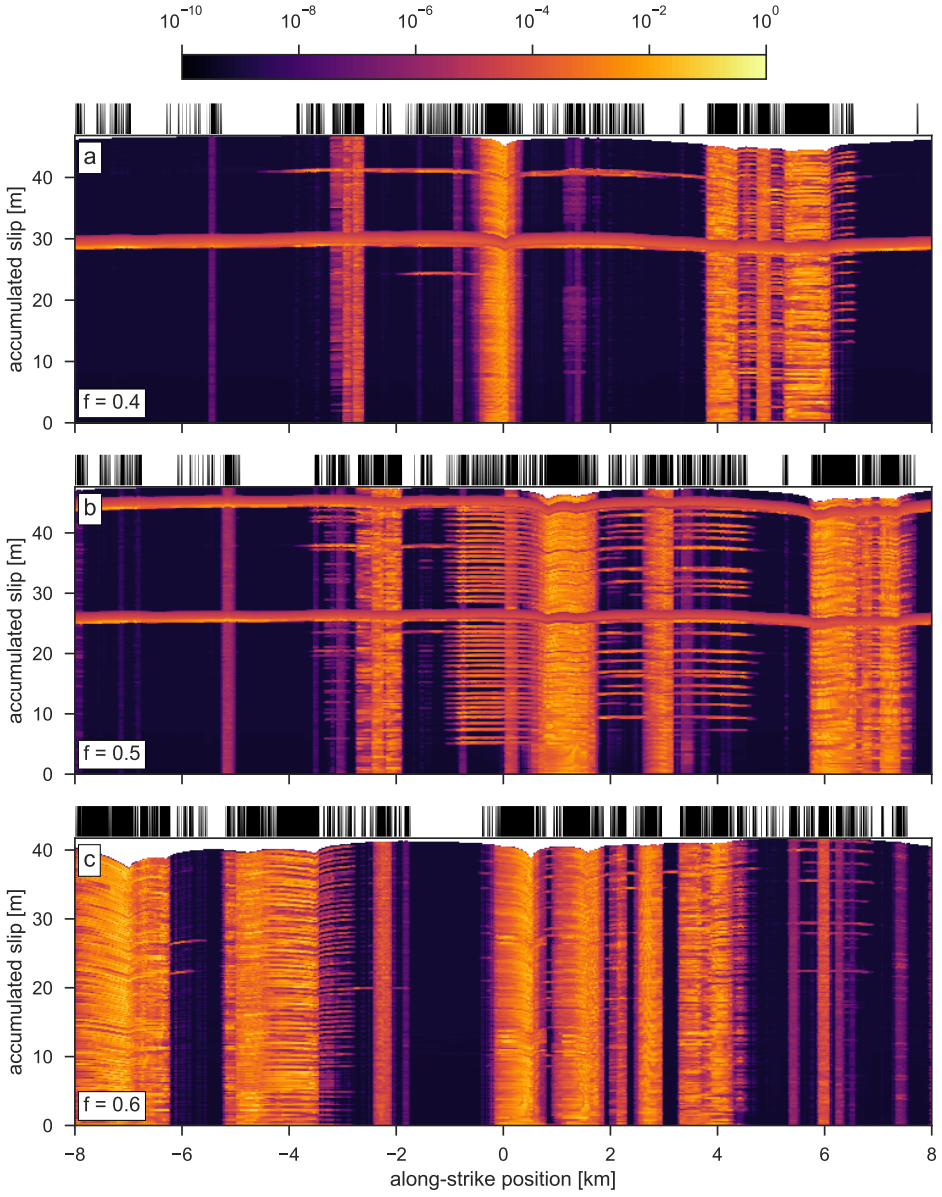

Fig. 6.8: (Caption on page 263)

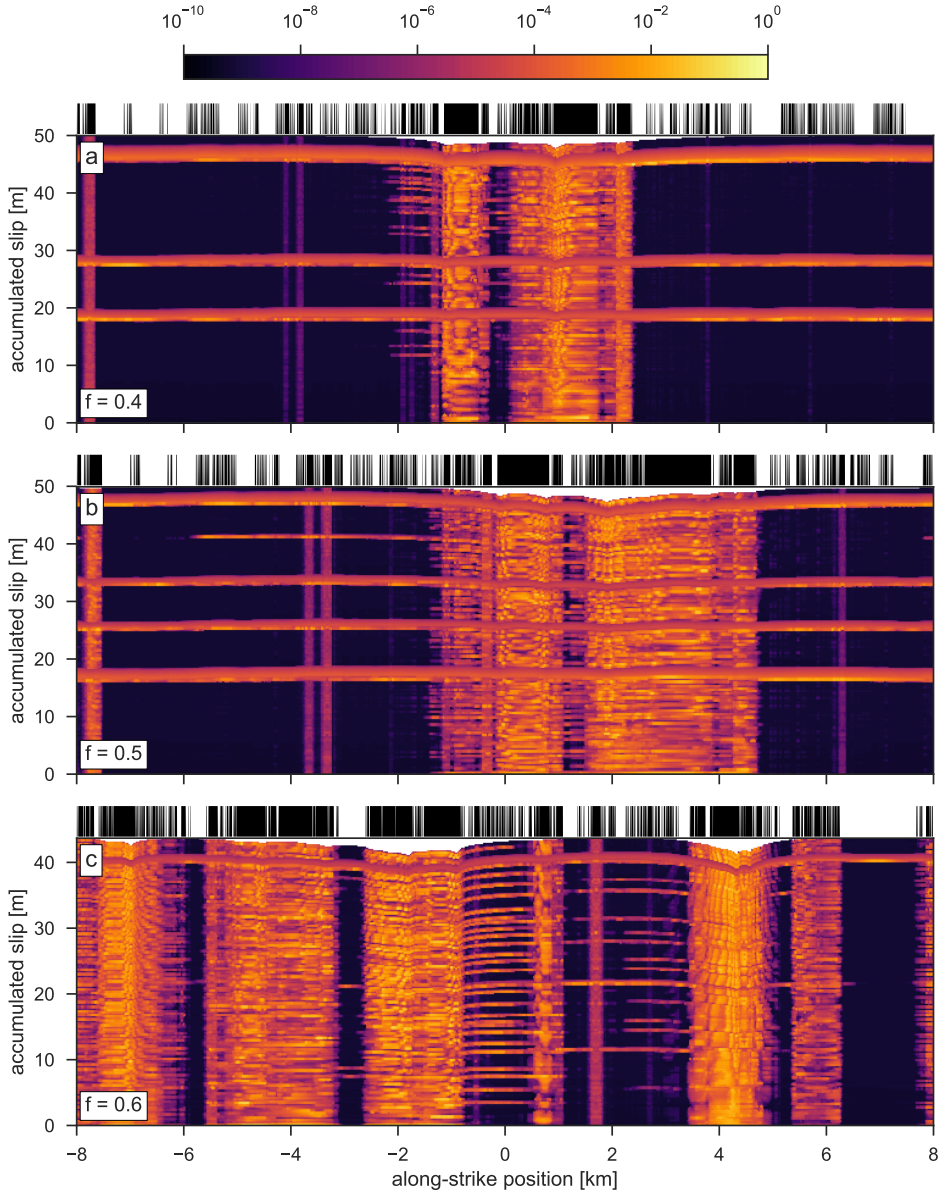

Fig. 6.9: (Caption on page 263)

Fig. 6.6: Filled contour maps of fault slip velocity (in $\mathrm{m\,s^{-1}}$) for simulation Set 1, with $f = 0.5$. a) $D = 1$ (same as Fig. 6.8b): numerous P-instabilities of various magnitude cluster around fault localities of high asperity density, and T-instabilities occur infrequently; b) $D = 1.5$: quasi-periodic T-instabilities are interspersed with small P-instabilities that increase in magnitude in the advent of a T-instability (see Fig. 6.10c); c) $D = 2$: P-instabilities exist only as small slow slip events. T-instabilities occur periodically with no precursory activity; For each simulation, the spatial distribution of asperities is plotted as a 'barcode' above each panel, with the each black bar representing an asperity.

Fig. 6.7: Filled contour maps of fault slip velocity (in $\mathrm{m\,s^{-1}}$) for simulation Set 2, with $f = 0.5$. a) $D = 1$ (same as Fig. 6.9b): numerous P-instabilities of various magnitude cluster around fault localities of high asperity density, and T-instabilities occur infrequently; b) $D = 1.5$: quasi-periodic T-instabilities are interspersed with small P-instabilities that do not increase in magnitude in the advent of a T-instability; c) $D = 2$: P-instabilities exist only as small slow slip events. T-instabilities occur periodically with no precursory activity; For each simulation, the spatial distribution of asperities is plotted as a 'barcode' above each panel, with the each black bar representing an asperity.

the asperity distribution of each simulation is indicated by the 'barcode' above each panel in Fig. 6.6, in which the black bars represent the asperities. In the simulation with $D = 1$ (Fig. 6.6a), unstable slip is predominantly produced in the form of small (a)seismic events that cluster around areas of high asperity density on the fault. Areas of low asperity density mostly creep at a steady rate. At the scale of the model fault, failure of single asperities or small clusters thereof can be classified as a P-instability, though at a lower hierarchical level (the scale of individual asperities), the definition of P-instabilities as formulated by *Luo and Ampuero* (2018) no longer holds when a cluster of asperities fails in a single event. Since the focus of this work is directed at fault-spanning events, we classify any type of partial fault rupture as a P-event, and classify complete fault rupture as a T-event. Within the simulated time of 2000 years, two fault-spanning T-instabilities are produced. No clearly interpretable precursory activity is seen that forecasts an imminent T-instability, and following a T-instability there appears to be a brief period of seismic quiescence near the centre of the fault.

Fig. 6.8: Filled contour maps of fault slip velocity (in $\mathrm{m\,s^{-1}}$) for simulation Set 1, with $D = 1$. a) $f = 0.4$: P-instabilities are sparsely covered over the model fault, with occasional P-events that extent over a larger area; b) $f = 0.5$ (same as Fig. 6.6a): several P-events extent outside of their characteristic source region; c) $f = 0.6$: P-instabilities are predominantly confined to their characteristic source regions; For each simulation, the spatial distribution of asperities is plotted as a 'barcode' above each panel, with the each black bar representing an asperity.

Fig. 6.9: Filled contour maps of fault slip velocity (in $\mathrm{m\,s^{-1}}$) for simulation Set 2, with $D = 1$. a) $f = 0.4$: P-instabilities are sparsely covered over the model fault, with occasional P-events that extent over a larger area; b) $f = 0.5$ (same as Fig. 6.7a): several P-events extent outside of their characteristic source region; c) $f = 0.6$: P-instabilities are predominantly confined to their characteristic source regions; For each simulation, the spatial distribution of asperities is plotted as a 'barcode' above each panel, with the each black bar representing an asperity.

In contrast to the simulation with $D = 1$, the simulation with $D = 1.5$ (Fig. 6.6b) exhibits frequent, quasi-periodic T-instabilities that constitute about half of the total fault slip budget. Each T-instability is preceded by P-instabilities that increase in magnitude in the advent of a T-instability. These P-instabilities also cluster near regions of higher asperity density, although the spatial asperity distribution is more diffuse than in the simulation with $D = 1$. Remarkably, in the simulation with $D = 2$ (Fig. 6.6c), there exist only two modes of unstable slip: the P-instabilities are periodic slow slip events that are each confined to a single asperity cluster just large enough to nucleate a frictional instability, and the T-instabilities occur periodically (approximately every 300 years) with no precursory activity. This bimodal distribution of unstable slip is clearly seen in a frequency-magnitude diagram (Fig. 6.10a).

The effect of varying f is illustrated in Fig. 6.8 in a similar way as in Fig. 6.6, with $D = 1$ and $f = 0.4$, 0.5, and 0.6. The seismic character of each of these simulations is very similar, with a frequency-magnitude distribution of P-events roughly following a power-law (see Fig. 6.10a), and the occasional occurrence of a T-instability in $f = 0.4$

and 0.5. The simulation with $f = 0.6$ does not display any T-instabilities, which will be discussed further in Section 6.6.1. For larger values of f, larger portions of the fault exhibit P-instabilities.

The results of simulation Set 2 are presented in Figures 6.7 and 6.9. While the behaviour seen in simulation Set 2 is broadly similar to Set 1, there are a few notable differences between the two, most likely caused by variations in local asperity density. Overall, the recurrence time of the T-instabilities in Set 2 with $D > 1$ is significantly longer than seen in Set 1, and accordingly the total displacement in one such T-instability is much larger. Also, no precursory events are seen in Set 2 with $D = 1.5$, which instead shows repeating small earthquakes. In the simulations with $D = 1$, the recurrence time of T-events is shorter in Set 2, although there is some aperiodicity to each cycle. Simulation Set 2 with $f = 0.6$ exhibits one (but small) T-instability, as opposed to its equivalent in Set 1.

In the heterogeneous fault simulations, supercycles and superimposed cycles can be defined by the occurrence of T-instabilities. We observe three classes of cycle behaviour: (i) quasi-periodic alternations between regular earthquakes and slow slip events (P-instabilities), and fault-spanning T-instabilities (e.g. Fig. 6.6a); (ii) clusters of seismicity terminated by a T-instability (Fig. 6.6b); (iii) periodic occurrences of single T-instabilities, with stable fault creep during interseismic times (Fig. 6.6c);

A quantitative way of comparing the various heterogeneous fault simulations, is by considering the (normalised) frequency-magnitude relations – see Fig. 6.10. In this figure, the effect of individual asperities and asperity clusters manifests itself as steep drops in frequency with increasing M_w, as a result of numerous repeating events on the same section of the fault (same M_w). This is particularly apparent for larger event magnitudes, as events nucleating in one given site fail to link up with other seismogenic sites, resulting in a corner-magnitude related to the largest seismogenic cluster of asperities. However, all simulations, with the exception of $f = 0.6$ in Set 1, show T-instability events that span the entire fault. For some simulations, such as $f = 0.5$ and $D = 1$, it could be argued that these anomalous events follow the frequency-magnitude relation defined by regular events, and that T-events simply extend the existing range of P-events. On the other hand, this argument does certainly not hold for simulations with $D > 1$, particularly when it is considered that these simulations

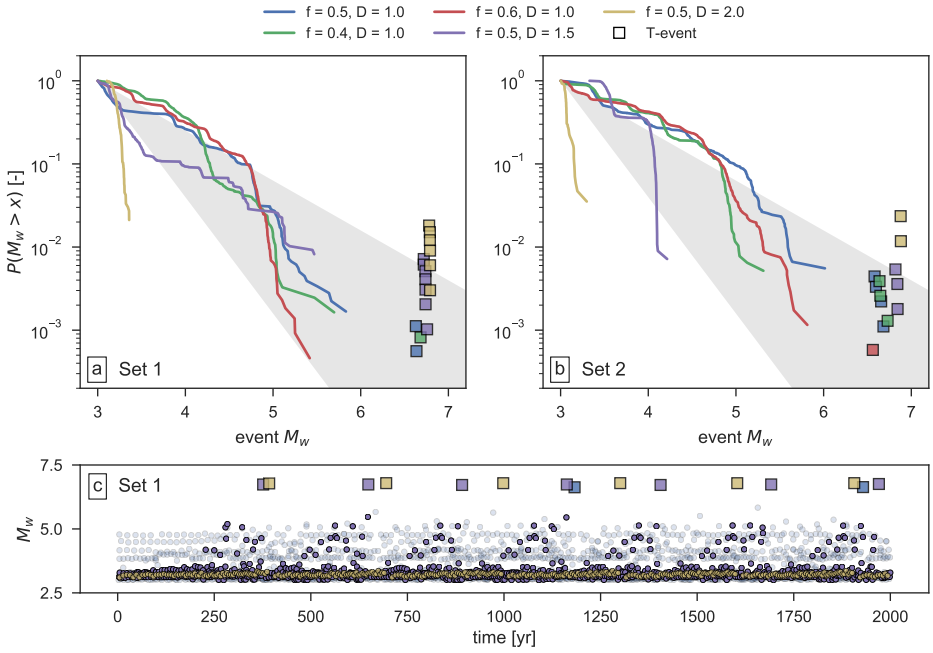

Fig. 6.10: Frequency-magnitude distributions of the heterogeneous fault simulations (including slow slip events). T-instabilities are marked as individual squares. Gray shaded areas indicate the range of Gutenberg-Richter b-values ($0.6 < b < 1.4$) observed by *Marzocchi et al.* (2016). a) Frequency-magnitude distributions simulations in Set 1, calculated only for $M_w > 3$; b) Frequency-magnitude distributions simulations in Set 2, calculated only for $M_w > 3$; c) Magnitude-time series for Set 1 with $f = 0.5$. For $D = 1.5$, there is a significant increase in P-instability magnitude leading up to a T-instability. For $D = 1$ and 2, no change in magnitude is observed. For clarity, the data for $D = 1$ is plotted in the background with higher transparency.

contain a large number of (small) slow slip events that would likely not be registered by surface monitoring stations, so that a real-world equivalent frequency-magnitude distribution would appear differently (or be absent).

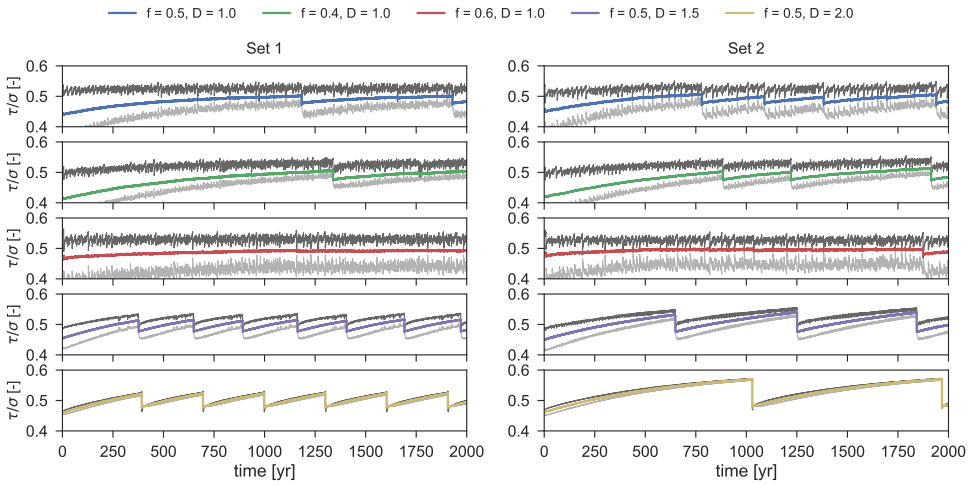

Fig. 6.11: Average coefficient of friction (τ/σ) under which the model fault operates, for all heterogeneous fault simulations (parameters as indicated in the legend). The average friction supported by the asperities and matrix is indicated by the dark and light gray curves, respectively.

6.5.2.2 Fault stress and slip deficit

Like in the single-asperity simulations, the local state of stress is of crucial importance in determining both the slip velocity and stability of a particular fault segment. To gain some insights into the evolution of fault stress, we calculate the coefficient of friction (τ/σ) at which the fault operates, averaged over the asperities, the matrix, and the total fault length (Fig. 6.11). By doing so, we observe the following:

1. For simulations characterised by $D = 1$, the average stress supported by the asperities varies around a time-constant value, i.e. the long-term asperity stress is constant, with small stress drops due to P-events. With each P-event, the average stress supported by the matrix is perturbed. This perturbation decays with time while the asperities are reloaded.

2. In the simulations with $D = 1$, and $f = 0.4$ and 0.5, long-term loading of the matrix by P-events and tectonic motion leads to a nett increase in fault stress, until a critical stress level is achieved and a T-instability is generated. Hence, the fault-scale behaviour draws strong parallels to the single-asperity behaviour reported in Section 6.5.1.

3. In the simulation with $D = 1$ and $f = 0.6$, the fault stress levels off to a time-constant value, after which all deformation is accommodated by P-events and creep of the matrix. In simulation Set 1 no T-instability is generated within the simulated time span of 2000 years, nor are there indications that it will occur in the future. In simulation Set 2, one T-instability is generated, but it is relatively small in magnitude. The average stress level that is reached in these simulations is close to the critical value of other simulations with $D = 1$.

4. In the simulations with $D > 1$, the average stress on the asperities is not constant in time and follows a similar stress evolution as the matrix. In simulation Set 1 with $D = 1.5$, P-instabilities of increasing magnitude emerge when stresses are sufficiently large. In both cases, periodic T-instabilities are generated when a critical value of stress is reached similar in value to the simulations with $D = 1$. However, the recurrence times observed in both simulation sets are markedly different, ranging from about 250 years in Set 1, to close to 1000 years in Set 2.

5. Although the simulations with $D = 2$ accommodate slip predominantly through stable creep, the long-term build-up of stress indicates that the fault-averaged creep rates are lower than the imposed loading velocity.

6.5.2.3 Nucleation and initiation of T-instabilities

Let us now consider the nucleation stage of T-instabilities for various values of D (Figs. 6.12 and 6.13; note that the vertical axis scale varies between panels). In the simulations with $D = 1$, consecutive P-instabilities cascade-up (i.e. their rupture areas link-up) over a period of about 4 days prior to the T-event, ultimately triggering a T-instability borne out of a large nucleus (spanning more than half of the periodic width of the fault). The hypocentres of the P-events migrate along the perimeter of

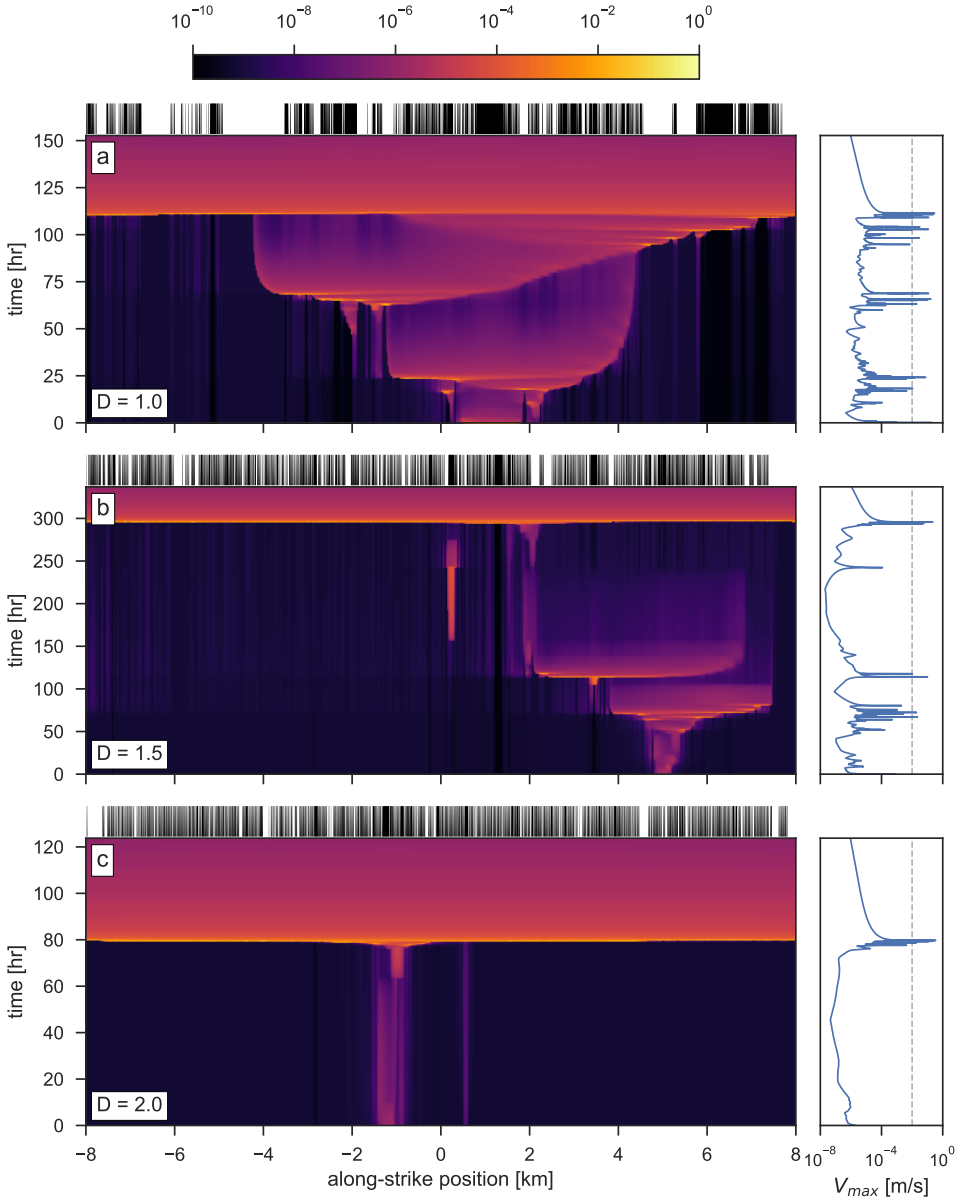

Fig. 6.12: (Caption on page 270)

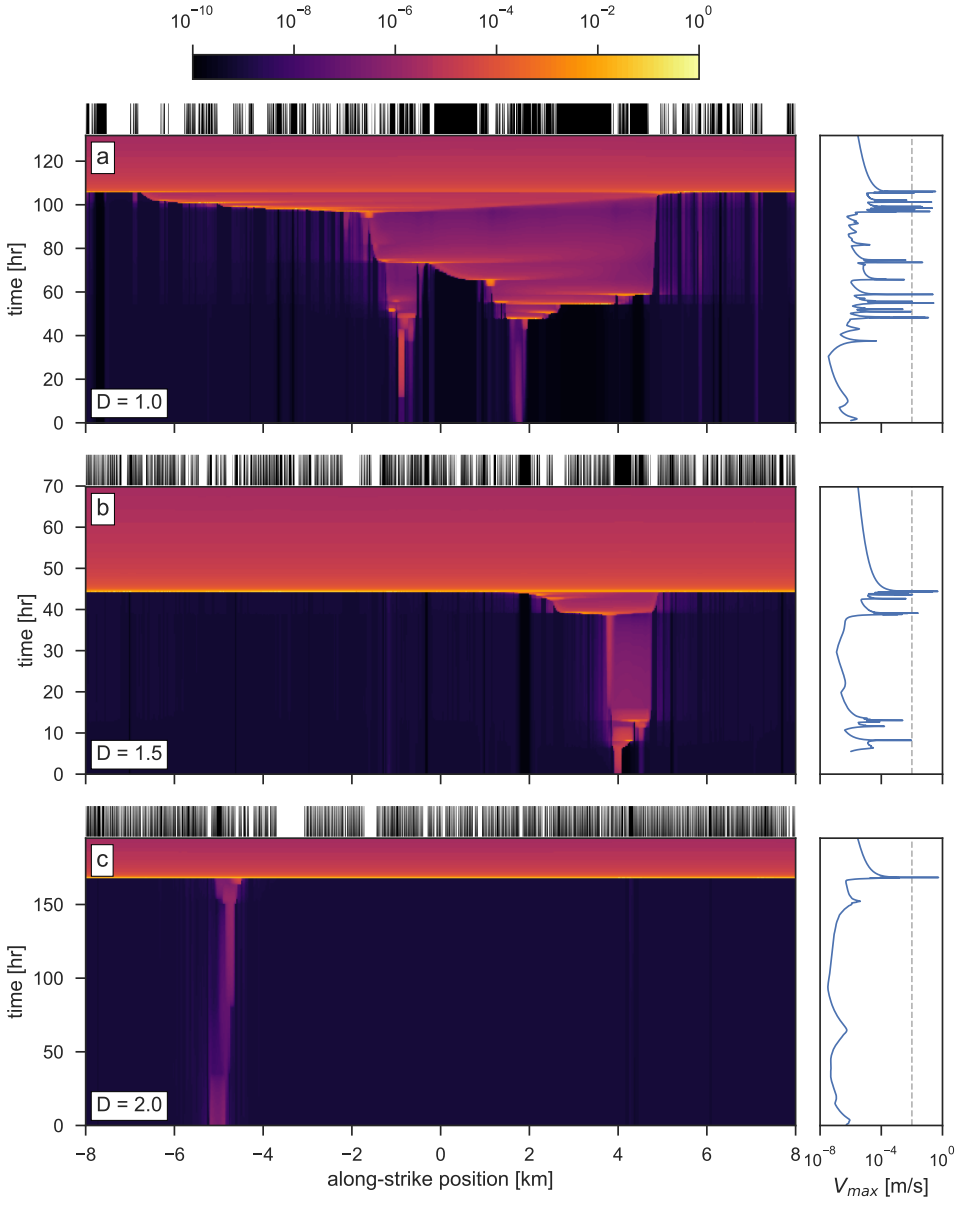

Fig. 6.13: (Caption on page 270)

Fig. 6.12: Filled contour maps of fault slip velocity (in m s^{-1}) imediately prior to nucleation of the last T-instability, for each simulation in Set 1 with $f = 0.5$. a) $D = 1.0$: P-instabilities dynamically cascade-up over a duration of about 4 days prior to the T-event, producing a sequence of foreshocks; b) $D = 1.5$: P-instabilities fail to cascade-up, but afterslip facilitates the nucleation of a T-instability. Note that the nucleus for the T-instability is small; c) $D = 2.0$: the T-event emerges from a small nucleus which rapidly grows into an instability.

Fig. 6.13: Filled contour maps of fault slip velocity (in m s^{-1}) imediately prior to nucleation of the last T-instability, for each simulation in Set 2 with $f = 0.5$. **a**) $D = 1.0$: P-instabilities dynamically cascade-up over a duration of about 2 days prior to the T-event; **b**) $D = 1.5$: P-instabilities cascade-up into a T-instability, but the extent of the final nucleation region is much smaller than observed in simulations with $D = 1$; **c**) $D = 2.0$: the T-event emerges from a small nucleus which rapidly grows into an instability.

the nucleus as a sequence of foreshocks, and the T-event itself shows a heterogeneous spatial distribution of slip velocity.

The simulation with $D = 1.5$ in Set 1 displays a failed cascade-up sequence, with a temporal gap of about one week between the last seismogenic P-instability and the T-event. However, the nucleation region of the T-instability appears to grow out of afterslip following the last P-event, hinting that nucleation of the T-instability is facilitated by afterslip. In simulation Set 2, P-events manage to cascade-up over a time-span of less than 2 days, though the nucleus for the T-instability is significantly smaller than observed in the simulations with $D = 1.0$

In contrast with the above, the simulations with $D = 2$ show no signs of cascading P-events. The T-instabilities nucleate seemingly spontaneously and abruptly from a minute nucleation patch, extending only a fraction of the total periodic fault width. In addition, the T-event is rather homogeneous in its spatial distribution of slip velocity.

6.6 Discussion

6.6.1 Mechanisms behind T-instabilities and generality of results

In the sections that follow, the micro-mechanics of earthquake nucleation are discussed extensively. We therefore begin the discussion with a detailed review of the origin of a frictional instability in the CNS model framework.

In the CNS model formulation adopted in this study, strain is accommodated through the parallel operation of non-dilatant pressure solution creep and dilatant granular flow, for which the constitutive relations are given by Eqns. (6.2) and (6.4), respectively. For the purpose of this discussion, we can consider the shear strength of the fault to follow one of two end-member cases, one in which pressure solution creep dominates over granular flow (i.e. $\dot{\gamma}_{ps} \gg \dot{\gamma}_{gr}$), and one where the converse is true ($\dot{\gamma}_{ps} \ll \dot{\gamma}_{gr}$). For each of these two end-member scenarios, the shear strength as a function of the imposed shear strain rate ($\dot{\gamma} = V_{imp}/h$) follows directly from the above-mentioned constitutive relations:

$$\tau_{ps} = \frac{\dot{\gamma}}{Z_{ps} f_1(\phi)} \tag{6.12a}$$

$$\tau_{gr} = \frac{\tilde{\mu} + \tan\psi}{1 - \tilde{\mu}\tan\psi}\sigma \tag{6.12b}$$

where τ_{ps} and τ_{gr} denote the end-member shear strengths of pressure solution and granular flow, respectively. Recall that $\tilde{\mu} = \tilde{\mu}^* + \tilde{a}\ln\left(\dot{\gamma}/\dot{\gamma}^*_{gr}\right)$ and $\tan\psi = 2H\left(\phi_c - \phi\right)$, which makes τ_{gr} an explicit function of strain rate and porosity. For simplicity, we consider a simple two-mechanism model where $\tau = \min\left(\tau_{ps}, \tau_{gr}\right)$ (e.g. *Reinen et al.*, 1992). In the numerical model approach as presented in Section 6.4.2, we solve for τ more accurately by solving the appropriate kinematic relations (taking $\dot{\gamma} = \dot{\gamma}_{ps} + \dot{\gamma}_{gr}$), but the simplified conceptual model discussed here carries sufficient detail to apprehend the nucleation process.

In the two-mechanism model (at steady-state), the boundary between the ductile creep regime and the cataclastic granular flow regime are marked by the intersection of the two end-member strength curves (i.e. $\tau_{ps} = \tau_{gr}$; see Fig. 6.14). Consider now a fault segment that underwent deformation in the creep regime for sufficiently long durations so that $\phi \to \phi_0$, marked by point 1 in Fig. 6.14a. This point could represent the phyllonitic matrix at steady-state, or the asperity gouge after a long interseismic period. Next, imposed tectonic loading or a perturbation in shear stress will drive point 1 towards higher strain rates and closer to the transition to granular flow, as indicated by point 2. In the case that no further stressing occurs, the initial perturbation will decay by ductile creep and so the system returns to point 1. However, for incremental slip of the asperity in the form of P-events, or for continuous loading (due to tectonic motion), the incremental or continuous build-up in stress will drive the system towards a critical point that marks the onset of granular flow (point 3). By its own nature, operation of granular flow induces dilatation, and so at the critical point the gouge porosity starts to increase ($\phi > \phi_0$). Following Eqn. (6.12b), an increase in porosity (i.e. a decrease in $\tan\psi$) causes substantial lowering of τ_{gr}, and so the fault rapidly weakens with increasing shear strain as ϕ increases in accordance with Eqn. (6.4b) and (6.5b) (point 4). Hence, for a sufficiently low self-stiffness, a frictional instability is generated and the fault accelerates. After the slip event, the fault returns to its initial state (point 1) and the same process may reoccur. A similar conceptual interpretation for the nucleation of instabilities was recently proposed by *Verberne et al.* (2017), on the basis of laboratory observations.

With the detailed description of the nucleation mechanism of frictional instabilities, we can continue to interpret the spectrum of slip behaviour displayed in the simulations, starting with the single-asperity system. In Fig. 6.2, it can be seen that for larger fault fractions occupied by the asperity (i.e. larger asperity and smaller matrix segments), a T-instability occurs more frequently. As remarked in Section 6.5.1, each P-event induces a stress perturbation in the matrix. With increasing value of f, the size of the matrix segment shrinks at the cost of the asperity, and so each P-instability exerts a larger perturbation on the matrix, facilitating the transition into the granular flow regime for a given level of stress supported by the matrix. For the simulation with $f = 0.8$, each stress perturbation from a P-event is sufficiently large to immediately trigger a T-instability. When the matrix exhibits faster creep (i.e. higher Z_{ps}; Fig. 6.3),

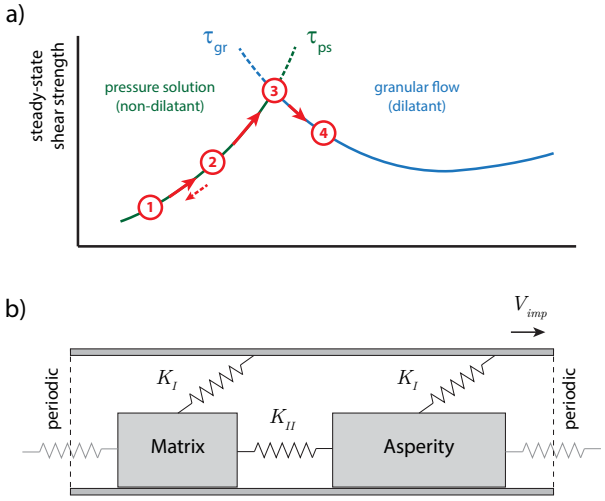

Fig. 6.14: **a**) Synoptic illustration of the nucleation of a frictional instability in the CNS model. 1: initial state of the system deforming by non-dilatant pressure solution creep; 2: a perturbation in stress causes enhanced creep rates. This perturbation may (partly) relax over time; 3: by incremental or continuous loading, the stress required to activate dilatant granular flow (the 'brittle strength') is reached (i.e. $\tau = \tau_c$ in Eqn. (6.18)); 4: as the system enters the (velocity-weakening) dilatant regime, a frictional instability may be generated; **b**) Schematic diagram of the geometry adopted for the analysis of a single-asperity system. After *Luo and Ampuero* (2018).

the matrix may accommodate long-term tectonic loading and short-term P-event stress perturbations entirely by ductile creep, so that no T-instabilities are generated.

Turning now to the randomly heterogeneous fault simulations, we observe similar behaviour to the single-asperity system, particularly in the simulations with $D = 1$, and $f = 0.4$ and 0.5 (top two panel rows in Fig. 6.11). In these simulations, the average stress supported by the matrix increases over time until a critical stress is achieved that triggers the nucleation of an instability in fault segments that were previously creeping stably in the ductile regime. Since large parts of the fault are near-critically stressed, the stress perturbation caused by an approaching rupture front facilitates cascade-style failure of the fault in its entirety. The occurrence of such a T-instability

on a heterogeneous fault could be analogous to great earthquakes in nature, such as megathrust ruptures. We will explore this idea further in Section 6.6.4.

Two peculiar model outcomes that are still left unexplained are the absence of T-instabilities in the simulation with $f = 0.6$ and $D = 1$ (exhibiting abundant P-events), and the occurrence of T-instabilities in simulation Set 1 with $D = 2$ (exhibiting only minute slow slip events; see Fig. 6.6). In the first case ($f = 0.6$), it can be seen in Fig. 6.11 that the average fault stress no longer increases after about 1000 years, which indicates that the long-term fault slip rates equal the tectonically imposed velocities, so that no elastic strain accumulates. In other words, the combination of stable creep of the matrix and seismic moment released by the P-events balances the slip budget. This is similar to the single-asperity simulations exhibiting high Z_{ps} that achieve a long-term, steady-state matrix stress value (e.g. Fig. 6.3a-d). The ductile creep rate of the matrix at this steady-state level of stress, in combination with unstable slip of the asperity, is sufficient to accommodate the imposed strain rate and so no T-instabilities are required to balance the slip budget.

Conversely, the simulations with $D = 1.5$, and in particular $D = 2$, show continuous build-up of elastic stress with little or no moment release by P-events. Note that, even though these simulations show stable creep on timescales shorter than about 250 years, still 50 % of the fault plane consists of (velocity-weakening) asperities that exhibit lower pressure solutions rates than the phyllonite matrix, and so deform at strain rates lower than what is imposed. For the chosen value of Z_{ps} of the matrix, and in the situation that no asperities would be present (i.e. $f = 0$), the fault would accommodate the imposed strain entirely by ductile creep and would therefore be perfectly stable. Hence, the asperities effectively act as a 'break' in moderating fault slip rates to lower values, and as a result the stresses on the fault increase over time. One crucial aspect here is that the spatial and size distribution of the asperities is diffuse owing to its high fractal dimension, so that strain accommodation is distributed over the entire fault and no single asperity or cluster of asperities is large enough to generate large instabilities (fast earthquakes). This observation complements previous numerical studies (*Dublanchet et al.*, 2013; *Luo and Ampuero*, 2018; *Skarbek et al.*, 2012; *Yabe and Ide*, 2017) that considered only f to control the seismic character of heterogeneous faults. Moreover, the model outcomes in this respect are in good agreement with the field observations

of *Fagereng* (2011), who concluded that deformation observed on an outcrop scale was localised for $D < 1.4$, and distributed for $D > 1.4$, with mixed-mode deformation features observed at $D \approx 1.4$. In the model simulations, we observe predominant seismic slip at $D = 1$, (short-term) stable creep at $D = 2$, and mixed-mode behaviour at $D = 1.5$. However, the simulations with $D \geq 1.5$ still exhibit long-term T-instabilities, for which no direct evidence was observed by *Fagereng* (2011).

6.6.2 Analysis of a single asperity

To quantify the conceptual model described above, we analyse the response of a single-asperity periodic fault (or more precisely: an infinite regular array of asperities). To this end, further simplifications are made to the geometry adopted in the numerical tests (see Section 6.4.3.1) by representing the fault by two discrete blocks that are each coupled to a load-point by a spring with stiffness K_I, and to each other by a spring with stiffness K_{II} (Fig. 6.14b). The asperity is identified by subscript a and exhibits pressure solution kinetics Z_a, whereas the matrix is identified by subscript m and exhibits pressure solution kinetics $Z_m > Z_a$. Following *Luo and Ampuero* (2018), the stress balance equations for each block can accordingly be written as:

$$\frac{\mathrm{d}\tau_a}{\mathrm{d}t} = K_I \left(V_{imp} - h\dot{\gamma}_a\right) + K_{II} h \left(\dot{\gamma}_m - \dot{\gamma}_a\right) \tag{6.13a}$$

$$\frac{\mathrm{d}\tau_m}{\mathrm{d}t} = K_I \left(V_{imp} - h\dot{\gamma}_m\right) + f' K_{II} h \left(\dot{\gamma}_a - \dot{\gamma}_m\right) \tag{6.13b}$$

where $f' = f/(1-f)$. We consider a timescale that is much longer than the recurrence time of P-instabilities nucleating from within the asperity. On this timescale, the average stress supported by the asperity remains constant ($\dot{\tau}_a = 0$; see e.g. Fig. 6.2b), so that $\dot{\gamma}_a$ can be written explicitly as:

$$\dot{\gamma}_a = \frac{K_I V_{imp} + K_{II} h \dot{\gamma}_m}{h\left(K_I + K_{II}\right)} \tag{6.14}$$

Since the matrix only deforms by ductile creep during the interseismic phase of a T-event cycle, it is taken that $\dot{\gamma}_m = \dot{\gamma}_{ps} = Z_m \tau_m f_1(\phi_0)$. Substitution of (6.14) in

(6.13b) then yields:

$$\frac{\mathrm{d}\tau_m}{\mathrm{d}t} = (V_{imp} - hZ_m\tau_m f_1(\phi_0)) \left(K_I + \frac{f' K_I K_{II}}{K_I + K_{II}} \right) \tag{6.15}$$

This relation describes the (long-term) evolution of the shear stress supported by the matrix. This first order differential equation has the following particular solution:

$$\tau_m(t) = \left(\tau_r - \frac{d}{c} \right) \exp(-ct) + \frac{d}{c} \tag{6.16}$$

where τ_r is the residual stress after a slip event (and $\tau_m(0) = \tau_r$), and with

$$c = hZ_m f_1(\phi_0) \left(K_I + \frac{f' K_I K_{II}}{K_I + K_{II}} \right) \tag{6.17a}$$

$$d = V_{imp} \left(K_I + \frac{f' K_I K_{II}}{K_I + K_{II}} \right) \tag{6.17b}$$

$$\frac{d}{c} = \frac{V_{imp}}{hZ_m f_1(\phi_0)} \tag{6.17c}$$

The nucleation of a T-instability is governed by the transition from non-dilatant ductile creep to dilatant granular flow, marked by a critical stress τ_c equal to the maximum granular flow shear strength, i.e.:

$$\tau_c = \tau_{gr}(\phi_0) \approx \frac{\tilde{\mu}^* + \tan\psi_0}{1 - \tilde{\mu}^* \tan\psi_0} \sigma \tag{6.18}$$

where $\tan\psi_0 = 2H(\phi_c - \phi_0)$. In this relation, the reference granular flow strain rate $\dot{\gamma}^*_{gr}$ that corresponds to a reference friction coefficient $\tilde{\mu}^*$ should be chosen in the vicinity of the nucleation strain rate (though $\tilde{\mu}$ is only weakly sensitive to velocity for small values of $\tilde{a}$).

In addition to continuous loading by the load-point or long-term slip in the asperity, the matrix also experiences stress perturbations from P-events nucleating in the asperity and propagating into the matrix. While at a given moment in time the stress on the matrix may be lower than τ_c, a stress perturbation of $\delta\tau$ may briefly (and locally) raise the stress above τ_c. Therefore, the minimum long-term stress that needs to be achieved

before a T-instability may nucleate is $\tau(t) \geq \tau_c - \delta\tau$. By setting $\tau(t) = \tau_c - \delta\tau$, one can solve for the time required to arrive at this critical stress by long-term loading:

$$t_c = \frac{1}{c} \ln \left(\frac{d - c\tau_r}{d - c\left[\tau_c - \delta\tau\right]} \right) \tag{6.19}$$

in which τ_r is the minimum (or residual) stress after the previous T-event, i.e. $\tau_r = \tau(t = 0)$. Note that t_c is only finite and real when $d > c\left[\tau_c - \delta\tau\right]$, which motivates the following stability criterion:

$$\zeta = \frac{hZ_m f_1\left(\phi_0\right)}{V_{imp}} \left(\tau_c - \delta\tau\right) \tag{6.20}$$

On the long-term, the matrix will be unstable when $\zeta < 1$. In other words, T-instabilities are anticipated in finite time when $\zeta < 1$, whereas only regular earthquakes (P-events) or creep are anticipated when $\zeta > 1$. In the trivial case that $K_{II} = 0$, i.e. when there exists no coupling between the matrix and the asperity, then $\zeta = 1$ simply marks the transition from ductile creep to granular flow ($\tau_{ps} = \tau_{gr}$) for a single spring-block.

The magnitude of the stress perturbation can be related to the stress drop in the asperity $\Delta\tau > 0$ through Eqn. (6.13):

$$\Delta\tau = \left(K_I + K_{II}\right) \delta d_a \tag{6.21a}$$

$$\delta\tau = f' K_{II} \delta d_a = \frac{f' K_{II}}{K_I + K_{II}} \Delta\tau \tag{6.21b}$$

Furthermore, to a first order, the stress drop $\Delta\tau$ can be approximated as the stress at nucleation (Eqn. (6.18)) minus the stress at critical state (for which $\tan\psi = 0$):

$$\Delta\tau \approx \tau_c - \tilde{\mu}^* \sigma = \frac{\left[1 + \left(\tilde{\mu}^*\right)^2\right] \tan\psi_0}{1 - \tilde{\mu}^* \tan\psi_0} \sigma \tag{6.22}$$

The criterion for the emergence of T-instabilities in finite time can now be written in terms of four dimensionless control parameters:

$$\zeta = \alpha \left(\mu_c - \kappa\Delta\mu\right) \tag{6.23}$$

with

$$\alpha = \frac{hZ_m f_1(\phi_0)\sigma}{V_{imp}} \tag{6.24a}$$

$$\mu_c = \frac{\tilde{\mu}^* + \tan\psi_0}{1 - \tilde{\mu}^* \tan\psi_0} \tag{6.24b}$$

$$\Delta\mu = \frac{\left[1 + (\tilde{\mu}^*)^2\right] \tan\psi_0}{1 - \tilde{\mu}^* \tan\psi_0} \tag{6.24c}$$

$$\kappa = \frac{f' K_{II}}{K_I + K_{II}} \tag{6.24d}$$

For large W/L, $K_{II} \gg K_I$, so that $\kappa \approx f'$. In the above, $\alpha\mu_c = \tau_c/\tau_{ps}$ holds the meaning of a 'rheological distance' from the critical stress τ_c, with $\alpha\mu_c > 1$ implying that on the long-term the matrix would deform at steady-state creep ($\tau_c > \tau_{ps}$) and be velocity-strengthening, so that the matrix would remain stable if not perturbed by a remote P-event. In the heterogeneous fault simulations, a value of $Z_m = 3 \times 10^{-15}$ Pa^{-1} s^{-1} corresponds to a value of $\alpha\mu_c$ of 1.12, and so stress transfer between the matrix and the asperities is required to generate a T-instability.

Lastly, the case that $t_c \leq 0$ should be considered, which implies that $\delta\tau \geq \tau_c - \tau_r$. In other words, the fault undergoes a T-instability when each individual stress perturbation $\delta\tau$ immediately raises the stress on the matrix block above τ_c, so that each P-event triggers a T-event. This occurs when:

$$\kappa \geq \frac{\mu_c - \mu_r}{\Delta\mu} \tag{6.25}$$

where $\mu_r = \tau_r/\sigma$. Under the approximation that $\kappa \approx f'$, and making the first-order assumption that μ_r is independent of f', one can solve for a critical value of $f' = f'_c = (\mu_c - \mu_r)/\Delta\mu$ above which each P-instability ruptures the entire fault. Note that this stability boundary is independent of pressure solution kinetics, and only depends on granular flow parameters.

To assess the accuracy of these asymptotic relations, we run additional simulations similar to the single asperity simulations described in Section 6.4.3.1, in which we

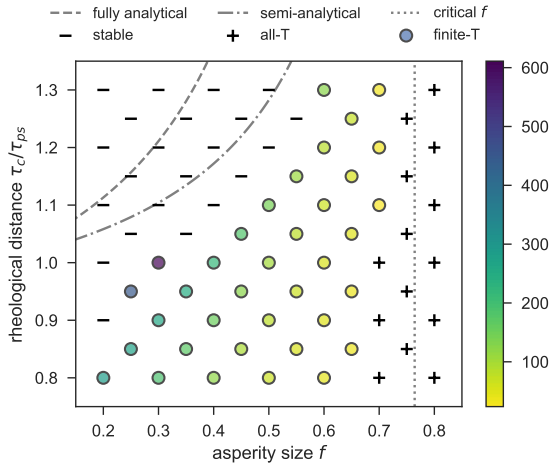

Fig. 6.15: Style of the instabilities generated by a single-asperity system, as a function of relative asperity size f and rheological distance $\alpha\mu_c = \tau_c/\tau_{ps}$. The style of deformation is characterised either by exhibiting no T-instabilities ('stable'), some T-instabilities with a larger number of P-instabilities ('finite-T'), or only T-instabilities ('all-T'). The analytically and semi-analytically predicted boundaries between these domains (based on Eqn. (6.23) and (6.25)) are indicated by the gray lines, the numerical observations are indicated by the symbols. The fill of the coloured circles represents the recurrence time of T-events (in years), as indicated by the colour bar.

systematically vary the asperity size f in the range of 0.2-0.8 and the rheological distance $\alpha\mu_c = \tau_c/\tau_{ps}$ in the range of 0.8-1.3, with $W/L = 100$. For each simulation in the covered parameter space the style of matrix deformation is characterised as exhibiting no T-instabilities ('stable'), only T-instabilities ('all-T'), or some T-instabilities with a larger number of P-instabilities ('finite-T') – see Fig. 6.15. In this figure, the predicted boundary between the finite-T and all-T domains appears as a vertical line defined by Eqn. (6.25). The boundary between the stable and finite-T domains (for which $\zeta = 1$ in Eqn. (6.23)) is estimated in two different ways: the fully analytical prediction adopts values of μ_c and $\Delta\mu$ as given by Eqn. (6.24b) and (6.24c), respectively. The semi-analytical prediction employs an average of the measured values of μ_c and $\kappa\Delta\mu$

in the numerical simulations, which are subsequently substituted in Eqn. (6.23). While the fully analytical prediction lies at an appreciable distance from the numerically determined transition from stable to finite-T behaviour, the semi-analytical prediction lies tangent to the numerical boundary and shows favourable agreement for the higher values of f explored, indicating that the mismatch between the fully analytical and numerical results is largely caused by inaccuracies in the approximation of μ_c and $\kappa\Delta\mu$.

One can now conclude from this exercise that our conceptual interpretation of a T-instability in the CNS model framework is supported by a more quantitative analysis, which reveals four dimensionless parameters (α, μ_c, κ, and $\Delta\mu$) that control the overall style of seismicity, i.e. the existence of T-instabilities in a periodic, single-asperity system. Although this analysis cannot be directly applied to the randomly heterogeneous fault simulations, it provides a measure of confidence of the interpretation and understanding of these systems.

6.6.3 Comparison with rate-and-state friction

On the basis of the previous analysis, we can now compare the interpretation of T-instabilities predicted by the CNS model with previous analyses based on rate-and-state friction. The occurrence of T-instabilities in a periodic single-asperity system was investigated in great detail by *Luo and Ampuero* (2018). Based on their observations, seven dimensionless parameters were identified to control the transition from P- to T-instabilities, and the seismic character of the system. In this discussion, we will restrict ourselves to the relative strength α_R and area ratio f', which are defined as:

$$\alpha_R \equiv \frac{(b_w - a_w)\,\sigma_w}{(a_s - b_s)\,\sigma_s} \tag{6.26a}$$

$$f' \equiv L_w/L_s \tag{6.26b}$$

In the above definitions, subscripts w and s denote the regions of velocity-weakening (VW) and velocity-strengthening (VS), respectively, a and b denote the RSF constitutive parameters (see Eqn. (6.1)), and L_x is the length of a particular region (either VW or VS). In this study, $\sigma_w = \sigma_s = \sigma$. Recall that the area ratios f' (used by *Luo*

and Ampuero, 2018) and f (used in this study) are related through $f' = f/(1-f)$. The relative strength parameter α_R represents the strength contrast between the velocity-weakening asperity, and velocity-strengthening matrix. Depending on the chosen values of α_R and f', the fault would rupture either partly in a P-instability, or fully in a T-instability. Mixed-mode behaviour, i.e. simulations exhibiting both P- and T-instabilities, only emerged for large values of α_R (strong VW of the asperity compared to the degree of VS of the matrix). Mixed-mode behaviour would manifest itself as P-instabilities preceding a T-instability in the form of foreshocks, or as supercycle behaviour defined by clustered occurrences of fault-spanning ruptures interspersed by P-instabilities. By increasing f', the critical value of α_R at which T-instabilities and mixed-mode behaviour emerge, decreases, i.e. the system becomes more prone to a T-instability when the area of the asperity is large. It was found that the critical value of α_R that marks the transition decreases approximately as $1/f'$.

Since classical rate-and-state friction (as adopted by *Luo and Ampuero*, 2018) assumes constant values of a and b, there exists no transition from velocity-strengthening ($(a-b) > 0$) to velocity-weakening ($(a-b) < 0$) with increasing slip velocity. Therefore, the occurrence of T-instabilities is purely of geometrical origin: if the size of the VS region is small (large f'), or if its resistance to accelerated slip is small (large α_R), a rupture nucleating in the VW asperity may traverse the VS region and link up with neighbouring asperities (note that the fault geometry adopted by *Luo and Ampuero* (2018) is periodic, so that the rupture emanating from the asperity links up with itself). This interpretation is supported by previous numerical work (e.g. *Tinti et al.*, 2005), detailed further by *Skarbek et al.* (2012), *Dublanchet et al.* (2013), *Luo and Ampuero* (2018), and others. However, in the CNS model, the equivalent values of $(a-b)$ in the ductile creep regime (i.e. $\mathrm{d}\left(\tau_{ps}/\sigma\right)/\mathrm{d}\ln V$) is of the order of τ_{ps}/σ, which is one or more orders of magnitude larger than the equivalent (steady-state) values of $(b-a)$ in the granular flow regime (see Chapter 5 for derivation and discussion). A value of $(a-b)$ of e.g. 0.3 in the creep regime may seem excessive compared to values typically reported by laboratory studies and used in numerical models (in the range of $\pm 10^{-2}$; see *Scholz*, 2002). However, most of the laboratory studies reporting these values of $(a-b)$ do not achieve pressure and/or temperature conditions required for steady-state deformation in the ductile creep regime. In experiments that do achieve such conditions, 'anomalous' values of $(a-b)$ are observed up to 0.2 (*Blanpied et al.*, 1998; *Shimamoto*,

1986; *Verberne et al.*, 2017). Furthermore, it has been argued that $(a-b)$ in this regime scales inversely proportional to the stress exponent n of the deformation mechanism, i.e. $(a-b) = \tau/n\sigma$, so that deformation mechanisms other than pressure solution may exhibit lower values of $(a-b)$ (*Chen et al.*, 2017b; *Shimamoto and Noda*, 2014). Therefore, reasonable values of α_R predicted for the ductile creep regime are of order 0.1 or less, which would require $f' > 10$ to facilitate T-instabilities in CNS-governed model faults. The fact that fault-spanning ruptures are observed in the single-asperity simulations presented in this work for $f' = 0.25$ (and possibly lower) indicates that the occurrence of the observed T-instabilities cannot be explained by geometry alone, and that the rheology of the fault, namely the transition from non-dilatant to dilatant deformation, plays a crucial role.

In a two asperity system, *Kaneko et al.* (2010) investigated the probability that both asperities rupture in a single event, as a function of their separation distance and strength contrast between the VW asperities and surrounding VS matrix. Similar to *Luo and Ampuero* (2018), a dimensionless control parameter B was defined to indicate the barrier efficiency of the interstitial VS patch, which could be approximated as:

$$B \approx \frac{20\,(a_s - b_s)\,\sigma}{\beta \Delta\tau_w} \frac{D_s}{D_w} \tag{6.27}$$

Here, D_s is the extent of the VS region separating the two asperities, each of length D_w, β is a geometric factor chosen as $1/2$ in the 2D simulations of *Kaneko et al.* (2010), and $\Delta\tau_w$ is the stress drop averaged over the VW asperity (typically of order 0.1σ). These author showed that the probability of a two-segment rupture, i.e. a rupture successfully traversing the VS segment, decreased proportional to B, reaching zero near $B \approx 1.5$. For $B > 2$, no two-segment ruptures were observed over 9000 years of simulated time, suggesting a hard threshold value of B above which the VS segment acts as a permanent barrier to dynamic rupture. When a value of $(a-b) = 0.1$ is taken (a realistic value for the deformation regime expected for a phyllonite matrix), then a threshold value of $B = 2$ would correspond to a ratio of $D_s/D_w = 0.05$. This value translates roughly to $f' = 40$. Since a two-segment rupture in the geometry of *Kaneko et al.* (2010) can be interpreted as a T-instability in the framework of *Luo and Ampuero* (2018), we can conclude on the basis of microphysical and rheological considerations that multi-segment ruptures occurring as proposed by *Kaneko et al.* (2010) and *Luo*

and Ampuero (2018) exist only when asperities are separated by an insignificantly small patch of phyllonitic matrix.

Similar to the work of *Kaneko et al.* (2010), the behaviour of a two asperity system was investigated numerically by *Noda and Lapusta* (2013), additionally considering the effects of high-velocity dynamic weakening (thermal pressurisation). In the study of *Noda and Lapusta* (2013), one of the two patches (patch A) exhibited $(a - b) < 0$, with a low dynamic weakening efficiency. The other patch (patch B) exhibited $(a - b) > 0$ in the quasi-static (aseismic) regime, but with efficient dynamic weakening under coseismic slip velocities. A key result of this work is that the nominally stable patch B could still be triggered to undergo a dynamic instability for a sufficiently large perturbation induced by patch A. This behaviour is analogous to the P- and T-instabilities observed in this study, with the T-instability being facilitated by a rheological transition. However, the slip velocity at which dynamic weakening becomes efficient lies in the range of coseismic slip velocities (*Tullis*, 2007), so that this mechanism is not viable at typical nucleation rates (10^{-9}-10^{-6} m s^{-1}). On the other hand, the rheological transitions predicted by the CNS model are not mutually exclusive with those due to dynamic weakening. Since it is likely that one or more dynamic weakening mechanisms operate in natural faults, it is conceivable that a fault segment experiences multiple rheological transitions going from nucleation slip rates to coseismic slip rates.

6.6.4 Interpreting T-instabilities as giant earthquakes

It was argued in previous sections that the T-instabilities produced in the numerical simulations are analogous to great and giant earthquakes occurring in nature. Time-dependent loading of a creeping matrix, along with a transition from non-dilatant to dilatant deformation, offers a mechanism by which a strongly velocity-strengthening matrix may propagate or even nucleate dynamic rupture instabilities, facilitating multi-asperity rupture. In this way, an entire fault segment (or multiple fault segments) may rupture in a single event as seen in great and giant earthquakes (e.g. *Johnson et al.*, 1996; *Lay et al.*, 2005). In a classical RSF interpretation of multi-asperity rupture, T-instabilities may only occur for a highly restricted and unrealistic range of parameters,

owing to the large values of $(a - b)$ of the ductile matrix, as resulting from the present model formulations (see previous Section 6.6.3).

In the numerical simulations, the stress supported by the ductile matrix was observed to continuously increase through incremental loading by regular earthquakes or slow slip events, or through predominantly stable creep at rates lower than the imposed loading velocity. Overall, fault stress increased due to an increasing global slip deficit, which was relieved by T-instabilities. Closing of the slip budget as required for conservation of seismic moment has been proposed as the underlying reason for giant earthquakes in subduction zone settings (*Kagan and Jackson*, 2013; *Satake and Fujii*, 2014; *Stevens and Avouac*, 2016), although these studies do not specify the exact micro-mechanism. The stress-driven transition from ductile creep to granular flow provides a plausible basis for conserving seismic moment on long (centennial to millenary) timescales. Furthermore, this mechanism exhibits two additional characteristics that have been inferred from (palaeo)seismological studies: firstly, T-instabilities have been observed in the simulations to occur both on seismically active and quiet faults, in agreement with natural observations from e.g. the regions of Cascadia, Andaman, Japan Trench, and Sumatra (*Goldfinger et al.*, 2012; *Ide*, 2013; *Satake*, 2015). Secondly, the observed T-instabilities do not occur randomly in time, but instead recur quasi-periodically depending on the long-term rate of seismic moment accumulation and release.

This interpretation now implies two different mechanisms for regular earthquakes and for giant earthquakes: the occurrence of the former is controlled by the size, spatial distribution, and rheological properties of (clusters of) asperities, which can be associated with competent lenses incorporated in tectonic mélanges (*Fagereng*, 2011; *Kimura et al.*, 2012). The frequency-magnitude distribution of regular earthquakes may follow from the asperity model proposed by *Lay and Kanamori* (1981), although in our simulations a single seismological asperity corresponds to a cluster of competent lenses, rather than a single identifiable object. This class of earthquakes is familiar to previous numerical work employing rate-and-state friction. By contrast, model T-instabilities and natural giant earthquakes result from fault-averaged accumulation of seismic moment, and their dependence on the asperity distribution is only implicit through the seismic moment release by regular earthquakes, slow slip events, and creep. It is conceivable that the giant earthquakes do not obey a typical Gutenberg-Richter

relationship, although our data are inconclusive in this respect. Lastly, large differences in the recurrence time of T-instabilities are observed in the simulations sharing similar statistical properties in the spatial and size distributions of asperities. It is presently unknown how stochastic noise expresses itself in simulations of higher dimensional faults, e.g. whether or not statistically averaged behaviour emerges controlled by rheological properties rather than asperity clustering and spacing. This topic deserves attention in future studies, particularly in estimating long-term seismic hazard and risk.

6.6.5 Implications of the adopted model rheology

One major advantage of microphysically-based models is that the validity of their assumptions can be rigorously assessed based on laboratory and field observations. As mentioned in Section 6.3.1, the microstructure originally envisioned by the CNS model is that of a porous aggregate consisting mostly of framework minerals, such as granular calcite or quartz. While this microstructure may be representative for fault strands cross-cutting or enclosing competent lenses (see Section 6.2.2), it can be questioned whether or not the same grain-scale mechanics apply to the phyllonitic matrix, which consists for the larger part of phyllosilicates arranged in an anastomosing foliation, with relatively low volumetric proportions of clastic minerals. The phyllonite microstructure (and corresponding mechanics) is likely better represented by the model of *Den Hartog and Spiers* (2014) ('H&S' from here on), which considers the grain-scale deformation mechanisms of isolated framework minerals embedded in a foliated phyllosilicate matrix. Notwithstanding the differences in model geometry, the H&S model predicts trends in fault rheology that are qualitatively similar to those predicted by the CNS model, as both models are based on a competition between dilatant and non-dilatant processes (see H&S, their Fig. 5). From this comparison, we can reasonably argue that an implementation of the H&S model may produce T-instabilities in the same way as observed in the simulations presented here, and that our observations may be inherent to any model that incorporates a transition from ductile creep to dilatant deformation.

From the numerical simulations and analysis of a single-asperity system, it is clear that the occurrence of T-instabilities is greatly promoted when the steady-state ductile

creep strength is close to the critical stress required to activate granular flow. In the rheological formulations adopted in this study, τ_{ps} is linearly sensitive to Z_{ps}, so that there exists only a narrow range for material properties (corresponding to a narrow depth range) that allow for the generation of T-instabilities. Furthermore, the magnitude of the stress drop within regions of the fault dominated by asperities may play an essential role in facilitating the generation of T-instabilities. In this study, dynamic weakening of the fault at coseismic velocities (*Tullis*, 2007) is not considered, so that the total stress drop during a P-event is limited by $\tilde{\mu}\sigma$. In the case that the fault strength reduces to near-zero during a sufficiently large P-event (or more generally if large coseismic slip distances are achieved), it is more likely that nearby regions that were previously creeping under low stress are forced into an instability. Similar argumentation may hold for dynamic shear stress transfer (*Thomas et al.*, 2014), which is not included in the quasi-dynamic formulation adopted here.

6.6.6 Forecasting and precursors of giant earthquakes: implications and outlook

An important aspect of short-term forecasting of earthquakes is the presence (or absence) of slip transients, such as accelerated creep, foreshocks, and non-volcanic tremor, associated with the nucleation phase of a seismic event. Numerous cases exist in which a main shock was preceded by seismologically detectable features (in hindsight; *Dodge et al.*, 1995; *Jones and Molnar*, 1979; *Kanamori and Cipar*, 1974; *Kato et al.*, 2012), whereas other cases displayed no clear signs of an imminent event (*Bakun et al.*, 2005; *Irwan et al.*, 2004; *Mellors et al.*, 2002). Hence, a basic understanding of the nucleation process may assist in interpreting this natural variability, and in assessing the hazard associated with e.g. an emerging tremor swarm.

Previously, two models for earthquake nucleation have been put forward (*Dodge et al.*, 1996; *Ellsworth and Beroza*, 1995): in the *preslip* model, a large seismic event nucleates from a region that grows largely independently of other, small slip events (e.g. foreshocks), which are carried by the expanding nucleation zone. Alternatively, the *cascade* model postulates that large events start out as an initially small event, which expands dynamically ('cascade-up') by linking up with other nuclei until the

rupture attains a size that satisfies the stability criterion exhibited by the larger event (the 'break-away' phase). The preslip model permits a large, seismologically detectable preparation stage with accelerated creep preceding a large seismic event, which could aid in the early detection of an earthquake and estimation of its final size (*Ellsworth and Beroza*, 1995). Conversely, in the cascade model it cannot a-priori be established whether a small earthquake remains isolated, or will ultimately cascade-up to a much larger event.

The lack of an aseismic nucleation phase prior to large earthquakes, as observed in nature (*Roeloffs*, 2006), seems to favour the cascade model. However, detailed numerical simulations performed by *Noda et al.* (2013b) reveal that the mode of nucleation depends primarily on the size of smaller asperities, compared to the nucleation length scale of the larger seismogenic asperity: in the case that 'parasitic' seismogenic asperities are small compared to the nucleation length of the main asperity, nucleation of a large frictional instability occurs predominantly through 'own nucleation' (preslip) within a large region surrounding the main asperity. In the case that the smaller asperities are large enough in size, the rupture of one such asperity may trigger failure of the main asperity, provided that it is ready for failure. In this way, the recurrence interval of large seismic events is not significantly altered, but the slow, preseismic nucleation stage is skipped. It should be remarked that in these simulations, the small velocity-weakening asperities are embedded within the larger asperity, so that the rupture does not have to traverse a velocity-strengthening region in order for an instability to cascade-up.

In the laboratory experiments of *McLaskey and Lockner* (2014), it was observed that large (stick-slip) instabilities share the same initial waveform as recordings of acoustic emissions, suggesting that stick-slips initiate from an acoustic emission that rapidly cascades-up to a stick-slip event. This waveform similarity has also been recognised in natural earthquakes (*Kilb and Gomberg*, 1999), alluding similar underlying mechanisms as in the laboratory experiments. However, *McLaskey and Lockner* (2014) noted that the production of acoustic emissions is driven by preslip preceding failure of the laboratory fault, so that the preslip and cascade-up models are intimately related (i.e. preslip facilitates acoustic emissions, but acoustic emissions are immediately responsible for triggering the large instability). These observations are on par with the simulation results of *Noda et al.* (2013b), where cascade-up was only observed when the larger

asperity was already close to failure.

The simulations reported in this study display T-instability nucleation modes (cascade-up and own nucleation) that have been similarly classified by *Noda et al.* (2013b). Unfortunately, in the heterogeneous fault simulations a measure for effective nucleation length for T-instabilities is not readily available, preventing a quantitative comparison with the parametric exploration of *Noda et al.* (2013b). It appears, however, that the nucleation length of T-instabilities decreases with increasing magnitude of the fractal dimension D, concurrent with a decreasing tendency for cascade-up mode of nucleation. These trends are consistent with the findings of *Noda et al.* (2013b), who observed no cascade-up mode of nucleation when the nucleation length of the main asperity was much smaller than the radius of the circular asperity (or alternatively when the size of the main asperity was much larger than that of the smaller asperities). On the other hand, in the simulations with $D = 2$, seismogenic P-instabilities are completely absent, so that cascade-up is a highly unlikely nucleation mode to start with. Nevertheless, nucleation of a T-instability, be it through cascade-up or own nucleation, occurs only when the fault approaches its critical stress level, i.e. it is 'ready' for failure, in agreement with the findings of *Noda et al.* (2013b) and *McLaskey and Lockner* (2014). The mode of nucleation then follows from the geometric distribution of asperities, rather than being a fundamental and universal property of the fault, which is perhaps not surprising given that seismological studies to date remain inconclusive regarding the unequivocal distinction between various nucleation models (*Kilb and Gomberg*, 1999; *Uchide and Ide*, 2010; *Umino et al.*, 2002).

For earthquake hazard assessments on timescales relevant for societal planning, a measure of the 'readiness' of the fault would be tremendously valuable. In seismological studies it has been observed that tidal and seasonal forcing systematically affects tremor and slow slip patterns (*Lambert et al.*, 2009; *Pollitz et al.*, 2013; *Rubinstein et al.*, 2008), from which it has been inferred that deep faults sections operate at extremely low friction (*Houston*, 2015), or near-lithostatic fluid pressure (*Thomas et al.*, 2009). Analytical and numerical studies that have investigated the response of a fault subjected to periodic loading, reveal that tremor activity rates are most sensitive to tidal modulation when $(a - b)$ is close to zero (*Ader et al.*, 2012). An important characteristic of the nucleation process of a T-instability (and frictional

instabilities in general), is the transition from velocity-strengthening ductile creep to velocity-weakening granular flow. Near the point of criticality, the velocity-dependence of shear strength approaches neutrality, i.e. $(a - b) \approx 0$. Provided that classical analyses of tidal modulation hold for CNS-governed fault rheologies, one can speculate on continuously probing the readiness of a fault based on its response to tide-induced tremor patterns. This warrants further investigation of the effect of tidal modulation on the behaviour of heterogeneous faults. Another potential avenue for future investigation is the correlation between earthquake magnitudes and various fault zone parameters (such as plate velocity, temperature distribution, and fluid pressure), as to support statistical correlations with (micro)physical arguments (e.g. *Heuret et al.*, 2011).

6.7 Conclusions

This study considers the seismic cycle behaviour of a spatially heterogeneous fault, of which the rheology is governed by a microphysical model formulation (*Chen and Spiers*, 2016; *Niemeijer and Spiers*, 2007). By using a microphysically-based seismic cycle simulator (Chapter 5; *Van den Ende et al.*, 2018a), the numerical modelling approach can be motivated and constrained directly by laboratory and field observations. From the analyses of heterogeneous faults, we conclude the following:

1. In single-asperity simulations, we observe that seismogenic asperities generate P-instabilities that are confined by fault segments exhibiting predominantly velocity-weakening behaviour (nominal to the tectonic loading velocity). Incremental slip in the asperities in the form of P-events, as well as far-field tectonic loading, may raise the stress supported by velocity-strengthening matrix fault segments. At a critical level of stress, an instability is triggered in the matrix, after which the entire fault ruptures in a single event (T-instability).

2. Similarly, heterogeneous faults exhibiting a random distribution in asperity size show a gradual increase in average stress, until the entire fault ruptures in a T-instability. T-instabilities are observed both in simulations that exhibit regular seismic events, and in simulations that are seismically quiescent, highlighting a different underlying mechanism from regular earthquakes.

3. The occurrence of T-instabilities is facilitated by a transition from non-dilatant, velocity-strengthening creep to dilatant, velocity-weakening granular flow. This transition is absent in classical rate-and-state friction formulations, but plays a central role in the stability of a heterogeneous fault that is governed by CNS microphysics (pressure solution and granular flow). Furthermore, it shows that fault materials characterised in laboratory tests as velocity-strengthening may still nucleate or facilitate unstable slip.

4. We argue that the T-instabilities as seen in the simulations are analogous to great ($M_w > 8$) and giant ($M_w > 9$) megathrust earthquakes seen in nature. The consequences of the proposed mechanisms behind T-instabilities and giant earthquakes are in agreement with a number of (palaeo)seismological observations, such as the occurrence of giant earthquakes in seismically quiet regions, their quasi-periodic recurrence, and possible violation of Gutenberg-Richter frequency-magnitude distributions based on regular earthquakes.

5. Ultimately, the occurrence of T-instabilities (and giant earthquakes) is driven by accumulating slip deficit over the entire fault region, resulting in a global increase in stress and a transition from stable to unstable frictional sliding. This holds important implications for long-term seismic hazard assessments, as giant earthquakes can no longer be considered to result from purely stochastic origins, but instead are governed by seismic moment accumulation and release.

Appendices

6.A Rendering the heterogeneous fault structure

Following *Fagereng* (2011), we assume that competent lenses (the asperities) obey a power-law distribution in size, i.e.:

$$F_X(x) = 1 - cx^{-D} \tag{6.A.1}$$

where F_X is the cumulative size distribution of asperity size X, D is the fractal dimension (or power-law exponent), and c is a proportionality constant. Strictly speaking, this cumulative distribution function does not exist for $D > 0$ on an infinite domain owing to a singularity at $x = 0$, but it can be redefined based on a rescaled probability density function integrated over a finite range of $0 < x_{min} \leq X \leq x_{max}$ and $D \neq 0$, which yields:

$$f'_X(x) = \frac{-Dx^{-D-1}}{x_{max}^{-D} - x_{min}^{-D}} \tag{6.A.2a}$$

$$F'_X(x) = \int_{x_{min}}^{x} f'_X(x)\mathrm{d}x = \frac{x^{-D} - x_{min}^{-D}}{x_{max}^{-D} - x_{min}^{-D}} \tag{6.A.2b}$$

In accordance with the above relations, the realisation of the asperity size distribution x can be generated from a uniform variate $\widehat{X}$ as:

$$x = \left(x_{min}^{-D} + \left[x_{max}^{-D} - x_{min}^{-D} \right] \widehat{X} \right)^{-1/D} \tag{6.A.3}$$

The procedure to render a fault with the desired statistical properties is then as follows:

1. First, the discrete asperity size distribution x_i is realised in accordance with Eqn. (6.A.3), with x_{min} corresponding to twice the fault element size, and $x_{max} = L$. Between simulations, D is systematically varied between 1 and 2, following the phacoid fractal dimensions reported by *Fagereng* (2011).

2. Next, a second size distribution (y_i) is realised that represents the spacing between neighbouring asperities, assuming that the 'gaps' between asperities obey the same power-law distribution.

3. In order to obtain the desired asperity occupation ratio f, x_i is multiplied by $f/(1-f)$ (i.e. the ratio of total asperity length over total matrix length) before being combined in an arrangement with y_i.

4. The spatial distribution of Z_{ps} for the asperities and the matrix is then sampled from a piece-wise alternating arrangement of x_i and y_i, respectively, where i ranges from 1 to N, so that $\sum_{i=1}^{N} (x_i + y_i) \geq L$. In other words, the spatial layout of the fault follows an arrangement $x_1, y_1, x_2, y_2, ..., x_N, y_N$.

Owing to the fault's finite size, stochastic noise causes some variability in the statistical properties of the fault geometry, e.g. by randomly introducing one excessively large asperity, which skews the asperity size distribution. To prevent this, we compare each realised asperity size distribution with the expected distribution (Eqn. (6.A.2b)), and the realised value of f with the one that is requested. For large deviations of the size distribution and f (> 5 %) from the expected values, the rendered fault structure is rejected and a new one generated.

6.B Generating the event catalogue

To investigate the effect of various structural and rheological parameters on the frequency-magnitude relations displayed in the heterogeneous fault simulations, we generate an event catalogue for each simulation. As some simulations accommodate fault slip through slow slip events, we incorporate both slow and fast events for which the rising edge slip velocity is larger than 10^{-6} m s^{-1}, and the falling edge velocity lower than 10^{-8} m s^{-1}. This velocity gap between the rising and falling edges prevents small drops in slip velocity to be counted as a separate event. For each event, the participating fault elements are identified, from which the average fault slip $\Delta\bar{x}$ and crack length l are calculated. The seismic moment M_0 (in N m) and moment magnitude, assuming a circular crack of radius $l/2$, are then given by (*Kanamori*, 1977):

$$M_0 = \pi G \Delta\bar{x} \left(\frac{l}{2}\right)^2 \tag{6.B.1a}$$

$$M_w = \frac{2}{3}\log_{10} M_0 - 6.06 \tag{6.B.1b}$$

The corresponding frequency-magnitude distribution is simply obtained from the notion that, in a sorted vector $\mathbf{M}$ (i.e. $M_i \geq M_{i-1}\ \forall\, i > 1, i \in \mathbb{N}$) comprising all events, the number of events in $\mathbf{M} > M_i$ decreases by one for each increment of i, so that the frequency-magnitude distribution of the sorted vector $\mathbf{M}$ becomes:

$$P(\mathbf{M} > M_i) = 1 - \frac{i}{|\mathbf{M}|} \tag{6.B.2}$$

where $|\mathbf{M}|$ denotes the number of events contained by $\mathbf{M}$. This procedure is more convenient than traditional binning techniques for the small catalogues produced in one-dimensional fault simulations, as it does not rely on binning procedures.

Chapter 7

Conclusions and outlook

This thesis considered the coupling of laboratory, field, and numerical methods in an integrated approach for modelling fault rock friction, with the ambition to gain new insights into earthquake mechanics. More specifically, the interplay between fluid-rock interactions and granular mechanics was investigated, both at the scale of a laboratory sample, and at the scale of the Earth's crust. With regard to the role of fluid-rock interactions, and the upscaling of laboratory results to nature, I conclude the following:

7.1 Main findings of this thesis and their implications

7.1.1 Long-term fault gouge densification

Previous laboratory work has shown that fault gouge compaction is essential to time-dependent restrengthening (*Chen and Spiers*, 2016; *Karner and Marone*, 2001; *Richardson and Marone*, 1999). Hence, in order to understand the restrengthening of faults during interseismic times, the mechanisms and rates of compaction need considering. In hydrostatic compaction tests on granular halite (*Schutjens*, 1991b) and quartz (*Niemeijer et al.*, 2002), it was found that analytical models for intergranular pressure solution severely overestimate experimental compaction strain rates, indicating that one or more physical aspects of fluid-assisted compaction are overlooked in theoretical treatments of pressure solution. In **Chapter 2**, I have shown that the discrepancy between theoretically predicted and experimentally measured compaction rates likely does not find its origin in frictional interactions between grains, or in the polydispersed (multi-valued) grain size distribution of test samples, both of which are typically neglected in theoretical analyses of pressure solution. Discrete Element Method (DEM) simulations have demonstrated that these two candidate mechanisms for the retardation of pressure solution cannot explain the trends in the experimental data and observed magnitudes of retardation.

Conversely, analytical and numerical models developed in **Chapter 3** that incorporate the structural evolution of grain boundaries by growth of contact asperities ('islands') obtained favourable agreements with the laboratory data of *Schutjens* (1991b),

indicating that surface-energy driven asperity growth can strongly reduce pressure solution creep rates. Fault gouges in which grain boundary evolution by asperity growth is operative may therefore experience compaction rates that are orders of magnitude slower than expected based on the kinetics of pressure solution alone. This in turn affects the rate of restrengthening of faults, particularly at low porosities.

7.1.2 The importance of time-dependent cohesion

In a suite of *slide-hold-slide* experiments, I inferred in **Chapter 4** that a halite gouge aggregate exhibits time-dependent strengthening not only through purely frictional restrengthening by compaction, but also by increasing sample-scale cohesion. In these experiments, a Mohr-Coulomb relation was assumed: $\tau = \mu\sigma_n + C_s$, in which τ is the overall shear strength of the sample, μ is the internal coefficient of friction, σ_n the imposed normal stress, and C_s the sample cohesion. For relatively short hold durations (< 3000 s), the overall increase in τ was mainly attributed to a time-dependent increase in μ. For longer hold durations the increase in μ diminished, but instead the sample cohesion C_s started to contribute significantly to τ, hence resulting in a continuous increase in τ with hold time. While the notion that time-dependent fault restrengthening receives contribution from cohesion is not new (*Muhuri et al.*, 2003; *Tenthorey and Cox*, 2006), it has nevertheless not yet been demonstrated experimentally that both μ and C_s each exhibit their own time-dependence.

In an attempt to explain the observed laboratory results, DEM simulations were run that replicated the laboratory slide-hold-slide procedure. As a mechanism for generating macroscopic cohesion, the nett growth of grain contact asperities with an assumed cohesive strength was considered. To this end, the grain boundary evolution model as developed in **Chapter 3** was adopted to describe the time-dependent increase in asperity contact area. In these simulations, it was found that the model fault exhibited time-dependent strengthening in a similar fashion as was inferred from the laboratory experiments, i.e. strengthening was caused mainly by compaction for short hold times, and by increasing sample cohesion for long hold durations. Furthermore, simulations with grain-scale cohesion displayed substantially higher slip velocities during the resliding phase than did the simulations without cohesion. In the laboratory

experiments, it was observed that for hold durations > 1000 s, the sample exhibited unstable and accelerated slip during resliding, producing a clearly audible acoustic emission in the process. The correspondence between accelerated slip in both the laboratory experiments and DEM simulations exhibiting cohesion further alluded to the presence of cohesion in the laboratory tests.

These results indicate that restrengthening of natural faults may be enhanced by a time-dependent increase in cohesion through surface-energy driven asperity growth. Moreover, since fault gouge cohesion introduces a slip weakening mechanism in addition to gouge dilatation, the stability of fault slip may be strongly affected by the cohesion gained through nett asperity growth, augmenting the seismogenic potential of faults where fluid-rock interactions occur at appreciable rates. The importance of lithification on fault strength and stability has been previously argued, e.g. by *Marone* (1998), and this argument now receives quantitative support from a microphysical model perspective.

7.1.3 Extrapolation of laboratory results through microphysical models

A major question relevant for laboratory work is that of extrapolation of the results to nature. Inevitably, natural faults span a range of spatial and temporal scales vastly inaccessible by laboratory experiments, and so procedures need to be developed that facilitate upscaling. Over the past decades, the empirical *rate-and-state friction* (RSF) framework has been employed to capture laboratory observations in analytical and numerical models. However, a major drawback of an empirical formulation is that its parameters do not have a transparent physical meaning, and so assessing the accuracy and validity of the model outcomes remains problematic. Alternatively, model formulations based on microphysical principles provide a clear interpretation of its parameters, and so may provide the means for extrapolation of laboratory results in a way that is more firmly seated on laboratory and field observations.

To test the potential for microphysical models to facilitate extrapolation, I have implemented the analytical model formulations proposed by *Niemeijer and Spiers* (2007) and *Chen and Spiers* (2016) (i.e. the *Chen-Niemeijer-Spiers* or 'CNS' model)

into a numerical seismic cycle simulation QDYN (*Luo et al.*, 2017a), as presented in **Chapter 5**. As a test case for this new implementation, a crustal strike-slip fault was simulated following the classical work of *Tse and Rice* (1986). To facilitate the comparison between classical rate-and-state friction and the CNS model, RSF constitutive parameters were measured in CNS simulations mimicking small-amplitude velocity-step tests as commonly employed in a laboratory setting, followed by inversion of the RSF formulation to the transient friction data. While RSF could accurately describe the CNS model behaviour in spring-block simulations of velocity-step tests, it failed to reproduce the crustal fault seismic cycle results of the CNS model implementation.

A wealth of laboratory data shows a velocity-dependence of RSF parameters (*Carpenter et al.*, 2016a; *Collettini et al.*, 2011; *Den Hartog et al.*, 2012; *Reinen et al.*, 1992; *Tesei et al.*, 2014), and marked transitions from steady-state velocity-strengthening to weakening and back to velocity-strengthening (*Niemeijer and Spiers*, 2006; *Reinen et al.*, 1992; *Shimamoto*, 1986). This feature is captured by the CNS model formulation, so that by comparing the CNS model with RSF in the context of upscaling, insights are gained into the effect of velocity-dependent RSF parameters. This comparison shows that fault slip behaviour is vastly different between the CNS and RSF simulations, highlighting the importance of incorporating a more physically underpinned velocity-dependence of friction in upscaling laboratory results. This is where microphysical model descriptions, such as the CNS model, may aid to clarify and generalise complex fault behaviour.

7.1.4 Micro-mechanics of earthquakes

Closely related to the velocity-dependence of friction is the notion of steady-state deformation regimes. The CNS model predicts three steady-state deformation regimes, each characterised by its own microstructural state and macroscopic frictional response. The mode of deformation is dependent on slip velocity, so that over the course of a seismic cycle, a given fault section may undergo deformation in all three deformation regimes. In particular, the transition from non-dilatant ductile creep to dilatant granular flow provides a rheological basis for earthquakes in nature (*Verberne et al.*,

2017, **Chapter 6**). The importance of this transition is exemplified by simulations where compositional heterogeneity of the fault gouge is considered.

Field investigations of exhumed fault zones have revealed that large faults are compositionally heterogeneous, often characterised by a block-in-matrix structure or tectonic mélange (*Fagereng and Sibson*, 2010; *Kimura et al.*, 2012; *Niemeijer and Vissers*, 2014). The mechanical contrast provided by the different compositional units may lead to non-smooth and non-uniform spatial distributions of stress and fault slip rates (*Fagereng and Sibson*, 2010). What field geological studies further indicate, is that the fault phyllonitic matrix material displays abundant evidence for pervasive pressure solution creep, whereas gouges associated with competent lenses ('asperities') show more cataclastic features attributed to granular flow. In the framework of the CNS model, such contrasting microstructural observations can be interpreted to stem from a contrast in pressure solution kinetics, or variations in the locally imposed strain rate. As such, the effect of compositional heterogeneity can be explored by varying the pressure solution kinetics over the model fault space, in accordance with outcrop-scale observations of fault zone structures (*Fagereng*, 2011; *Faulkner et al.*, 2003; *Kimura et al.*, 2012). This spatial variation of rheological properties has been found to give rise to the following model behaviour:

- The matrix predominantly exhibits stable, ductile creep, whereas small instabilities (earthquakes) are generated by (clusters of) asperities. These events only rupture a (small) portion of the model fault.
- Over time, stress on matrix portions of the fault increases due to tectonic loading, or by static stress distribution due to non-uniform slip on the fault.
- At a critical level of stress, marking the transition from ductile creep to granular flow, the matrix becomes unstable as it transitions into a dilatant (velocity-weakening) mode of deformation. When this happens, the rupture is no longer confined to a region controlled by a geometrical distribution of asperities. Instead, the fault ruptures over its entire length in a single event.

The occurrence of fault-spanning seismic events in the simulations can be considered the model equivalent of anomalously large and multi-segment earthquakes in nature, such as

great ($M_w > 8$) and giant ($M_w > 9$) megathrust earthquakes. These earthquakes have been argued to arise from the requirement of balancing the long-term slip budget of a fault, a hypothesis that is supported by the numerical models presented in **Chapter 6**. The rheological transition from the ductile creep regime to the dilatant granular flow regime now offers a microphysical mechanism that facilitates the nucleation and propagation of anomalously large earthquakes. Moreover, fault-spanning ruptures have also been generated by model faults that are otherwise seismically quiet, possibly finding their natural counterpart in 'silent' subduction regions, such as Cascadia, Alaska, and Andaman (*Ide*, 2013).

7.2 General implications for numerical modelling of fault friction

Previous laboratory and field studies have convincingly demonstrated that faults cannot be represented by a simple, zero-width crack between rock interfaces, and that gouge plays a pivotal role in controlling the dynamics of fault slip (*Carpenter et al.*, 2014; *Collettini et al.*, 2011; *Fagereng and Sibson*, 2010; *Faulkner et al.*, 2003; *Holdsworth et al.*, 2011; *Niemeijer and Spiers*, 2006). It is therefore important to consider the dynamics of gouge deformation, notably the porosity reduction due to fluid-rock interactions. Classical microphysical explanations for friction are mostly sought in the directions of tribology and metallurgy (*Boneh and Reches*, 2017; *Brechet and Estrin*, 1994; *King and Tabor*, 1954), which overlook this important aspect of fault rheology. Moreover, numerical models for fault slip are most commonly based on empirical constitutive relations, inhibiting knowledge exchange between laboratory and field studies on the one hand, and modelling studies on the other.

In this thesis, I have shown that numerical models which incorporate fluid-rock interactions produce realistic rock deformation behaviour, both at the scale of a laboratory sample (**Chapters 2**, **3**, and **4**) and at the scale of the Earth's crust (**Chapters 5** and **6**). This demonstrates the feasibility of using relatively complex microphysical descriptions of fault rheology in numerical simulations of natural systems. In this way, numerous questions related to upscaling can be addressed in future work,

and new opportunities are provided for numerically investigating fault mechanics based on laboratory and geological observations.

Finally, it should be noted that a number of similarities have been identified between rate-and-state friction and the microphysical models employed in this study, despite their differences in origin. This suggests that many of the analytical and numerical tools that have been developed over the past four decades may still be used to understand the behaviour of microphysical models (see e.g. *Chen and Niemeijer*, 2017).

7.3 Unresolved issues and future research perspectives

7.3.1 The kinetics of fluid-rock interactions

In all of the topics covered by this thesis, fluid-rock interactions (pressure solution in particular), play a central role in the micro-scale mechanics of friction. Therefore, accurate determination of the kinetics of dissolution, diffusion, and precipitation of ionic species is required to constrain the outcomes of the various models. These kinetics can be obtained from laboratory experiments (e.g. from compaction or bulk dissolution tests), but great uncertainties remain in estimating the *in situ* fault zone conditions, such as temperature and pore fluid chemistry, and their effects on the fluid-rock interactions.

Even under well-controlled laboratory conditions, analytical models for pressure solution have been reported to overestimate the strain rates measured in compaction tests on quartz sand (*Niemeijer et al.*, 2002; *Van Noort et al.*, 2008a). In these analytical formulations, the kinetics of quartz dissolution were adopted from independent laboratory assessments of quartz dissolution rates in distilled water (*Rimstidt and Barnes*, 1980). However, the kinetics of quartz dissolution have been found to be strongly affected by fluid chemistry, which could be significantly enhanced (*Rimstidt*, 2015) or diminished (*Niemeijer and Spiers*, 2002) based on the presence of metallic cations. This may offer an explanation for the observed effects of pore fluid chemistry

(ionic strength and pH) on the frictional behaviour of gouges (*Hunfeld et al.*, 2017). Furthermore, as the composition of the pore fluid may vary over a seismic cycle (*Wintsch et al.*, 1995), temporal variations in compaction behaviour and frictional strength may be an important feature of natural faults that is presently underappreciated in laboratory experiments and theoretical treatments.

The above example underlines that there still exists much uncertainty in the detailed mechanisms and kinetics of fluid-rock interactions. This hampers fault friction modelling efforts of which the underlying rheology is controlled by fluid-rock interactions, like those presented in this thesis.

7.3.2 The relevance of grain boundary evolution in nature

In **Chapters 3** and **4**, it was discussed how grain boundary evolution by asperity growth could impact pressure solution and fault strengthening rates. The laboratory and numerical experiments reported in these chapters were all conducted on mono-mineralic materials, whereas previous work has demonstrated that grain boundary evolution is less efficient for bi-mineral interfaces, particularly when the two crystals exhibit low crystallographic compatibility (*Beeler and Hickman*, 2015; *Zubtsov et al.*, 2004). As natural faults are often heterogeneous in their gouge mineralogy, the efficiency and relevance of grain boundary evolution in nature can be questioned.

In considering the relevant physical processes operating at the scale of a single contact asperity (island), great uncertainties exist regarding the local distribution of stresses and driving forces that control the dynamics of the island-channel structure. Classical models for pressure solution (e.g. *Lehner*, 1990; *Spiers and Schutjens*, 1990) consider a scale over which local variations in grain boundary structure average out. However, for a fully rigorous assessment of the process of grain boundary evolution, one needs to consider an even smaller scale for which average quantities can no longer be maintained. A probabilistic approach may be required to address the dynamics of the island-channel structure in a fully quantitative way.

In **Chapter 4**, I proposed that surface-energy driven growth of asperity contact area could act as a mechanism for time-dependent cohesion, of which the efficiency

may affect the strength and stability of natural faults. This relation between the nm-scale structure of a stressed grain contact and km-scale fault mechanics warrants future laboratory tests on poly-mineralic gouges to investigate the time-dependence of aggregate cohesion, as well as more detailed analyses of the process of grain boundary evolution at the scale of a single island.

7.3.3 Granular flow parameters H, ϕ_c

As shown in **Chapter 5**, the choice of granular flow parameter strongly controls the dynamics and frictional stability of faults in the CNS model. For a relatively narrow range of the geometric parameter H and critical state porosity ϕ_c, predictions of fault slip could traverse a spectrum from stable sliding and slow slip, to fast earthquakes. In terms of classical rate-and-state friction, these granular flow parameters dictate the magnitude of $(a - b)$ (the parameter b in particular). At present, it is difficult to predict or measure the exact values of H and ϕ_c, and so they remain unconstrained ('free') parameters in numerical simulations based on the CNS model.

Two possible venues that could be explored to constrain these granular flow parameters, are microstructural analyses of sheared gouges, and DEM simulations: by systematically estimating the dilatancy angle $\tan\psi$ and porosity ϕ in micrographs, it may be possible to obtain relations between these two quantities described by H and ϕ_c. Similarly, the bulk averaged values of $\tan\psi$ and ϕ can be obtained from DEM simulations. In DEM, particle size distributions can be controlled directly, and so the relation between granular flow parameters and the structure of the gouge can be investigated.

Since the fault dynamics predicted by the CNS model is strongly dependent on the underlying model for granular flow, rigorous testing of the hypotheses posed by the CNS model can only be done when its underlying parameters are sufficiently well constrained. Doing so also improves the predictive capabilities of the model, and facilitates extrapolation to nature.

7.3.4 Localisation and nanograin formation

A major advantage of DEM over continuum methods is that the mechanics of granular flow do not need to be described explicitly in the form of a constitutive law. This allows for many more degrees of freedom in a randomly organised granular packing. Due to this, spontaneous localisation of strain may develop during DEM simulations (*Morgan and Boettcher*, 1999), in a similar way as is observed in laboratory experiments (e.g. *Chambon et al.*, 2006). In this thesis, little attention has been given to localisation of strain, although it is expected that it controls the overall frictional response of the aggregate (*Rathbun and Marone*, 2010). Using DEM, the dynamics of localisation and delocalisation can be systematically studied, and may provide handles for investigating localisation behaviour in laboratory experiments and in nature.

Localisation of strain is often identified by intense grain comminution, and an intimate relation between these two is expected. It has been observed that within localised zones of both natural and experimental gouges, grains may be reduced below a size of 1 µm, a process commonly referred to as nanograin formation. These nanograins have been associated with fault mirror surfaces (*Kirkpatrick et al.*, 2013; *Siman-Tov et al.*, 2013) and a strong crystallographic preferred orientation within the localised zone (*Verberne et al.*, 2013), suggesting some crystal plastic deformation mechanism to accommodate the imposed strain. Based on microstructural observations, it is expected that the physical processes envisioned by microphysical models (grain sliding and compaction by pressure solution) may contribute differently to strain accommodation in nanogouges than in 'microgouges' (gouges exhibiting a nominal grain size of micrometres), and so other physical processes need to be considered. Since the presence of nanogouges has been documented in natural faults, as well as in experimental faults, the rheology of nanogouges likely plays an important role in the overall slip behaviour of faults.

7.3.5 Dynamic weakening

Another aspect of fault rock friction that has been systematically ignored in this thesis is the dramatic reduction in shear strength at high (coseismic) slip velocities – the so-

called *dynamic weakening* (*Tullis*, 2007). The operation of dynamic weakening has been studied intensively in high-velocity rotary shear experiments, and several underlying mechanisms have been proposed, including flash weakening (*Goldsby and Tullis*, 2011; *Rice*, 2006), silica gel formation (*Di Toro et al.*, 2004; *Goldsby and Tullis*, 2002), phase changes (*Chen et al.*, 2017a), and thermo-chemical pressurisation (*Lachenbruch*, 1980; *Mase and Smith*, 1985). Flash weakening, in conjunction with rate-and-state friction, has been widely considered in both analytical and numerical investigations into fault rock friction (*Noda*, 2008; *Noda et al.*, 2011; *Rempel and Weaver*, 2008; *Thomas et al.*, 2014), although the exact micro- or nano-scale mechanism by which the weakening occurs has not yet been identified, so that similar challenges are faced as for the classical rate-and-state friction framework. This obscurity also affects the way in which microphysical models, such as the CNS model, can be extended with existing models for dynamic weakening, as the interaction between the two models requires knowledge of the operation of both models at the micro-scale. When all of the physical (and chemical) processes relevant for fault friction are described at the scale of a grain contact, all of the interactions between each process naturally emerges to produce a complete description of fault rock friction at a macroscopic scale, spanning the entire range from low to high velocity.

References

Ader, T. J., Ampuero, J.-P., Avouac, J.-P., 2012. The role of velocity-neutral creep on the modulation of tectonic tremor activity by periodic loading. Geophysical Research Letters 39 (16).

Aharonov, E., Scholz, C. H., 2017. A physics-based rock-friction constitutive law: steady-state friction. Journal of Geophysical Research: Solid Earth.

Alkattan, M., Oelkers, E. H., Dandurand, J.-L., Schott, J., 1997. Experimental studies of halite dissolution kinetics, 1 The effect of saturation state and the presence of trace metals. Chemical Geology 137 (3-4), 201–219.

Ampuero, J.-P., Ben-Zion, Y., 2008. Cracks, pulses and macroscopic asymmetry of dynamic rupture on a bimaterial interface with velocity-weakening friction. Geophysical Journal International 173 (2), 674–692.

Ampuero, J.-P., Ripperger, J., Mai, P. M., 2006. Properties of dynamic earthquake ruptures with heterogeneous stress drop. In: Earthquakes: Radiated Energy and the Physics of Faulting. Vol. 170. American Geophysical Union, pp. 255–261.

Ampuero, J.-P., Rubin, A. M., 2008. Earthquake nucleation on rate and state faults – Aging and slip laws. Journal of Geophysical Research 113 (B1), B01302.

Ampuero, J.-P., Vilotte, J.-P., Sánchez-Sesma, F. J., 2002. Nucleation of rupture under slip dependent friction law: Simple models of fault zone. Journal of Geophysical Research: Solid Earth 107 (B12), ESE 2–1–ESE 2–19.

Andrews, D. J., 1976a. Rupture propagation with finite stress in antiplane strain. Journal of Geophysical Research 81 (20), 3575–3582.

Andrews, D. J., 1976b. Rupture velocity of plane strain shear cracks. Journal of Geophysical Research 81 (32), 5679–5687.

Angevine, C. L., Turcotte, D. L., Furnish, M. D., 1982. Pressure solution lithification as a mechanism for the stick-slip behavior of faults. Tectonics 1 (2), 151–160.

Anthony, J. L., Marone, C., 2005. Influence of particle characteristics on granular friction. Journal of Geophysical Research B: Solid Earth 110 (8), 1–14.

Ariyoshi, K., Matsuzawa, T., Ampuero, J.-P., Nakata, R., Hori, T., Kaneda, Y., Hino, R., Hasegawa, A., 2012. Migration process of very low-frequency events based on a chain-reaction model and its application to the detection of preseismic slip for megathrust earthquakes. Earth, Planets and Space 64 (8), 693–702.

Atkinson, B. K., 1984. Subcritical crack growth in geological materials. Journal of Geophysical Research 89 (B6), 4077.

Avnir, D., Farin, D., Pfeifer, P., 1984. Molecular fractal surfaces. Nature 308 (5956), 261–263.

Bakun, W. H., Aagaard, B., Dost, B., Ellsworth, W. L., Hardebeck, J. L., Harris, R. A., Ji, C., Johnston, M. J. S., Langbein, J., Lienkaemper, J. J., Michael, A. J., Murray, J. R., Nadeau, R. M., Reasenberg, P. A., Reichle, M. S., Roeloffs, E. A., Shakal, A., Simpson, R. W., Waldhauser, F., 2005. Implications for prediction and hazard assessment from the 2004 Parkfield earthquake. Nature 437 (7061), 969–974.

Bakun, W. H., Lindh, A. G., 1985. The Parkfield, California, Earthquake Prediction Experiment. Science 229 (4714), 619–624.

Bakun, W. H., McEvilly, T. V., 1984. Recurrence models and Parkfield, California, earthquakes. Journal of Geophysical Research: Solid Earth 89 (B5), 3051–3058.

Barbot, S., Lapusta, N., Avouac, J.-P., 2012. Under the Hood of the Earthquake Machine: Toward Predictive Modeling of the Seismic Cycle. Science 336 (6082), 707–710.

Baumberger, T., Berthoud, P., Caroli, C., 1999. Physical analysis of the state-and rate-dependent friction law. II. Dynamic friction. Physical review B 60 (6), 3928–3939.

Beeler, N. M., Hickman, S. H., 2015. Direct measurement of asperity contact growth in quartz at hydrothermal conditions. Journal of Geophysical Research: Solid Earth 120 (5), 3599–3616.

Beeler, N. M., Hickman, S. H., Wong, T.-F., 2001. Earthquake stress drop and laboratory-inferred interseismic strength recovery. Journal of Geophysical Research: Solid Earth 106 (B12), 30701–30713.

Beeler, N. M., Tullis, T. E., 1997. The roles of time and displacement in velocity-dependent volumetric strain of fault zones. Journal of Geophysical Research: Solid Earth 102 (B10), 22595–22609.

Beeler, N. M., Tullis, T. E., Goldsby, D. L., 2008. Constitutive relationships and physical basis of fault strength due to flash heating. Journal of Geophysical Research 113 (B1), B01401.

Beeler, N. M., Tullis, T. E., Weeks, J. D., 1994. The roles of time and displacement in the evolution effect in rock friction.

Benedetti, L. C., Manighetti, I., Gaudemer, Y., Finkel, R., Malavieille, J., Pou, K., Arnold, M., Aumaître, G., Bourlès, D., Keddadouche, K., 2013. Earthquake synchrony and clustering on Fucino faults (Central Italy) as revealed from in situ 36 Cl exposure dating. Journal of Geophysical Research: Solid Earth 118 (9), 4948–4974.

Benedetti, L. C., van der Woerd, J., 2014. Cosmogenic Nuclide Dating of Earthquakes, Faults, and Toppled Blocks. Elements 10 (5), 357–361.

Bernabé, Y., Evans, B., 2007. Numerical modelling of pressure solution deformation at axisymmetric asperities under normal load. Geological Society, London, Special Publications 284 (1), 185–205.

Bernabé, Y., Evans, B., 2014. Pressure solution creep of random packs of spheres. Journal of Geophysical Research: Solid Earth 119 (5), 4202–4218.

Bizzarri, A., Cocco, M., Andrews, D. J., Boschi, E., 2001. Solving the dynamic rupture problem with different numerical approaches and constitutive laws. Geophysical Journal International 144 (3), 656–678.

Bjørkum, P. A., 1996. How Important is Pressure in Causing Dissolution of Quartz in Sandstones? Journal of Sedimentary Research 66 (1), 147–154.

Blanpied, M. L., Lockner, D. A., Byerlee, J. D., 1991. Fault stability inferred from granite sliding experiments at hydrothermal conditions. Geophysical Research Letters 18 (4), 609–612.

Blanpied, M. L., Lockner, D. A., Byerlee, J. D., 1992. An earthquake mechanism based on rapid sealing of faults. Nature 358 (6387), 574–576.

Blanpied, M. L., Lockner, D. A., Byerlee, J. D., 1995. Frictional slip of granite at hydrothermal conditions. Journal of Geophysical Research 100 (B7), 13045.

Blanpied, M. L., Marone, C. J., Lockner, D. A., Byerlee, J. D., King, D. P., 1998. Quantitative measure of the variation in fault rheology due to fluid-rock interactions. Journal of Geophysical Research 103 (B5), 9691.

Boatwright, J., Cocco, M., 1996. Frictional constraints on crustal faulting. Journal of Geophysical Research 101, 13895.

Boneh, Y., Reches, Z., 2017. Geotribology - Friction, wear, and lubrication of faults. Tectonophysics.

Bonner, J. L., 2003. Thermal Constraints on Earthquake Depths in California. Bulletin of the Seismological Society of America 93 (6), 2333–2354.

Bos, B., Peach, C. J., Spiers, C. J., 2000a. Frictional-viscous flow of simulated fault gouge caused by the combined effects of phyllosilicates and pressure solution. Tectonophysics 327.

Bos, B., Peach, C. J., Spiers, C. J., 2000b. Slip behavior of simulated gouge-bearing faults under conditions favoring pressure solution. Journal of Geophysical Research: Solid Earth 105 (B7), 16699–16717.

Bos, B., Spiers, C. J., 2000. Effect of phyllosilicates on fluid-assisted healing of gouge-bearing faults. Earth and Planetary Science Letters 184, 199–210.

Bos, B., Spiers, C. J., 2002a. Fluid-assisted Healing Processes in Gouge-bearing Faults: Insights from Experiments on a Rock Analogue System. Pure and Applied Geophysics 159 (11-12), 2537–2566.

Bos, B., Spiers, C. J., 2002b. Frictional-viscous flow of phyllosilicate-bearing fault rock: Microphysical model and implications for crustal strength profiles. Journal of Geophysical Research 107.

Boulton, C., Carpenter, B. M., Toy, V. G., Marone, C., 2012. Physical properties of surface outcrop cataclastic fault rocks, Alpine Fault, New Zealand. Geochemistry, Geophysics, Geosystems 13 (1).

Boulton, C., Moore, D. E., Lockner, D. A., Toy, V. G., Townend, J., Sutherland, R., 2014. Frictional properties of exhumed fault gouges in DFDP-1 cores, Alpine Fault, New Zealand. Geophysical Research Letters 41 (2), 356–362.

Bowden, F. P., Hughes, T. P., 1939. The Mechanism of Sliding on Ice and Snow. Proceedings of the Royal Society A: Mathematical, Physical and Engineering Sciences 172 (949), 280–298.

Bowden, F. P., Moore, A. J. W., Tabor, D., 1943. The Ploughing and Adhesion of Sliding Metals. Journal of Applied Physics 14 (2), 80–91.

Bowden, F. P., Tabor, D., 1964. The friction and lubrication of solids. Oxford University Press, Oxford.

Brace, W. F., Byerlee, J. D., 1966. Stick-slip as a mechanism for earthquakes. Science 153 (3739), 990–992.

Brace, W. F., Byerlee, J. D., 1970. California Earthquakes: Why Only Shallow Focus? Science 168 (3939), 1573–1575.

Bradbury, K. K., Evans, J. P., Chester, J. S., Chester, F. M., Kirschner, D. L., 2011. Lithology and internal structure of the San Andreas fault at depth based on characterization of Phase 3 whole-rock core in the San Andreas Fault Observatory at Depth (SAFOD) borehole. Earth and Planetary Science Letters 310 (1-2), 131–144.

Branch, M. A., Coleman, T. F., Li, Y., 1999. A Subspace, Interior, and Conjugate Gradient Method for Large-Scale Bound-Constrained Minimization Problems. SIAM Journal on Scientific Computing 21 (1), 1–23.

Brantley, S. L., 1992. The effect of fluid chemistry on quartz microcrack lifetimes. Earth and Planetary Science Letters 113 (1-2), 145–156.

Brantut, N., Heap, M. J., Meredith, P. G., Baud, P., 2013. Time-dependent cracking and brittle creep in crustal rocks: A review. Journal of Structural Geology 52, 17–43.

Brantut, N., Platt, J. D., 2017. Dynamic Weakening and the Depth Dependence of Earthquake Faulting. In: Thomas, M. Y., Mitchell, T. M., Bhat, H. S. (Eds.), Fault Zone Dynamic Processes: Evolution of Fault Properties During Seismic Rupture, Geophysical Monograph 227. John Wiley & Sons, Inc., pp. 171–194.

Brechet, Y., Estrin, Y., 1994. The effect of strain rate sensitivity on dynamic friction of metals. Scripta metallurgica et materialia 30 (11), 1449–1454.

Bridgman, P. W., 1936. Shearing Phenomena at High Pressure of Possible Importance for Geology. In: Proceedings of the American Academy of Arts and Sciences. Vol. 71. pp. 387–460.

Brodsky, E. E., Kirkpatrick, J. D., Candela, T., 2016. Constraints from fault roughness on the scale-dependent strength of rocks. Geology 44 (1), 19–22.

Brown, S. R., Scholz, C. H., 1985. Broad bandwidth study of the topography of natural rock surfaces. Journal of Geophysical Research 90 (B14), 12575.

Buijze, L., Niemeijer, A. R., Han, R., Shimamoto, T., Spiers, C. J., 2017. Friction properties and deformation mechanisms of halite(-mica) gouges from low to high sliding velocities. Earth and Planetary Science Letters 458, 107–119.

Bullock, R. J., De Paola, N., Holdsworth, R. E., Trabucho-Alexandre, J., 2014. Lithological controls on the deformation mechanisms operating within carbonate-hosted faults during the seismic cycle. Journal of Structural Geology 58, 22–42.

Bureau, L., Baumberger, T., Caroli, C., 2002. Rheological aging and rejuvenation in solid friction contacts. The European physical journal. E, Soft matter 8 (3), 331–7.

Bürgmann, R., Dresen, G., 2008. Rheology of the Lower Crust and Upper Mantle: Evidence from Rock Mechanics, Geodesy, and Field Observations. Annual Review of Earth and Planetary Sciences 36 (1), 531–567.

Bürgmann, R., Kogan, M. G., Steblov, G. M., Hilley, G., Levin, V. E., Apel, E., 2005. Interseismic coupling and asperity distribution along the Kamchatka subduction zone. Journal of Geophysical Research 110 (B7), B07405.

Byerlee, J. D., 1970. The mechanics of stick-slip. Tectonophysics 9 (5), 475–486.

Campillo, M., Ionescu, I. R., 1997. Initiation of antiplane shear instability under slip dependent friction. Journal of Geophysical Research: Solid Earth 102 (B9), 20363–20371.

Candela, T., Renard, F., Klinger, Y., Mair, K., Schmittbuhl, J., Brodsky, E. E., 2012. Roughness of fault surfaces over nine decades of length scales. Journal of Geophysical Research: Solid Earth 117 (B8).

Carpenter, B. M., Collettini, C., Viti, C., Cavallo, A., 2016a. The influence of normal stress and sliding velocity on the frictional behaviour of calcite at room temperature: insights from laboratory experiments and microstructural observations. Geophysical Journal International 205 (1), 548–561.

Carpenter, B. M., Ikari, M. J., Marone, C., 2016b. Laboratory observations of time-dependent frictional strengthening and stress relaxation in natural and synthetic fault gouges. Journal of Geophysical Research: Solid Earth 121 (2), 1183–1201.

Carpenter, B. M., Marone, C., Saffer, D. M., 2009. Frictional behavior of materials in the 3D SAFOD volume. Geophysical Research Letters 36 (5), L05302.

Carpenter, B. M., Scuderi, M. M., Collettini, C., Marone, C., 2014. Frictional heterogeneities on carbonate-bearing normal faults: Insights from the Monte Maggio Fault, Italy. Journal of Geophysical Research: Solid Earth 119 (12), 9062–9076.

Chambon, G., Schmittbuhl, J., Corfdir, A., 2006. Frictional response of a thick gouge sample: 1. Mechanical measurements and microstructures. Journal of Geophysical Research 111 (B9), B09308.

Chang, K.-J., Taboada, A., 2009. Discrete element simulation of the Jiufengershan rock-and-soil avalanche triggered by the 1999 Chi-Chi earthquake, Taiwan. Journal of Geophysical Research 114 (F3), F03003.

Chen, J., Niemeijer, A. R., 2017. Seismogenic Potential of a Gouge-filled Fault and the Criterion for Its Slip Stability: Constraints From a Microphysical Model. Journal of Geophysical Research: Solid Earth 122 (12), 9658–9688.

Chen, J., Niemeijer, A. R., Fokker, P. A., 2017a. Vaporization of fault water during seismic slip. Journal of Geophysical Research: Solid Earth 122 (6), 4237–4276.

Chen, J., Niemeijer, A. R., Spiers, C. J., 2017b. Microphysically Derived Expressions for Rate-and-State Friction Parameters, a , b , and D c. Journal of Geophysical Research: Solid Earth 122 (12), 9627–9657.

Chen, J., Spiers, C. J., 2016. Rate and state frictional and healing behavior of carbonate fault gouge explained using microphysical model. Journal of Geophysical Research: Solid Earth, 1–42.

Chen, J., Verberne, B. A., Spiers, C. J., 2015a. Effects of healing on the seismogenic potential of carbonate fault rocks: Experiments on samples from the Longmenshan Fault, Sichuan, China. Journal of Geophysical Research: Solid Earth 120 (8), 5479–5506.

Chen, J., Verberne, B. A., Spiers, C. J., 2015b. Interseismic re-strengthening and stabilization of carbonate faults by "non-Dieterich" healing under hydrothermal conditions. Earth and Planetary Science Letters 423, 1–12.

Chester, F. M., 1994. Effects of temperature on friction: constitutive equations and experiments with quartz gouge. Journal of Geophysical Research 99 (B4), 7247–7261.

Chester, F. M., Chester, J. S., 1998. Ultracataclasite structure and friction processes of the Punchbowl fault, San Andreas system, California. Tectonophysics 295 (1-2), 199–221.

Chester, F. M., Evans, J. P., Biegel, R. L., 1993. Internal structure and weakening mechanisms of the San Andreas Fault. Journal of Geophysical Research: Solid Earth 98 (B1), 771–786.

Chester, F. M., Higgs, N. G., 1992. Multimechanism friction constitutive model for ultrafine quartz gouge at hypocentral conditions. Journal of Geophysical Research: Solid Earth 97 (B2), 1859–1870.

Chester, F. M., Logan, J. M., 1987. Composite planar fabric of gouge from the Punchbowl Fault, California. Journal of Structural Geology 9 (5-6), 621–IN6.

Cisternas, M., Atwater, B. F., Torrejón, F., Sawai, Y., Machuca, G., Lagos, M., Eipert, A., Youlton, C., Salgado, I., Kamataki, T., Shishikura, M., Rajendran, C. P., Malik, J. K., Rizal, Y., Husni, M., 2005. Predecessors of the giant 1960 Chile earthquake. Nature 437 (7057), 404–407.

Clague, J. J., 1997. Evidence for large earthquakes at the Cascadia Subduction Zone. Reviews of Geophysics 35 (4), 439–460.

Cleary, P. W., Sawley, M. L., 2002. DEM modelling of industrial granular flows: 3D case studies and the effect of particle shape on hopper discharge. Applied Mathematical Modelling 26 (2), 89–111.

Cloos, M., 1992. Thrust-type subduction-zone earthquakes and seamount asperities: A physical model for seismic rupture. Geology 20 (7), 601.

Cochard, A., Rice, J. R., 1997. A spectral method for numerical elastodynamic fracture analysis without spatial replication of the rupture event. Journal of the Mechanics and Physics of Solids 45 (8), 1393–1418.

Cole, D. M., Hopkins, M. A., 2016. The contact properties of naturally occurring geologic materials: experimental observations. Granular Matter 18 (3), 62.

Collettini, C., Holdsworth, R. E., 2004. Fault zone weakening and character of slip along low-angle normal faults: insights from the Zuccale fault, Elba, Italy. Journal of the Geological Society 161 (6), 1039–1051.

Collettini, C., Niemeijer, A. R., Viti, C., Smith, S. A. F., Marone, C., 2011. Fault structure, frictional properties and mixed-mode fault slip behavior. Earth and Planetary Science Letters 311 (3-4), 316–327.

Croizé, D., Bjørlykke, K., Jahren, J., Renard, F., 2010. Experimental mechanical and chemical compaction of carbonate sand. Journal of Geophysical Research 115 (B11), B11204.

Cui, L., O'Sullivan, C., 2006. Exploring the macro- and micro-scale response of an idealised granular material in the direct shear apparatus. Géotechnique 56 (7), 455–468.

Cundall, P. A., Strack, O. D. L., 1979. A discrete numerical model for granular assemblies. Géotechnique 29 (1), 47–65.

Damsgaard, A., Egholm, D. L., Piotrowski, J. A., Tulaczyk, S., Larsen, N. K., Tylmann, K., 2013. Discrete element modeling of subglacial sediment deformation. Journal of Geophysical Research: Earth Surface 118 (4), 2230–2242.

Day, S. M., 1982. Three-dimensional simulation of spontaneous rupture: the effect of nonuniform prestress. Bulletin of the Seismological Society of America 72 (6), 1881–1902.

De Boer, R. B., Nagtegaal, P. J. C., Duyvis, E. M., 1977. Pressure solution experiments on quartz sand. Geochimica et Cosmochimica Acta 41 (2), 257–264.

De Meer, S., Spiers, C. J., 1997. Uniaxial compaction creep of wet gypsum aggregates. Journal of Geophysical Research: Solid Earth 102 (B1), 875–891.

De Meer, S., Spiers, C. J., 1999. Influence of pore-fluid salinity on pressure solution creep in gypsum. Tectonophysics 308 (3), 311–330.

De Meer, S., Spiers, C. J., Nakashima, S., 2005. Structure and diffusive properties of fluid-filled grain boundaries: An in-situ study using infrared (micro) spectroscopy. Earth and Planetary Science Letters 232 (3-4), 403–414.

De Meer, S., Spiers, C. J., Peach, C. J., Watanabe, T., 2002. Diffusive properties of fluid-filled grain boundaries measured electrically during active pressure solution. Earth and Planetary Science Letters 200 (1-2), 147–157.

De Paola, N., Collettini, C., Faulkner, D. R., Trippetta, F., 2008. Fault zone architecture and deformation processes within evaporitic rocks in the upper crust. Tectonics 27 (4).

Demurtas, M., Fondriest, M., Balsamo, F., Clemenzi, L., Storti, F., Bistacchi, A., Di Toro, G., 2016. Structure of a normal seismogenic fault zone in carbonates: The Vado di Corno Fault, Campo Imperatore, Central Apennines (Italy). Journal of Structural Geology 90, 185–206.

Den Hartog, S. A. M., Niemeijer, A. R., Spiers, C. J., 2012. New constraints on megathrust slip stability under subduction zone P–T conditions. Earth and Planetary Science Letters 353-354, 240–252.

Den Hartog, S. A. M., Niemeijer, A. R., Spiers, C. J., 2013. Friction on subduction megathrust faults: Beyond the illite–muscovite transition. Earth and Planetary Science Letters 373, 8–19.

Den Hartog, S. A. M., Spiers, C. J., 2014. A microphysical model for fault gouge friction applied to subduction megathrusts. Journal of Geophysical Research: Solid Earth 119 (2), 1510–1529.

Desbois, G., Urai, J. L., de Bresser, J. H. P., 2012. Fluid distribution in grain boundaries of natural fine-grained rock salt deformed at low differential stress (Qom Kuh salt fountain, central Iran): Implications for rheology and transport properties. Journal of Structural Geology 43, 128–143.

Dewers, T. A., Hajash, A., 1995. Rate laws for water-assisted compaction and stress-induced water-rock interaction in sandstones. Journal of Geophysical Research: Solid Earth 100 (B7), 13093–13112.

Dewhurst, D. N., Boult, P. J., Jones, R. M., Barclay, S. A., 2005. Fault Healing and Fault Sealing in Impure Sandstones. In: Boult, P. J., Kaldi, J. (Eds.), Evaluating fault and cap rock seals: AAPG Hedberg Series. No. 2. pp. 37–56.

Di Toro, G., Goldsby, D. L., Tullis, T. E., 2004. Friction falls towards zero in quartz rock as slip velocity approaches seismic rates. Nature 427 (6973), 436–439.

Dieterich, J. H., 1972. Time-dependent friction in rocks. Journal of Geophysical Research 77 (20), 3690–3697.

Dieterich, J. H., 1978. Time-dependent friction and the mechanics of stick-slip. Pure and Applied Geophysics 116 (4-5), 790–806.

Dieterich, J. H., 1979. Modeling of rock friction: 1. Experimental results and constitutive equations. Journal of Geophysical Research 84 (B5), 2161.

Dieterich, J. H., 1992. Earthquake nucleation on faults with rate-and state-dependent strength. Tectonophysics 211 (1-4), 115–134.

Dieterich, J. H., Kilgore, B. D., 1994. Direct observation of frictional contacts: New insights for state-dependent properties. Pure and Applied Geophysics 143 (1-3), 283–302.

Dieterich, J. H., Kilgore, B. D., 1996. Imaging surface contacts: power law contact distributions and contact stresses in quartz, calcite, glass and acrylic plastic. Tectonophysics 256 (1-4), 219–239.

Dodge, D. A., Beroza, G. C., Ellsworth, W. L., 1995. Foreshock sequence of the 1992 Landers, California, earthquake and its implications for earthquake nucleation. Journal of Geophysical Research: Solid Earth 100 (B6), 9865–9880.

Dodge, D. A., Beroza, G. C., Ellsworth, W. L., 1996. Detailed observations of California foreshock sequences: Implications for the earthquake initiation process. Journal of Geophysical Research: Solid Earth 101 (B10), 22371–22392.

Dove, P. M., 1999. The dissolution kinetics of quartz in aqueous mixed cation solutions. Geochimica et Cosmochimica Acta 63 (22), 3715–3727.

Dragert, H., Hyndman, R. D., 1995. Continuous GPS monitoring of elastic strain in the Northern Cascadia Subduction Zone. Geophysical Research Letters 22 (7), 755–758.

Dublanchet, P., Bernard, P., Favreau, P., 2013. Interactions and triggering in a 3-D rate-and-state asperity model. Journal of Geophysical Research: Solid Earth 118 (5), 2225–2245.

Elliott, D., 1973. Diffusion Flow Laws in Metamorphic Rocks. Geological Society of America Bulletin 84 (8), 2645–2664.

Ellsworth, W. L., Beroza, G. C., 1995. Seismic Evidence for an Earthquake Nucleation Phase. Science 268 (5212), 851–855.

Evans, J. P., Chester, F. M., 1995. Fluid-rock interaction in faults of the San Andreas system: Inferences from San Gabriel fault rock geochemistry and microstructures. Journal of Geophysical Research 100 (B7), 13007.

Fagereng, Å., 2011. Geology of the seismogenic subduction thrust interface. Geological Society, London, Special Publications 359 (1), 55–76.

Fagereng, Å., Den Hartog, S. A. M., 2016. Subduction megathrust creep governed by pressure solution and frictional–viscous flow. Nature Geoscience 10 (1), 51–57.

Fagereng, Å., Sibson, R. H., 2010. Melange rheology and seismic style. Geology 38 (8), 751–754.

Faulkner, D. R., Jackson, C. A. L., Lunn, R. J., Schlische, R. W., Shipton, Z. K., Wibberley, C. A. J., Withjack, M. O., 2010. A review of recent developments concerning the structure, mechanics and fluid flow properties of fault zones. Journal of Structural Geology 32 (11), 1557–1575.

Faulkner, D. R., Lewis, A. C., Rutter, E. H., 2003. On the internal structure and mechanics of large strike-slip fault zones: field observations of the Carboneras fault in southeastern Spain. Tectonophysics 367 (3-4), 235–251.

Favreau, P., Ionescu, I. R., Campillo, M., 1999. On dynamic sliding with rate- and state-dependent friction laws. Geophysical Journal International 139 (3), 671–678.

Fehlberg, E., 1969. Low-Order Classical Runge-Kutta Formulas with Step-Size Control and Their Application to some Heat-Transfer Problems. NASA Technical Report 315.

Feucht, L. J., Logan, J. M., 1990. Effects of chemically active solutions on shearing behavior of a sandstone. Tectonophysics 175 (1-3), 159–176.

Fondriest, M., Smith, S. A. F., Di Toro, G., Zampieri, D., Mittempergher, S., 2012. Fault zone structure and seismic slip localization in dolostones, an example from the Southern Alps, Italy. Journal of Structural Geology 45, 52–67.

Fortt, A. L., Schulson, E. M., 2009. Velocity-dependent friction on Coulombic shear faults in ice. Acta Materialia 57 (15), 4382–4390.

Frye, K. M., 2002. Effect of humidity on granular friction at room temperature. Journal of Geophysical Research 107 (B11), 1–13.

Fukuyama, E., Mikumo, T., Olsen, K. B., 2003. Estimation of the Critical Slip-Weakening Distance: Theoretical Background. Bulletin of the Seismological Society of America 93 (4), 1835–1840.

Gal, D., Nur, A., Aharonov, E., 1998. Stability analysis of a pressure-solution surface. Geophysical Research Letters 25 (8), 1237–1240.

Ghoussoub, J., Leroy, Y. M., 2001. Solid–fluid phase transformation within grain boundaries during compaction by pressure solution. Journal of the Mechanics and Physics of Solids 49 (10), 2385–2430.

Giger, S. B., Cox, S. F., Tenthorey, E., 2008. Slip localization and fault weakening as a consequence of fault gouge strengthening — Insights from laboratory experiments. Earth and Planetary Science Letters 276 (1-2), 73–84.

Giles, M. R., Indrelid, S. L., James, D. M. D., 1998. Compaction — the great unknown in basin modelling. Geological Society, London, Special Publications 141 (1), 15–43.

Goldfinger, C., Ikeda, Y., Yeats, R. S., Ren, J., 2013. Superquakes and Supercycles. Seismological Research Letters 84 (1), 24–32.

Goldfinger, C., Nelson, C. H., Johnson, J. E., 2003. Holocene earthquake records from the Cascadia subduction zone and northern San Andreas fault based on precise dating of offshore turbitides. Annual Review of Earth and Planetary Sciences 31 (1), 555–577.

Goldfinger, C., Nelson, C. H., Morey, A. E., Johnson, J. E., Patton, J. R., Karabanov, E., Gutierrez-Pastor, J., Eriksson, A. T., Gracia, E., Dunhill, G., Enkin, R. J., Dallimore, A., Valiier, T., 2012. Turbidite Event History — Methods and Implications for Holocene Paleoseismicity of the Cascadia Subduction Zone. U.S. Geological Survey Professional Paper 1661-F, 170.

Goldsby, D. L., Tullis, T. E., 2002. Low frictional strength of quartz rocks at subseismic slip rates. Geophysical Research Letters 29 (17), 25–1–25–4.

Goldsby, D. L., Tullis, T. E., 2011. Flash Heating Leads to Low Frictional Strength of Crustal Rocks at Earthquake Slip Rates. Science 334 (6053), 216–218.

Gomberg, J., 2010. Slow-slip phenomena in Cascadia from 2007 and beyond: A review. Geological Society of America Bulletin 122 (7-8), 963–978.

Gomberg, J., Wech, A. G., Creager, K. C., Obara, K., Agnew, D., 2016. Reconsidering earthquake scaling. Geophysical Research Letters 43 (12), 6243–6251.

Gratier, J.-P., 1987. Pressure solution-deposition creep and associated tectonic differentiation in sedimentary rocks. Geological Society, London, Special Publications 29 (1), 25–38.

Gratier, J.-P., Dysthe, D. K., Renard, F., 2013. The Role of Pressure Solution Creep in the Ductility of the Earth's Upper Crust. Advances in Geophysics 54, 47–179.

Gratier, J.-P., Guiguet, R., Renard, F., Jenatton, L., Bernard, D., 2009. A pressure solution creep law for quartz from indentation experiments. Journal of Geophysical Research 114 (B3), B03403.

Grauls, D., 1997. Minimum Principal Stress as Control of Overpressures in Sedimentary Basins. In: Hendry, J. (Ed.), Geofluids II '97. pp. 219–222.

Greenwood, J. A., Williamson, J. B. P., 1966. Contact of Nominally Flat Surfaces. Proceedings of the Royal Society A: Mathematical, Physical and Engineering Sciences 295 (1442), 300–319.

Griggs, D. T., Turner, F. J., Heard, H. C., 1960. Deformation of Rocks at 500° to 800° C. In: Geological Society of America Memoirs. Geological Society of America, pp. 39–104.

Gu, J.-C., Rice, J. R., Ruina, A. L., Tse, S. T., 1984. Slip motion and stability of a single degree of freedom elastic system with rate and state dependent friction. Journal of the Mechanics and Physics of Solids 32 (3), 167–196.

Guha-Sapir, D., Hoyois, P., Below, R., Wallemacq, P., 2016. Annual Disaster Statistical Review 2016: The Numbers and Trends. Tech. rep., CRED, Brussels.

Guo, Y., Morgan, J. K., 2004. Influence of normal stress and grain shape on granular friction: Results of discrete element simulations. Journal of Geophysical Research 109, 1–16.

Guo, Y., Morgan, J. K., 2006. The frictional and micromechanical effects of grain comminution in fault gouge from distinct element simulations. Journal of Geophysical Research: Solid Earth 111 (B12).

Guo, Y., Morgan, J. K., 2008. Fault gouge evolution and its dependence on normal stress and rock strength—Results of discrete element simulations: Gouge zone micromechanics. Journal of Geophysical Research 113, 1–19.

Gutenberg, B., Richter, C. F., 1944. Frequency of earthquakes in California. Bulletin of the Seismological Society of America 34 (4), 185–188.

Gutenberg, B., Richter, C. F., 1956. Earthquake magnitude, intensity, energy, and acceleration: (Second paper). Bulletin of the Seismological Society of America 46 (2), 105–145.

Hadizadeh, J., Mittempergher, S., Gratier, J.-P., Renard, F., Di Toro, G., Richard, J., Babaie, H. A., 2012. A microstructural study of fault rocks from the SAFOD: Implications for the deformation mechanisms and strength of the creeping segment of the San Andreas Fault. Journal of Structural Geology 42, 246–260.

Hardin, B., 1989. Effect of Rigid Boundaries on Measurement of Particle Concentration. Geotechnical Testing Journal 12 (2), 143.

Hawthorne, J. C., Rubin, A. M., 2013. Laterally propagating slow slip events in a rate and state friction model with a velocity-weakening to velocity-strengthening transition. Journal of Geophysical Research: Solid Earth 118 (7), 3785–3808.

He, C., Luo, L., Hao, Q.-M., Zhou, Y., 2013. Velocity-weakening behavior of plagioclase and pyroxene gouges and stabilizing effect of small amounts of quartz under hydrothermal conditions. Journal of Geophysical Research: Solid Earth 118 (7), 3408–3430.

He, C., Ma, S., Huang, J., 1998. Transition between stable sliding and stick-slip due to variation in slip rate under variable normal stress condition. Geophysical Research Letters 25 (17), 3235–3238.

He, C., Tan, W., Zhang, L., 2016. Comparing dry and wet friction of plagioclase: Implication to the mechanism of frictional evolution effect at hydrothermal conditions. Journal of Geophysical Research: Solid Earth 121 (9), 6365–6383.

He, C., Wang, Z., Yao, W., 2007. Frictional sliding of gabbro gouge under hydrothermal conditions. Tectonophysics 445 (3-4), 353–362.

Heald, M. T., 1955. Stylolites in sandstones. The Journal of Geology 63 (2), 101–114.

Heslot, F., Baumberger, T., Perrin, B., Caroli, B., Caroli, C., 1994. Creep, stick-slip, and dry-friction dynamics: Experiments and a heuristic model. Physical Review E 49 (6), 4973–4988.

Heuret, A., Lallemand, S., Funiciello, F., Piromallo, C., Faccenna, C., 2011. Physical characteristics of subduction interface type seismogenic zones revisited. Geochemistry, Geophysics, Geosystems 12 (1).

Hickman, S. H., Evans, B., 1991. Experimental pressure solution in halite: the effect of grain/interphase boundary structure. Journal of the Geological Society 148 (3), 549–560.

Hickman, S. H., Evans, B., 1992. Growth of Grain Contacts in Halite by Solution-transfer: Implications for Diagenesis, Lithification, and Strength Recovery. In: Evans, B., Wong, T. (Eds.), Fault Mechanics and Transport Properties of Rocks. Academic Press, pp. 253–280.

Hickman, S. H., Evans, B., 1995. Kinetics of pressure solution at halite-silica interfaces and intergranular clay films. Journal of Geophysical Research 100 (B7), 13113.

Hillers, G., Ben-Zion, Y., Mai, P. M., 2006. Seismicity on a fault controlled by rate- and state-dependent friction with spatial variations of the critical slip distance. Journal of Geophysical Research 111 (B1), B01403.

Hillers, G., Mai, P. M., Ben-Zion, Y., Ampuero, J.-P., 2007. Statistical properties of seismicity of fault zones at different evolutionary stages. Geophysical Journal International 169 (2), 515–533.

Hiraga, T., Nishikawa, O., Nagase, T., Akizuki, M., Kohlstedt, D. L., 2002. Interfacial energies for quartz and albite in pelitic schist. Contributions to Mineralogy and Petrology 143 (6), 664–672.

Hirose, T., Shimamoto, T., 2003. Fractal dimension of molten surfaces as a possible parameter to infer the slip-weakening distance of faults from natural pseudotachylytes. Journal of Structural Geology 25 (10), 1569–1574.

Holdsworth, R. E., Stewart, M., Imber, J., Strachan, R. A., 2001. The structure and rheological evolution of reactivated continental fault zones: a review and case study. Geological Society, London, Special Publications 184 (1), 115–137.

Holdsworth, R. E., van Diggelen, E. W. E., Spiers, C. J., de Bresser, J. H. P., Walker, R. J., Bowen, L., 2011. Fault rocks from the SAFOD core samples: Implications for weakening at shallow depths along the San Andreas Fault, California. Journal of Structural Geology 33 (2), 132–144.

Holness, M. B., 1992. Equilibrium dihedral angles in the system quartz-CO2H2ONaCl at 800oC and 1–15 kbar: the effects of pressure and fluid composition on the permeability of quartzites. Earth and Planetary Science Letters 114 (1), 171–184.

Houston, H., 2015. Low friction and fault weakening revealed by rising sensitivity of tremor to tidal stress. Nature Geoscience 8 (5), 409–415.

Hunfeld, L. B., Niemeijer, A. R., Spiers, C. J., 2017. Frictional Properties of Simulated Fault Gouges from the Seismogenic Groningen Gas Field Under In Situ P - T -Chemical Conditions. Journal of Geophysical Research: Solid Earth 122 (11), 8969–8989.

Ida, Y., 1972. Cohesive force across the tip of a longitudinal-shear crack and Griffith's specific surface energy. Journal of Geophysical Research 77 (20), 3796–3805.

Ida, Y., 1973. The maximum acceleration of seismic ground motion. Bulletin of the Seismological Society of America 63 (3), 959–968.

Ide, S., 2013. The proportionality between relative plate velocity and seismicity in subduction zones. Nature Geoscience 6 (9), 780–784.

Ide, S., Aochi, H., 2005. Earthquakes as multiscale dynamic ruptures with heterogeneous fracture surface energy. Journal of Geophysical Research: Solid Earth 110 (B11), 1–10.

Ide, S., Takeo, M., 1997. Determination of constitutive relations of fault slip based on seismic wave analysis. Journal of Geophysical Research: Solid Earth 102 (B12), 27379–27391.

Ikari, M. J., Carpenter, B. M., Marone, C., 2016a. A microphysical interpretation of rate-dependent and state-dependent friction for fault gouge. Geochemistry, Geophysics, Geosystems 16 (8), 2775–2795.

Ikari, M. J., Carpenter, B. M., Vogt, C., Kopf, A. J., 2016b. Elevated time-dependent strengthening rates observed in San Andreas Fault drilling samples. Earth and Planetary Science Letters 450, 164–172.

Ikari, M. J., Kopf, A. J., 2011. Cohesive strength of clay-rich sediment. Geophysical Research Letters 38 (16).

Ikari, M. J., Niemeijer, A. R., Marone, C., 2011. The role of fault zone fabric and lithification state on frictional strength, constitutive behavior, and deformation microstructure. Journal of Geophysical Research: Solid Earth 116 (8), 1–25.

Iler, R. K., 1973. Effect of adsorbed alumina on the solubility of amorphous silica in water. Journal of Colloid and Interface Science 43 (2), 399–408.

Imber, J., Holdsworth, R. E., Butler, C. A., Strachan, R. A., 2001. A reappraisal of the Sibson-Scholz fault zone model: The nature of the frictional to viscous ("brittle-ductile") transition along a long-lived, crustal-scale fault, Outer Hebrides, Scotland. Tectonics 20 (5), 601–624.

Imber, J., Holdsworth, R. E., Smith, S. A. F., Jefferies, S. P., Collettini, C., 2008. Frictional-viscous flow, seismicity and the geology of weak faults: a review and future directions. Geological Society, London, Special Publications 299 (1), 151–173.

Irwan, M., Kimata, F., Hirahara, K., Sagiya, T., Yamagiwa, A., 2004. Measuring ground deformations with 1-Hz GPS data: the 2003 Tokachi-oki earthquake (preliminary report). Earth, Planets and Space 56 (3), 389–393.

Israelachvili, J. N., 1986. Intermolecular and Surface Forces (With Applications to Colloidal and Biological Systems). Academic Press, London.

Ito, Y., Ikari, M. J., 2015. Velocity- and slip-dependent weakening in simulated fault gouge: Implications for multimode fault slip. Geophysical Research Letters 42 (21), 9247–9254.

Ito, Y., Obara, K., 2006. Dynamic deformation of the accretionary prism excites very low frequency earthquakes. Geophysical Research Letters 33 (2), L02311.

Jefferies, S. P., Holdsworth, R. E., Wibberley, C. A. J., Shimamoto, T., Spiers, C. J., Niemeijer, A. R., Lloyd, G. E., 2006. The nature and importance of phyllonite development in crustal-scale fault cores: an example from the Median Tectonic Line, Japan. Journal of Structural Geology 28 (2), 220–235.

Johnson, J. M., Satake, K., Holdahl, S. R., Sauber, J., 1996. The 1964 Prince William Sound earthquake: Joint inversion of tsunami and geodetic data. Journal of Geophysical Research: Solid Earth 101 (B1), 523–532.

Jones, E., Oliphant, T., Peterson, P., Others, 2001. SciPy: Open source scientific tools for Python. URL: `https://www.scipy.org/`.

Jones, L. M., Molnar, P., 1979. Some characteristics of foreshocks and their possible relationship to earthquake prediction and premonitory slip on faults. Journal of Geophysical Research: Solid Earth 84 (B7), 3596–3608.

Jones, R. M., Dewhurst, D. N., Hillis, R. R., Mildren, S. D., 2002. Geomechanical Fault Characterization: Impact on Quantitative Fault Seal Risking. In: SPE/ISRM Rock Mechanics Conference. Society of Petroleum Engineers, pp. 466–473.

Kagan, Y. Y., 1997. Seismic moment-frequency relation for shallow earthquakes: Regional comparison. Journal of Geophysical Research: Solid Earth 102 (B2), 2835–2852.

Kagan, Y. Y., Jackson, D. D., 2013. Tohoku Earthquake: A Surprise? Bulletin of the Seismological Society of America 103 (2B), 1181–1194.

Kanamori, H., 1977. The energy release in great earthquakes. Journal of Geophysical Research 82 (20), 2981–2987.

Kanamori, H., 2003. Earthquake prediction: An overview. In: Lee, W. H., Kanamori, H., Jennings, P. C., Kisslinger, C. (Eds.), International Geophysics. Academic Press, pp. 1205–1216.

Kanamori, H., Cipar, J. J., 1974. Focal process of the great Chilean earthquake May 22, 1960. Physics of the Earth and Planetary Interiors 9 (2), 128–136.

Kaneko, Y., Ampuero, J.-P., 2011. A mechanism for preseismic steady rupture fronts observed in laboratory experiments. Geophysical Research Letters 38 (21).

Kaneko, Y., Avouac, J.-P., Lapusta, N., 2010. Towards inferring earthquake patterns from geodetic observations of interseismic coupling. Nature Geoscience 3 (5), 363–369.

Kaneko, Y., Carpenter, B. M., Nielsen, S. B., 2017. Nucleation process of magnitude 2 repeating earthquakes on the San Andreas Fault predicted by rate-and-state fault models with SAFOD drill core data. Geophysical Research Letters 44 (1), 162–173.

Kaneko, Y., Nielsen, S. B., Carpenter, B. M., 2016. The onset of laboratory earthquakes explained by nucleating rupture on a rate-and-state fault. Journal of Geophysical Research: Solid Earth 121 (8), 6071–6091.

Kaproth, B. M., Kacewicz, M., Muhuri, S. K., Marone, C., 2016. Permeability and frictional properties of halite-clay-quartz faults in marine-sediment: The role of compaction and shear. Marine and Petroleum Geology 78, 222–235.

Karner, S. L., Chester, F. M., Kronenberg, A. K., Chester, J. S., 2003. Subcritical compaction and yielding of granular quartz sand. Tectonophysics 377 (3-4), 357–381.

Karner, S. L., Marone, C., 2001. Fractional restrengthening in simulated fault gouge: Effect of shear load perturbations. Journal of Geophysical Research: Solid Earth 106 (B9), 19319–19337.

Karner, S. L., Marone, C., Evans, B., 1997. Laboratory study of fault healing and lithification in simulated fault gouge under hydrothermal conditions. Tectonophysics 277 (1-3), 41–55.

Kato, A., Obara, K., Igarashi, T., Tsuruoka, H., Nakagawa, S., Hirata, N., 2012. Propagation of Slow Slip Leading Up to the 2011 Mw 9.0 Tohoku-Oki Earthquake. Science 335 (6069), 705–708.

Kawamoto, E., Shimamoto, T., 1998. The strength profile for bimineralic shear zones: an insight from high-temperature shearing experiments on calcite-halite mixtures. Tectonophysics 295 (1-2), 1–14.

Kilb, D., Gomberg, J., 1999. The initial subevent of the 1994 Northridge, California, earthquake: Is earthquake size predictable? Journal of Seismology 3 (4), 409–420.

Kimura, G., Yamaguchi, A., Hojo, M., Kitamura, Y., Kameda, J., Ujiie, K., Hamada, Y., Hamahashi, M., Hina, S., 2012. Tectonic mélange as fault rock of subduction plate boundary. Tectonophysics 568-569, 25–38.

King, R. F., Tabor, D., 1954. The Strength Properties and Frictional Behaviour of Brittle Solids. Proceedings of the Royal Society A: Mathematical, Physical and Engineering Sciences 223 (1153), 225–238.

Kirkpatrick, J. D., Rowe, C. D., Ujiie, K., Moore, J. C., Regalla, C., Remitti, F., Toy, V. G., Wolfson-Schwehr, M., Kameda, J., Bose, S., Chester, F. M., 2015. Structure and lithology of the Japan Trench subduction plate boundary fault. Tectonics 34 (1), 53–69.

Kirkpatrick, J. D., Rowe, C. D., White, J. C., Brodsky, E. E., 2013. Silica gel formation during fault slip: Evidence from the rock record. Geology 41 (9), 1015–1018.

Koehn, D., Malthe-Sørenssen, A., Passchier, C. W., 2006. The structure of reactive grain-boundaries under stress containing confined fluids. Chemical Geology 230 (3-4), 207–219.

Kuo, L.-W., Li, H., Smith, S. A. F., Di Toro, G., Suppe, J., Song, S.-R., Nielsen, S. B., Sheu, H.-S., Si, J., 2014. Gouge graphitization and dynamic fault weakening during the 2008 Mw 7.9 Wenchuan earthquake. Geology 42 (1), 47–50.

Lachenbruch, A. H., 1980. Frictional heating, fluid pressure, and the resistance to fault motion. Journal of Geophysical Research: Solid Earth 85 (B11), 6097–6112.

Lambert, A., Kao, H., Rogers, G., Courtier, N., 2009. Correlation of tremor activity with tidal stress in the northern Cascadia subduction zone. Journal of Geophysical Research 114 (9), B00A08.

Landry, H., Lague, C., Roberge, M., 2006. Discrete element representation of manure products. Computers and electronics in agriculture 51, 17–34.

Landry, J. W., Grest, G. S., Silbert, L. E., Plimpton, S. J., 2003. Confined granular packings: Structure, stress, and forces. Physical Review E 67 (4), 041303.

Lapusta, N., Rice, J. R., 2003. Nucleation and early seismic propagation of small and large events in a crustal earthquake model. Journal of Geophysical Research: Solid Earth 108 (B4), 1–18.

Lapusta, N., Rice, J. R., Ben-Zion, Y., Zheng, G., 2000. Elastodynamic analysis for slow tectonic loading with spontaneous rupture episodes on faults with rate- and state-dependent friction. Journal of Geophysical Research: Solid Earth 105 (B10), 23765–23789.

Lay, T., Kanamori, H., 1981. An Asperity Model of Large Earthquake Sequences. In: Simpson, D. W., Richards, P. G. (Eds.), Earthquake Prediction. Maurice Ewing Series. American Geophysical Union, Washington D. C., pp. 579–592.

Lay, T., Kanamori, H., Ammon, C. J., Nettles, M., Ward, S. T., Aster, R. C., Beck, S. L., Bilek, S. L., Brudzinski, M. R., Butler, R., DeShon, H. R., Ekström, G., Satake, K., Sipkin, S., 2005. The Great Sumatra-Andaman Earthquake of 26 December 2004. Science 308 (5725), 1127–1133.

Leeman, J., Scuderi, M. M., Marone, C., Saffer, D. M., 2015. Stiffness evolution of granular layers and the origin of repetitive, slow, stick-slip frictional sliding. Granular Matter 17 (4), 447–457.

Leeman, J. R., Saffer, D. M., Scuderi, M. M., Marone, C., 2016. Laboratory observations of slow earthquakes and the spectrum of tectonic fault slip modes. Nature Communications 7, 11104.

Lehner, F. K., 1990. Thermodynamics of rock deformation by pressure solution. In: Barber, D. J., Meredith, P. G. (Eds.), Deformation processes in minerals, ceramics and rocks. Unwin Hyman, London, Dordrecht, pp. 296–333.

Lehner, F. K., 1995. A model for intergranular pressure solution in open systems. Tectonophysics 245 (3-4), 153–170.

Lehner, F. K., Bataille, J., 1985. Nonequilibrium thermodynamics of pressure solution. Pure and Applied Geophysics 122 (1), 53–85.

Lehner, F. K., Leroy, Y. M., 2004. Sandstone Compaction by Intergranular Pressure Solution. In: Guéguen, Y., Boutéca, M. (Eds.), Mechanics of Fluid-Saturated Rocks. Elsevier-Academic Press, Ch. 3, pp. 115–170.

Lewis, S., Holness, M. B., 1996. Equilibrium halite-H2O dihedral angles: High rock-salt permeability in the shallow crust? Geology 24 (5), 431.

Liu, Y., Rice, J. R., 2009. Slow slip predictions based on granite and gabbro friction data compared to GPS measurements in northern Cascadia. Journal of Geophysical Research 114 (B9), B09407.

Lockner, D. A., Tanaka, H., Ito, H., Ikeda, R., Omura, K., Naka, H., 2009. Geometry of the Nojima Fault at Nojima-Hirabayashi, Japan – I. A Simple Damage Structure Inferred from Borehole Core Permeability. Pure and Applied Geophysics 166 (10-11), 1649–1667.

Logan, J. M., Friedman, M., Higgs, N. G., Dengo, C., Shimamoto, T., 1979. Experimental studies of simulated gouge and their application to studies of natural fault zones. In: Proc. Conf. VIII - Analysis of Actual Fault Zones in Bedrock. U.S.G.S. open file report 79-1239, pp. 305–343.

Luo, Y., Ampuero, J.-P., 2018. Stability of faults with heterogeneous friction properties and effective normal stress. Tectonophysics 733, 257–272.

Luo, Y., Ampuero, J.-P., Galvez, P., Van den Ende, M. P. A., Idini, B., 2017a. QDYN: a Quasi-DYNamic earthquake simulator (v1.1). URL: `https://github.com/ydluo/qdyn`.

Luo, Y., Ampuero, J.-P., Miyakoshi, K., Irikura, K., 2017b. Surface Rupture Effects on Earthquake Moment-Area Scaling Relations. Pure and Applied Geophysics 174 (9), 3331–3342.

Mair, K., Abe, S., 2008. 3D numerical simulations of fault gouge evolution during shear: Grain size reduction and strain localization. Earth and Planetary Science Letters 274 (1-2), 72–81.

Mair, K., Frye, K. M., Marone, C., 2002. Influence of grain characteristics on the friction of granular shear zones. Journal of Geophysical Research 107 (B10), 1–9.

Mair, K., Marone, C., 1999. Friction of simulated fault gouge for a wide range of velocities and normal stresses. Journal of Geophysical Research: Solid Earth 104 (B12), 28899–28914.

Mair, K., Renard, F., Gundersen, O., 2006. Thermal imaging on simulated faults during frictional sliding. Geophysical Research Letters 33 (19), L19301.

Majumdar, A., Tien, C. L., 1990. Fractal characterization and simulation of rough surfaces. Wear 136 (2), 313–327.

Mannen, K., Yoong, K. H., Suzuki, S., Matsushima, Y., Ota, Y., Kain, C. L., Goff, J., 2018. History of ancient megathrust earthquakes beneath metropolitan Tokyo inferred from coastal lowland deposits. Sedimentary Geology 364, 258–272.

Marketos, G., 2013. Opening up High Performance Computing to the Discrete Element Method User Community. Tech. rep., UK National Supercomputing Service.

Marketos, G., Bolton, M., 2007. Quantifying the extent of crushing in granular materials: A probability-based predictive method. Journal of the Mechanics and Physics of Solids 55 (10), 2142–2156.

Marketos, G., Bolton, M. D., 2010. Flat boundaries and their effect on sand testing. International Journal for Numerical and Analytical Methods in Geomechanics 32 (March 2007).

Marone, C., 1997. On the rate of frictional healing and the constitutive law for time- and slip-dependent friction. International journal of rock mechanics and mining sciences & geomechanics abstracts 34 (187), 347.

Marone, C., Kilgore, B. D., 1993. Scaling of the critical slip distance for seismic faulting with shear strain in fault zones. Nature 362 (6421), 618–621.

Marone, C., Saffer, D. M., 2015. The Mechanics of Frictional Healing and Slip Instability During the Seismic Cycle. In: Treatise on Geophysics. Elsevier, pp. 111–138.

Marone, C., Scholz, C. H., 1988. The depth of seismic faulting and the upper transition from stable to unstable slip regimes. Geophysical Research Letters 15 (6), 621–624.

Marone, C., Scholz, C. H., 1989. Particle-size distribution and microstructures within simulated fault gouge. Journal of Structural Geology 11 (7), 799–814.

Marone, C., Vidale, J. E., Ellsworth, W. L., 1995. Fault healing inferred from time dependent variations in source properties of repeating earthquakes. Geophysical Research Letters 22 (22), 3095–3098.

Marone, C. J., 1998. Laboratory-Derived Friction Laws and Their Application To Seismic Faulting. Annual Review of Earth and Planetary Sciences 26 (1), 643–696.

Marone, C. J., Raleigh, C. B., Scholz, C. H., 1990. Frictional behavior and constitutive modeling of simulated fault gouge. Journal of Geophysical Research 95 (B5), 7007.

Marone, C. J., Scholtz, C. H., Bilham, R., 1991. On the mechanics of earthquake afterslip. Journal of Geophysical Research 96 (B5), 8441.

Marzocchi, W., Sandri, L., Heuret, A., Funiciello, F., 2016. Where giant earthquakes may come. Journal of Geophysical Research: Solid Earth 121 (10), 7322–7336.

Mase, C. W., Smith, L., 1985. Pore-fluid pressures and frictional heating on a fault surface. Pure and Applied Geophysics 122 (2-4), 583–607.

McCaffrey, R., 1997. Influences of recurrence times and fault zone temperatures on the age-rate dependence of subduction zone seismicity. Journal of Geophysical Research: Solid Earth 102 (B10), 22839–22854.

McCaffrey, R., 2008. Global frequency of magnitude 9 earthquakes. Geology 36 (3), 263.

McLaren, P., Bowles, D., 1985. The effects of sediment transport on grain size distributions. Journal of Sedimentary Petrology 55 (4), 457–470.

McLaskey, G. C., Lockner, D. A., 2014. Preslip and cascade processes initiating laboratory stick slip. Journal of Geophysical Research: Solid Earth 119 (8), 6323–6336.

Mellors, R. J., Sichoix, L., Sandwell, D. T., 2002. Lack of Precursory Slip to the 1999 Hector Mine, California, Earthquake as Constrained by InSAR. Bulletin of the Seismological Society of America 92 (4), 1443–1449.

MiDi, G., 2004. On dense granular flows. The European Physical Journal E 14 (4), 341–365.

Mikumo, T., Olse, K. B., Fukuyama, E., Yagi, Y., 2003. Stress-Breakdown Time and Slip-Weakening Distance Inferred from Slip-Velocity Functions on Earthquake Faults. Bulletin of the Seismological Society of America 93 (1), 264–282.

Miller, M. M., Melbourne, T., Johnson, D. J., Sumner, W. Q., 2002. Periodic Slow Earthquakes from the Cascadia Subduction Zone. Science 295 (5564), 2423–2423.

Mitchell, E. K., Fialko, Y., Brown, K. M., 2013. Temperature dependence of frictional healing of Westerly granite: Experimental observations and numerical simulations. Geochemistry, Geophysics, Geosystems 14 (3), 567–582.

Mitchell, E. K., Fialko, Y., Brown, K. M., 2016. Velocity-weakening behavior of Westerly granite at temperature up to 600C. Journal of Geophysical Research: Solid Earth 121 (9), 6932–6946.

Mochizuki, K., Yamada, T., Shinohara, M., Yamanaka, Y., Kanazawa, T., 2008. Weak Interplate Coupling by Seamounts and Repeating M 7 Earthquakes. Science 321 (5893), 1194–1197.

Modenese, C., Utili, S., Houlsby, G. T., 2012. A Numerical Investigation of Quasi-static Conditions for Granular Media. In: Wu, C.-Y. (Ed.), Discrete Element Modelling of Particulate Media. pp. 187–195.

Moernaut, J., Van Daele, M., Fontijn, K., Heirman, K., Kempf, P., Pino, M., Valdebenito, G., Urrutia, R., Strasser, M., De Batist, M., 2018. Larger earthquakes recur more periodically: New insights in the megathrust earthquake cycle from lacustrine turbidite records in south-central Chile. Earth and Planetary Science Letters 481, 9–19.

Mohamed, A., Gutierrez, M. S., 2010. Comprehensive study of the effects of rolling resistance on the stress-strain and strain localization behavior of granular materials. Granular Matter 12 (5), 527–541.

Montési, L. G. J., 2004. Controls of shear zone rheology and tectonic loading on postseismic creep. Journal of Geophysical Research: Solid Earth 109 (B10).

Moore, D. E., Lockner, D. A., 2007. Friction of the Smectite Clay Montmorillonite A Review and Interpretation of Data. In: Dixon, T. H., Moore, C. (Eds.), The Seismogenic Zone of Subduction Thrust Faults. Columbia University Press, New York Chichester, West Sussex, pp. 317–345.

Morency, C., Huismans, R. S., Beaumont, C., Fullsack, P., 2007. A numerical model for coupled fluid flow and matrix deformation with applications to disequilibrium compaction and delta stability. Journal of Geophysical Research 112 (B10), B10407.

Morgan, J. K., 2015. Effects of cohesion on the structural and mechanical evolution of fold and thrust belts and contractional wedges: Discrete element simulations. Journal of Geophysical Research: Solid Earth 120 (5), 3870–3896.

Morgan, J. K., Boettcher, M. S., 1999. Numerical simulations of granular shear zones using the distinct element method: 1. Shear zone kinematics and the micromechanics of localization. Journal of Geophysical Research 104 (B2), 2703.

Muhuri, S. K., Dewers, T. A., Scott, T. E., Reches, Z., 2003. Interseismic fault strengthening and earthquake-slip instability: Friction or cohesion? Geology 31 (10), 881.

Nakashima, S., 1995. Diffusivity of ions in pore water as a quantitative basis for rock deformation rate estimates. Tectonophysics 245 (3-4), 185–203.

Nakata, A. F. L., Hyde, M., Hyodo, H., Murata, H., 1999. A probabilistic approach to sand particle crushing in the triaxial test. Géotechnique 49 (5), 567–583.

Nakatani, M., 2001. Conceptual and physical clarification of rate and state friction: Frictional sliding as a thermally activated rheology. Journal of Geophysical Research 106 (B7), 13347.

Nakatani, M., Mochizuki, H., 1996. Effects of shear stress applied to surfaces in stationary contact on rock friction. Geophysical Research Letters 23 (8), 869–872.

Nakatani, M., Scholz, C. H., 2004. Frictional healing of quartz gouge under hydrothermal conditions: 1. Experimental evidence for solution transfer healing mechanism. Journal of Geophysical Research 109 (B7), B07201.

Nakatani, M., Scholz, C. H., 2006. Intrinsic and apparent short-time limits for fault healing: Theory, observations, and implications for velocity-dependent friction. Journal of Geophysical Research 111 (B12), B12208.

Nelson, A. R., Kelsey, H. M., Witter, R. C., 2006. Great earthquakes of variable magnitude at the Cascadia subduction zone. Quaternary Research 65 (03), 354–365.

Ng, T.-T., 2006. Input Parameters of Discrete Element Methods. Journal of Engineering Mechanics 132 (7), 723–729.

Nielsen, S. B., Di Toro, G., Hirose, T., Shimamoto, T., 2008. Frictional melt and seismic slip. Journal of Geophysical Research 113 (B1), B01308.

Niemeijer, A. R., Boulton, C., Toy, V. G., Townend, J., Sutherland, R., 2016. Large-displacement, hydrothermal frictional properties of DFDP-1 fault rocks, Alpine Fault, New Zealand: Implications for deep rupture propagation. Journal of Geophysical Research: Solid Earth 121 (2), 624–647.

Niemeijer, A. R., Di Toro, G., Griffith, W. A., Bistacchi, A., Smith, S. A. F., Nielsen, S. B., 2012. Inferring earthquake physics and chemistry using an integrated field and laboratory approach. Journal of Structural Geology 39, 2–36.

Niemeijer, A. R., Elsworth, D., Marone, C., 2009. Significant effect of grain size distribution on compaction rates in granular aggregates. Earth and Planetary Science Letters 284 (3-4), 386–391.

Niemeijer, A. R., Marone, C., Elsworth, D., 2008. Healing of simulated fault gouges aided by pressure solution: Results from rock analogue experiments. Journal of Geophysical Research 113 (B4), B04204.

Niemeijer, A. R., Spiers, C. J., 2002. Compaction creep of quartz-muscovite mixtures at 500 C: Preliminary results on the influence of muscovite on pressure solution. Geological Society, London, Special Publications 200 (1), 61–71.

Niemeijer, A. R., Spiers, C. J., 2005. Influence of phyllosilicates on fault strength in the brittle-ductile transition: insights from rock analogue experiments. Geological Society, London, Special Publications 245 (1), 303–327.

Niemeijer, A. R., Spiers, C. J., 2006. Velocity dependence of strength and healing behaviour in simulated phyllosilicate-bearing fault gouge. Tectonophysics 427 (1-4), 231–253.

Niemeijer, A. R., Spiers, C. J., 2007. A microphysical model for strong velocity weakening in phyllosilicate-bearing fault gouges. Journal of Geophysical Research 112 (B10), B10405.

Niemeijer, A. R., Spiers, C. J., Bos, B., 2002. Compaction creep of quartz sand at 400-600C: experimental evidence for dissolution-controlled pressure solution. Earth and Planetary Science Letters 195, 261–275.

Niemeijer, A. R., Vissers, R. L. M., 2014. Earthquake rupture propagation inferred from the spatial distribution of fault rock frictional properties. Earth and Planetary Science Letters 396, 154–164.

Noda, H., 2008. Frictional constitutive law at intermediate slip rates accounting for flash heating and thermally activated slip process. Journal of Geophysical Research: Solid Earth 113 (9), 1–12.

Noda, H., 2016. Implementation into earthquake sequence simulations of a rate- and state-dependent friction law incorporating pressure solution creep. Geophysical Journal International 205 (2), 1108–1125.

Noda, H., Hori, T., 2014. Under what circumstances does a seismogenic patch produce aseismic transients in the later interseismic period? Geophysical Research Letters 41 (21), 7477–7484.

Noda, H., Lapusta, N., 2010. Three-dimensional earthquake sequence simulations with evolving temperature and pore pressure due to shear heating: Effect of heterogeneous hydraulic diffusivity. Journal of Geophysical Research 115 (B12), B12314.

Noda, H., Lapusta, N., 2013. Stable creeping fault segments can become destructive as a result of dynamic weakening. Nature 493 (7433), 518–521.

Noda, H., Lapusta, N., Kanamori, H., 2013a. Comparison of average stress drop measures for ruptures with heterogeneous stress change and implications for earthquake physics. Geophysical Journal International 193 (3), 1691–1712.

Noda, H., Lapusta, N., Rice, J. R., 2011. Earthquake sequence calculations with dynamic weakening mechanisms. In: Borja, R. I. (Ed.), Multiscale and Multiphysics Processes in Geomechanics: Results of the Workshop on Multiscale and Multiphysics Processes in Geomechanics, Stanford, June 23–25, 2010. Springer Berlin Heidelberg, Berlin, Heidelberg, pp. 149–152.

Noda, H., Nakatani, M., Hori, T., 2013b. Large nucleation before large earthquakes is sometimes skipped due to cascade-up-Implications from a rate and state simulation of faults with hierarchical asperities. Journal of Geophysical Research: Solid Earth 118 (6), 2924–2952.

Noda, H., Sawai, M., Shibazaki, B., 2017. Earthquake sequence simulations with measured properties for JFAST core samples. Philosophical Transactions of the Royal Society A: Mathematical, Physical and Engineering Sciences 375 (2103), 20160003.

Noda, H., Shimamoto, T., 2010. A rate- and state-dependent ductile flow law of polycrystalline halite under large shear strain and implications for transition to brittle deformation. Geophysical Research Letters 37 (9).

Noda, H., Shimamoto, T., 2012. Transient behavior and stability analyses of halite shear zones with an empirical rate-and-state friction to flow law. Journal of Structural Geology 38, 234–242.

Norbeck, J. H., McClure, M. W., Horne, R. N., 2016. Revisiting stimulation mechanism at Fenton Hill and an investigation of the influence of fault heterogeneity on the Gutenberg-Richter b-value for rate-and-state earthquake simulations. 41st Workshop on Geothermal Reservoir Engineering, 1–22.

Obara, K., 2002. Nonvolcanic Deep Tremor Associated with Subduction in Southwest Japan. Science 296 (5573), 1679–1681.

Obara, K., Ito, Y., 2005. Very low frequency earthquakes excited by the 2004 off the Kii peninsula earthquakes: A dynamic deformation process in the large accretionary prism. Earth, Planets and Space 57 (4), 321–326.

Ohnaka, M., 2003. A constitutive scaling law and a unified comprehension for frictional slip failure, shear fracture of intact rock, and earthquake rupture. Journal of Geophysical Research: Solid Earth 108 (B2), 1–21.

Ohnaka, M., 2013. The Physics of Rock Failure and Earthquakes. Cambridge University Press, Cambridge.

Ohta, Y., Freymueller, J., Hreinsdottir, S., Suito, H., 2006. A large slow slip event and the depth of the seismogenic zone in the south central Alaska subduction zone. Earth and Planetary Science Letters 247 (1-2), 108–116.

Ohtani, T., Fujimoto, K., Ito, H., Tanaka, H., Tomida, N., Higuchi, T., 2000. Fault rocks and past to recent fluid characteristics from the borehole survey of the Nojima fault ruptured in the 1995 Kobe earthquake, southwest Japan. Journal of Geophysical Research: Solid Earth 105 (B7), 16161–16171.

Okada, Y., 1985. Surface deformation due to shear and tensile faults in a half-space. Bulletin of the Seismological Society of America 75 (4), 1135–1154.

Okubo, P. G., 1989. Dynamic rupture modeling with laboratory-derived constitutive relations. Journal of Geophysical Research 94 (B9), 12321.

Ortoleva, P. J., 1994. Geochemical self-organization. Oxford University Press, New York.

O'Sullivan, C., Bray, J. D., Li, S., 2003. A new approach for calculating strain for particulate media. International Journal for Numerical and Analytical Methods in Geomechanics 27 (10), 859–877.

Pacheco, J. F., Sykes, L. R., Scholz, C. H., 1993. Nature of seismic coupling along simple plate boundaries of the subduction type. Journal of Geophysical Research: Solid Earth 98 (B8), 14133–14159.

Palciauskas, V. V., Domenico, P. A., 1989. Fluid pressures in deforming porous rocks. Water Resources Research 25 (2), 203–213.

Parry, W. T., 1998. Fault-fluid compositions from fluid-inclusion observations and solubilities of fracture-sealing minerals. Tectonophysics 290 (1-2), 1–26.

Paterson, M. S., 1995. A theory for granular flow accommodated by material transfer via an intergranular fluid. Tectonophysics 245 (3-4), 135–151.

Peng, Z., Gomberg, J., 2010. An integrated perspective of the continuum between earthquakes and slow-slip phenomena. Nature Geoscience 3 (9), 599–607.

Perfettini, H., Avouac, J.-P., 2004. Postseismic relaxation driven by brittle creep: A possible mechanism to reconcile geodetic measurements and the decay rate of aftershocks, application to the Chi-Chi earthquake, Taiwan. Journal of Geophysical Research: Solid Earth 109 (B2), 1–15.

Perfettini, H., Avouac, J.-P., 2007. Modeling afterslip and aftershocks following the 1992 Landers earthquake. Journal of Geophysical Research 112 (B7), B07409.

Perfettini, H., Molinari, A., 2017. A Micromechanical Model of Rate and State Friction: 1. Static and Dynamic Sliding. Journal of Geophysical Research: Solid Earth.

Petersen, M. D., Moschetti, M. P., Powers, P. M., Mueller, C. S., Haller, K. M., Frankel, A. D., Zeng, Y., Rezaeian, S., Harmsen, S. C., Boyd, O. S., Field, E. H., Chen, R., Luco, N., Wheeler, R. L., Williams, R. A., Olsen, A. H., Rukstales, K. S., 2015. Seismic-hazard maps for the conterminous United States, 2014: U.S. Geological Survey Scientific Investigations Map 3325, 6 sheets, scale 1: 7,000,000. Tech. rep., U.S. Geological Survey.

Philibosian, B., Sieh, K., Avouac, J.-P., Natawidjaja, D. H., Chiang, H.-W., Wu, C.-C., Shen, C.-C., Daryono, M. R., Perfettini, H., Suwargadi, B. W., Lu, Y., Wang, X., 2017. Earthquake supercycles on the Mentawai segment of the Sunda megathrust in the seventeenth century and earlier. Journal of Geophysical Research: Solid Earth 122 (1), 642–676.

Platt, J. D., Brantut, N., Rice, J. R., 2015. Strain localization driven by thermal decomposition during seismic shear. Journal of Geophysical Research: Solid Earth 120 (6), 4405–4433.

Plimpton, S. J., 1995. Fast Parallel Algorithms for Short-Range Molecular Dynamics. Journal of Computational Physics 117 (1), 1–19.

Pluymakers, A. M. H., Niemeijer, A. R., 2015. Healing and sliding stability of simulated anhydrite fault gouge: Effects of water, temperature and CO2. Tectonophysics 656, 111–130.

Pluymakers, A. M. H., Spiers, C. J., 2014. Compaction creep of simulated anhydrite fault gouge by pressure solution: theory vs. experiments and implications for fault sealing. In: Faulkner, D., Mariani, E., Mecklenburgh, J. (Eds.), Rock Deformation from Field, Experiments and Theory: A Volume in Honour of Ernie Rutter. Vol. 409. Geological Society, London, pp. 107–124.

Pollitz, F. F., Wech, A. G., Kao, H., Bürgmann, R., 2013. Annual modulation of non-volcanic tremor in northern Cascadia. Journal of Geophysical Research: Solid Earth 118 (5), 2445–2459.

Potyondy, D. O., Cundall, P. A., 2004. A bonded-particle model for rock. International Journal of Rock Mechanics and Mining Sciences 41 (8), 1329–1364.

Power, W. L., Tullis, T. E., 1989. The relationship between slickenside surfaces in fine-grained quartz and the seismic cycle. Journal of Structural Geology 11 (7), 879–893.

Putelat, T., Dawes, J. H. P., Willis, J. R., 2011. On the microphysical foundations of rate-and-state friction. Journal of the Mechanics and Physics of Solids 59 (5), 1062–1075.

Rabinowicz, E., 1965. Friction and Wear of Materials. Wiley, London.

Raj, R., 1982. Creep in polycrystalline aggregates by matter transport through a liquid phase. Journal of Geophysical Research 87 (B6), 4731.

Rathbun, A. P., Marone, C., 2010. Effect of strain localization on frictional behavior of sheared granular materials. Journal of Geophysical Research 115 (B1), 1–16.

Ratzov, G., Cattaneo, A., Babonneau, N., Déverchère, J., Yelles, K., Bracene, R., Courboulex, F., 2015. Holocene turbidites record earthquake supercycles at a slow-rate plate boundary. Geology 43 (4), 331–334.

Reid, H. F., 1910. The Mechanics of the Earthquake. Tech. rep., State Earthquake Investigation Commission, Washington, D.C.

Reinen, L. A., Tullis, T. E., Weeks, J. D., 1992. Two-mechanism model for frictional sliding of serpentinite. Geophysical Research Letters 19 (15), 1535–1538.

Reinen, L. A., Weeks, J. D., 1993. Determination of rock friction constitutive parameters using an iterative least squares inversion method. Journal of Geophysical Research 98 (B9), 15937.

Rempel, A. W., Weaver, S. L., 2008. A model for flash weakening by asperity melting during high-speed earthquake slip. Journal of Geophysical Research 113 (B11), B11308.

Renard, F., Beauprêtre, S., Voisin, C., Zigone, D., Candela, T., Dysthe, D. K., Gratier, J.-P., 2012. Strength evolution of a reactive frictional interface is controlled by the dynamics of contacts and chemical effects. Earth and Planetary Science Letters 344, 20–34.

Renard, F., Dysthe, D. K., Feder, J., Bjørlykke, K., Jamtveit, B., 2001. Enhanced pressure solution creep rates induced by clay particles: Experimental evidence in salt aggregates. Geophysical Research Letters 28 (7), 1295–1298.

Renard, F., Ortoleva, P. J., Gratier, J.-P., 1997. Pressure solution in sandstones: influence of clays and dependence on temperature and stress. Tectonophysics 280 (3-4), 257–266.

Renard, F., Park, A., Ortoleva, P. J., Gratier, J.-P., 1999. An integrated model for transitional pressure solution in sandstones. Tectonophysics 312 (2-4), 97–115.

Revil, A., 2001. Pervasive pressure solution transfer in a quartz sand. Journal of Geophysical Research: Solid Earth 106 (B5), 8665–8686.

Rice, J. R., 1992. Fault Stress States, Pore Pressure Distributions, and the Weakness of the San Andreas Fault. In: Evans, B., Wong, T.-F. (Eds.), Fault Mechanics and Transport Properties of Rocks. Academic Press, pp. 475–503.

Rice, J. R., 1993. Spatio-temporal complexity of slip on a fault. Journal of Geophysical Research 98 (B6), 9885.

Rice, J. R., 2006. Heating and weakening of faults during earthquake slip. Journal of Geophysical Research: Solid Earth 111 (B5).

Rice, J. R., Lapusta, N., Ranjith, K., 2001. Rate and state dependent friction and the stability of sliding between elastically deformable solids. Journal of the Mechanics and Physics of Solids 49 (9), 1865–1898.

Rice, J. R., Ruina, A. L., 1983. Stability of Steady Frictional Slipping. Journal of Applied Mechanics 50 (2), 343.

Richardson, E., Marone, C., 1999. Effects of normal stress vibrations on frictional healing. Journal of Geophysical Research: Solid Earth 104 (B12), 28859–28878.

Rimstidt, J. D., 2015. Rate equations for sodium catalyzed quartz dissolution. Geochimica et Cosmochimica Acta 167, 195–204.

Rimstidt, J. D., Barnes, H. L., 1980. The kinetics of silica-water reactions. Geochimica et Cosmochimica Acta 44 (11), 1683–1699.

Robin, P.-Y. F., 1978. Pressure solution at grain-to-grain contacts. Geochimica et Cosmochimica Acta 42 (9), 1383–1389.

Roda, M., Marketos, G., Westerweel, J., Govers, R., 2017. Morphological Expressions of Crater Infill Collapse: Model Simulations of Chaotic Terrains on Mars. Geochemistry, Geophysics, Geosystems 18 (10), 3687–3699.

Roeloffs, E. A., 2006. Evidence for aseismic deformation rate changes prior to earthquakes. Annual Review of Earth and Planetary Sciences 34 (1), 591–627.

Rogers, G., Dragert, H., 2003. Episodic Tremor and Slip on the Cascadia Subduction Zone: The Chatter of Silent Slip. Science 300 (5627), 1942–1943.

Rowe, C. D., Meneghini, F., Moore, J. C., 2011. Textural record of the seismic cycle: strain-rate variation in an ancient subduction thrust. Geological Society, London, Special Publications 359 (1), 77–95.

Rubin, A. M., 2008. Episodic slow slip events and rate-and-state friction. Journal of Geophysical Research 113 (B11), B11414.

Rubin, A. M., 2011. Designer friction laws for bimodal slow slip propagation speeds. Geochemistry, Geophysics, Geosystems 12 (4).

Rubin, A. M., Ampuero, J.-P., 2005. Earthquake nucleation on (aging) rate and state faults. Journal of Geophysical Research: Solid Earth 110 (B11), 1–24.

Rubinstein, J. L., La Rocca, M., Vidale, J. E., Creager, K. C., Wech, A. G., 2008. Tidal Modulation of Nonvolcanic Tremor. Science 319 (5860), 186–189.

Ruff, L., Kanamori, H., 1980. Seismicity and the subduction process. Physics of the Earth and Planetary Interiors 23 (3), 240–252.

Ruina, A. L., 1980. Friction laws and instabilities: A quasistatic analysis of some dry frictional behavior. Ph.D. thesis, Cornell.

Ruina, A. L., 1983. Slip instability and state variable friction laws. Journal of Geophysical Research: Solid Earth 88 (B12), 10359–10370.

Rutter, E. H., 1976. The kinetics of rock deformation by pressure solution. Philosophical Transactions of the Royal Society of Londen. Series A, Mathematical and Physical Sciences 283 (1312), 203–219.

Rutter, E. H., 1983. Pressure solution in nature, theory and experiment. Journal of the Geological Society 140 (5), 725–740.

Saffer, D. M., Marone, C. J., 2003. Comparison of smectite- and illite-rich gouge frictional properties: application to the updip limit of the seismogenic zone along subduction megathrusts. Earth and Planetary Science Letters 215 (1-2), 219–235.

Sahimi, M., 2003. Heterogeneous Materials I: Linear Transport and Optical Properties. Springer, New York.

Satake, K., 2015. Geological and historical evidence of irregular recurrent earthquakes in Japan. Philosophical Transactions of the Royal Society A: Mathematical, Physical and Engineering Sciences 373 (2053), 20140375.

Satake, K., Atwater, B. F., 2007. Long-Term Perspectives on Giant Earthquakes and Tsunamis at Subduction Zones. Annual Review of Earth and Planetary Sciences 35 (1), 349–374.

Satake, K., Fujii, Y., 2014. Review: Source Models of the 2011 Tohoku Earthquake and Long-Term Forecast of Large Earthquakes. Journal of Disaster Research 9 (3), 272–280.

Sawai, M., Niemeijer, A. R., Plümper, O., Hirose, T., Spiers, C. J., 2016. Nucleation of frictional instability caused by fluid pressurization in subducted blueschist. Geophysical Research Letters 43 (6), 2543–2551.

Schellart, W. P., Rawlinson, N., 2013. Global correlations between maximum magnitudes of subduction zone interface thrust earthquakes and physical parameters of subduction zones. Physics of the Earth and Planetary Interiors 225, 41–67.

Schenk, O., Urai, J. L., 2004. Microstructural evolution and grain boundary structure during static recrystallization in synthetic polycrystals of Sodium Chloride containing saturated brine. Contributions to Mineralogy and Petrology 146 (6), 671–682.

Schlagenhauf, A., Manighetti, I., Benedetti, L. C., Gaudemer, Y., Finkel, R., Malavieille, J., Pou, K., 2011. Earthquake supercycles in Central Italy, inferred from 36Cl exposure dating. Earth and Planetary Science Letters 307 (3-4), 487–500.

Schmid, S. M., Handy, M. R., 1991. Towards a Genetic Classiftcation of Fault Rocks : Geological Usage and Tectonophysical lmplications. Press, London, 339–361.

Scholz, C. H., 1988. The brittle-plastic transition and the depth of seismic faulting. Geologische Rundschau 77 (1), 319–328.

Scholz, C. H., 1998. Earthquakes and friction laws. Nature, 37–42.

Scholz, C. H., 2002. The Mechanics of Earthquakes and Faulting. Cambridge University Press, Cambridge.

Scholz, C. H., Aviles, C. A., Wensnousky, S. G., 1986. Scaling differences between large interplate and intraplate earthquakes. Bulletin of the Seismological Society of America 76 (1), 65–70.

Scholz, C. H., Engelder, J. T., 1976. The role of asperity indentation and ploughing in rock friction — I. International Journal of Rock Mechanics and Mining Sciences & Geomechanics Abstracts 13 (5), 149–154.

Schutjens, P. M. T. M., 1991a. Experimental compaction of quartz sand at low effective stress and temperature conditions. Journal of the Geological Society 148 (3), 527–539.

Schutjens, P. M. T. M., 1991b. Intergranular pressure solution in halite aggregates and quartz sands: an experimental investigation. Ph.D. thesis, Utrecht University.

Schutjens, P. M. T. M., Spiers, C. J., 1999. Intergranular Pressure Solution in Nacl: Grain-To-Grain Contact Experiments under the Optical Microscope. Oil & Gas Science and Technology 54 (6), 729–750.

Scrutton, A., Grootscholten, P. A. M., 1981. A study on the dissolution and growth of sodium chloride crystals. Transactions of the Institution of Chemical Engineers 59 (4), 238–246.

Scuderi, M. M., Collettini, C., Viti, C., Tinti, E., Marone, C., 2017. Evolution of shear fabric in granular fault gouge from stable sliding to stick slip and implications for fault slip mode. Geology 45 (8), G39033.1.

Scuderi, M. M., Marone, C., Tinti, E., Di Stefano, G., Collettini, C., 2016. Precursory changes in seismic velocity for the spectrum of earthquake failure modes. Nature Geoscience 9 (9), 695–700.

Seabold, S., Perktold, J., 2010. Statsmodels: Econometric and statistical modeling with python. In: Proceedings of the 9th Python in Science Conference. pp. 57–61.

Seno, T., 2003. Fractal asperities, invasion of barriers, and interplate earthquakes. Earth, Planets and Space 55 (11), 649–665.

Shampine, L. F., Watts, H. A., Davenport, S. M., 1976. Solving Nonstiff Ordinary Differential Equations - The State of the Art. SIAM Review 18 (3), 376–411.

Shanhua, X., Songbo, R., Youde, W., 2015. Three-Dimensional Surface Parameters and Multi-Fractal Spectrum of Corroded Steel. PLOS ONE 10 (6), e0131361.

Shibazaki, B., Iio, Y., 2003. On the physical mechanism of silent slip events along the deeper part of the seismogenic zone. Geophysical Research Letters 30 (9), 1489.

Shimamoto, T., 1986. Transition Between Frictional Slip and Ductile Flow for Halite Shear Zones at Room Temperature. Science 231 (4739), 711–714.

Shimamoto, T., Noda, H., 2014. A friction to flow constitutive law and its application to a 2-D modeling of earthquakes. Journal of Geophysical Research: Solid Earth 119 (11), 8089–8106.

Shimizu, I., 1995. Kinetics of pressure solution creep in quartz: theoretical considerations. Tectonophysics 245 (3-4), 121–134.

Sibson, R. H., 1977. Fault rocks and fault mechanisms. Journal of the Geological Society 133 (3), 191–213.

Sibson, R. H., 1982. Fault zone models, heat flow, and the depth distribution of earthquakes in the continental crust of the United States. Bulletin of the Seismological Society of America 72 (1), 151–163.

Sibson, R. H., 1990. Conditions for fault-valve behaviour. Geological Society, London, Special Publications 54 (1), 15–28.

Sieh, K., Natawidjaja, D. H., Meltzner, A. J., Shen, C.-C., Cheng, H., Li, K.-S., Suwargadi, B. W., Galetzka, J., Philibosian, B., Edwards, R. L., 2008. Earthquake Supercycles Inferred from Sea-Level Changes Recorded in the Corals of West Sumatra. Science 322 (5908), 1674–1678.

Siman-Tov, S., Aharonov, E., Sagy, A., Emmanuel, S., 2013. Nanograins form carbonate fault mirrors. Geology 41 (6), 703–706.

Skarbek, R. M., Rempel, A. W., Schmidt, D. A., 2012. Geologic heterogeneity can produce aseismic slip transients. Geophysical Research Letters 39 (21).

Sleep, N. H., 2005. Physical basis of evolution laws for rate and state friction. Geochemistry, Geophysics, Geosystems 6 (11).

Sleep, N. H., Blanpied, M. L., 1992. Creep, compaction and the weak rheology of major faults. Nature 359 (6397), 687–692.

Smeraglia, L., Bettucci, A., Billi, A., Carminati, E., Cavallo, A., Di Toro, G., Natali, M., Passeri, D., Rossi, M., Spagnuolo, E., 2017. Microstructural evidence for seismic and aseismic slips along clay-bearing, carbonate faults. Journal of Geophysical Research: Solid Earth 122 (5), 3895–3915.

Smith, S. A. F., Billi, A., Toro, G. D., Spiess, R., 2011. Principal Slip Zones in Limestone: Microstructural Characterization and Implications for the Seismic Cycle (Tre Monti Fault, Central Apennines, Italy). Pure and Applied Geophysics 168 (12), 2365–2393.

Spagnuolo, E., Nielsen, S. B., Violay, M., Di Toro, G., 2016. An empirically based steady state friction law and implications for fault stability. Geophysical Research Letters 43 (7), 3263–3271.

Spagnuolo, E., Plümper, O., Violay, M., Cavallo, A., Di Toro, G., 2015. Fast-moving dislocations trigger flash weakening in carbonate-bearing faults during earthquakes. Scientific Reports 5, 16112.

Spiers, C. J., De Meer, S., Niemeijer, A. R., Zhang, X., 2004. Kinetics of rock deformation by pressure solution and the role of thin aqueous films. In: Nakashima, S., Spiers, C. J., Mercury, L., Fenter, P. A., Hochella, M. F. J. (Eds.), Physicochemistry of Water in Geological and Biological Systems. Universal Academy Press, Tokyo, pp. 129–158.

Spiers, C. J., Schutjens, P. M. T. M., 1990. Densification of crystalline aggregates by fluid-phase diffusional creep. In: Barber, D. J., Meredith, P. G. (Eds.), Deformation processes in minerals, ceramics and rocks. Unwin Hyman, London, pp. 334–353.

Spiers, C. J., Schutjens, P. M. T. M., Brzesowsky, R. H., Peach, C. J., Liezenberg, J. L., Zwart, H. J., 1990. Experimental determination of constitutive parameters governing creep of rocksalt by pressure solution. Geological Society, London, Special Publications 54 (1), 215–227.

Stauffer, D., Aharony, A., 1992. Introduction to Percolation Theory, 2nd Edition. Taylor & Francis, London.

Stein, S., Okal, E. A., 2007. Ultralong Period Seismic Study of the December 2004 Indian Ocean Earthquake and Implications for Regional Tectonics and the Subduction Process. Bulletin of the Seismological Society of America 97 (1A), S279–S295.

Stevens, V. L., Avouac, J.-P., 2016. Millenary Mw > 9.0 earthquakes required by geodetic strain in the Himalaya. Geophysical Research Letters 43 (3), 1118–1123.

Stöckhert, B., Wachmann, M., Küster, M., Bimmermann, S., 1999. Low effective viscosity during high pressure metamorphism due to dissolution precipitation creep: the record of HP–LT metamorphic carbonates and siliciclastic rocks from Crete. Tectonophysics 303 (1-4), 299–319.

Storti, F., Billi, A., Salvini, F., 2003. Particle size distributions in natural carbonate fault rocks: Insights for non-self-similar cataclasis. Earth and Planetary Science Letters 206 (1-2), 173–186.

Suppe, J., 2014. Fluid overpressures and strength of the sedimentary upper crust. Journal of Structural Geology 69 (PB), 481–492.

Sykes, L. R., Shaw, B. E., Scholz, C. H., 1999. Rethinking Earthquake Prediction. Pure and Applied Geophysics 155 (2-4), 207–232.

Tada, R., Siever, R., 1989. Pressure Solution During Diagenesis. Annual Review of Earth and Planetary Sciences 17 (1), 89–118.

Takahashi, M., van den Ende, M. P. A., Niemeijer, A. R., Spiers, C. J., 2017. Shear localization in a mature mylonitic rock analog during fast slip. Geochemistry, Geophysics, Geosystems 18 (2), 513–530.

Tenthorey, E., Cox, S. F., 2006. Cohesive strengthening of fault zones during the interseismic period: An experimental study. Journal of Geophysical Research 111 (B9), B09202.

Tenthorey, E., Cox, S. F., Todd, H. F., 2003. Evolution of strength recovery and permeability during fluid–rock reaction in experimental fault zones. Earth and Planetary Science Letters 206 (1-2), 161–172.

Ter Heege, J. H., De Bresser, J. H. P., Spiers, C. J., 2004. Composite flow laws for crystalline materials with log-normally distributed grain size: Theory and application to olivine. Journal of Structural Geology 26 (9), 1693–1705.

Tesei, T., Collettini, C., Barchi, M. R., Carpenter, B. M., Di Stefano, G., 2014. Heterogeneous strength and fault zone complexity of carbonate-bearing thrusts with possible implications for seismicity. Earth and Planetary Science Letters 408, 307–318.

Thomas, A. M., Nadeau, R. M., Bürgmann, R., 2009. Tremor-tide correlations and near-lithostatic pore pressure on the deep San Andreas fault. Nature 462 (7276), 1048–1051.

Thomas, M. Y., Avouac, J.-P., Lapusta, N., 2017. Rate-and-state friction properties of the Longitudinal Valley Fault from kinematic and dynamic modeling of seismic and aseismic slip. Journal of Geophysical Research: Solid Earth 122 (4), 3115–3137.

Thomas, M. Y., Lapusta, N., Noda, H., Avouac, J.-P., 2014. Quasi-dynamic versus fully dynamic simulations of earthquakes and aseismic slip with and without enhanced coseismic weakening. Journal of Geophysical Research: Solid Earth 119 (3), 1986–2004.

Tinti, E., Bizzarri, A., Cocco, M., 2005. Modeling the dynamic rupture propagation on heterogeneous faults with rate- and state-dependent friction. Annals of Geophysics 48 (2), 327–345.

Torok, J., Fazekas, S., Unger, T., Wolf, D. E., 2005. Relationship between particle size and normal force. In: Garcia-Rojo, Hermann, McNamana (Eds.), Powders and Grains. Taylor & Francis Group, London, pp. 1273–1277.

Trütner, S., Hüpers, A., Ikari, M. J., Yamaguchi, A., Kopf, A. J., 2015. Lithification facilitates frictional instability in argillaceous subduction zone sediments. Tectonophysics 665, 177–185.

Tse, S. T., Rice, J. R., 1986. Crustal earthquake instability in relation to the depth variation of frictional slip properties. Journal of Geophysical Research 91 (B9), 9452.

Tsutsumi, A., Shimamoto, T., 1997. High-velocity frictional properties of gabbro. Geophysical Research Letters 24 (6), 699–702.

Tullis, J., Yund, R. A., 1987. Transition from cataclastic flow to dislocation creep of feldspar: Mechanisms and microstructures. Geology 15 (7), 606.

Tullis, T. E., 2007. Friction of Rock at Earthquake Slip Rates. In: Treatise on Geophysics. Vol. 4. Elsevier, pp. 131–152.

Uchide, T., Ide, S., 2010. Scaling of earthquake rupture growth in the Parkfield area: Self-similar growth and suppression by the finite seismogenic layer. Journal of Geophysical Research 115 (B11), B11302.

Umino, N., Okada, T., Hasegawa, A., 2002. Foreshock and Aftershock Sequence of the 1998 M 5.0 Sendai, Northeastern Japan, Earthquake and Its Implications for Earthquake Nucleation. Bulletin of the Seismological Society of America 92 (6), 2465–2477.

Urai, J. L., Spiers, C. J., Zwart, H. J., Lister, G. S., 1986. Weakening of rock salt by water during long-term creep. Nature 324 (6097), 554–557.

Urata, Y., Yamashita, F., Fukuyama, E., Noda, H., Mizoguchi, K., 2017. Apparent Dependence of Rate- and State-Dependent Friction Parameters on Loading Velocity and Cumulative Displacement Inferred from Large-Scale Biaxial Friction Experiments. Pure and Applied Geophysics 174 (6), 2217–2237.

Van den Ende, M., Chen, J., Ampuero, J.-P., Niemeijer, A., 2018a. A comparison between rate-and-state friction and microphysical models, based on numerical simulations of fault slip. Tectonophysics 733, 273–295.

Van den Ende, M. P. A., Marketos, G., Niemeijer, A. R., Spiers, C. J., 2018b. Investigating compaction by intergranular pressure solution using the Discrete Element Method. Journal of Geophysical Research: Solid Earth 123.

Van der Marck, S. C., 1996. Network Approach to Void Percolation in a Pack of Unequal Spheres. Physical Review Letters 77 (9), 1785–1788.

Van Noort, R., Spiers, C. J., 2009. Kinetic effects of microscale plasticity at grain boundaries during pressure solution. Journal of Geophysical Research 114 (B3), 1–12.

Van Noort, R., Spiers, C. J., Pennock, G. M., 2008a. Compaction of granular quartz under hydrothermal conditions: Controlling mechanisms and grain boundary processes. Journal of Geophysical Research 113 (B12), B12206.

Van Noort, R., Visser, H. J. M., Spiers, C. J., 2008b. Influence of grain boundary structure on dissolution controlled pressure solution and retarding effects of grain boundary healing. Journal of Geophysical Research: Solid Earth 113 (3), 1–15.

Verberne, B. A., Chen, J., Niemeijer, A. R., de Bresser, J. H. P., Pennock, G. M., Drury, M. R., Spiers, C. J., 2017. Microscale cavitation as a mechanism for nucleating earthquakes at the base of the seismogenic zone. Nature Communications 8 (1), 1645.

Verberne, B. A., de Bresser, J. H. P., Niemeijer, A. R., Spiers, C. J., De Winter, D. A. M., Plümper, O., 2013. Nanocrystalline slip zones in calcite fault gouge show intense crystallographic preferred orientation: Crystal plasticity at sub-seismic slip rates at 18–150 °C. Geology 41 (8), 863–866.

Verberne, B. A., Niemeijer, A. R., De Bresser, J. H. P., Spiers, C. J., 2015. Mechanical behavior and microstructure of simulated calcite fault gouge sheared at 20-600C: Implications for natural faults in limestones. Journal of Geophysical Research: Solid Earth 120 (12), 8169–8196.

Verberne, B. A., Plumper, O., De Winter, D. A. M., Spiers, C. J., 2014a. Superplastic nanofibrous slip zones control seismogenic fault friction. Science 346 (6215), 1342–1344.

Verberne, B. A., Spiers, C. J., Niemeijer, A. R., De Bresser, J. H. P., De Winter, D. A. M., Plümper, O., 2014b. Frictional Properties and Microstructure of Calcite-Rich Fault Gouges Sheared at Sub-Seismic Sliding Velocities. Pure and Applied Geophysics 171 (10), 2617–2640.

Vermeer, P. A., De Borst, R., 1984. Non-Associated Plasticity for Soils, Concrete and Rock. HERON 29 (3).

Violay, M., Nielsen, S. B., Spagnuolo, E., Cinti, D., Di Toro, G., Di Stefano, G., 2013. Pore fluid in experimental calcite-bearing faults: Abrupt weakening and geochemical signature of co-seismic processes. Earth and Planetary Science Letters 361, 74–84.

Visher, G. S., 1969. Grain Size Distributions and Depositional Processes. Journal of Sedimentary Petrology 39 (3), 1074–1106.

Visser, H. J. M., 1999. Mass transfer processes in crystalline aggregates containing a fluid phase. Ph.D. thesis, Utrecht University.

Visser, H. J. M., Spiers, C. J., Hangx, S. J. T., 2012. Effects of interfacial energy on compaction creep by intergranular pressure solution: Theory versus experiments on a rock analog (NaNO3). Journal of Geophysical Research 117 (B11), B11211.

Wallace, L. M., Reyners, M., Cochran, U., Bannister, S., Barnes, P. M., Berryman, K., Downes, G., Eberhart-Phillips, D., Fagereng, Å., Ellis, S., Nicol, A., McCaffrey, R., Beavan, R. J., Henrys, S., Sutherland, R., Barker, D. H. N., Litchfield, N., Townend, J., Robinson, R., Bell, R., Wilson, K., Power, W., 2009. Characterizing the seismogenic zone of a major plate boundary subduction thrust: Hikurangi Margin, New Zealand. Geochemistry, Geophysics, Geosystems 10 (10).

Wang, K., Bilek, S. L., 2011. Do subducting seamounts generate or stop large earthquakes? Geology 39 (9), 819–822.

Wang, Y., Tonon, F., 2009. Modeling Lac du Bonnet granite using a discrete element model. International Journal of Rock Mechanics and Mining Sciences 46 (7), 1124–1135.

Weiss, J., Pellissier, V., Marsan, D., Arnaud, L., Renard, F., 2016. Cohesion versus friction in controlling the long-term strength of a self-healing experimental fault. Journal of Geophysical Research: Solid Earth, 1–25.

Weng, H., Yang, H., 2017. Seismogenic width controls aspect ratios of earthquake ruptures. Geophysical Research Letters 44 (6), 2725–2732.

Working Group on California Earthquake Probabilities, 1988. Probabilities of large earthquakes occurring in California on the San Andreas fault. U.S. Geological Survey Open-File Report 88-398.

White, S., 2001. Textural and microstructural evidence for semi-brittle flow in natural fault rocks with varied mica contents. International Journal of Earth Sciences 90 (1), 14–27.

Wintsch, R. P., Christoffersen, R., Kronenberg, A. K., 1995. Fluid-rock reaction weakening of fault zones. Journal of Geophysical Research: Solid Earth 100 (B7), 13021–13032.

Wong, P.-Z., Howard, J., Lin, J.-S., 1986. Surface Roughening and the Fractal Nature of Rocks. Physical Review Letters 57 (5), 637–640.

Woodcock, N. H., Mort, K., 2008. Classification of fault breccias and related fault rocks. Geological Magazine 145 (3), 435–440.

Yabe, S., Ide, S., 2017. Slip-behavior transitions of a heterogeneous linear fault. Journal of Geophysical Research: Solid Earth 122 (1), 387–410.

Yamashita, T., Ohnaka, M., 1992. Precursory surface deformation expected from a strike-slip fault model into which rheological properties of the lithosphere are incorporated. Tectonophysics 211 (1-4), 179–199.

Yang, X.-S., 2000. Pressure solution in sedimentary basins: effect of temperature gradient. Earth and Planetary Science Letters 176 (2), 233–243.

Yasuhara, H., 2003. A mechanistic model for compaction of granular aggregates moderated by pressure solution. Journal of Geophysical Research 108 (B11), 2530.

Yasuhara, H., Marone, C. J., Elsworth, D., 2005. Fault zone restrengthening and frictional healing: The role of pressure solution. Journal of Geophysical Research 110, 1–11.

Zahouani, H., Vargiolu, R., Loubet, J.-L., 1998. Fractal models of surface topography and contact mechanics. Mathematical and Computer Modelling 28 (4-8), 517–534.

Zhang, L., He, C., 2016. Frictional properties of phyllosilicate-rich mylonite and conditions for the brittle-ductile transition. Journal of Geophysical Research: Solid Earth 121 (4), 3017–3047.

Zhang, X., Salemans, J., Peach, C. J., Spiers, C. J., 2002. Compaction experiments on wet calcite powder at room temperature: evidence for operation of intergranular pressure solution. Geological Society, London, Special Publications 200 (1), 29–39.

Zhang, X., Spiers, C. J., Peach, C. J., 2010. Compaction creep of wet granular calcite by pressure solution at 28C to 150C. Journal of Geophysical Research 115 (B9), B09217.

Zheng, B., Elsworth, D., 2012. Evolution of permeability in heterogeneous granular aggregates during chemical compaction: Granular mechanics models. Journal of Geophysical Research: Solid Earth 117 (B3).

Zheng, B., Elsworth, D., 2013. Strength evolution in heterogeneous granular aggregates during chemo–mechanical compaction. International Journal of Rock Mechanics and Mining Sciences 60, 217–226.

Zheng, G., Rice, J. R., 1998. Conditions under which velocity-weakening friction allows a self-healing versus a cracklike mode of rupture. Bulletin of the Seismological Society of America 88 (6), 1466–1483.

Zubtsov, S., Renard, F., Gratier, J.-P., Guiguet, R., Dysthe, D. K., Traskine, V., 2004. Experimental pressure solution compaction of synthetic halite/calcite aggregates. Tectonophysics 385 (1-4), 45–57.

Acknowledgements

Writing an acknowledgement, "*how hard could it possibly be?*" (de Bresser, 2018)[1]. Well... I did not know fear until I started to realise I could forget people, misspell names, or otherwise not do justice to the contributions people have made to this thesis. What do you do, when you realise too late you've made a mistake in the only section of the thesis that people actually read? Print a corrigendum? Tweet a public apology? Become religious and pray for forgiveness? I have considered uploading a digital copy of these pages to an online repository, and assign a DOI which I could cite here ("*for the latest version of these acknowledgements, the reader is referred to...*"). I could then update the online version following-up on each complaint I receive. But this would merely be a temporary solution, as digital services and storage facilities come and go. Coming to think of it, all products of humanity have a finite life-span, many of which shorter than the life-expectancy of you, the reader of these acknowledgements[2].

I need something that will last through the ages, something permanent, something... infinite. Allegedly[3], Albert Einstein once said: "*Two things are infinite: the universe and human stupidity; and I'm not sure about the former*". Since the universe is generally thought to be finite in extent, the prospect of harnessing human stupidity to somehow store an updated version of this section, seems daunting. But Einstein has been proved wrong on several occasions (the extent of the universe and the probabilistic interpretation of quantum mechanics are two notable examples), and so there is still

[1] Translated quote from his inaugural lecture, taken horribly out of context.
[2] This is a statistical assessment, not a threat.
[3] Whether or not Einstein actually said this, is still (and will forever be) a matter of debate.

hope for me. One other thing that is as infinite as human stupidity, is the irrational number π (= 3.141592653... and a bit). At present, the number of known decimal places in π well exceeds 10^{13}, with no signs of systematic repetition on the horizon. Let me now show you a magic trick: since the number of decimals in π is infinite, I can guarantee that the number sequence "...08051212152315181204..." will appear somewhere within π. If you now translate each pair of numbers (08, 05, 12, 12, etc.) to a letter in the alphabet, you get *helloworld*. If I also assigned numbers to punctuation, spaces, and capital letters, I could 'store' any arbitrary string of text within the bowels of π. So to solve my problem, I could refer to a range of decimals of π (e.g. decimal positions 2 587 110 689 to 2 587 113 801). The reader would look up these numbers, translate them into text, and read that particular version of the acknowledgements. If I wanted to update my text, I would simply refer to a different segment of π that matches my intended text.

There are two main issues with this plan: first of all, I'd still need to communicate the decimal range that contains my acknowledgements to (prospective) readers, but in the modern era of global communication, this is perhaps not a big deal. The second problem is that I don't know where exactly a given 10 000-digit long sequence will appear. With my luck, it is quite likely that my target decimal range is all the way at the end of π. Although the latter problem is merely a technicality, it is a problem nonetheless, which currently prevents me from updating my acknowledgements when readers start to complain. Thus, I am faced with the biggest challenge of my early academic career: writing an acknowledgement in one take, with no mitsakes.

Here I go, wish me luck[4]...

First off, I'd like to start with the person who wished me good luck just prior to the interview for my PhD position: Magda Mathot-Martens. Magda's best wishes proved heavy, and tipped the scales of the selection to my favour. During my PhD project, Magda has taken great care for my finances and administration, and she has frequently reminded me of my timesheets being overdue. So thanks for everything, Magda, and I'll be back for more of those best wishes soon.

[4] You should definitely do this out loud

Also during my job interview, I met with George Marketos for the first time. George has taught me the dark arts of Discrete Elements with geological patience. Every time I wanted to rush to my next code objective and glance over 'minor' benchmark discrepancies, George pulled me back and made sure I identified and patched these bugs before they could do harm. In spite of his best efforts, I kept having bugs until two weeks before the deadline of submitting this thesis, motivating the quote I put on page −2. On occasion, I have tested George's patience, which has sometimes led to a bit of frictional heating, for which I apologise. George, I thank you for helping me getting started with DEM, and sharing your code with me. Without your help, this project would probably not have taken off.

Those of you who have actually read my thesis (or the table of contents) will have noticed that I switched from DEM to BEM (boundary elements) in between Chapters 4 and 5. I guess most credit for this switch goes to Pablo Ampuero, and also to Yingdi Luo. When the outlook for my experimental and DEM work looked a bit bleak, I decided to have a look at Pablo's and Yingdi's seismic cycle simulator QDYN. Even though my level of FORTRAN was/is on par with my level of Mandarin Chinese (not good), the code was so elegantly written that it took me only a few hours to implement the *Chen-Niemeijer-Spiers* (CNS) model, which formed the basis for Chapters 5 and 6 (and likely many more publications will follow). During Pablo's sabbatical here at Utrecht University, I got deeply impressed by Pablo's knowledge of earthquake source mechanics and numerical modelling thereof. "*You do not really understand something unless you can explain it to your grandmother*" is a quote wrongfully attributed to Albert Einstein[5], but it no less applies to Pablo, who has managed to explain to me how QDYN really works, and why it doesn't work when I use it. I very much enjoyed our discussions and collaborations on the QDYN-chapters of this thesis, and I'm curious to see what the future brings for this open-source project.

Now that the *Chen-Niemeijer-Spiers* model has been mentioned, I think I should address each of these persons one by one. Starting with one of my paranymphs and Chinese magician, Jianye Chen, who taught me I should not push down on the top piston of a direct shear assembly when tightening the tourniquets. I vividly remember Chen's talk at the EGU 2015, during which he unleashed an early version of the CNS

[5]The likely source for this quote is Ernest Rutherford's statement that "*an alleged scientific discovery has no merit unless it can be explained to a barmaid*".

model upon an unsuspecting scientific community. After his presentation, we discussed the implementation of the CNS 'philosophy' into numerical models, and this discussion has continued to go on with yet no end in sight. They say that "*great minds think alike*"[6], and our like-mindedness has led to dazzling discussions and intricate ideas to be implemented in future models. Chen, I greatly enjoyed working with you on our microphysical models, and I will continue to do so.

At this point in the acknowledgements, I realise that I should have perhaps changed the order of addressing people and put the boss, André Niemeijer, first. After all, without André's SEISMIC project, this PhD position would not have existed, and I would not be writing these acknowledgements right now. André, I am deeply grateful for this opportunity to work at one of the finest rock mechanics labs in the world. During these four years, you allowed me to follow my own interests, and random-walk my way through my project. My random walk would not have gotten me very far, though, if it wasn't for your gentle guidance. What's more important still, is the example that you offered of a skilful and successful scientist. I hope that by following your example, I may one day celebrate a bit of academic success of my own.

"*Great Scott! Look at the time!*". It is high time I should address the S in CNS, Chris Spiers. Chris: I am truly honoured to have worked with and have been mentored by one of the greatest scientists in our field. I believe this statement is underlined by your well-earned EGU medal, which we celebrated in Vienna with a large group of people who all thought the same way. Ever since we first met in Camarasa, you have offered me mentorship for being a better student, scientist, and person. Perhaps in a few years time, when you decide to spend some more time in Camarasa to prove that San Salvador is bounded on the east by a lateral ramp rather than by a tear fault, do give me a call. I'd be happy to drive you around again (Doc and Marty back on the road, even though, "*where we're going, we don't need roads...*"), and I'll try to prove you wrong.

Right... Seven down, seventy or so more to go.

Let's continue with my fellow/former SEISMIC team members, Evangelos Korkolis, Zahra Amirzada, Nina Hellebrekers, and Dawin Baden. I've had a fantastic time with

[6] "*... and are equally modest*" – Rob Govers

you guys, playing with the ring shear(s), flooring apartments, fixing your Python codes, and setting-up the 'stick-slipper' (a.k.a. the spring-slider) several times over. People sometimes claim that they are more productive when working within a project group. I can tell you that this is most certainly not true, since way too often you guys have seduced me to go for caffeinated or alcoholic drinks, order pizza, watch a movie in N.112, etc. I could have had my Nobel prize by now... Nonetheless, I want to thank you for the friendship and team spirit you've given me, and I think you've made the SEISMIC project a success.

To the Big Five of NAM: Buffalo Bart, Luuk the Leopard, Ronnie Rhino, Loes the Lion, and Amin the Alephant. You've all contributed much to the social cohesion in the lab, in spite of all your cracks, ruptures, and flaws. The other NAM postdocs Hadi Mehranpour, Yuntao Ji, and Jeroen van Stappen have brought in their expertise from far-away exotic places, like Iran, China, and Belgium. And the NAM + Mariska Tuesday meetings would of course be inappropriately named if it wasn't for Mariska Schimmel, with whom I now share the academic trauma of the capillary tube experiments. Stay strong Mariska, and read Chapter 4, which will offer some insights into healing.

Then there are some people who will always be creepers to me: Piercarlo Giacomel, Anna Kätker, Caspar Sinn, and Wen Zhou. I find it amazing how one project has contained such a wide spectrum of personalities, and it has been my pleasure to have discussed with each of you some salty topics. On the topic of salt I should mention Yu Yang as well, although her time with us has been brief. I thank the the swellers Jinfeng "Ross" Liu and Miao Zhang for keeping me company late at night (in the office, that is...). Whenever you turned off the lights, I figured it was about time to call it a day myself.

I would like to give a special mention to two role-models of mine, Tim Wolterbeek and Suzanne Hangx. Tim has been my example of critical thinking and out-of-the-box problem solving, and has observed my every step up the academic ladder since the 2nd year BSc LAVA course. We have had many (late-night) discussions about model assumptions, experimental uncertainty, and world domination, which has changed the way I look at my modelling work (particularly the latter topic was highly influential). Suzanne has been my greatest fan and big sister in the HPT family, and I always felt greatly motivated by her encouragements. Suze also poked and prodded me until I

started to do a bit of networking on conferences, which marked the start of my quest to lower my Erdős number (and possibly to achieve a finite Erdős-Bacon number). It has been my great pleasure to have been in the Camarasa fieldwork with these two people (Tim and Suzanne, that is, not Erdős and Bacon).

To Maartje H and Maartje H: it has been fun to say hi when encountering the both of you together. Maartje, I know I should have mentioned you in the SEISMIC paragraph above, but it is more fun to do it this way. Maartje, because you interrupted me while writing these acknowledgements, I forgot what else I wanted to say... Something about that epic cycling trip we did with Giannis Zarikos in Camarasa, most likely. Other Camarasa fieldwork friends I'd like to thank are Suzanne Atkins, Peter McPhee, Nevena Andric, notably for the *G and T* and the Rakija. Also thanks to the Three Musketeers of Cariatiz, Arjen Mascini, Frans Aben, and Sander Osinga. An academic wind blew over the Spanish sierras that year, since somehow we all ended up at research institutes. Perhaps next time we can have our reunion at a conference instead of the TNO canteen.

From Spain to Japan, I'd like to thank our Japanese visitors, Miki Takahashi, Ayumi Okamoto, and Michiyo Sawai for their scientific and cultural contributions to the lab (*hanami*!). Miki's teachings in origami have been particularly useful for making leak-proof paper and aluminium foil boxes for various purposes.

I will now break a long-standing tradition of forgetting to mention Sabine den Hartog in thesis acknowledgements. While working on my thesis, I've regularly picked up yours as a standard/cheat sheet, which to me marks the level of quality I should be aiming for. It has been good seeing you once every while on conferences or in Utrecht, and perhaps we will be (almost) neighbours very soon!

Continuing now with some other HPT relatives who have spread their wings a little while ago: Anne Pluymakers was never shy to give me honest advice, and Elisenda Bakker has frequently filled the HPT halls with singing and laughter (things turned a bit quiet when you left). With Nawaz Muhammad I learnt the ropes at the lab, preparing samples, conducting experiments, processing the data, and making/analysing microstructures. Together with Colin Peach and (now professor) Hans de Bresser, we have spent a lot of time mangling the stress relaxation data. It has been an honour guarding your back as one of your paranymphs.

Many thanks to Theo van Zessen for granting me access to the PBS cluster. I cannot imagine how I would have managed not running batches of DEM/QDYN simulations all in once. In relation to my modelling work, I should also acknowledge all of the help I directly and indirectly received from the people on Stack Overflow. Fellow programmers reading this will immediately know what I'm talking about. For those who don't: imagine that a component of your experimental set-up is broken. You take it to one of the technicians, and as if by magic it gets fixed right away. When my code is broken, I go to Stack Overflow, and as if by magic I gets fixed right away (or it breaks my system).

This then immediately brings me to the masters of the craft and (former) occupants of the workshop/coffee corner: Gert Kastelein, Floris van Oort, Peter van Krieken, Thony van der Gon Netscher (our very own Chuck Norris), Gerard Kuijpers, and Han de Witte. You've been a great help to me in materialising and upgrading my scotch tape designs, and you have been (together with Leonard Bik) good company during our early-morning coffee breaks. To Eimert de Graaff I'd like to say: I don't know when you will read this, but when you do, you will hopefully be a bit better already. Your friends from HPT are all very eager to make that boat trip with you. Get well soon...

Thanks to the TNO team Thibault Candela, Sander, Peter Fokker, Jan ter Heege, and Joost Roholl. The Lupras (and associated free lunch) were very nice, and I've enjoyed the discussions we've had that somehow always took place in the vicinity of food. I should also not forget to mention the people who have regularly fed me, Claudia Giese, Sietske Verboom, and Chris, who together with Magda also reminded me to eat more[7]. There were also other UU suspects who always arrived at the scene when there was food, coffee, or beer around (I'm talking about you, Markus Ohl, Paul Oonk, Alejandro Rodriguez + JK). You have my thanks for sharing the restaurant bills with me. I'm afraid that starvation will be imminent as soon as I leave the HPT lab, but perhaps my future colleagues can prevent that from happening.

To my paranymphs, Evangelos and Chen: thanks for siding with me against my opponents. Remember that, when I faint, you are entitled to answer two questions each, so please read my thesis and make it count!

[7]Literally now, while I'm writing this paragraph, at 20:14 in the evening on Secretary's Day, Magda magically appears to tell me to eat. I'm not kidding...

Evangelos always praised the way in which ik midden in de zin van voertaal veranderde, en ik doe dit nu maar weer eens om een aantal mensen te bedanken die niet direct met HPT verbonden zijn. Allereerst bedank ik mijn vrienden van Aquapoldro, met wie ik het grootste deel van mijn waterpolocarrière heb doorgebracht. Niet alleen voor die vele uren in het zwembad en in de sportschool, maar vooral ook voor de vele uren waarbij ik verstek heb laten gaan om in Utrecht aan mijn andere carrière te werken. Ik waardeer het zeer dat ik met jullie in mijn laatste polojaar toch nog een keer het kampioenschap heb kunnen vieren. Daarnaast bedank ik mijn altijd afwezige huisgenootje Enja Blasse: we hebben vier jaar intensief langs elkaar geleefd, met als belangrijkste resultaat een tevreden-kleurige muur met daaraan een foto van ringstaartmaki's. Wat meer kan ik wensen?

Ik heb op meerdere plekken in dit dankwoord liefkozend naar mijn HPT vrienden en collega's gerefereerd als familie, maar er is natuurlijk nog een andere familie tot wie ik mij als laatste wil wenden. Pap, mam, Paul, Frank opa en oma: waar moet ik beginnen? Waarschijnlijk moet ik hiervoor ver teruggaan in mijn geheugen. Ik herinner mij een mapje met in eerste instantie leeg papier, ongeveer ter grootte van dit proefschrift. Op één van de velletjes papier was een stukje tekst geschreven: dat ik dit mapje maar snel zou vullen met wetenswaardigheden over de aarde, het heelal, en andere zaken die ik tegenkwam in boeken en landkaarten, en dat ik later maar een slimme jongen moge worden. Ik herinner mij een oude stoommachine, vuur proberen te maken met een vuurboog, en andere *hands-on* activiteiten wanneer ik in Assen logeerde. Ik herinner mij vele fossielenjachten tijdens vakanties, met vondsten soms zo groot dat ze niet mee te nemen waren. Was ik zonder deze aanmoedigingen hier nu geweest? Hoogstwaarschijnlijk niet. Dit proefschrift is daarom minstens zoveel jullie verdienste als dat het de mijne is. Dank jullie wel, voor alles...

All right dear non-native reader, you can follow along again. I wonder how I will look back onto this thesis, one day when I am old and grumpy, reading these acknowledgements again. Maybe it is not such a good idea to make these acknowledgements permanent. Maybe it is for the best that these words will remain hidden within the decimals of π, and that instead you will simply carry them with you, where they matter most...

Curriculum Vitae

Name: Martijn Peter Anton van den Ende

Born: 24 September 1990, Den Haag, the Netherlands

Education

2011 – 2013	MSc Earth Sciences, Utrecht University, Utrecht
2008 – 2011	BSc Earth Sciences, Utrecht University, Utrecht
2002 – 2008	Stedelijk Gymnasium, Apeldoorn